

ABSTRACT

Title of Document: PRINCIPLES OF INFORMATION
PROCESSING IN NEURONAL
AVALANCHES

Hongdian Yang, Ph.D., 2011

Directed By: Professor Rajarshi Roy, Institute for Physical
Science and Technology
Dr. Dietmar Plenz, National Institutes of Health

How the brain processes information is poorly understood. It has been suggested that the imbalance of excitation and inhibition (E/I) can significantly affect information processing in the brain. Neuronal avalanches, a type of spontaneous activity recently discovered, have been ubiquitously observed *in vitro* and *in vivo* when the cortical network is in the E/I balanced state. In this dissertation, I experimentally demonstrate that several properties regarding information processing in the cortex, *i.e.* the entropy of spontaneous activity, the information transmission between stimulus and response, the diversity of synchronized states and the discrimination of external stimuli, are optimized when the cortical network is in the E/I balanced state, exhibiting neuronal avalanche dynamics. These experimental studies not only support the hypothesis that the cortex operates in the critical state, but also suggest that criticality is a potential principle of information processing in the cortex. Further, we study the interaction

structure in population neuronal dynamics, and discovered a special structure of higher order interactions that are inherent in the neuronal dynamics.

PRINCIPLES OF INFORMATION PROCESSING IN NEURONAL
AVALANCHES

By

HONGDIAN YANG

Dissertation submitted to the Faculty of the Graduate School of the
University of Maryland, College Park, in partial fulfillment
of the requirements for the degree of
Doctor of Philosophy
2011

Advisory Committee:

Professor Rajarshi Roy, Chair

Dr. Dietmar Plenz, Co-chair

Professor Edward Ott

Associate Professor Wolfgang Losert

Assistant Professor Patrick Kanold

Associate Professor Jose Helim Aranda-Espinoza (Dean's representative)

© Copyright by
HONGDIAN YANG
2011

Acknowledgements

I am very grateful to everyone who makes my neuroscience research and this Ph.D. dissertation possible in every aspect.

First to my advisors, Dr. Rajarshi Roy and Dr. Dietmar Plenz. It is a great honor and pleasure to finish my Ph.D. with your guidance and supervision. What I have learned from Raj is not limited to the rigorous skills and critical thinking required for a researcher, but also how to face problems in life. Most of what I have known about neuroscience is from Dietmar, and he nurtured my experimental skills and analytical thinking in this field.

To my lab colleagues, especially Dr. Woodrow Shew and Dr. Shan Yu. Sometimes postdocs are like mentors to graduate students. Indeed, during my years in the lab, I have closely collaborated with Woody and Shan, and learned a great deal from them. The discussions are refreshing and stimulating, and our collaborations are fruitful. I thank Andreas Klaus, Dr. Oren Shriki, and Timothy Bellay. Talking and discussing with you is always a pleasure, and the clashing of ideas and thoughts always excites me. I also thank Craig Stewart, Dr. Gireesh Dharmaraj and Dr. Thomas Petermann for the help with experimental setup.

I thank my friends, in particular Chengyun Huang, Yu Fu and Yajun Zhang, for always standing behind me. You shared my joys and sorrows, and you helped me out when I was down. I am grateful to have such good friends in my life.

Finally to my beloved parents. No words can express my gratitude for raising me up as who I am. Mom, you always care about my life, and Dad, your concern and encouragement about my research and life mean a lot to me. Thank you for always supporting me!

Table of Contents

Acknowledgements	ii
Table of Contents	iv
List of Tables.....	viii
List of Figures	x
Chapter 1: Introduction	1
1.1 How does the brain process information?.....	1
1.2 Neuron: the basic information processing unit	5
1.3 The complexity of neuronal network	7
1.4 A healthy brain is a balanced brain.....	8
1.5 Attempts to apply the theory of criticality to cortical dynamics.....	9
1.6 Spontaneous vs. sensory-evoked neuronal activity.....	11
1.7 Neuronal avalanches	13
1.8 Advantages of being critical.....	17
1.9 Questions remained for the critical brain hypothesis.....	18
1.10 Dissertation outline	19
Bibliography.....	22
Chapter 2: Experimental design, data analysis methods and computational models..	28
2.1 MEA recordings in organotypic cortex cultures	28
2.2 Stimulus-evoked activity in vitro	30
2.3 Pharmacology in vitro	31
2.4 MEA recordings in monkeys	32
2.5 MEA recordings in rats	34
2.6 Unit recordings in cat.....	34
2.7 Definitions of bursts and neuronal avalanches.....	35
2.8 Definition of κ	36
2.9 Model	41
Bibliography.....	43
Chapter 3: Information capacity and transmission are maximized in balanced cortical networks with neuronal avalanches.....	45
3.1 Introduction.....	45
3.2 Methods.....	47

3.2.1	Cross correlation in unit activity in awake monkey.....	47
3.2.2	A brief review of information theory.....	47
3.2.3	Binary patterns and entropy H.....	48
3.2.4	Mutual information MI.....	50
3.2.5	Likelihood of participation L.....	52
3.2.6	Data shuffling to destroy interactions.....	53
3.2.7	Model.....	53
3.2.8	Statistical Analysis.....	53
3.3	Results.....	54
3.3.1	Peak information capacity of ongoing activity for intermediate E/I and neuronal avalanches.....	57
3.3.2	Peak information transmission between stimulus and response for intermediate E/I and neuronal avalanches.....	60
3.3.3	Competition between activity rates and interactions explains peak in entropy.....	63
3.3.4	Experimental results confirmed in a computational network-level model.....	66
3.3.5	<i>In vivo</i> entropy matches <i>in vitro</i> prediction.....	68
3.4	Discussion.....	72
	Bibliography.....	76
Chapter 4: Maximal variability of phase synchrony in cortical networks with neuronal avalanches.....		
		79
4.1	Introduction.....	79
4.2	Methods.....	81
4.2.1	Phase synchrony.....	81
4.2.2	Phase and phase difference histogram.....	82
4.2.3	Anti-phase locking.....	82
4.2.4	Network synchrony and burst synchrony.....	83
4.2.5	Entropy measurements.....	85
4.2.6	Power spectra.....	86
4.2.7	Statistical analysis.....	87
4.3	Results.....	87
4.3.1	Neuronal burst area and duration have moderate mean and maximum entropy at $\kappa \sim 1$	87
4.3.2	Neuronal synchrony has moderate mean and maximum entropy at $\kappa \sim 192$	92
4.3.3	Anti-phase locking in disinhibited cortical networks with $\kappa > 1$	99
4.4	Discussion.....	101
4.4.1	$\kappa > 1$ identifies a pathological state of synchrony typical for epilepsy..	101
4.4.2	$\kappa \sim 1$ identifies a critical phase transition.....	102
4.4.3	Anti-phase synchrony for $\kappa > 1$	105
4.4.4	Comparison to the cortex dynamics <i>in vivo</i>	106
	Bibliography.....	107

Chapter 5: Neuronal avalanches imply maximal dynamic range in cortical networks at criticality.....	114
5.1 Introduction.....	114
5.2 Methods.....	116
5.2.1 Dynamic range	116
5.2.2 Model	116
5.3 Results.....	116
5.3.1 Quantifying the cortical network state based on κ	117
5.3.2 Stimulus-evoked activity and dynamic range	121
5.3.3 Maximal Dynamic range at criticality, $\kappa \cong 1$	124
5.4 Discussion.....	127
Bibliography.....	129
Chapter 6: Higher-order Interactions characterized in cortical activity.....	132
6.1 Introduction.....	132
6.2 Methods.....	134
6.2.1 Electrophysiological recordings.....	134
6.2.2 LFP analysis	135
6.2.3 Spike analysis.....	136
6.2.4 Ising Model	137
6.2.5 DG model.....	138
6.2.6 Model performance measures	139
6.2.7 Calculating interactions of different orders.....	142
6.3 Results.....	142
6.3.1 Higher-order interactions are essential for ongoing cortical dynamics..	142
6.3.2 Avalanche dynamics contain internal thresholding for spatial coupling	145
6.3.3 Accurate approximation of nLFP activity by a simple parametric model	148
6.3.4 The nature of higher-order interactions generated by thresholding	154
6.3.5 Accurate approximation of the ongoing and evoked spiking activity....	156
6.3.6 Efficient characterization of population activity.....	158
6.3.7 Control analysis.....	162
6.4 Discussion.....	166
Bibliography.....	171
Chapter 7: Conclusion and discussion	175
7.1 Conclusion.....	175
7.2 Discussion	177
7.2.1 Converging the views of criticality, balanced E/I and optimal brain functions.....	178
7.2.2 Criticality might be a preferred state for the brain	179
7.2.3 Pharmacological manipulation of E/I is a complicated process.....	180

7.2.4 Questions that remain.....	180
7.3 Future directions.....	181
7.3.1 Implications from the DG model	181
7.3.2 Imaging.....	182
7.3.3 Optimal functions <i>in vivo</i>	183
Bibliography.....	183
Bibliography.....	187

List of Tables

Table 3.1: *In vivo* results match *in vitro* predictions. Given the range of κ found in the *in vivo* recordings ($1 < \kappa < 1.1$), our *in vitro* results provide the predictions of H, L, and MI shown in the first row. The corresponding measurements from the awake monkeys (second row) and anesthetized rats (third row) match the *in vitro* predictions, *i.e.* they are not significantly different ($p < 0.05$). Corresponding data are shown in Fig. 3.7B. All numbers are mean \pm SD.....69

Table 3.2: In line with previous studies, our *in vivo* monkey results were robust to changes in the detection threshold for nLFPs. For thresholds -2.5, -3 and -3.5 SD we found no significant changes as shown here (mean \pm s.e.m.).....71

Table 6.1: Comparison of the performance of the DG and the Ising model in approximating the nLFP patterns. Compact Gr. and Random Gr. represent the results for spatially compact (cf. inset of Fig. 6.1D, main text) groups and randomly chosen groups, respectively. Note that all 3-electrode groups were randomly chosen. N is the number of groups analyzed. D is the JS divergence, *i.e.*, $D_{JS}(P_{data}||P_{model})$. “DG < Ising” is the percentage of groups for which the JS divergence of the DG model is smaller than that of the Ising model. Results are presented as mean \pm SD. P-values for KS test and Mann-Whitney U test were $< 10^{-9}$ in all cases, demonstrating that the JS divergence for the two models came from different distributions.....152

Table 6.2: Comparison of the performance of the DG and the Ising model in approximating the spike patterns. pp and sync stand for pattern probability and number of concurrent spikes (neuronal synchrony), respectively. N_group is the number of groups analyzed. N_neuron is the number of neurons that included. D is the JS divergence, *i.e.*, $D_{JS}(P_{data}||P_{model})$. “DG < Ising” is the percentage of groups for which the JS divergence of the DG model is smaller than that of the Ising model. Results are presented as mean \pm SD. P_{KS} , P_U and P_S are p-values for KS test, Mann-Whitney U test and paired-sample Wilcoxon signed rank test, respectively. The paired test is appropriate here as the two models are fitted to the same individual neuronal groups.....157

List of Figures

Figure 2.1: Preparation of culture and example population event. *A*, Light-microscopic image of a somatosensory cortex and dopaminergic midbrain region (VTA) coronal slice cultured on a 60 channel microelectrode array. *Yellow dot*: stimulation site. *Black dots*: recording sites. *B*. Shown is an example of a population event revealed by widespread fluctuations in the local field potential (LFP) recorded by the micro-electrode array. Each trace is 600 ms of recorded LFP from one electrode in the array.....29

Figure 2.2: Positive correlation between LFP amplitude and unit activity. Number of extracellular spikes correlates with the size of simultaneously recorded nLFP burst ($R = 0.84 \pm 0.13$; $n = 5$). Each point represents total number of spikes versus the corresponding spontaneous nLFP burst size.....30

Figure 2.3: Negative LFP peaks (nLFPs) correspond to the times of spiking during ongoing activity. *A*, Local units increase their firing rates around the occurrence of nLFPs. Average peri-event time histogram (PETH) of spike firing rate relative to the occurrence of nLFPs recorded by the same electrode (ongoing activity; pre-motor cortex; bin width = 2 ms; 53 single units; monkey A). Time zero (nLFP time) is marked by the blue vertical line. *B*, Average LFP waveforms turn negative around the time of unit firing. Spike triggered average (STA) in LFP waveform averaged over 53 single units (the same data set as in *A*). The time of spikes (time zero) is marked by the blue vertical line. Three neurons with extremely high firing rates (>30 spikes/s) were not included to avoid the masking of other neurons, though they showed very similar results. The artifacts due to the residue of spike waveforms left in LFPs was removed in both *A* and *B*.....33

Figure 2.4: Time threshold τ in burst definition. Shown is an example of an inter-peak interval distribution of nLFPs on the array from one experiment. Two time scales are prominent: (1) short time intervals between peaks within periods of activity and (2) long time intervals reflecting periods with no activity (identified by the hump in this example). *Red line*: choice of τ36

Figure 2.5: Definition of κ . *Left*: Probability distribution functions (PDFs) of spontaneous cluster sizes for a normal (no-drug, *black*), disinhibited (PTX, *red*), and hypo-excitabile (AP5/DNQX, *blue*) cultures. *Broken line*: $-3/2$ power-law. Cluster size s is the sum of nLFP peak amplitudes within the cluster; $P(s)$ is the probability of observing a cluster of size s . *Right*: Corresponding cumulative distribution functions (CDFs) and quantification of the network state using κ , which measures deviation from a $-1/2$ power-law CDF (*broken line*). *Vertical gray lines*: The 10 distances summed to compute κ , shown for one example PTX condition (*red*).....37

Figure 2.6: Estimating σ using κ . *A*, Using our model, we compared the true value of σ to an estimate based on activity clusters. The black dashed line has slope 1, representing a perfect estimate. The new measure κ (*red*) accurately estimated the underlying branching parameter over a wide range of subcritical to supercritical states. In contrast, an estimate of the branching parameter σ based on calculating ratios of descendants to ancestors, *i.e.* active sites during period $t+1$ divided by active sites during period t , varied significantly in its precision depending on network state and time periods used. A reliable estimate was achieved when the correct temporal resolution for each network state was available and when comparing the first two consecutive time steps of a cluster (*light blue*; $\sigma_{est} = A(2)/A(1)$;

$A(t1)$ and $A(t2)$ are the number of active neurons during time $t1$ and $t2$ respectively). Importantly, when the exact temporal resolution was not known, estimates tended to stray widely from the real value for subcritical and supercritical dynamics. For $\sigma_{est} = A(11:20)/A(1:10)$ (black) and subcritical dynamics, clusters tended to die during $t1 = 1:10$, leading to an underestimate of σ . Conversely, clusters tended to expand supralinearly for $t2 = 11:20$ in supercritical dynamics, leading to an overestimate of σ . For comparison, other variations of sampling situations were also plotted (green: $\sigma_{est} = A(29:31)/A(26:28)$; dark blue: $\sigma_{est} = A(9:11)/A(6:8)$).

B, Comparison in the accuracy of estimating true σ using various metrics to quantify differences between CDF (network model). Red: κ with 10 logarithmically spaced β_k values provides the most reliable and linear estimate of σ . Blue: modified κ with linear spacing of β_k values reveals increased mismatch for extreme sub-critical and supercritical dynamics. Green: Kolmogorov-Smirnov statistic using the maximal distance between two CDF performed worst.....39

Figure 3.1: Relationship between mutual information (MI) and correlation coefficient (CC). The black points compare MI and CC for all *in vitro* experiments. The dashed line is an estimated lower bound, which is reached for $L = 0.5$. The upper line is an estimated upper bound, which is reached for very low or very high L . The estimated bounds were obtained numerically for a single pair of binary vectors (10,000 events), each with the same L (0.1 to 0.9) and CC (0.1 to 0.9). These bounds are only approximate, because in the experiments, L is not the same from one electrode to another.....52

Figure 3.2: Measuring the neural activation pattern repertoire for a range of E/I conditions. **A**, Example LFP recordings under conditions of reduced E (left), unperturbed

E/I (middle), and reduced I (right). Scale bars: 250 ms x 10 μ V (left, middle) and 250 ms x 100 μ V (right). Population events were defined based on large negative deflections ($< -4SD$, green). **B**, (top) Single examples of population events represented as binary patterns: 1 = active site, 0 = inactive. (bottom) Rasters including 100 consecutive population events represented as binary patterns; each row represents one event, each column represents one recording site. Left: reduced E. Middle: unperturbed. Right: reduced I. **C**, Shape of event size distributions reveal changes in E/I, which are quantified with κ (see Methods; broken line: power law with exponent of -1.5).....56

Figure 3.3: Ongoing activity - peak information capacity at intermediate E/I ratio specified by $\kappa \approx 1$. **A**, Information capacity (entropy H) of the pattern repertoire is maximized when no drugs perturb the E/I ratio. Significant differences marked with * ($p < 0.05$). Box plot lines indicate lower quartile, median, upper quartile; whiskers indicate range of data, excluding outliers (+, >1.5 times the interquartile range). **B**, The statistic κ , provides a graded measure of E/I condition based on network dynamics (Methods). **C**, Entropy H peaks near $\kappa \approx 1$. Each point represents one recording of ongoing activity ($n = 47$, 8x8 MEA, 1 hr, color indicates drug condition; red = PTX, blue = AP5/DNQX, black = no drug). Line is the binned average of points. **D**, The peak in entropy H is robust to changes in spatial resolution (green, 4x4 coarse-binned, 1 hr), spatial extent (orange, 4x4 subregion, 1 hr) and duration (purple, 4x4 coarse-binned, 12 min) of recording. (black, same data as in **A**). Error bars indicate mean \pm s.e.m.....58

Figure 3.4: Results robust to bin choices. The results shown in Fig. 3.3C, D (black, green) for H vs. κ for 8x8 patterns (top) and coarse-binned 4x4 patterns (bottom) were recomputed

with different averaging bins. The different bin partitions are shown below the curves with corresponding colors.....60

Figure 3.5: Stimulus-evoked activity - peak information transmission at intermediate E/I ratio specified by $\kappa \approx 1$. *A*, Single shock stimuli with 10 different amplitudes (10-200 μ A) were applied 40 times each using a single electrode. The pattern repertoire of stimulus-evoked activity has maximum entropy near $\kappa \approx 1$. This holds for 8x8 response patterns (black line) as well as coarse resolution 4x4 patterns (green line). Points correspond to 8x8 patterns: light blue – AP5/DNQX, gray – no drug, pink – PTX. *B*, The efficacy of information transfer, *i.e.* mutual information of stimulus and response, also peaks near $\kappa \approx 1$. The dashed line indicates the highest possible mutual information given 10 stimulus levels. (black - 8x8; green – 4x4). Error bars indicate s.e.m.....62

Figure 3.6: Peak information capacity explained. A detailed analysis of *in vitro* experimental results (top, Fig. 3.3D, green) and model results. *A, B* Upper bounds on entropy are set by 1) the average likelihood that sites participate in patterns (dashed) and 2) the number of patterns observed (dash-dot). When the effects of interactions are removed by shuffling (Methods), the entropy reaches these bounds (black), but the measured entropy (green) is always lower due to interactions. *C, D* Rise in participation likelihood L as E/I ratio is increased. This rise accounts for the bounds (dashed) shown in A,B. *E, F* Rise in interactions between sites (mutual information, red) is proportional to the loss in information capacity ΔH (blue). All error bars indicate s.e.m.....65

Figure 3.7: *In vivo* properties predicted from *in vitro* results. *A*, Population event size distributions from ongoing activity in two awake monkeys (blue) and an example rat (green) are near a power-law with exponent -1.5 (dashed line), *i.e.* they exhibit neuronal avalanches

and $\kappa \approx 1$. **B**, In line with *in vitro* and model predictions for $\kappa \approx 1$, *in vivo* entropy was high and mutual information between recording sites was moderate. (stars - two recordings on different days from each monkey; squares - anesthetized rats, $n = 6$). The spatial extent of recorded area was approximately matched.....69

Figure 3.8: Histograms of pairwise correlation coefficients of unit activity in the awake monkeys. As reported previously (Ecker *et al.*, 2010; Renart *et al.*, 2010) the average across all pairs is near zero and positive. The histogram of all pairwise CC values for monkey 1 (left) and monkey 2 (right) are shown. The mean \pm sem CC values were 0.050 ± 0.002 and 0.015 ± 0.001 for monkey 1 and monkey 2 respectively.....71

Figure 4.1: Spontaneous neuronal burst activity in cortex organotypic cultures grown on integrated planar microelectrode arrays (MEA). **A**, Light-microscopic image of a neural culture including somatosensory cortex and ventral tegmental area (VTA) grown on a 60 channel MEA. Black dots indicate the location of the $n = 59$ recording electrodes. The ground electrode is outside the imaged region. **B**, Examples of local field potential (LFP) traces simultaneously recorded during a burst of neural activity (no drugs applied). The spatial arrangement of LFP traces matches that of the electrodes from which they were recorded. *Inset*: magnified view of three LFP traces. **C**, Average normalized power spectra for normal (black, no drug, $n = 8$), disfacilitated (blue, DNQX/AP5, $n = 8$), and disinhibited conditions (red, PTX, $n = 8$). The spectra were typically broadband without strong peaks under normal and disfacilitated conditions, while prominent β -oscillations (10 – 20 Hz) emerged under disinhibited conditions. Error bars indicate \pm SEM.....89

Figure 4.2: Burst area and duration have moderate mean and maximum entropy near $\kappa = 1$. *A*, Network dynamics were parameterized using κ . Low κ , $\kappa \approx 1$, and high κ indicate disfacilitated, neuronal avalanche, and disinhibited dynamics respectively. As network activity increased with an increase in κ , the average spatial extent of spontaneous bursts rose slowly for small κ , and more steeply near $\kappa = 1$. Each point is the averaged burst area from a 1 hr recording. *B*, The diversity, *i.e.* Shannon entropy, of burst area was highest near $\kappa = 1$. *C*, The average duration of bursts also rose strongly near $\kappa = 1$ and saturated for high κ . *D*, Entropy of burst duration peaked near $\kappa = 1$. Error bars indicate \pm SEM.....91

Figure 4.3: Assessing phase synchrony from multi-site LFP recordings. *A*, Example LFP amplitude trace recorded from a single electrode under disinhibited condition. A 100 ms period (red box) is expanded (lower trace). *B*, Using the Hilbert transform, the LFP amplitude trace is converted to a corresponding phase trace. Top: Expanded phase period. Note that phase near $\pm\pi$ corresponds to negative LFP peaks, while phase near zero coincides with positive LFP peaks (arrows). Lower trace shows corresponding phase for the full time period in *A*. *C*, Examples for lack of phase-locking (left), in-phase locking (middle) and combined in-phase and anti-phase locking (right) taken from four sites (colors). Top row: LFP traces. Middle row: phase traces. High phase synchrony appears as times when many sites display a similar phase trace simultaneously (middle), while dispersed phases indicate lack of synchrony (left). Anti-phase locking appears as ‘bundles’ of in-phase traces separated by π (right; double headed arrow). Note low LFP amplitudes during lack of synchrony. Bottom row: The phases at the time indicated by the black arrow are visualized on a unit circle. The phase synchrony measure, r , is the distance (length of red arrow) between the origin and the center of mass of the phases. Note that anti-phase locking tends to reduce r .93

Figure 4.4: Phase synchrony dynamics for example bursts under different conditions of network excitability. *A*, Moderate levels of phase synchrony under normal condition. Time of the burst indicated by the black bar. Top: Dynamic phase histogram. Color indicates the number of electrodes with a given phase (vertical axis) at a given time (horizontal axis). Phase ‘bundles’ marked by yellow/red pixels over time indicate many sites with the same phase, *i.e.* in-phase locking. Middle: Dynamic phase difference histogram. Color indicates the number of electrode pairs with a given phase difference (vertical axis) at a given time (horizontal axis). Phase differences near 0 indicate in-phase locking. The gray histogram to the right is the time average of the dynamic phase difference histogram. Note dominance of in-phase locking. Bottom: Phase synchrony r . Dashed line indicates $r = 0$. Phase synchrony r is high during periods of in-phase locking. *B*, Disfacilitated activity is characterized by brief and weakly synchronized bursts. Same as *A*, but during an example burst in the presence of DNQX/AP5. *C*, Disinhibited activity is characterized by strongly synchronized long-lasting bursts, anti-phase locking (phase differences near π), and an underlying prominent ~ 20 Hz β -oscillation. Same as *A*, but in the presence of PTX. Burst duration extends beyond period shown. Quantification of anti-phase locking, *APL*, is illustrated in time-averaged dynamic phase difference histogram (right).....95

Figure 4.5: Neural synchrony attains moderate mean and maximum entropy near $\kappa = 1$. *A*, Mean network synchrony showing a slow rise low κ , a sharp increase near $\kappa = 1$ (gray area), and saturation for high κ . *B*, The entropy of network synchrony showing a peak close to $\kappa = 1$. *C*, Mean instantaneous network synchrony showing a gradual rise with κ indicating that the increase in burst duration does not fully explain the rising trend in *A*. Gray line: control, computed during duration-matched non-burst periods. *D*, Entropy of instantaneous network synchrony is maximal near $\kappa = 1$. *E*, Mean instantaneous burst synchrony does not

change with κ . Thus, burst area and duration are sufficient to explain rising trend in mean synchrony. Gray line: control, computed for electrodes which do not participate in bursts. **F**, The peak in entropy persists for instantaneous burst synchrony.....98

Figure 4.6: The relation of average synchrony and entropy of synchrony with respect to κ is independent of spatial extent and spatial resolution of MEA recordings. The data shown and described in Fig. 4.5 were recomputed using two different arrangements of MEA electrodes. **A**, 4x4 compact group of electrodes covering a 800 μm x 800 μm recording area near the center of the array (red). **B**, 4x4 sparse group of electrodes covering the full 1600 μm x 1600 μm area, but with half the spatial resolution (blue). **C – H**, Same figure legend as in Fig. 4.5A – F.....100

Figure 5.1: Measuring spontaneous and stimulus-evoked activity from cortical networks. **A**, Light-microscopic image of a somatosensory cortex and dopaminergic midbrain region (VTA) coronal slice cultured on a 60 channel microelectrode array. *Yellow dot*: stimulation site. *Black dots*: recording sites. **B**, Number of extracellular spikes correlates with the size of simultaneously recorded nLFP burst ($R = 0.84 \pm 0.13$; $n = 5$). Each point represents total number of spikes versus the corresponding spontaneous nLFP burst size. **C**, Example recordings of spontaneous LFP fluctuations (*left*) and nLFP rasters (*right*) for three drug conditions (*top*–AP5/DNQX, *middle*–no drug, *bottom*–PTX.) **D**, Examples of LFP evoked by 70 μA stimulus (*left*) and rasters recorded during the application of four stimuli of amplitudes 50, 40, 90, 150 μA (*yellow line*: stimulus time) (*right*) for three drug conditions. For both spontaneous (**C**) and stimulus-evoked (**D**) activity AP5/DNQX (PTX) typically results in reduced (increased) amplitude LFP events with lesser (greater) spatial extent. In

(C), (D), black dots on the LFP traces indicate nLFP events, raster point color indicates nLFP amplitude, and all scale bars (*left*) represent 50 μV , 100 ms.....118

Figure 5.2: Change in the ratio of excitation/inhibition moves cortical networks away from criticality. *A*, *Top*: Probability distribution functions (PDFs) of spontaneous cluster sizes for a normal (no-drug, *black*), disinhibited (PTX, *red*), and hypo-excitable (AP5/DNQX, *blue*) cultures. *Broken line*: $-3/2$ power-law. Cluster size s is the sum of nLFP peak amplitudes within the cluster; $P(s)$ is the probability of observing a cluster of size s . *Bottom*: Corresponding cumulative distribution functions (CDFs) and quantification of the network state using κ , which measures deviation from a $-1/2$ power-law CDF (*broken line*). *Vertical gray lines*: The 10 distances summed to compute κ , shown for one example PTX condition (*red*). *B*, Simulated cluster size PDFs (*top*) and corresponding CDFs (*bottom*) for different values of the model control parameter σ . *C*, Summary statistics of average κ values for normal, hypo-excitable, and disinhibited conditions (* $p < 0.05$ from normal). *D*, In simulations, κ accurately estimates σ . *Broken line*: $\kappa = \sigma$. *Colored dots*: examples shown in *B*.....120

Figure 5.3: Peri-stimulus time histograms (PSTHs) of evoked activity. nLFP versus time averaged over 40 stimuli at each stimulus level (color coded) are compared for three drug conditions (left – PTX, middle – no drug, right – AP5/DNQX). In the AP5/DNQX condition the system is relatively insensitive due to suppressed excitation, *i.e.* the PSTH is flat until a stimulus level of about 60 μA is reached. In the PTX condition, the largest stimulus levels result in very similar PSTHs, demonstrating the tendency for response to saturate when

inhibition is suppressed. Note that the response to a given stimulus level, R , in the main text was defined as the integral of the PSTH.....122

Figure 5.4: Stimulus-response curves and dynamic range Δ . *A*, Experimental response R evoked by current stimulation of amplitude S for three example cultures with different κ values. *Orange arrows*: range from S_{min} to S_{max} ; length is proportional to Δ . Note that Δ is largest for $\kappa \cong 1$. *B*, Model response evoked by different numbers of initially activated sites; Δ is largest for $\sigma \cong 1$. Like the experiment, each point is calculated from 40 stimuli. *Error bars*: 1 S.E. *C*, Experimental summary statistics for Δ under different pharmacological conditions (* $p < 0.05$ from normal). *D*, Simulation summary statistics for Δ comparing different ranges of κ . (* $p < 0.05$ from $\sigma \cong 1$).....123

Figure 5.5: Network tuning curve for dynamic range Δ near criticality. *A*, In experiments, Δ peaks close to $\kappa \cong 1$ and drops rapidly with distance from criticality. Paired measurements share the same symbol shape; normal (no-drug) condition was measured just before the drug condition. *Circles*: unpaired measurement. *B*, In simulations, Δ is also maximum for $\kappa \cong 1$. Symbol indicates network size (*circles*: $N = 250$; *squares*: $N = 500$; *triangles*: $N = 1000$). Lines represent binned averages.....125

Figure 5.6: Effect of limited stimulus range on Δ . *A*, The *black* line is a re-plot of binned and averaged data from Fig. 5.5A of the main text. The *blue* and *red* lines represent the same experiments, but reprocessed using only < 150 and $< 100 \mu\text{A}$ respectively. The peak of Δ near $\kappa = 1$ is attenuated, but still exists. *B*, In the model, we verify that we should expect

attenuation of the $\Delta(\kappa)$ curve, when the stimulation range is decreased. The strong peak vanishes only for a severely truncated range ($S_{\max} = 16$).....126

Figure 5.7: Effect of network size on Δ . Increasing the system size from $N = 250$ to $N = 1000$ model neurons causes only slight shifts in Δ . For $\sigma < 1$ there is a tendency for slightly lower Δ at higher N127

Figure 6.1: Power law organization of neuronal avalanches identifies interactions between locally synchronized neuronal groups and the insufficiency of pair-wise model in explaining it. *A*, Lateral view of the macaque brain showing the position of the multi-electrode array in pre-motor cortex (*red square; not to scale*). *PS*, Principal Sulcus. *CS*, Central Sulcus. *B*, Example period of continuous LFP at a single electrode. Asterisks indicate the peak negative deflections in the LFP (nLFPs) detected by thresholding (*broken line; -2.5SD*). *C*, Identification of nLFP clusters and patterns. *Top*: nLFPs that occur in the same time bin or consecutive bins ($\Delta t = 2$ ms) define a spatiotemporal cluster, whose size was measured by its number of nLFPs (two clusters of size 4 and 5 shown; gray areas). *Bottom*: Patterns represent the spatial information of clusters only. *D*, Neuronal avalanche dynamics are identified when the sizes of all clusters distribute according to a power law with slope close of -1.5. The cut-off of the power law reflects the finite size of the microelectrode array and changes with the area of the array used for analysis. Four distributions from the same original data set (*solid lines*, Monkey A) using different areas (*inset*), *i.e.*, number of electrodes (n), are superimposed. The power law reflects interactions between neuronal groups from different sites and vanishes for shuffled data (*broken lines*). A theoretical power law with slope of -1.5 is provided for reference (*dotted line*). *E* and *F*, the Ising model (*red*) fails to reconstruct the power law distribution of the 10-eletrode group as showing in *D*

(orange) (*E*) and other thirty randomly chosen, spatially compact 10-electrode groups (*F*). For comparison, the prediction when no interactions are assumed is also given (Independent model; *Ind.*, grey).....144

Figure 6.2: Coherence potentials indicate the presence of intrinsic threshold in the nLFP cluster formation. *A*, Coherence potential analysis utilizes the full baseline excursion of the nLFP waveform (*red*). *B*, The nLFP waveform at a target electrode is compared with the simultaneously recorded LFP at other electrodes (*black rectangle*). Similarities for each pairwise comparison are quantified by the Pearson correlation coefficient r . Comparisons for randomly chosen, length-matched LFP segments from the source electrode serve as control (random; *green rectangle*). *C*, Similarity in nLFP waveforms at distant sites increases non-linearly with the increase in nLFP amplitude. Plotted are the fraction of electrodes on the array with high similarity ($r > 0.8$) with the source electrode nLFP as a function of nLFP amplitude (Note that it is different from the minimal nLFP amplitude used in Thiagarajan *et al.*, 2010). *Black*: average increase in nLFP waveform similarity over all target channels ($n = 91$). *Green*: Expectation in similarity for random comparisons. Arrows mark threshold (-2.5 SD) used for nLFP detection in the current neuronal avalanche analysis. *D*, The non-linear coherence potential function is revealed for high-similarity requirements. Coherence potential probability plotted as a function of minimal similarity $r > R_{min}$. Note the increase in non-linearity with higher similarity requirement. *E*, Difference between functions in (*D*) and expectation from random controls.....147

Figure 6.3: Dichotomized Gaussian (DG) model. *A*, The distribution of a 3-dimensional Gaussian and its projections at individual 2-dimensional subspaces. Marginal distributions at a 2-dimensional space are represented by probability density contours. Λ : pair-wise

covariance. **B**, Converting continuous variables to binary variables (events) by thresholding. Three continuous Gaussian variables with pair-wise covariance as specified in (A) and without high-order interactions. *Red line*: threshold applied to each variable. To fit the DG model to the data, the pair-wise covariance (Λ) of the multi-dimensional Gaussian and the level of each threshold need to be adjusted in such a way that the resulting binary variables have the identical event rates and pair-wise correlations as the data.....149

Figure 6.4: The DG model predicts 2nd as well as higher-order interactions in neuronal avalanches significantly better than the Ising model. **A**, The DG model (*blue*) reconstructs the power law in avalanche size probability (*dots*) more accurately than the Ising model (*red*). The results for data, the Ising and Ind model are replotted from Fig. 6.1E (top panel). **B**, The DG model is also superior in predicting the probabilities of individual patterns (corresponding data from a). Observed pattern probability P is plotted against model predictions. Solid line indicates equality. Most common pattern (all zeros; inactive) not shown for visual clarity. **C**, Quantification of model prediction demonstrates 1–2 orders of magnitude of improvement when using the DG model as compared to the Ising model. *Left*: Cumulative distribution of JS divergence between the observed and predicted cluster size distribution for $n = 30$ randomly chosen, spatially compact 10-electrode groups out of $n = 91$ electrodes (monkey A; cf. Fig. 6.1F). *Right*: Corresponding analysis for pattern probability distributions. Time bins of the original data set were randomly assigned to one of two sets. Model parameters were determined from one set only and predictions were made for the second set. *Half-data*: to use the results measured in one half to predict the corresponding behavior of the other half. **D**, The DG model accurately predicts 2nd (θ_{ij}) and 3rd order (θ_{ijk}) interactions. In comparison, the Ising model is less accurate for 2nd order interactions (*arrow*) and fails completely to predict 3rd order interactions (ellipsoid, *arrow*). Measured interactions

of 1st to 3rd order (θ_i , θ_{ij} , and θ_{ijk} , respectively) are plotted against model predictions for $n = 98$ randomly chosen 3-electrode groups from 91-electrode activity (monkey A). **E**, Corresponding measured pattern probability plotted against model predictions (over all 3-electrode groups). Solid line indicates equality. **F**, The DG model accurately predicts the power law in avalanche sizes also for systems much larger than 10 sites. Prediction for $n = 24, 47, 91$ electrode sites are shown (cf. Fig. 6.1D).....153

Figure 6.5: The magnitude of higher-order interactions introduced by thresholding depends on event rate and strength of pair-wise correlations. **A**, 3rd order interactions in the binary variables cannot be neglected if, for the Gaussian variable, the covariance is strong and the mean is far below or above 0. Change in the magnitude of 3rd order interaction (θ_{ijk}) is shown as a function of the mean (γ) and the covariance (A) of an underlying 3-dimensional Gaussian, $\mathbf{u} \sim N(\gamma, A)$. θ_{ijk} was calculated for binary variables obtained by applying the threshold $u_i > 0$. The white dot marks the average mean and covariance of the hidden Gaussians estimated in the DG model for nLFPs (cf. Fig. 6.4D). **B**, Differences in pattern probabilities between the Ising and the DG model, here quantified as entropy difference, are most pronounced when, for the binary variables, the rate deviates far away from 0.5 and pair-wise correlations are strong, as is the case for avalanche nLFPs (high-rate regime produces a symmetric plot; not shown). Entropy difference is plotted as a function of average rate and pair-wise correlation. Dot (*red*) marks the average rate and pair-wise correlation for nLFP (average of 91 channels and all pairs). For both (**A**) and (**B**), simulations assume homogenous rate and pair-wise correlations for simplicity.....155

Figure 6.6: For strongly coupled sub-groups, the DG model predicts spike patterns in ongoing and stimulus-evoked activities significantly better than the Ising model. A-C, Ongoing spiking activity during avalanche dynamics in monkey A. *A*, DG and Ising model prediction in pattern probability (thirty 10-neuron groups with strongest pair-wise correlation). *Inset*: zoomed-in view, showing that the DG model more accurately predicted high probability patterns. *B*, Cumulative distributions of JS divergence for the groups shown in (*A*). *C*, Measured and predicted interactions for more than 200 3-neuron groups with strongest pair-wise correlation. *Inset*, measured (*x-axis*) and predicted (*y-axis*) pattern probabilities (pp) for the same 3-neuron groups. For more details, see legend of Fig. 6.4B–D. **D-F,** Corresponding results for spiking activity evoked by drifting gratings recorded in area 17 of an anesthetized cat (Cat A, probe 1).....159

Figure 6.7: The DG model requires less data to characterize pattern probabilities compared to direct estimates. A, The DG model outperformed the direct sampling method in predicting pattern probabilities for nLFPs. Variably sized samples were drawn from 15-min of recording (training set) to predict pattern probability in another 15 min data set (testing set). Performance quantified by average JS divergence per pattern in the testing set and plotted against the sample size taken from the training set. *B*, The DG model needs much less amount of data to reach the same accuracy compared with direct sampling. Two reference recordings were chosen for the direct sampling method, with 6-min and 15-min in lengths respectively (arrows in *A*). Then various proportions of the reference recording were used for the DG model. The difference in performance of these two methods, measure by the ratio of JS divergence, was plotted against the amount of samples used by the DG model. The ratio of one, which indicates the equal performance, was marked by the dotted line and the sample sizes to reach equal performance were marked by arrows. *C*, The ratio of JS

divergence was plotted against the sample size taken from the training set for both the nLFP and spiking activities. Almost all data points were significantly larger than 1 (sign rank test, $p < 0.05$), except for the leftmost two points for ongoing spikes, which correspond to smallest sample sizes and, therefore, largest measurement errors. The total sample sizes were 9×10^5 , 9×10^4 and 4.5×10^5 for nLFP, ongoing and evoked spikes, respectively. In all panels, data is represented as mean \pm SD. Twenty randomly chosen 10-element groups for nLFP (monkey A), ongoing spikes (monkey A) and evoked spikes (cat 1, probe 1) were analyzed.161

Figure 6.8: Temporal correlation in avalanche dynamics and the performances of different models in predicting the single-bin (un-degenerated) nLFP activities. *A-B*, The power law distribution of nLFP cluster sizes indicates a unique spatiotemporal correlation structure and is not found for bin-shuffled data, in which the spatial correlation within individual time bins were reserved but the temporal correlation among different time bins were removed. *A*, 10-electrode sub-group. *B*, 91-electrode group. *Insets*: the areas used for analysis. *C-G*, The DG model accurately predicts the single-bin (un-degenerated) nLFP activities. The data set used in *C-G* is the same as in Fig. 6.4A-F and all the analyses were performed in a corresponding way, except that the activity patterns were un-degenerated. For more details, see legend of Fig. 6.4A-F165

Chapter 1: Introduction

1.1 How does the brain process information?

Our seat of emotion, memory, perception, learning, and consciousness is located in the human brain. In particular, the cerebral cortex is the key component in the brain that embeds and orchestrates these higher brain functions. It receives and processes sensory, visual, auditory, and olfactory stimuli, generates output signals to control motor behavior, it also associates and coordinates multiple modalities of information. The cortex is a layered structure and each layer has a destined function: sensory signals collected from sensory receptors, for example, the photoreceptors in the eye, through thalamic relay nuclei provide inputs to layer IV in primary visual cortex. They are then processed further in superficial layers II and III, sent down to deeper layers V and VI, and out of primary visual cortex to other brain regions including higher cortical areas. For instance, if attention needs to be shifted to a particular object, sensory information is sent to prefrontal cortex where eye movement is planned, then through the relay by superior colliculus in the midbrain as well as to other subcortical regions such as striatum in the basal ganglia in order to control saccadic eye movements.

As illustrated, performing even a simple eye movement involves multiple brain regions. To understand how these regions communicate with each other and how the brain stores, transmits and processes information, or generally speaking, the principle

of information processing, is a central question in neuroscience. Regarding the example of vision, a more specific but often raised version of this question is the following: What are the mechanisms that relate different modalities of information, such as spatially or temporally contiguous events in the external world, in order to form a coherent image about when and where these external events occur? It is known that at early stages of sensory processing, different modalities of input, e.g. the color, shape, and orientation of a red horizontally oriented bar, are processed separately by distinct groups of neurons in the visual cortex. However, at a higher level, these extracted features need to be integrated such that the subject perceives a coherent image of a red bar. How are different modalities of sensory information converged? This so-called '**binding problem**' (Roskies, 1999; Malsburg, 1999) is extremely common, like associating a person's voice to appearance, or relating the image of an apple to its taste, *etc.* One suggested solution to the binding problem is converging the representations of lower level features to a so called higher level 'grandmother neuron', a specific neuron that will only respond in the presence of a red bar, for instance. In fact, neurons that are highly selective to a very complex stimulus have been found in the visual processing stream at higher cortical level. For example, 'face cells' only respond to the face of a particular person, Angelina Jolie or Brad Pitt, an extraordinary feat of selectivity given the computational demands of categorizing people's faces among the myriads of possible viewing angles and small changes in appearances. Unfortunately, this solution can never be exhaustively applied to every possible stimulus in the outside world. If every single higher level neuron in the visual cortex responds to a specific combination of color, shape,

orientation, movement, *etc*, the number of all possible combinations far exceeds the total number of available neurons, which is at the order of 10^{10} in humans.

This problem also exists in the classical neural network, primarily proposed by Hebb, where a neuron has one degree of freedom and a brain state is described by a vector of neural activities (Hebb, 1949). The population coding or the cell assembly idea originated from the classical neural network fails when the external stimulus is more complex, for example if a green ellipse is superimposed on the image of a red bar. The four neuronal groups that respond to red, green, bar and ellipse are simultaneously firing. How can the brain associate red to the bar while it associates green to the ellipse? How can the brain prevent combining red with the ellipse and green with the bar? It is known as the ‘superposition catastrophe’ (Malsburg, 1999) and the classical neural network models fail.

Malsburg suggested that each neuronal group carry two distinct signals, one represents the effectiveness of stimulus, and the other is a tag to a specific object. The ‘effectiveness’ is carried by firing rate, and the ‘tag’ is signified by the synchronized spiking activity. The idea is that the activities of neurons representing different features of the same object are temporally correlated: the activities of ‘red’ neurons are correlated with the activities of ‘bar’ neurons, and ‘green’ neurons are correlated with ‘ellipse’ neurons, but ‘red’ are not correlated with ‘ellipse’. Developed and extended by Singer’s group and others, synchronized neuronal activity is proposed as a coding strategy employed in the brain. Such temporally correlated activity would

have a stronger influence on downstream neurons that process the binding information than uncorrelated ones (Singer, 1999; Fries, 2009). Since Gray *et al.* discovered that synchrony facilitated feature binding in vision, neuronal synchronizations, particularly in the form of phase-locked 30 – 80 Hz oscillations, so-called gamma-oscillations, have been extensively studied, and have been proposed to coordinate separate brain regions to function coherently (Gray *et al.*, 1989; Singer, 1999; Varela *et al.*, 2001; Fries *et al.*, 2007; Fries, 2009). The importance of neuronal synchronization for normal cortex function is further supported by the abnormal levels of synchrony in many brain disorders, for example, decreased synchrony in schizophrenia and increased synchrony in epilepsy (Uhlhaas and Singer, 2006).

The synchrony coding hypothesis has raised as much enthusiasm as critiques. Shadlen and Movshon pointed out some flaws in it: 1) what neurons could readout the upstream synchrony codes? If there are synchrony detecting neurons, this hypothesis is barely different from the original ‘grandmother cells’ idea; 2) the inability to distinguish special synchrony ‘tags’ from more common synchrony, which results in stronger influence on downstream neurons; 3) the lack of direct evidence that synchrony acts as the signal for binding, *etc* (Shadlen and Movshon, 1999). In addition, other studies identified conflicting results of change in synchrony in brain disorders (Netoff *et al.* 2002; Garcia Dominguez *et al.* 2005; also see Uhlhaas *et al.* 2006).

To conclude, till now there has been no converging theory of how the cortical networks process information.

1.2 Neuron: the basic information processing unit

It is worth mentioning how a single neuron receives input and generates output, because it is the fundamental unit to process information in the brain and has been relatively well studied.

A neuron is composed of a cell body, as well as dendrites, through which inputs from other neurons are received, and axons, through which output signals are sent. The intracellular volume of the neuron is separated from the extracellular space by a thin lipid bi-layer across which a negative membrane potential is maintained through ion-selective channels. The membrane potential is created by the difference of ion concentrations between the two regions, mainly a high extracellular sodium concentration and a high intracellular potassium concentration. In the absence of major inputs, the membrane potential fluctuates around -70 mV, which is also called the resting potential. There are two primary types of neurons, excitatory and inhibitory. Excitatory neurons send excitatory signals to other neurons, meaning they tend to activate others, and inhibitory neurons do the contrary, when active, they tend to suppress the activity of other neurons. Each matured neuron constantly receives both excitatory and inhibitory inputs from many of its neighbors. Excitatory inputs, consisting of influx of ions like Ca^{2+} and Na^+ , will increase/depolarize the cell's membrane potential, while inhibitory signals, like influx of Cl^- , will

decrease/hyperpolarize membrane potential. Within a small time window, usually several milliseconds, the total excitation may exceed inhibition by a certain amount, *i.e.* the membrane potential is depolarized above a threshold, usually around -40 mV. Once the membrane potential reaches threshold, the activity of a combination of voltage-dependent ion-selective channels will generate a short-lasting, stereotypic positive membrane potential change up to +50 mV, called the action potential or spike. The action potential can be viewed as an all-or-none electrical event that rapidly propagates from the cell body to the end of its axon, and is relayed from neuron to neuron through synapses, a structure between the axon of presynaptic neuron and dendrites of postsynaptic neuron. Thus, while the subthreshold membrane potential functions as an analog integration of many inputs, the action potential conveys a binary signal of sufficient excitation, *i.e.* threshold crossing. When the action potential propagates to the end of the axon of the presynaptic neuron, neural transmitters are released at the synapse, reach the postsynaptic site at the dendrites of the target neurons and trigger the opening of ion channels and selective influx of charged ions. For excitatory cortical neurons, the neurotransmitter released is glutamate, which opens Ca^{2+} and Na^{+} channels that depolarize the postsynaptic neurons. In contrast, inhibitory cortical neurons release the neurotransmitter GABA, which opens Cl^{-} channels that make the postsynaptic membrane potential more negative. If the postsynaptic neuron receives many inputs in a short time window, these inputs will superimpose and if the net effect results in a suprathreshold depolarization, it will generate an action potential and this propagation of neuronal activity continues.

Although many of the mechanisms regarding neuronal signal propagation are reasonably well understood, even at the single neuron level, brain dynamics can be inherently complex. For example, the elaborate arborization of dendrites allows inputs from different groups of neurons to be compartmentalized and active conductance, such as voltage gated calcium channels, introduce further degrees of input processing at the single neuron level. Importantly, the complexity found at single neurons extends to the network.

1.3 The complexity of neuronal network

Coordinating the dynamics of thousands or millions of neurons pushes the complexity of brain networks to another level. At the microcircuit scale, each neuron receives inputs from about 10^4 other neurons on average and distributes its output to a similar large number of neurons. Excitatory neurons have local as well as distant projections, whereas inhibitory neurons project only locally. Thus, thousands of neurons form functional groups. In addition, neurons are wired differently. For instance, in a local circuit with both pyramidal neurons (P) and interneurons (I), there are four types of chemical synaptic connections, P-P, P-I, I-I, I-P, plus gap junctions I-I, and they can form various loops like recurrent inhibition, mutual excitation, mutual inhibition, *etc.* Extending this complexity even further, the cortex consists of many types of interneurons, which process inputs differently and reveal different anatomical preferences in targeting postsynaptic neurons. For example, fast spiking interneurons target the soma of pyramidal neurons, whereas some regular spiking interneurons

target the dendrites of pyramidal neurons. So called chandelier cells play an important role in schizophrenia and target preferentially the axon initiation segments of pyramidal neurons. The signal processing in these more local groups can be sequential or parallel, and the dynamics arising from it is highly nonlinear. Finally, long-range connections between pyramidal neurons link different functional groups at the macroscopic scale (> 1 mm) involving many different cortical areas with different sensory, motor, and associative functions. The complexity in cell types and wiring at the mesoscopic and macroscopic scales suggest that dynamics in the cortex will be highly non-linear.

Although nonlinear systems are usually difficult to study, I will show in my dissertation that simple principles still can be generalized from studies that characterize the complexity of signals in the brain.

1.4 A healthy brain is a balanced brain

It turns out that the brain operates with a balance of excitatory (E) and inhibitory (I) synaptic transmission. Intracellular recordings *in vitro* and *in vivo* have revealed that the temporal evolution of E and I synaptic conductance are strongly correlated and highly similar (Shu *et al.*, 2003; Wehr and Zador, 2003; Haider *et al.*, 2006; Okun and Lampl, 2008): as E conductance increases in a local population, I conductance also increases, and temporally follows the trajectory of E, resulting in a nearly complete cancellation. Typically the onset of I delays the onset of E for a short period of several milliseconds. It is during this brief imbalanced window that the membrane

potential rapidly depolarizes and generates spikes. However, on a longer time scale, the global change of E and I should be balanced. It is suggested that such balance is important for neuronal responsiveness and the emergence and disappearance of transient sub-networks (Haider and McCormick, 2009).

Based on these findings, we further propose that the balance of E and I is a general principle in a healthy brain, and is crucial for the brain's normal functions. Imagine the case when E overwhelms I, inhibition is insufficient to suppress neuron firing, a few active neurons can recruit more and more neurons, and recurrent excitation will lead the network to a locked-in synchronized state, commonly known as epileptic, *i.e.* seizure, activity. On the contrary, when I dominates E, activation can not be initiated, and the neuronal network is unable to transmit signals.

1.5 Attempts to apply the theory of criticality to cortical dynamics

In physics, complexity and balanced connectivity are often associated with criticality (Chialvo, 2010). The fact that dynamics in the brain is complex and balanced has led to the conjecture that criticality is an underlying dynamical principle. In the 1950s, Cragg and Temperley suggest a conceptual link between neuronal networks and magnetic systems (Cragg and Temperley, 1955). Several decades later, the hypothesis emerged that the brain might be balanced at criticality (Kürten, 1988; Chen *et al.*, 1995; Herz and Hopfield, 1995; Bienenstock and Lehmann, 1999), followed by more detailed computational models and simulations (van Vreeswijk and Sompolinsky, 1996; Kinouchi and Copelli, 2006; Levina *et al.*, 2007; Millman *et al.*, 2010).

Unfortunately, the technique of high density parallel recordings is currently not sufficiently developed, making it difficult for these models to be confirmed experimentally at the mesoscopic or single neuron level. On the other hand, large scale brain imaging and behavioral, cognitive experiments have consistently pushed forward the idea that brain dynamics is highly variable, similar to what has been observed in physical systems at criticality (Kelso, 1992; Friston, 1997; Kelso *et al.*, 1998; Linkenkaer-Hansen *et al.*, 2001; Stam and de Bruin, 2004; Miller *et al.*, 2009).

Criticality, critical phenomenon, and second order phase transition, are used interchangeably and usually refer to physical systems associated with a critical point.

A system poised at the critical point is usually associated with the properties of 1) power law divergence of correlation length, meaning that distant elements are correlated; 2) power law divergence of certain macroscopic quantities, for example, compressibility and susceptibility, from which a critical exponent can be derived; and 3) scale invariance, or fractal structure, which means certain properties of the system stay invariant even when the system is observed at different spatial or temporal scales. One such physical system that can exhibit criticality is magnetic material of iron or cobalt. For example, iron is ferromagnetic at low temperature. Thermal fluctuations, however, can overcome atom-atom interactions between ‘magnetic dipoles’ by increasing temperature, and the ferromagnetic phase turns into a paramagnetic phase above a critical temperature, the Curie temperature. The critical point of the magnetic system is right at the Curie temperature, where the magnetic susceptibility is power

law divergent and the size of the magnetic clusters with same orientations is power law distributed.

It has been hypothesized that the brain might be balanced at criticality, with the support of models and mostly indirect experimental studies, and it was not until 2003 that this hypothesis has been directly and systematically examined. Pioneered by the laboratory of Dietmar Plenz at the National Institute of Mental Health and followed by others, ‘neuronal avalanches’ have been defined as spontaneous activity observed in superficial layers of cortex *in vitro* and *in vivo*, and provide important experimental evidence that cortex operates close to the critical state (Beggs and Plenz, 2003; 2004; Stewart and Plenz, 2006; Mazzoni *et al.*, 2007; Plenz and Thiagarajan, 2007; Stewart and Plenz, 2008; Gireesh and Plenz, 2008; Pasquale *et al.*, 2008; Petermann *et al.*, 2009; Hahn *et al.*, 2010). Neuronal avalanches describe a statistical property of spontaneous cortical dynamics that emerges when the network is in a state of balanced excitation and inhibition.

But why is spontaneous activity interesting?

1.6 Spontaneous vs. sensory-evoked neuronal activity

The fact that neurons are spontaneously active even in the absence of external sensory input has been known for many decades, but it was generally regarded as noise and functionally unimportant. Only recently the importance of spontaneous neuronal activity has been gradually realized (for a review, see Ringach 2009).

Spontaneous activity is crucial in shaping the neuronal structure during early stages of development, and is correlated over space and time (Katz and Shatz, 1996; Cang *et al.*, 2005; Kanold, 2009). For example, in the visual cortex, several features of cortical functional architecture, such as ocular dominance columns, orientation tuning and orientation columns, are already established by spontaneously generated waves of action potentials before eye opening, therefore in the absence of any visual experience. Visual experience can only modify the existing structure instead of establishing it. Further, disrupting spontaneous activity in mouse retina during the first week postnatal will result in defective anatomical mapping from lateral geniculate nucleus to visual cortex.

The spontaneous firing of a single neuron is related to the activity pattern of its neighbors (Tsodyks *et al.*, 1999), the spatial-temporal firing patterns of neuronal groups are repeatable (Ikegaya *et al.*, 2004; Ji and Wilson, 2007), and they reflect and resemble sensory-evoked activity patterns (Kenet *et al.*, 2003; Han *et al.*, 2008). It is thought that ongoing activity reflects the intrinsic network connectivity, which in turn is constantly shaped by external stimuli. Recent experiments showed that the similarity between spontaneous and sensory evoked activity increases during development, suggesting progressive internal adaptations to external environment (Berkes *et al.*, 2011). It is also found that the realm of sensory-evoked activity patterns is confined by that of spontaneous activity (Luczak *et al.*, 2009).

Correlation in spontaneous activity is comparable to that of sensory-evoked activity and contributes considerably to the trial-to-trial variability observed in animal experiments *in vivo*. More precisely, about half of the variability found in the optimal response to the same visual point or bar stimulus can be well explained by the variability of spontaneous activity just before the onset of stimulus (Arieli *et al.*, 1996). In line with these early results, natural stimuli only moderately modulate ongoing activity, instead of completely erasing its existence (Chiu and Weliky, 2004).

Given the evidence of such close interplay between spontaneous and sensory-evoked activity, and that ongoing activity outlines the ensembles of evoked activity, the study of ongoing neuronal activity will not only shed light on the internal structure and constraints of neuronal network, but also provide insights into how neurons respond to external stimuli.

1.7 Neuronal avalanches

Neuronal avalanches consist of bursts of elevated population activity, correlated in space and time, which are distinguished by a particular statistical character: active clusters of size s occur with probability $P(s) \sim s^\alpha$, *i.e.*, a power law with exponent $\alpha = -1.5$. Neuronal avalanches have several key properties: (1) they arise during development when superficial layers form *in vitro* and *in vivo* (Gireesh and Plenz, 2008). More specifically, during the second week postnatal in superficial layers of somatosensory cortex in rats, the significant increase in the power of nested θ and β/γ oscillations coincides with the emergence of neuronal avalanche dynamics, both

reflecting the establishment of long range correlations in the network, (2) they are homeostatically maintained (Homeostasis: a system regulates its internal environment and tends to maintain a stable and constant condition) for weeks in isolated cortex (Stewart and Plenz, 2008). During the first two weeks of development *in vitro*, size distribution of cortical dynamics can be quantified as a power law with exponent larger than -1.5, which gradually reaches -1.5 toward the end of second week, and maintain this value for several more weeks. (3) they constitute the dominant form of ongoing cortical activity in awake monkeys (Petermann *et al.*, 2009), and (4) they require balanced synaptic transmissions and can be abolished by disrupting either E or I (Stewart and Plenz, 2006; Gireesh and Plenz, 2008), (5) their pharmacological regulation is characterized by an inverted-U profile of NMDA/Dopamine D1 receptor interaction and intact fast inhibitory transmission, suggesting that the dynamics is an intrinsic property of the cortex (Stewart and Plenz, 2006), (6) they are scale invariant. Generally speaking, given synchronized activity bursts of sizes s and $k * s$ (where k is a constant), there will always be a fixed ratio $k^{-1.5}$ between the corresponding probabilities of occurrence. Such properties of neuronal avalanches resemble the dynamics observed in other systems poised at the boundary between ordered and disordered, the dynamics in critical state.

The ubiquitous observation of neuronal avalanche dynamics in many different preparations, *i.e. in vitro* cultures, acute slices, *in vivo* anesthetized cats, rats and awake monkeys, indicate that neuronal avalanches, and the underlying mechanism of criticality, are potential dynamic principles of cortical network.

The robust -1.5 exponent observed in neuronal avalanches further suggests that it may be in the same universality class with a group of interesting physical models called directed percolation, which study the problem of liquid percolating through rock layers. Typical percolation models are constructed on an $N * N$ lattice and the parameter is probability P by which the current site could occupy its neighbor. It is found that when P is below a critical value P_C , no giant clusters exist that could span the dimension of the system, while when P is above P_C , such a giant cluster always exists. It is when $P = P_C$ that the giant clusters begin to emerge and the distribution of the cluster sizes follows a power law with exponent -1.5, which is the same as in neuronal avalanches (Aon *et al.*, 2004; Plenz and Thiagarajan, 2007; Beggs, 2008; Buice and Cowan, 2009).

A more intuitive model, which is descended from percolation theory, is the branching process model (Beggs and Plenz, 2003; Haldeman and Beggs, 2005; Poil *et al.*, 2008; Tagliazucchi and Chialvo, 2011). This model is originally used to study the population growth in species (Jagers, 1975). The process is taken place over time or generations, and each entity in a previous generation (ancestors) is connected to N other entities in the following generation (descendants), with probability P of successfully giving birth to each of them and the probability of $1 - P$ to fail. An important parameter to describe this process is the branching parameter σ , the average ratio of the number of descendants to the number of ancestors. σ describes the tendency of population growth. If σ is 1, equivalent to $P = 1/N$ in the model, it

means on average the number of ancestors and that of descendents are the same, thus the propagation is stable, and the distribution of the size of blood-bonded generations is a -1.5 power law. If $\sigma > 1$ or $P > 1/N$, the population always expand, for instance $\sigma = 2$, at each generation, the number of alive entities doubles; if $\sigma < 1$ or $P < 1/N$, the propagation is not sustainable, in the case of $\sigma = 0.5$, every following generation will be halved in numbers, and eventually no descendents will be generated. $\sigma = 1$ or $P = 1/N$ is the critical point. It has been demonstrated that in normal, unperturbed cortical networks σ is very close to 1 (Beggs and Plenz, 2003).

The branching model and the neuronal network resemble each other in many aspects. Similar to the dynamics in branching process, the neural signal propagation can be viewed as a chain reaction, with one group of upstream neurons activating one group of downstream neurons. In addition, in the percolation and branching process models, a parameter has to be finely tuned to reach the critical state, the activation probability P or the branching parameter σ . As discussed, the occurrence of neuronal avalanches depends on an optimal concentration of neuromodulators and the balance of excitatory and inhibitory synaptic transmission. In other words, the neuronal network also needs tuning.

Therefore, neuronal networks and avalanche dynamics can be characterized by models derived from criticality, but why should the cortex operate at criticality?

1.8 Advantages of being critical

The hypothesis that the brain operates near the critical point attracts much attention because it not only provides a general framework to the neural network and supported by experiments and models, but also the success of predictions of optimal computational power of neuronal network in many aspects.

In theory, divergence of correlation length is a signature of criticality. It also is a desirable feature in cortical dynamics. It serves as a balanced ability to form both short and long range correlations while avoiding the extremes: Too strong and widespread correlations would cause the network to operate in a locked-in state; too weak and local correlations make long-range information transmission impossible. It is thought a balance between the two extremes will lead to diverse, non-stereotyped and non-isolated neural activity, and is advantageous to large computational powers in information processing tasks. As mentioned in previous sections, even the completion of a simple task, such as a saccadic eye movement, requires the coordination among local and distant neuronal groups. Criticality enables neuronal groups to maintain local correlation structure as well as communicate with distant and separate cortical regions.

Studies of several different physical models showed optimization of computation or information processing at criticality. For example, cellular automata showed maximal computational power when operating close to criticality (Crutchfield and Young, 1989; Langton, 1990). Later, it was suggested that neural networks might operate

near criticality (Bornholdt and Röhl, 2003; de Arcangelis *et al.*, 2006; Meisel and Gross, 2009), and the optimization of information processing of critical neural network models have been studied (Bertschinger and Natschläger, 2004; Haldeman and Beggs, 2005; Kinouchi and Copelli, 2006; Tanaka *et al.*, 2009). Intuitively, systems poised close to criticality are variable, transiently stationary and susceptible to fluctuations. Such metastability can be beneficial to the brain in many aspects: it is a state where local segregation and global integration can coexist, where the measure of complexity is maximized (Kelso, 2008), and maximal diversity could serve as a solution to the combinatorial binding problem. This transient nature is also consistent with the current idea of synchrony coding, where transient synchrony is required for handling multiple functions (Rodriguez *et al.*, 1999).

1.9 Questions remained for the critical brain hypothesis

The critical brain hypothesis is very tempting in that it is a general framework to understand the brain, a universal mechanism and principle to describe cortical dynamics and potential advantages for brain functions. However, most of the supporting evidence from experiments so far is the power law distribution in active cluster size that is robustly found in different experimental settings, ranging from the isolated cortex preparation *in vitro* to the intact brain in awake animals. A main focus of my dissertation is to experimentally demonstrate the optimal information processing functions in cortical networks exhibiting critical dynamics, *i.e.* neuronal avalanches, and to understand the underlying interaction structure that give rise to cortical dynamics.

1.10 Dissertation outline

In this dissertation, I present the studies of several information processing functions in cortical networks while E/I balance is changed, and I find that all of these functions are optimized when cortical network exhibits avalanche dynamics, *i.e.* the network is in the E/I balanced state..

In Chapter 2, the common experimental procedures, analysis methods and computational models are introduced. Methods that are specific to a particular topic will be described separately in the corresponding chapter.

In Chapter 3, we study the diversity of the repertoire of neuronal activity patterns, which constrains the ability of the network to store, transfer and process information. We measured activity patterns obtained from multisite local field potential recordings in cortex cultures, urethane anesthetized rats, and awake macaque monkeys. First, we quantified the information capacity of the pattern repertoire of ongoing and stimulus-evoked activity using Shannon entropy. Next, we quantified the efficacy of information transmission between stimulus and response using mutual information. By systematically changing the ratio of excitation/inhibition (E/I) *in vitro* and in a network model, we discovered that both information capacity and information transmission are maximized at a particular intermediate E/I, at which ongoing activity emerges as neuronal avalanches. Next, we used our *in vitro* and model results to

correctly predict *in vivo* information capacity and interactions between neuronal groups during ongoing activity. Close agreement between our experiments and model suggest that neuronal avalanches and peak information capacity arise because of criticality and are general properties of cortical networks with balanced E/I (Shew *et al.*, 2011).

In Chapter 4, we continue the study of optimization principles in ongoing neuronal activity by examining the synchronization among different groups of neurons and the repertoire of synchronized neuronal assemblies. Neural synchrony are often manifested in fundamental brain functions such as perception of sensory stimuli, motor control, attention, and working memory, which require coordinated interactions among large networks of neurons in the cerebral cortex. Theory predicts that variability of synchrony dynamics is maximized when coupling between neurons is tuned precisely to a critical level, but this remains untested in experiments with brain tissue. Such variability is important, because a diverse and variable repertoire of brain functions is thought to require a diverse and variable repertoire of synchronized neural groups. Here we studied various neural networks by tuning synaptic ‘coupling’ through a wide range and measuring the resulting neural synchrony. We discovered that three phenomena occur near a critical coupling level: 1) maximized variability of synchronous neural groups, 2) onset of synchrony, and 3) neuronal avalanches. Our findings suggest that the cortex benefits from optimized properties of neural synchrony by operating near criticality. This chapter not only complements the findings in Chapter 3, but also extends the results to the continuous regime.

In Chapter 5, the study is focused on the optimization of neuronal response to external stimuli, which could be inferred from the optimization principles discovered in ongoing activity, given the close relationship between ongoing and stimulus-evoked activity, and has also been predicted by criticality models in physics. We demonstrate that cortical networks that generate neuronal avalanches benefit from a maximized dynamic range, *i.e.*, the ability to respond to the greatest range of stimuli. By changing the ratio of excitation and inhibition in the cultures, we derive a network tuning curve for stimulus processing as a function of distance from criticality, in agreement with predictions from our simulations. Our findings suggest that in the cortex, 1) balanced excitation and inhibition establishes criticality, which maximizes the range of inputs that can be processed, and 2) spontaneous activity and input processing are unified in the context of critical phenomena (Shew *et al.*, 2009).

In Chapter 6, the interaction structures of neuronal avalanches, as well as population spiking activity are investigated. The dynamics built on intricate cortical networks reflect complex interactions among many neurons during ongoing activity and stimulus processing. Recently, a pair-wise interaction model (Ising model) has been suggested to be sufficient to reconstruct most of the observed neuronal dynamics. Here we show that this Ising model approach fails to capture essential features in ongoing neuronal avalanche dynamics of awake monkeys as well as evoked activities in cat visual cortex. Instead, these dynamics are accurately predicted by a pair-wise Gaussian interaction model, in which high-order interactions are introduced through a

simple non-linear, *i.e.* thresholding, operation. Our results hold for different scales of neuronal dynamics, reflected by LFPs and spike activities. We suggest that cortical dynamics naturally contain high-order interactions that arise from intrinsic non-linear processes, such as local field potential and spike generation, which crucially contribute to cortical information processing.

Chapter 7 contains concluding remarks and suggests directions for future investigations.

Bibliography

Aon MA, Cortassa S, O'Rourke B (2004) Percolation and criticality in a mitochondrial network. *Proceedings of the National Academy of Sciences of the United States of America* 101:4447-52

Arcangelis L de, Perrone-Capano C, Herrmann H (2006) Self-Organized Criticality Model for Brain Plasticity. *Physical Review Letters* 96:1-4 Available at:

Arieli A, Sterkin A, Grinvald A, Aertsen A (1996) Dynamics of ongoing activity: explanation of the large variability in evoked cortical responses. *Science (New York, N.Y.)* 273:1868-71

Beggs JM (2008) The criticality hypothesis: how local cortical networks might optimize information processing. *Philosophical transactions. Series A, Mathematical, physical, and engineering sciences* 366:329-43

Beggs JM, Plenz D (2003) Neuronal avalanches in neocortical circuits. *The Journal of neuroscience* 23:11167-77

Beggs JM, Plenz D (2004) Neuronal avalanches are diverse and precise activity patterns that are stable for many hours in cortical slice cultures. *The Journal of neuroscience* 24:5216-29

Berkes P, Orban G, Lengyel M, Fiser J (2011) Spontaneous Cortical Activity Reveals Hallmarks of an Optimal Internal Model of the Environment. *Science* 331:83-87

- Bertschinger N, Natschläger T (2004) Real-time computation at the edge of chaos in recurrent neural networks. *Neural computation* 16:1413-36
- Bienenstock E, Lehmann D (1999) Regulated Criticality in the Brain? *Advances in Complex Systems* 1:361-384
- Bornholdt S, Röhl T (2003) Self-organized critical neural networks. *Physical Review E* 67:1-5
- Buice M a, Cowan JD (2009) Statistical mechanics of the neocortex. *Progress in biophysics and molecular biology* 99:53-86
- Cang J, Rentería RC, Kaneko M, Liu X, Copenhagen DR, Stryker MP (2005) Development of precise maps in visual cortex requires patterned spontaneous activity in the retina. *Neuron* 48:797-809
- Chen D-mei, Wu S, Guot A, Yang ZR (1995) Self-organized criticality in a cellular automaton model of pulse-coupled integrate-and-fire neurons. *Journal of Physics A: Mathematical and General* 28:5177
- Chialvo DR (2010) Emergent complex neural dynamics. *Nature Physics* 6:744-750
- Chiu C, Weliky M (2004) Small modulation of ongoing cortical dynamics by sensory input during natural vision. *Nature*
- Cragg BG, Temperley HN (1955) Memory: the analogy with ferromagnetic hysteresis. *Brain : a journal of neurology* 78:304-16
- Crutchfield J, Young K (1989) Inferring statistical complexity. *Physical Review Letters* 63:105-108
- Fries P (2009) Neuronal gamma-band synchronization as a fundamental process in cortical computation. *Annual review of neuroscience* 32:209-24
- Fries P, Nikolić D, Singer W (2007) The gamma cycle. *Trends in neurosciences* 30:309-16
- Friston KJ (1997) Transients, metastability, and neuronal dynamics. *NeuroImage* 5:164-71
- Garcia Dominguez L, Wennberg R a, Gaetz W, Cheyne D, Snead OC, Perez Velazquez JL (2005) Enhanced synchrony in epileptiform activity? Local versus distant phase synchronization in generalized seizures. *The Journal of neuroscience* 25:8077-84

Gireesh ED, Plenz D (2008) Neuronal avalanches organize as nested theta- and beta/gamma-oscillations during development of cortical layer 2/3. *Proceedings of the National Academy of Sciences of the United States of America* 105:7576-81

Gray CM, Koenig P, Engel AK, Singer W (1989) Oscillatory responses in cat visual cortex exhibit inter-columnar synchronization which reflects global stimulus properties. *Nature* 23:334–337

Hahn G, Petermann T, Havenith MN, Yu S, Singer W, Plenz D, Nikolic D (2010) Neuronal avalanches in spontaneous activity *in vivo*. *Journal of neurophysiology*:3312-3322

Haider B, Duque A, Hasenstaub AR, McCormick D (2006) Neocortical network activity *in vivo* is generated through a dynamic balance of excitation and inhibition. *The Journal of neuroscience* 26:4535-45

Haider B, McCormick D (2009) Rapid neocortical dynamics: cellular and network mechanisms. *Neuron* 62:171-89

Haldeman C, Beggs J (2005) Critical Branching Captures Activity in Living Neural Networks and Maximizes the Number of Metastable States. *Physical Review Letters* 94:1-4

Han F, Caporale N, Dan Y (2008) Reverberation of recent visual experience in spontaneous cortical waves. *Neuron* 60:321-7

Hebb DO (1949). *The Organization of Behavior* (New York: Wiley)

Herz A, Hopfield J (1995) Earthquake cycles and neural reverberations: Collective oscillations in systems with pulse-coupled threshold elements. *Physical review letters* 75:1222-1225

Ikegaya Y, Aaron G, Cossart R, Aronov D, Lampl I, Ferster D, Yuste R (2004) Synfire chains and cortical songs: temporal modules of cortical activity. *Science* (New York, N.Y.) 304:559-64

Jagers P (1975) *Branching Processes with Biological Applications*. Wiley, Chichester.

Ji D, Wilson M a (2007) Coordinated memory replay in the visual cortex and hippocampus during sleep. *Nature neuroscience* 10:100-7

Kanold PO (2009) Subplate neurons: crucial regulators of cortical development and plasticity. *Frontiers in neuroanatomy* 3:16

Katz LC, Shatz CJ (1996) *Synaptic Activity and the Construction of Cortical Circuits*. *Science* 274:1133-1138

- Kelso J (1992) A phase transition in human brain and behavior. *Physics Letters A* 169:134-144
- Kelso JAS (2008) An Essay on Understanding the Mind. *Ecological psychology : a publication of the International Society for Ecological Psychology* 20:180-208
- Kelso JA, Fuchs A, Lancaster R, Holroyd T, Cheyne D, Weinberg H (1998) Dynamic cortical activity in the human brain reveals motor equivalence. *Nature* 392:814-8
- Kenet T, Bibitchkov D, Tsodyks M, Grinvald A, Arieli A (2003) Spontaneously emerging cortical representations of visual attributes. *Nature* 425:954-6
- Kinouchi O, Copelli M (2006) Optimal dynamical range of excitable networks at criticality. *Nature Physics* 2:348-351
- Kürten KE (1988) Critical phenomena in model neural networks. *Physics Letters A* 129:157-160
- Langton CG (1990) Computation at the edge of chaos : phase transition and emergent computation. *Physica D: Nonlinear Phenomena* 42:12
- Levina a, Herrmann JM, Geisel T (2007) Dynamical synapses causing self-organized criticality in neural networks. *Nature Physics* 3:857-860
- Linkenkaer-Hansen K, Nikouline VV, Palva JM, Ilmoniemi RJ (2001) Long-range temporal correlations and scaling behavior in human brain oscillations. *The Journal of neuroscience* 21:1370-7
- Luczak A, Barthó P, Harris KD (2009) Spontaneous events outline the realm of possible sensory responses in neocortical populations. *Neuron* 62:413-25
- Malsburg CVD (1999) The What and Why of Binding : The Modeler ' s Perspective. *Neuron* 24:95-104
- Mazzoni A, Broccard FD, Garcia-Perez E, Bonifazi P, Ruaro ME, Torre V (2007) On the dynamics of the spontaneous activity in neuronal networks. *PloS one* 2:e439
- Meisel C, Gross T (2009) Adaptive self-organization in a realistic neural network model. *Physical Review E* 80:1-6
- Miller KJ, Sorensen LB, Ojemann JG, Nijs M den (2009) Power-law scaling in the brain surface electric potential. *PLoS computational biology* 5:e1000609
- Millman D, Mihalas S, Kirkwood A, Niebur E (2010) Self-organized criticality occurs in non-conservative neuronal networks during “up” states. *Nature Physics* 6:801-805

Netoff TI, Schiff SJ (2002) Decreased neuronal synchronization during experimental seizures. *The Journal of neuroscience* 22:7297-307

Okun M, Lampl I (2008) Instantaneous correlation of excitation and inhibition during ongoing and sensory-evoked activities. *Nature neuroscience* 11:535-7

Pasquale V, Massobrio P, Bologna LL, Chiappalone M, Martinoia S (2008) Self-organization and neuronal avalanches in networks of dissociated cortical neurons. *Neuroscience* 153:1354-69

Petermann T, Thiagarajan TC, Lebedev M a, Nicolelis M a L, Chialvo DR, Plenz D (2009) Spontaneous cortical activity in awake monkeys composed of neuronal avalanches. *Proceedings of the National Academy of Sciences of the United States of America* 106:15921-6

Plenz D, Thiagarajan TC (2007) The organizing principles of neuronal avalanches: cell assemblies in the cortex? *Trends in neurosciences* 30:101-10

Poil S-S, Ooyen A van, Linkenkaer-Hansen K (2008) Avalanche dynamics of human brain oscillations: relation to critical branching processes and temporal correlations. *Human brain mapping* 29:770-7

Ringach DL (2009) Spontaneous and driven cortical activity: implications for computation. *Current opinion in neurobiology* 19:439-44

Rodriguez E, George N, Lachaux JP, Martinerie J, Renault B, Varela FJ (1999) Perception's shadow: long-distance synchronization of human brain activity. *Nature* 397:430-3

Roskies AL (1999) The Binding Problem. *Neuron* 24:7-9

Shadlen MN, Movshon J a (1999) Synchrony unbound: a critical evaluation of the temporal binding hypothesis. *Neuron* 24:67-77, 111-25

Shew WL, Yang H, Petermann T, Roy R, Plenz D (2009) Neuronal Avalanches Imply Maximum Dynamic Range in Cortical Networks at Criticality. *The Journal of Neuroscience* 29:15595-15600.

Shew WL, Yang H, Yu S, Roy R, Plenz D (2011) Information Capacity and Transmission Are Maximized in Balanced Cortical Networks with Neuronal Avalanches. *Journal of Neuroscience* 31: 55-63.

Shu Y, Hasenstaub A, McCormick DA (2003) Turning on and off recurrent balanced cortical activity. *Nature* 423

Singer W (1999) Neuronal Synchrony : A Versatile Code for the Definition of Relations ? Most of our knowledge about the functional organization. *Neuron* 24:49-65

Stam CJ, Bruin EA de (2004) Scale-free dynamics of global functional connectivity in the human brain. *Human brain mapping* 22:97-109

Stewart CV, Plenz D (2006) Inverted-U profile of dopamine-NMDA-mediated spontaneous avalanche recurrence in superficial layers of rat prefrontal cortex. *The Journal of neuroscience* 26:8148-59

Stewart CV, Plenz D (2008) Homeostasis of neuronal avalanches during postnatal cortex development *in vitro*. *Journal of neuroscience methods* 169:405-16

Tagliazucchi E, Chialvo DR (2011) The collective brain is critical. *arXiv*:1-14

Tanaka T, Kaneko T, Aoyagi T (2009) Recurrent infomax generates cell assemblies, neuronal avalanches, and simple cell-like selectivity. *Neural computation* 21:1038-67

Tsodyks M, Kenet T, Grinvald a, Arieli a (1999) Linking spontaneous activity of single cortical neurons and the underlying functional architecture. *Science (New York, N.Y.)* 286:1943-6

Uhlhaas PJ, Singer W (2006) Neural synchrony in brain disorders: relevance for cognitive dysfunctions and pathophysiology. *Neuron* 52:155-68

Varela F, Lachaux J-philippe, Rodriguez E, Martinerie J (2001) THE BRAINWEB : PHASE LARGE-SCALE INTEGRATION. *Nature Review Neuroscience* 2:229

Vreeswijk C van, Sompolinsky H (1996) Chaos in neuronal networks with balanced excitatory and inhibitory activity. *Science (New York, N.Y.)* 274:1724-6

Wehr M, Zador AM (2003) Balanced inhibition underlies tuning and sharpens spike timing in auditory cortex. *Nature* 426:442-6

Chapter 2: Experimental design, data analysis methods and computational models

2.1 MEA recordings in organotypic cortex cultures

Coronal slices from rat somatosensory cortex (350 μm thick) and midbrain (ventral tegmental area, VTA; 500 μm thick) were taken from newborn rats (postnatal day 0–2; Sprague–Dawley) and cultured on a poly-D-lysine-coated 8x8 multi-electrode array (MEA, Multi Channel Systems; 30 μm electrode diameter; 200 μm inter-electrode distance). This co-culture system (Fig. 2.1A) captures many aspects of the development of superficial cortical layers observed *in vivo* (Stewart and Plenz, 2008 and Gireesh and Plenz, 2008). The slice cultures were grown inside a sterile, closeable chamber attached to the MEA. Individual MEAs were attached to a recording head stage inside an incubator (MEA1060 w/ blanking circuit; x1200 gain; bandwidth 1 – 3000 Hz; 12 bit A/D in range 0 – 4096 mV; Multi Channel Systems, Inc.). The recording setup allowed for repeated measurements under stable, sterile conditions from single cultures for weeks. After plasma/thrombin-based adhesion of the tissue to the MEA, standard culture medium was added (600 μl , 50% basal medium, 25% Hank’s Buffered Salt Solution, HBSS, 25% horse serum; Sigma-Aldrich). MEAs were then affixed to a slowly rocking tray inside a custom built incubator ($\pm 65^\circ$ angle, 0.005 Hz frequency, $35.5 \pm 0.5^\circ\text{C}$). Spontaneous local field potential (LFP; 1 – 200 Hz; 4 kHz sampling rate; measured against common reference electrode inside the bath, Fig. 2.1B) was obtained from 1 hr of continuous

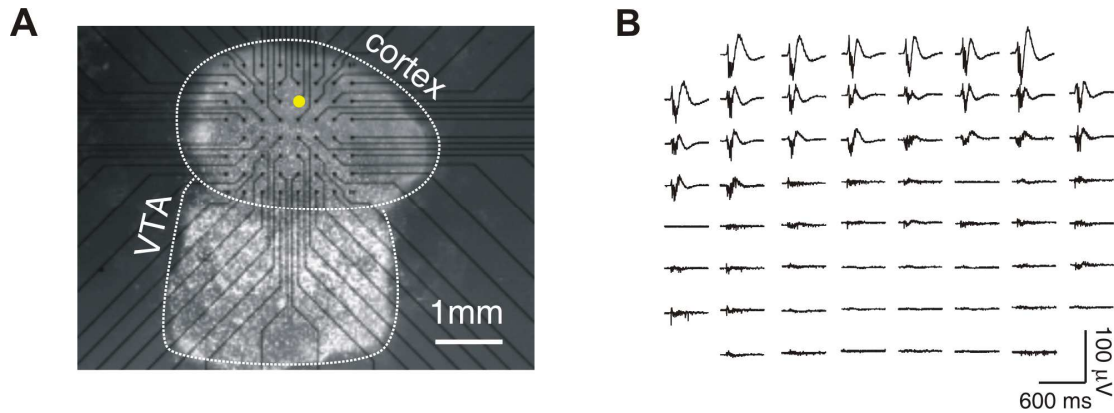


Figure 2.1: Preparation of culture and example population event. *A*, Light-microscopic image of a somatosensory cortex and dopaminergic midbrain region (VTA) coronal slice cultured on a 60 channel microelectrode array. *Yellow dot*: stimulation site. *Black dots*: recording sites. *B*. Shown is an example of a population event revealed by widespread fluctuations in the local field potential (LFP) recorded by the micro-electrode array. Each trace is 600 ms of recorded LFP from one electrode in the array.

recordings of extracellular activity, and low-pass filtered off-line with a cutoff at 100 or 50 Hz (phase neutral, 4th order Butterworth).

Local field potential (LFP) measures the combined electrical signals of synchronized activity from a population of neurons. It has been employed in many studies to investigate cortical functions, and is thought most correlated to fMRI signals. Its origin is currently not well understood, but it is generally considered as synchronized synaptic inputs to the observed area. A recently study suggested that LFP signal is originated within 250 μM of the recording electrode (Katzner *et al.*, 2009). However, we found a monotonic relationship between the amplitude of LFP and multi-unit activity, suggesting that LFP could also reflect output in the cortical tissue.

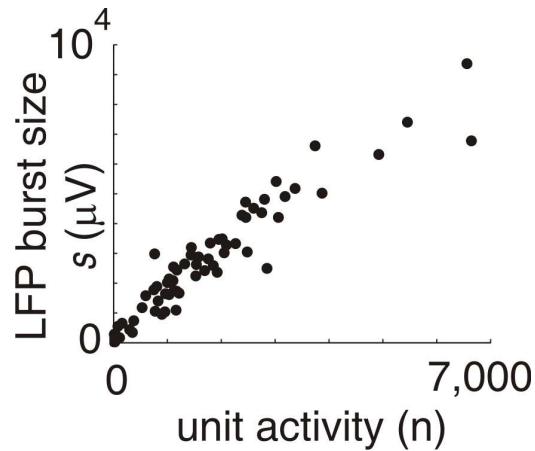


Figure 2.2: Positive correlation between LFP amplitude and unit activity. Number of extracellular spikes correlates with the size of simultaneously recorded nLFP burst ($R = 0.84 \pm 0.13$; $n = 5$). Each point represents total number of spikes versus the corresponding spontaneous nLFP burst size.

To establish a correlation between LFP and neuronal spiking activity, in $n = 5$ cultures, extracellular activity was recorded for 15 min at 25 kHz. In addition to extracting LFP, the extracellular signal was filtered in the frequency band 300–3000 Hz and ~ 78 single units were identified per culture using threshold detection and PCA-based spike sorting (Offline Sorter; Plexon). Fig. 2.2 demonstrates that the LFP amplitudes are positively correlated with the intensity of population spiking activity.

2.2 *Stimulus-evoked activity in vitro*

Immediately following each 1 h recording of spontaneous activity, stimulus-evoked activity was measured. Stimuli were applied at 5 s intervals at one electrode located approximately at the center of the culture, in superficial cortical layers (yellow dot in Fig. 2.1A). Stimuli were current-controlled, single shocks with bipolar square

waveform: 50 μ s with amplitude $-S$ followed by 100 μ s with amplitude $+S/2$, where $6 < S < 200 \mu$ A. We tested one set of stimulus amplitudes with fine resolution ($S = 10 - 200 \mu$ A in steps of 10μ A), and another with coarser resolution ($S = 6, 12, 24, 50, 65, 80, 100, 150, 200 \mu$ A). Each stimulus level was repeated 40 times in pseudo randomized order resulting in a total recording duration of 2000 (coarse) or 4000 (fine) seconds. Each stimulus-evoked response was recorded using all electrodes except the stimulation electrode during 500 ms following stimulation. A blanking circuit disconnected the recording amplifiers during stimulation, thus significantly reduced stimulus artifacts (Multi Channel Systems). Sample rate and filtering was identical to that used for spontaneous activity recordings.

2.3 Pharmacology in vitro

Bath-application of antagonists for fast glutamatergic or GABAergic (GABA: gamma-Aminobutyric acid) synaptic transmission was used to change the ratios of excitation to inhibition (E/I) in cortical network. The normal condition (no-drug) followed by a drug condition for each culture was typically studied within a short time (~ 3 hrs) to minimize potential non-stationarities during development. Stock solutions were prepared for the GABA_A receptor antagonist picrotoxin (PTX), the N-methyl-D-aspartic acid (NMDA) receptor antagonist DL-2-Amino-5-phosphonopentanoic acid (AP5), and the α -amino-3-hydroxyl-5-methyl-4-isoxazole-propionate (AMPA) receptor antagonist 6,7-Dinitroquinoxaline-2,3-dione (DNQX). Working solutions were obtained by adding 6 μ l of these stock solutions to 600 μ l of culture medium in the MEA chamber to reach the following final drug

concentrations: (in μM) 5 PTX, 20 AP5, 10 AP5 + 0.5 DNQX, 20 AP5 + 1 DNQX. After measurement under each drug condition, the culture was washed by replacing the culture medium with 300 μl of conditioned medium mixed with 300 μl of fresh, unconditioned medium. Conditioned medium was collected from the same culture the day before drug application. Most cultures recovered to their pre-drug condition within about 24 hrs following wash.

2.4 MEA recordings in monkeys

All procedures were in accordance with National Institutes of Health guidelines and were approved by the National Institute of Mental Health Animal Care and Use Committee. 96-channel MEA (10 * 10 grid with no corner electrodes, 400 μm separation, and 1.0 mm electrode length) (BlackRock Microsystem) were chronically implanted in the left arm representation region of premotor cortex of two monkeys (*Macaca mulatta*, adults, one male and one female). Ongoing activity was recorded for 30 minutes. Monkeys were awake but not engaged by any task or controlled sensory stimulation. Extracellular signals were sampled at 30 kHz and filtered offline (1–100 Hz; phase neutral, fourth-order Butterworth). Negative peaks in LPF (nLFPs) were related to the activity of local neuronal populations (Fig. 2.3).

Spike sorting was performed with Plexon offline spike sorter (V2.8.8). 56 and 40 well isolated units were found for monkey 1 and monkey 2 respectively. Three principal components (PCA), peak-trough amplitude, and nonlinear energy were used as the sorting features. We defined ‘well isolated’ as follows: in a 2-D projection of

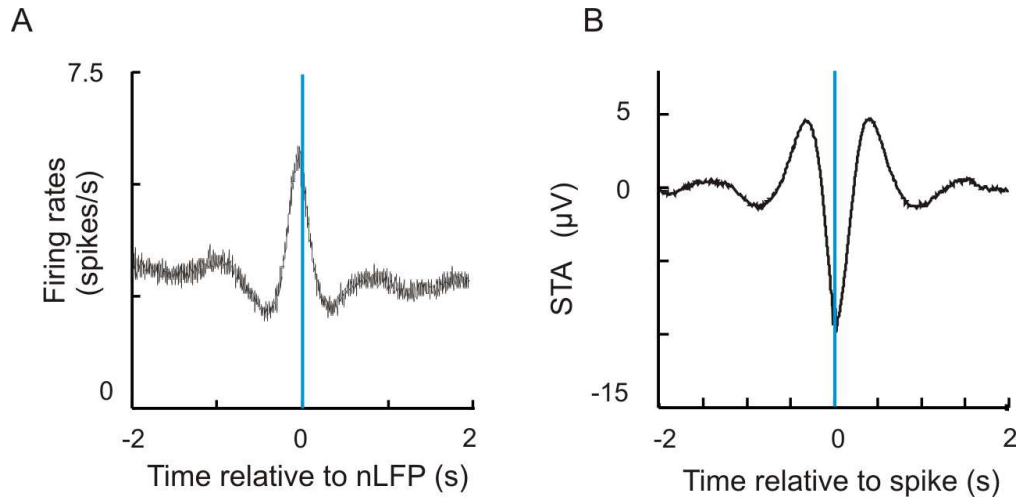


Figure 2.3: Negative LFP peaks (nLFPs) correspond to the times of spiking during ongoing activity. *A*, Local units increase their firing rates around the occurrence of nLFPs. Average peri-event time histogram (PETH) of spike firing rate relative to the occurrence of nLFPs recorded by the same electrode (ongoing activity; pre-motor cortex; bin width = 2 ms; 53 single units; monkey A). Time zero (nLFP time) is marked by the blue vertical line. *B*, Average LFP waveforms turn negative around the time of unit firing. Spike triggered average (STA) in LFP waveform averaged over 53 single units (the same data set as in *A*). The time of spikes (time zero) is marked by the blue vertical line. Three neurons with extremely high firing rates (>30 spikes/s) were not included to avoid the masking of other neurons, though they showed very similar results. The artifacts due to the residue of spike waveforms left in LFPs was removed in both *A* and *B*.

at least 2 of the sorting features the unit must have a mean which is strongly different from the mean of noise waveforms ($p \leq 0.001$, multivariate ANOVA). If more than one unit was recorded from the same electrode, the difference between means of each unit was also required to be significant at this strict level ($p \leq 0.001$, multivariate ANOVA).

These experiments were performed by Drs. S. Yu, A. Mitz and R. Saunders.

2.5 MEA recordings in rats

Rats aged 15–25 days were anesthetized with urethane (1.25–1.75 g/kg body weight, i.p.). The MEA (NeuroNexus Technologies) was inserted in the coronal plane into the somatosensory cortex (~ 3 mm lateral, 1 mm caudal to bregma). The animal was hydrated frequently (Ringer's lactate solution; 0.5–1 ml/h, i.p.) and was monitored for respiratory rate (80–120/min), tail color, and tail pinch reflex. Anesthesia was maintained with supplemental doses of urethane (~ 0.25 g/kg). After the recordings, the brains were fixed in paraformaldehyde, sectioned, and Nissl-stained to reconstruct the electrode locations. See details in Gireesh and Plenz, 2008.

2.6 Unit recordings in cat

Visually evoked activities were recorded from cortical area 17 in two adult, anesthetized cats. The animals were artificially ventilated and the anesthesia was maintained with a mixture of 70% N₂O and 30% O₂, supplemented with 0.5 – 0.6% halothane. Extracellular spike activities were recorded by one or two silicon-based MEAs (4×4 electrode array; 200 μm inter-electrode distance; NeuroNexus). The probes were inserted roughly perpendicular to the surface of cortex at depths of approximately 1 mm. The visual stimuli (presented by ActiveStim, <http://activestim.com/>) consisted of full-contrast, drifting sinusoidal gratings that

spatially covered the receptive fields of all recorded neurons. Each trial was completed with 3 – 4 s long presentations of a drifting grating with orientations randomly chosen from a set of 12 directions (0° to 360° range; steps of 30°). About 30 minutes of visually evoked responses were recorded for each cat. Single units were identified offline using a customized, PCA-based program. For more details, see previous publication with the same data sets (Yu *et al.*, 2008). These experiments were performed by Drs. S. Yu and D. Nikolić.

2.7 Definitions of bursts and neuronal avalanches

For each electrode, we identified negative peaks in the LFP (nLFP) that fell below a certain threshold (-4 SD *in vitro* and $-2.5, -3$ SD *in vivo*) of the electrode noise. An example of the raw LFP recording from which we extract an nLFP cluster is shown in Fig. 2.1B. Each negative peak in LFP fluctuation will be designated an nLFP with a time stamp and amplitude. We then defined bursts as spatiotemporal clusters of nLFPs, within which consecutive nLFPs were separated by less than a time τ . The threshold τ was chosen to be greater than the short timescale of inter-nLFP intervals within a burst, but less than the longer timescale of inter-burst quiescent periods ($\tau = 86 \pm 71$ ms for all cultures). Fig. 2.4 shows a typical histogram of time intervals between nLFPs on the array (single experiment). Red line: choice of τ . Results were robust for a large range in the choice of τ .

The size s of a burst was quantified as the absolute sum of all nLFP amplitudes within the burst. The area of a burst was defined as the number of electrodes that

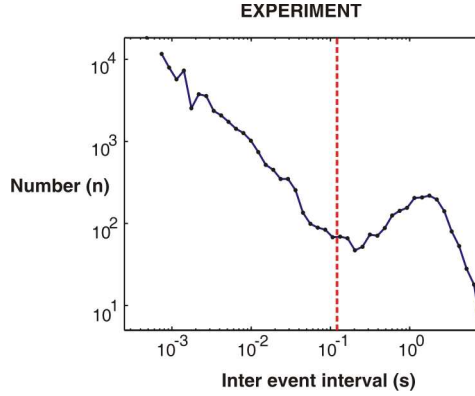


Figure 2.4: Time threshold τ in burst definition. Shown is an example of an inter-peak interval distribution of nLFPs on the array from one experiment. Two time scales are prominent: (1) short time intervals between peaks within periods of activity and (2) long time intervals reflecting periods with no activity (identified by the hump in this example). *Red line*: choice of τ .

participated. The duration of a burst was defined as the interval between the first and last nLFP within the burst (Beggs and Plenz, 2003; 2004).

2.8 Definition of κ

Neuronal avalanches entail a probability density function (PDF) of burst size s which follows a power-law with exponent $\alpha = -3/2$ (Beggs and Plenz, 2003; Gireesh and Plenz, 2008; Petermann *et al.*, 2009). Thus, the corresponding cumulative density function (CDF) for avalanche sizes $F^{NA}(\beta)$, which specifies the fraction of measured cluster sizes $s < \beta$, is a $-1/2$ power law function, $F^{NA}(\beta) = (1 - \sqrt{l/L})^{-1} (1 - \sqrt{l/\beta})$ for minimum size l and maximum size L . Here we define a novel nonparametric

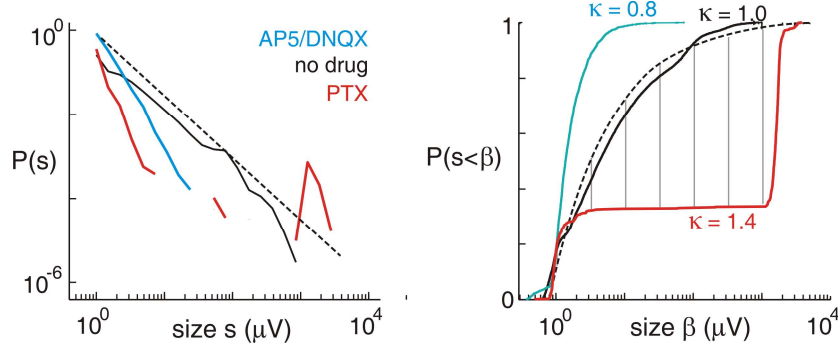


Figure 2.5: Definition of κ . *Left:* Probability distribution functions (PDFs) of spontaneous cluster sizes for a normal (no-drug, *black*), disinhibited (PTX, *red*), and hypo-excitable (AP5/DNQX, *blue*) cultures. *Broken line:* $-3/2$ power-law. Cluster size s is the sum of nLFP peak amplitudes within the cluster; $P(s)$ is the probability of observing a cluster of size s . *Right:* Corresponding cumulative distribution functions (CDFs) and quantification of the network state using κ , which measures deviation from a $-1/2$ power-law CDF (*broken line*). *Vertical gray lines:* The 10 distances summed to compute κ , shown for one example PTX condition (*red*).

measure, κ , to quantify the difference between a measured burst size CDF, $F(\beta)$, and the reference CDF, $F^{NA}(\beta)$,

$$\kappa = 1 + \frac{1}{m} \sum_{k=1}^m (F^{NA}(\beta_k) - F(\beta_k)), \quad (2.1)$$

where the β_k are $m = 10$ discrete burst sizes logarithmically spaced between the minimum and maximum burst sizes observed in the experiments (Fig. 2.5). Our use of cumulative distributions rather than the PDFs to calculate κ avoids sensitivity to binning choices, which are necessary for constructing a PDF.

In previous work by our lab, we used a different measure than κ for characterizing the spontaneous activity of the system (Beggs and Plenz, 2003). Here we discuss our motivations for this change. In previous work, an estimate of the parameter σ was computed from experimental data with a method based on counting the number of electrodes which recorded negative LFP peaks within successive time periods. The ratio of the active electrode count in the second time period to the count in the first time period was taken as the σ estimate. This method yielded $\sigma \cong 1$ during neuronal avalanches as expected from theory. Later, this measure was found to give unexpected results for apparently supercritical states (Haldeman and Beggs, 2005; Plenz, 2005). To better understand these observations, we tested the method for estimating σ using our model (described in detail in the following section), where the true σ is known and exact counting of numbers of active sites is feasible. Using time periods with various durations and starting times within a cluster, we found that the previously used method for estimating σ was very accurate when the network was critical. However, away from the critical state, this method was highly sensitive to the temporal resolution (Fig. 2.6A). This may explain why the previous method robustly and correctly estimated $\sigma \cong 1$ for neuronal avalanches, but was unreliable for supercritical states.

As a measure of the system state, κ avoids the above difficulties primarily because it does not depend on precise temporal resolution. The comparison of κ with σ demonstrates its superiority over previous methods of estimating σ . We tried several alternative definitions for κ , which all outperformed the previous method of

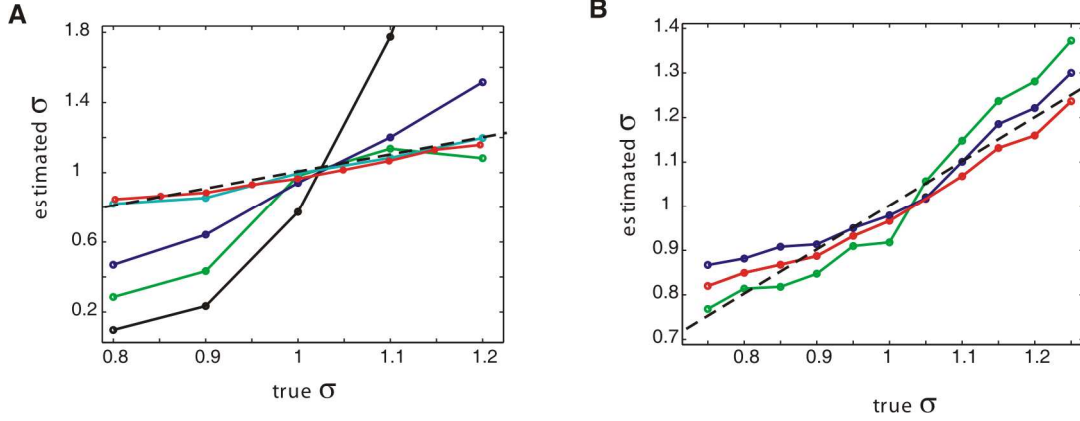


Figure 2.6: Estimating σ using κ . *A*, Using our model, we compared the true value of σ to an estimate based on activity clusters. The black dashed line has slope 1, representing a perfect estimate. The new measure κ (*red*) accurately estimated the underlying branching parameter over a wide range of subcritical to supercritical states. In contrast, an estimate of the branching parameter σ based on calculating ratios of descendants to ancestors, *i.e.* active sites during period $t+1$ divided by active sites during period t , varied significantly in its precision depending on network state and time periods used. A reliable estimate was achieved when the correct temporal resolution for each network state was available and when comparing the first two consecutive time steps of a cluster (*light blue*; $\sigma_{est} = A(2)/A(1)$; $A(t1)$ and $A(t2)$ are the number of active neurons during time $t1$ and $t2$ respectively). Importantly, when the exact temporal resolution was not known, estimates tended to stray widely from the real value for subcritical and supercritical dynamics. For $\sigma_{est} = A(11:20)/A(1:10)$ (*black*) and subcritical dynamics, clusters tended to die during $t1 = 1:10$, leading to an underestimate of σ . Conversely, clusters tended to expand supralinearly for $t2 = 11:20$ in supercritical dynamics, leading to an overestimate of σ . For comparison, other variations of sampling situations were also plotted (*green*: $\sigma_{est} = A(29:31)/A(26:28)$; *dark blue*: $\sigma_{est} = A(9:11)/A(6:8)$).

B, Comparison in the accuracy of estimating true σ using various metrics to quantify differences between CDF (network model). *Red*: κ with 10 logarithmically spaced β_k values provides the most reliable and linear estimate of σ . *Blue*: modified κ with linear spacing of β_k values reveals increased mismatch for extreme sub-critical and supercritical dynamics. *Green*: Kolmogorov-Smirnov statistic using the maximal distance between two CDF performed worst.

estimating σ and are compared to each other. Our choice of definition was guided by the aim to make the match between κ and σ as close as possible using the model data. Our use of cumulative distributions rather than the PDFs to calculate κ avoids sensitivity to binning choices, which are necessary for constructing a PDF. κ is in the same family of nonparametric comparisons of cumulative distributions as the Kolmogorov-Smirnov (KS) test and the Kuiper's test. The KS statistic is the single maximum difference between two cumulative distributions and Kuiper's test is the sum of the absolute values of the maximum positive difference and the maximum negative difference. Compared to Kuiper's test, κ simply takes the sum of more than two differences without the absolute value. We note that the Kolmogorov-Smirnov statistic does a rather poor job for our purposes. Furthermore, our choice of logarithmic spacing of the β_k values provides a more linear relationship between κ and σ compared to a linear spacing of β_k (Fig. 2.6B).

Finally, we point out that several aspects of the definition are very robust. For example, if we alter the upper end of the range of burst sizes used to generate the reference CDF, from 10^3 to 10^5 μV , the measured κ values change only slightly (data

not shown). We note that the typical maximum burst size measured from a given culture also ranged from 10^3 to 10^5 μV . Furthermore, κ is nearly unchanged with respect to the number of differences computed between the two CDFs for all $m > 5$ (m as defined above; data not shown). However, since it is a statistical measure, κ is naturally more prone to error when sample sizes are low. To account for this, we only included experiments in our analysis in which we observed at least 200 spontaneous nLFP clusters.

2.9 Model

The model consisted of N all-to-all coupled, binary-state neurons and the following dynamical rules: If neuron j spiked at time t (*i.e.* $s_j(t) = 1$), then postsynaptic neuron i will spike at time $t+1$ with probability p_{ij} . As such, the p_{ij} are N^2 numbers representing the synaptic coupling strengths between each pair of neurons. The p_{ij} are asymmetric, $p_{ij} \neq p_{ji}$, positive, time-independent, uniformly-distributed random numbers with mean and standard deviation of order N^{-1} . If a set of neurons $J(t)$ spikes at time t , then the probability that neuron i fires at time $t+1$ is exactly $p_{iJ}(t) = 1 - \prod_{j \in J(t)} (1 - p_{ij})$. To implement the probabilistic nature and variability of unitary synaptic efficacy, neuron i actually fires at time $t+1$ only if $p_{iJ}(t) > \zeta(t)$, where $\zeta(t)$ is a random number from a uniform distribution on $[0,1]$. Population events were modeled by activating a single initial site (like an electrical shock applied at a single electrode or a spontaneous activation in the experiments) and recording the

resulting activations that propagated through the network. These dynamics were defined by

$$s_i(t+1) = \theta[p_{iJ}(t) - \zeta(t)] = \theta\left[1 - \prod_{j \in J(t)} (1 - p_{ij}) - \zeta(t)\right], \quad (2.2)$$

where $\theta[x]$ is the unit step function. As in our experiments, we explored a range of network excitability by tuning the mean value of p_{ij} from $0.75/N$ to $1.25/N$ in steps of $0.05/N$ by scaling all p_{ij} by a constant. For such small mean p_{ij} , the model reduces to probabilistic integrate-and-fire, *i.e.* $p_{iJ} \approx \sum_{j \in J(t)} p_{ij}$ to order N^{-2} accuracy. If the mean p_{ij}

is exactly N^{-1} , then, n spikes at time t will, on average, excite n postsynaptic spikes time $t+1$, which constitutes criticality in our model (Beggs and Plenz, 2003; Kinouchi and Copelli, 2006). When mean p_{ij} is larger than or less than N^{-1} , the system is supercritical or subcritical, respectively. We define the control parameter of the model $\sigma \equiv N^{-1} \sum_i \sum_j p_{ij}$. In the context of dynamics, σ reflects the average ratio of spiking descendants to spiking ancestors in consecutive time steps. At criticality, $\sigma = 1$; the coupling strengths are balanced such that, on average, the number of active sites neither grows nor decays with time (note that the instantaneous activity level fluctuates greatly).

To obtain response as a function of stimulus in the model, we simulated increasing stimulus amplitude S by increasing the number of initially activated neurons ($S = 1, 2, 4, 16, 32, 64, 128$ initially active neurons for system size of 500). Finally, we note that our model is very similar to $N-1$ dimensional directed percolation (Buice and

Cowan, 2007). Therefore, at high dimension ($N > 5$) and weak coupling it is expected that the model behaves as a branching process, where σ is the branching parameter and the $-3/2$ power-law is predicted at criticality.

Bibliography

Beggs JM, Plenz D (2003) Neuronal avalanches in neocortical circuits. *The Journal of neuroscience* 23:11167-77

Beggs JM, Plenz D (2004) Neuronal avalanches are diverse and precise activity patterns that are stable for many hours in cortical slice cultures. *The Journal of neuroscience* 24:5216-29

Buice M, Cowan J (2007) Field-theoretic approach to fluctuation effects in neural networks. *Physical Review E* 75:1-14

Gireesh ED, Plenz D (2008) Neuronal avalanches organize as nested theta- and beta/gamma-oscillations during development of cortical layer 2/3. *Proceedings of the National Academy of Sciences of the United States of America* 105:7576-81

Haldeman C, Beggs J (2005) Critical Branching Captures Activity in Living Neural Networks and Maximizes the Number of Metastable States. *Physical Review Letters* 94:1-4

Katzner S, Nauhaus I, Benucci A, Bonin V, Ringach DL, Carandini M (2009) Local origin of field potentials in visual cortex. *Neuron* 61:35-41

Kinouchi O, Copelli M (2006) Optimal dynamical range of excitable networks at criticality. *Nature Physics* 2:348-351

Petermann T, Thiagarajan TC, Lebedev M a, Nicolelis M a L, Chialvo DR, Plenz D (2009) Spontaneous cortical activity in awake monkeys composed of neuronal avalanches. *Proceedings of the National Academy of Sciences of the United States of America* 106:15921-6

Plenz D (2005) Comment on “Critical Branching Captures Activity in Living Neural Networks and Maximizes the Number of Metastable States.” *Physical Review Letters* 95:219801-219801

Stewart CV, Plenz D (2008) Homeostasis of neuronal avalanches during postnatal cortex development *in vitro*. *Journal of neuroscience methods* 169:405-16

Yu S, Huang D, Singer W, Nikolic D (2008) A small world of neuronal synchrony.
Cerebral cortex 18:2891-901

Chapter 3: Information capacity and transmission are maximized in balanced cortical networks with neuronal avalanches¹

3.1 Introduction

In the cortex, populations of neurons continuously receive input from upstream neurons, integrate it with their own ongoing activity, and generate output destined for downstream neurons. Such cortical information processing and transmission is limited by the repertoire of different activated configurations available to the population. The extent of this repertoire may be quantified by its entropy H ; in the context of information theory, entropy characterizes the information capacity of the population (Shannon, 1948; Rieke *et al.*, 1997; Dayan and Abbott, 2001). Information capacity is important because, as the name suggests, it defines upper limits on aspects of information processing. For example, consider the information transmitted from input to output by a population that only has two states in its repertoire ($H \leq 1$ bit). No matter how much information the input contains, the information content of its output cannot exceed 1 bit. A network with low entropy presents a bottleneck for information transmission in the cortex. Thus, it is important to understand the mechanisms that modulate the entropy of cortical networks.

Cortical activity depends on the ratio of fast excitatory (E) to inhibitory (I) synaptic inputs to neurons in the network. This E/I ratio remains fixed on average even during

¹ This chapter is published in *Journal of Neuroscience* 31:55-63, 2011. I contributed to *in vitro* and anesthetized rat recordings, all data analysis, interpretation of the data and manuscript preparation.

highly fluctuating activity levels (Shu *et al.*, 2003; Okun and Lampl, 2008). However, it is currently not known whether a particular E/I ratio is advantageous for certain aspects of information processing. The existence of such an optimal ratio is suggested by two competing effects of E/I on entropy. First, a large E/I ratio, *i.e.* if excitation is insufficiently restrained by inhibition, can cause very high correlations between neurons (Dichter and Ayala, 1987). Since increased correlations decrease entropy (Rieke *et al.*, 1997; Dayan and Abbot, 2001), we anticipate that a sufficiently large E/I ratio limits information transmission. This is consistent with findings that moderate levels of correlation can play an important role in population coding (Pola *et al.*, 2003; Jacobs *et al.*, 2009). At the other extreme, *i.e.* a small E/I ratio, weak excitatory drive is expected to reduce correlations as well as the overall level of neural activity. Although reduced correlations can lead to higher entropy, this increase may be counteracted by a concurrent drop in activity. Sufficiently suppressed activity also reduces entropy (Rieke *et al.*, 1997; Dayan and Abbot, 2001). Accordingly, we hypothesize that cortical entropy and information transmission are maximized for an intermediate E/I ratio.

Here we tested our hypothesis experimentally in cortex cultures, anesthetized rats, and awake monkeys and compared our results with predictions from a computational model. We discovered an optimal intermediate E/I ratio distinguished by 1) maximal entropy and 2) maximal information transmission between input and network output. This finding was based on analysis of both ongoing and stimulus-evoked population activity. Moreover, at this optimal E/I ratio, ongoing activity emerges in the form of

neuronal avalanches (Beggs and Plenz, 2003) and interactions within the network are moderate. Agreement with our model suggests that by maintaining this particular E/I ratio the cortex operates near criticality and optimizes information processing.

3.2 Methods

3.2.1 Cross correlation in unit activity in awake monkey

To compute spike count cross correlations between each pair of units recorded during ongoing activity we followed established methods (Renart *et al.*, 2010). First, to obtain spike count vectors, the spike time stamps of each unit were 1) binned with 1 ms temporal resolution, 2) convolved with a Gaussian window with 50 ms width. The cross correlation coefficient was computed between all pairs (2145 pairs for monkey 1, 780 pairs for monkey 2) of spike count vectors.

3.2.2 A brief review of information theory

Information theory is originally developed to solve problems in data processing operations, and the two main concerned issues are data compression and error correction, which are represented by two quantities, entropy and mutual information.

Entropy quantifies the amount of information contained in a message, in unit of bit. It measures the uncertainty associated in predicting a random variable. The bigger the uncertainty, the more information the message can convey. When the variable is

discrete, for example, random discrete variable X with possible values $\{x_1, x_2, x_3, \dots, x_n\}$. The probability of observing x_i is $p(x_i)$, then the entropy of X is defined as:

$$H(X) = -\sum_{i=1}^n p(x_i) \log_2 p(x_i). \text{ The lower bound of } H \text{ is } 0, \text{ in condition of } p(x_j) = 1,$$

and the upper bound is $\log_2(n)$, with equal probability $p(x_i) = 1/n$.

Mutual information quantifies the inter-dependence between two variables, X and Y .

It measures how much uncertainty about one variable can be reduced by knowing the

other: $MI(X, Y) = \sum_x \sum_y p(x, y) \log_2 \left(\frac{p(x, y)}{p(x)p(y)} \right)$. $p(x, y)$ is the joint probability of X

and Y . If X and Y are independent, $p(x, y) = p(x) * p(y)$, mutual information is zero,

no information is gained for one by knowing the other. If X and Y are identical,

$$MI(x, y) = H(X) = H(Y).$$

3.2.3 Binary patterns and entropy H

Each population event is represented by an 8×8 binary pattern with one bit per

recording electrode. A bit is set to 1 if the corresponding electrode is active during

the event; otherwise it is set to 0. The entropy of this set of patterns is defined as

$$H = -\sum_{i=1}^n p_i \log_2 p_i, \tag{3.1}$$

where n is the number of unique binary patterns and p_i is the probability that pattern i

occurs. In Fig. 3.3D, the black curve is based on the 8×8 binary patterns which

represent the 60 electrodes of the MEA. We also studied entropy at different spatial

resolutions by coarse-binning and for different spatial extents by using sub-regions of the MEA. The green curves in Figs 3.3D, 3.5, and 3.6A were obtained by reducing spatial resolution through coarse-binning of 8x8 patterns into square 4x4 patterns. Each bit in the 4x4 pattern was dependent on the state of 4 neighbouring 2x2 electrode sets; if at least one electrode was active the bit was set to 1. Reduced spatial extent was tested with 16-bit patterns based on only 16 electrodes arranged in a 4x4 square (Fig. 3.3D). As pointed out in the results, these 4x4 patterns also reduce potential undersampling bias when compared to 8x8 patterns.

For stimulus-evoked activity, binary patterns were defined based on LFP activity measured during 500 ms following the stimulus. If the measured response at an electrode exceeded -8SD of the noise, then the corresponding bit was set to 1, otherwise it was set to 0. The stimulation electrode was always set to 0.

Note that the lack of corner electrodes on the MEA means that the corner bits of 8x8 patterns are always zero. This implies that the maximum entropy we could possibly record for 8x8 patterns is 2^{60} rather than 2^{64} . For coarse-binned 4x4 patterns, the likelihood that the corner bits are active is slightly lower (about 25% lower). These effects are present for all E/I ratios examined. Therefore, they may affect the absolute values of entropy measurements, but they are not important for our conclusions, which are primarily based on changes in entropy. This is further confirmed by the robustness of our results to selecting 4x4 subregions from the center of the MEA for which corner electrodes are not missing (Fig. 3.3D).

The calculation of entropy entails estimating the occurrence probability for each pattern. Therefore, H generally will depend on number N of observed patterns unless N is so large that the probability of each pattern is well represented by the samples recorded. H will be underestimated for sufficiently small N but becomes independent of N for sufficiently large N . To estimate potential ‘undersampling bias’ we computed corrected values following the quadratic extrapolation method (e.g. Magri *et al.*, 2009). First, we randomly selected a fraction f of samples from the full set of N patterns. We recomputed the entropy for fractions $f = 0.1$ to 1 in steps of 0.1. We repeated this 10 times for each f . Next, we fit the average H versus f data with the following function:

$$H(f) = H_0 - \frac{a}{fN} - \frac{b}{(fN)^2} \quad (3.2)$$

The fit parameter H_0 is the estimated corrected value reported in the results section.

3.2.4 Mutual information MI

From a set of N binary patterns, we defined a participation vector q_i (length N) for each recording site i . $q_i(j) = 1$ or 0 indicated that site i was active or inactive during event j . The interaction between site i and site j was quantified by the mutual information (Rieke *et al.*, 1997; Dayan and Abbott, 2001) of q_i and q_j defined as

$$MI(q_i; q_j) = \sum_{a \in \{0,1\}} \sum_{b \in \{0,1\}} p(q_i = a, q_j = b) \log_2 \left(\frac{p(q_i = a, q_j = b)}{p(q_i = a)p(q_j = b)} \right), \quad (3.3)$$

where $p(x)$ is the probability of x , $p(x,y)$ is the joint probability x and y . MI quantifies (in bits) the information shared by the two sites and provides similar information as a cross correlation (CC, Fig. 3.1), which is a more traditional approach to measure pairwise interaction. Our reason for working with mutual information is two-fold. First, MI is less sensitive to noise when interactions are very weak. Second, MI arises from information theory and, thus, is a more natural fit with the study of entropy. Nonetheless, MI and CC are closely related. In Fig 3.1 we compare both quantities for the *in vitro* data. Also marked in Fig 3.1 are estimated theoretical bounds on the relationship between MI and CC . The lower bound is reached for $L = 0.5$, while the upper bound corresponds to the extreme values of $L = 0$ and $L = 1$.

The MI values reported in Results were averages over all pairs of sites,

$$MI = \frac{2}{M(M-1)} \sum_{i=1}^{M-1} \sum_{j=i+1}^M MI(q_i; q_j). \quad (3.4)$$

For the *in vitro* experiments, we also used mutual information in a different way to quantify the efficacy of information transmission between stimulus and response. Here we computed $MI(S;R) = H(R) - H(R|S)$. $H(R)$ is the entropy of the full set of response patterns for all stimuli. $H(R|S)$ is the conditional entropy, *i.e.* the response entropy for single stimuli, averaged across the different stimuli (Rieke *et al.*, 1997; Dayan and Abbott, 2001).

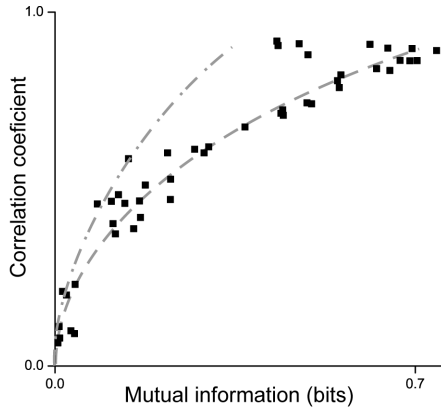


Figure 3.1: Relationship between mutual information (MI) and correlation coefficient (CC). The black points compare MI and CC for all *in vitro* experiments. The dashed line is an estimated lower bound, which is reached for $L = 0.5$. The upper line is an estimated upper bound, which is reached for very low or very high L . The estimated bounds were obtained numerically for a single pair of binary vectors (10,000 events), each with the same L (0.1 to 0.9) and CC (0.1 to 0.9). These bounds are only approximate, because in the experiments, L is not the same from one electrode to another.

3.2.5 Likelihood of participation L

Likelihood of participation L_i for site i was defined as the fraction of patterns in which the site participated:

$$L_i = \frac{1}{N} \sum_{j=1}^N q_i(j). \quad (3.5)$$

The average likelihood of participation L for all M sites is defined as

$$L = \frac{1}{NM} \sum_{i=1}^M \sum_{j=1}^N q_i(j). \quad (3.6)$$

3.2.6 Data shuffling to destroy interactions

For the purpose of understanding how the entropy changes due to interactions between sites, we created surrogate data sets by shuffling the events in which sites participated. The 1s and 0s were randomly reordered in each participation vector q_i such that interactions between sites were destroyed, but L_i and N remained fixed.

3.2.7 Model

Very similar to the model described in the chapter of experimental design, this model consisted of $M = 16$ binary sites (1 = active, 0 = inactive). Each site was intended to model the activity of a large group of neurons like the nLFP recorded at an electrode in the experiments. Each population event in the model was represented with a 16 bit binary pattern (1 = the site was active at least once during the response to the stimulus, otherwise 0). By simulating 1000 population events (always initiated at the same site), we generated a set of patterns for which the entropy was computed. From the event size distribution of network events we computed κ . The event size was defined as the sum of all activations from all sites during the population event. The range of average p_{ij} values studied with the model resulted in a range of $\kappa = 0.6$ to 1.6.

3.2.8 Statistical Analysis

For determining the statistical significance of differences in entropy for different drug conditions and in κ for different drug conditions, we first used a one-way ANOVA to establish that at least one drug category was different from at least one other. Next we performed a post-hoc test of significant pairwise differences between the drug categories using a t-test with the Bonferroni correction for multiple comparisons. The same procedure was used to assess significance of differences in H and MI for different categories of κ .

3.3 Results

In all of our experiments, multi-electrode array (MEA) recordings of the local field potential (LFP, Fig. 3.2A) were used to obtain patterns of cortical population activity. We defined a recording site as ‘active’ if it presented a large, negative deflection in the LFP (Fig. 3.2A, green). We have demonstrated that such negative LFP deflections correlate with increased firing rates of the local neuronal population for each of the experimental preparations studied here: superficial layers of organotypic cultures (Shew *et al.*, 2009), urethane anesthetized rat (Gireesh and Plenz, 2008) and awake monkeys (Petermann *et al.*, 2009). We define a ‘population event’ as a set of electrodes which were active together within a short time. In our analysis, each population event was represented by a binary spatial pattern with one bit per recording site and 1 or 0 indicating an active or inactive site respectively (Fig. 3.2B; top). For each one hour recording *in vitro* ($n = 47$) or 30 min recording *in vivo* ($n = 4$ monkey, $n = 6$ rat), we typically observed 10^3 to 10^4 population events.

First, we systematically explored a range of E/I conditions in cortex slice cultures. A reduced E/I ratio was obtained by bath-application of antagonists of AMPA- and NMDA-glutamate receptor mediated synaptic transmission (DNQX, 0.5-1 μ M; AP5, 10-20 μ M). This resulted in population events that were typically small in spatial extent (Figs. 3.2B and C, left). Conversely, an increased E/I ratio was obtained with an antagonist of fast GABA_A-receptor mediated synaptic inhibition (Picrotoxin; PTX, 5 μ M), which led to stereotyped, spatially extended population events (Figs. 3.2B and C, right). The drug concentrations used here are well below the level for complete ion channel blockade. In contrast, unperturbed E/I (Figs. 3.2B and C, middle) typically yielded a diverse pattern repertoire. The raster plots in Fig. 3.2B (bottom) display examples of 100 consecutive population events recorded under the three different E/I conditions. Fig. 3.2C displays example probability distributions of population event sizes for the three E/I conditions. We performed 11 recordings with reduced AP5/DNQX, 27 with no drug, and 9 with PTX. For each recording, we measured both ongoing activity and stimulus-evoked activity. For all recordings, we assessed the information capacity by computing the Shannon entropy of the full set of recorded binary patterns (Shannon, 1948); Rieke *et al.*, 1997; Dayan and Abbott, 2001; see also Methods).

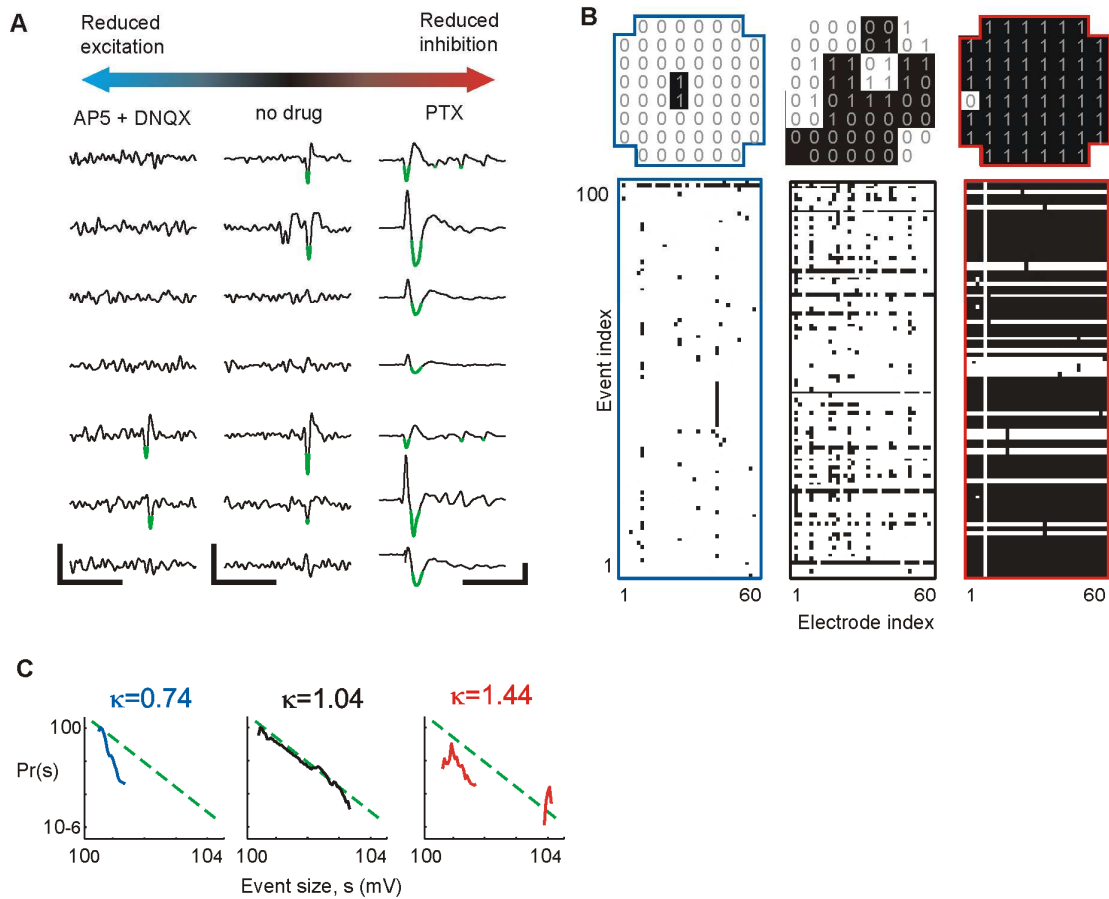


Figure 3.2: Measuring the neural activation pattern repertoire for a range of E/I conditions. *A*, Example LFP recordings under conditions of reduced E (left), unperturbed E/I (middle), and reduced I (right). Scale bars: 250 ms x 10 μ V (left, middle) and 250 ms x 100 μ V (right). Population events were defined based on large negative deflections ($< -4SD$, green). *B*, (top) Single examples of population events represented as binary patterns: 1 = active site, 0 = inactive. (bottom) Rasters including 100 consecutive population events represented as binary patterns; each row represents one event, each column represents one recording site. Left: reduced E. Middle: unperturbed. Right: reduced I. *C*, Shape of event size distributions reveal changes in E/I, which are quantified with κ (see Methods; broken line: power law with exponent of -1.5).

3.3.1 Peak information capacity of ongoing activity for intermediate E/I and neuronal avalanches

Our first finding was that the entropy H for ongoing activity peaks at an intermediate E/I ratio. This was demonstrated with two different approaches. First, we compared entropy to the three pharmacological categories: AP5/DNQX, no drug, and PTX. We found that under the unperturbed E/I condition the average H was significantly higher than either the reduced E/I condition of the AP5/DNQX or the increased E/I condition of PTX (Fig. 3.3A, ANOVA, $p < 0.05$). Second, we compared entropy to a previously developed statistical measure called κ , which characterizes E/I based on population dynamics of the network (Shew *et al.*, 2009). An advantage over the three pharmacology categories is that κ is a graded measure, thus providing a continuous function of entropy H versus E/I. κ quantifies the shape of the population event size distribution, which is sensitive to changes in E/I (Fig. 3.2C): $\kappa < 1$ indicated reduced E/I and $\kappa > 1$ indicated increased E/I (Fig. 3.3B). Indeed, κ was significantly different for the two pharmacological manipulations compared to the no-drug condition (Fig. 3.3B; $p < 0.05$). When we plotted entropy versus κ (Fig. 3.3C), we discovered a peaked function with maximum entropy occurring for $\kappa \approx 1$. This confirms our finding of peak entropy for the no drug condition (Fig. 3.3A) and provides a more refined view of the data; the peak occurred at $\kappa^* = 1.16 \pm 0.12$ (mean \pm SD, uncertainty determined by rebinning the experimental data, see Fig. 3.4). The statistical significance of the peak in H was confirmed by comparing H for the ten experiments with κ closest to 1 with the ten experiments with smallest κ and ten with largest κ ($p < 0.05$).

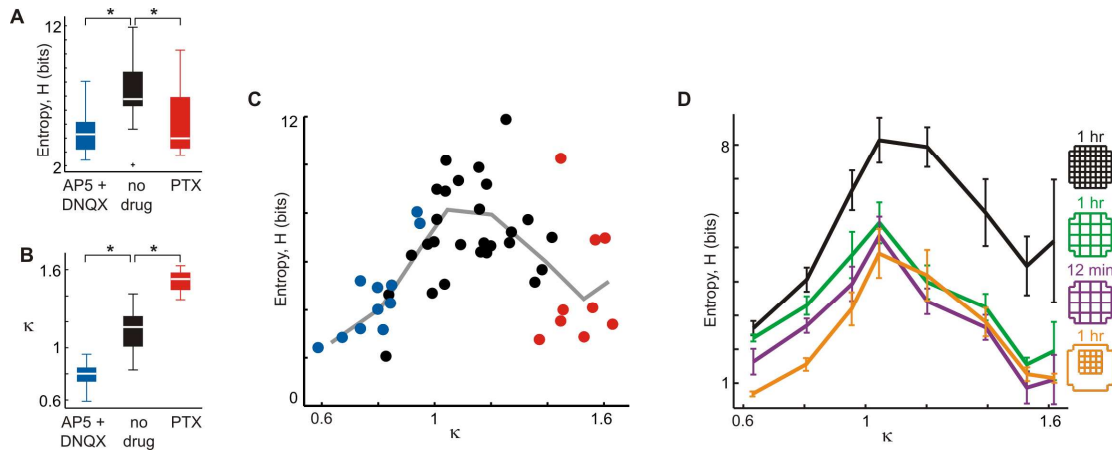


Figure 3.3: Ongoing activity - peak information capacity at intermediate E/I ratio specified by $\kappa \approx 1$.

A, Information capacity (entropy H) of the pattern repertoire is maximized when no drugs perturb the E/I ratio. Significant differences marked with * ($p < 0.05$). Box plot lines indicate lower quartile, median, upper quartile; whiskers indicate range of data, excluding outliers (+, >1.5 times the interquartile range). **B**, The statistic κ , provides a graded measure of E/I condition based on network dynamics (Methods). **C**, Entropy H peaks near $\kappa \approx 1$. Each point represents one recording of ongoing activity ($n = 47$, 8×8 MEA, 1 hr, color indicates drug condition; red = PTX, blue = AP5/DNQX, black = no drug). Line is the binned average of points. **D**, The peak in entropy H is robust to changes in spatial resolution (green, 4×4 coarse-binned, 1 hr), spatial extent (orange, 4×4 subregion, 1 hr) and duration (purple, 4×4 coarse-binned, 12 min) of recording. (black, same data as in A). Error bars indicate mean \pm s.e.m.

In addition to providing a graded measure of E/I, κ assesses the statistical character of ongoing cortical population dynamics. Specifically, $\kappa \approx 1$ is the signature of neuronal avalanches (Shew *et al.*, 2009), a type of population dynamics defined by a power-law population event size distribution with a power-law exponent near -1.5 (Beggs and Plenz, 2003; 2004; Gireesh and Plenz, 2008; Petermann *et al.*, 2009; Shew *et al.*,

2009). The computation of κ entails first computing the difference between a measured event size distribution and a theoretical reference distribution defined as a power-law with exponent -1.5 (Fig. 3.2C, green dashed). Next, this difference is added to 1 to make it comparable to the branching parameter, resulting in $\kappa = 1$ for an exact match with a -1.5 power law, *i.e.* neuronal avalanches. In this context, our findings indicate that entropy is maximized under conditions which result in neuronal avalanches.

Next we tested the robustness of the peak in H with respect to changes in spatial and temporal scales of recordings. First, as shown in Fig. 3.3D (green), we found that the peak in H remained close to $\kappa = 1$ ($\kappa^* = 1.01 \pm 0.02$), even when the original 8x8 patterns were coarse-grained to obtain 4x4 patterns at half the spatial resolution (see Methods). Second, the peak was also maintained when the spatial extent of the recorded area was reduced by 75% (4x4 electrodes near center of the MEA; Fig. 3.3D). Thirdly, we confirmed that the peak persisted for a restricted recording duration of 12 minutes rather than one hour (Fig. 3.3D, purple). The robustness of our finding to shorter recording durations is important since estimations of entropy depend on the number of samples recorded. Finally, the peak is robust to different choices of the bins used to produce the average curve (Fig. 3.4). The variability of the peaks of these curves was used to estimate the uncertainty in the conclusion that peak entropy occurs at $\kappa^* = 1.16 \pm 0.12$.

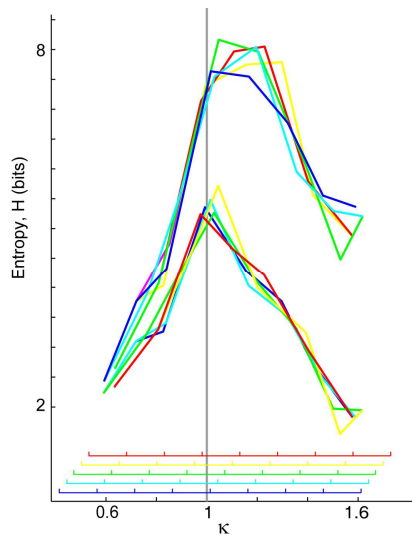


Figure 3.4: Results robust to bin choices. The results shown in Fig. 3.3C, D (black, green) for H vs. κ for 8x8 patterns (top) and coarse-binned 4x4 patterns (bottom) were recomputed with different averaging bins. The different bin partitions are shown below the curves with corresponding colors.

3.3.2 Peak information transmission between stimulus and response for intermediate E/I and neuronal avalanches

We now present measurements of stimulus-evoked activation patterns. A priori, one can expect a different distribution of stimulus-evoked patterns compared to ongoing activity and thus different entropy. Indeed studies suggest that ongoing activity is more diverse than typical stimulus-evoked activity (Fiser *et al.*, 2004; Luczak *et al.*, 2009; Churchland *et al.*, 2010). However, if the entropy of evoked patterns changes with E/I in the same way that we found for ongoing activity, then evoked entropy may also peak near $\kappa = 1$. This possibility is in line with significant evidence that ongoing activity in the cortex is intimately related to stimulus-evoked activity (Kenet *et al.*, 2003; Ji and Wilson, 2007; Han *et al.*, 2008; Luczak *et al.*, 2009). For instance,

stimulus-evoked activity patterns recur during ongoing activity, both at the population level (Kenet *et al.*, 2003; Han *et al.*, 2008) and the level of spike sequences (Ji and Wilson, 2007). Therefore, our next aim was to test whether our finding of peak entropy near $\kappa = 1$ also holds for stimulus-evoked activity.

Stimuli consisted of 10 different amplitude single bipolar shocks each applied 40 times in randomized order through a single electrode of the MEA within cortical layers II/III (Methods). A binary pattern was constructed to represent each response during the 20 – 500 ms after the stimulus. The evoked entropy H was calculated for the set of 400 stimulus-evoked activation patterns for each E/I. As found for ongoing activity, the evoked entropy was highest near $\kappa \approx 1$ for both fine and coarse spatial resolution (Fig. 3.5A; black - 8x8, green - coarse-grained 4x4, $p < 0.05$).

In the introduction, we gave a simple example in which information transmission from input to output was limited due to low entropy. With our measurements of network responses (*i.e.* output) to stimuli (*i.e.* input), we can directly test whether efficacy of information transmission is optimized when entropy is maximized. This idea is concisely summarized in the following equation: $MI(S;R) = H(R) - H(R|S)$. Here, $MI(S;R)$ is the mutual information of stimulus and response which quantifies the information transmission (Rieke *et al.*, 1997; Dayan and Abbott, 2001). $H(R)$ is

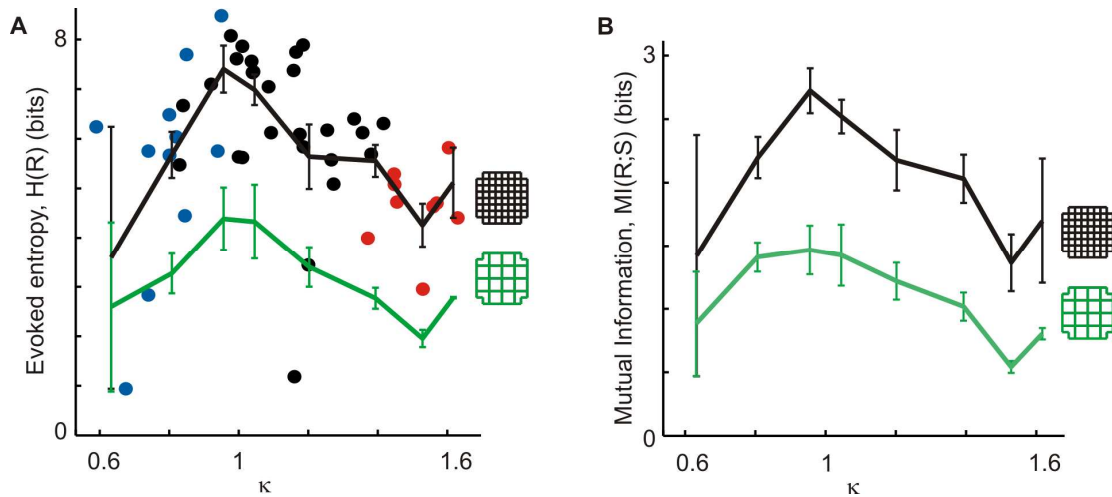


Figure 3.5: Stimulus-evoked activity - peak information transmission at intermediate E/I ratio specified by $\kappa \approx 1$. **A**, Single shock stimuli with 10 different amplitudes (10-200 μA) were applied 40 times each using a single electrode. The pattern repertoire of stimulus-evoked activity has maximum entropy near $\kappa \approx 1$. This holds for 8x8 response patterns (black line) as well as coarse resolution 4x4 patterns (green line). Points correspond to 8x8 patterns: light blue – AP5/DNQX, gray – no drug, pink – PTX. **B**, The efficacy of information transfer, *i.e.* mutual information of stimulus and response, also peaks near $\kappa \approx 1$. The dashed line indicates the highest possible mutual information given 10 stimulus levels. (black - 8x8; green – 4x4). Error bars indicate s.e.m.

the entropy of the full set of response patterns for all stimuli, while $H(R|S)$ is the conditional entropy, *i.e.* the average entropy per stimulus. As shown above, $H(R)$ is maximized near $\kappa \approx 1$. Since, $H(R|S)$ is always positive, $MI(S;R)$ is bounded by $H(R)$, and thus potentially also peaks near $\kappa = 1$. Indeed, we measured $MI(S;R)$ under different E/I conditions and found that stimulus-response mutual information was maximized near $\kappa \approx 1$ (Fig. 3.5B; black - 8x8, green - coarse-grained 4x4, $p < 0.05$).

3.3.3 Competition between activity rates and interactions explains peak in entropy

To identify and quantify the mechanisms leading to the peak in entropy near $\kappa = 1$, we analyzed in more detail the coarse-grained 4x4 patterns measured during ongoing activity (Fig. 3.3D, green). A priori, the total number of unique patterns that are possible is 2^{16} , implying a maximum $H \leq \log_2(2^{16}) = 16$ bits. This maximum would be reached if all 2^{16} patterns occurred with equal probability. However, during a 1 hr recording, the network did not generate all possible patterns, nor were different patterns equally likely, resulting in H that was always below 16 bits. The peak in H was explained by three main factors that changed with the E/I ratio: *i*) the number N of patterns observed during the recording, *ii*) the likelihood L that sites participate in patterns, and *iii*) the strength of interactions between sites. The first two effects are related to the rates of observed activity and impose upper bounds on H : effect *i* requires $H \leq \log_2(N)$ (dash-dot line in Fig. 3.6A) and effect *ii* limits H in a way that depends on L (dashed line Fig. 3.6A). Specifically, the highest possible entropy for a given L can be computed by assuming that sites are independent,

$$H < -\sum_{i=1}^M (L_i \log_2 L_i + (1 - L_i) \log_2 (1 - L_i)), \quad (3.7)$$

where M is the number of recording sites and L_i is the likelihood of participation for site i . This formula is based on the fact that the entropy of two independent systems combined is the sum of their individual entropies. Since a single site i is either active

(with probability L_i) or inactive (with probability $1-L_i$), its entropy is $-L_i \log_2 L_i - (1-L_i) \log_2 (1-L_i)$. Thus, adding the entropy of all sites, we obtain the formula above. When $L < 1/2$, increasing L increases the upper bound on H . When $L > 1/2$, increasing L decreases the upper bound on H . We found that L increased over the range of E/I conditions we studied (Fig. 3.6C), while the number of patterns N did not show a systematic trend.

We turn now to effect *iii*. Increased interactions between sites always reduce H due to the increased redundancy of the information at different sites (Schneidman *et al.*, 2003). We found that site-to-site interactions during ongoing activity increased with E/I (Fig. 3.6E), and quantified this trend in two ways. First we computed mutual information (MI) between the activity recorded from different pairs of sites (Fig. 3.6E; red). Note that above we used mutual information in a different way, computed between stimulus and response $MI(R;S)$ to assess information transmission. Second, we estimated the effect of interactions by computing the drop in entropy resulting from shuffling the data. The shuffling procedure destroyed interactions by randomizing the set of population events in which each site participated, while keeping L and N fixed (Methods). The entropy of the shuffled data for the corresponding original κ value is shown in Fig. 3.6A (black) and, as expected, nearly reached the bounds set by the combined effects *i* and *ii*. The difference in entropy ΔH between the measured and shuffled data is due to interactions (Fig. 3.6E, blue). ΔH has previously been used to quantify redundancy (Dayan and Abbott, 2001).

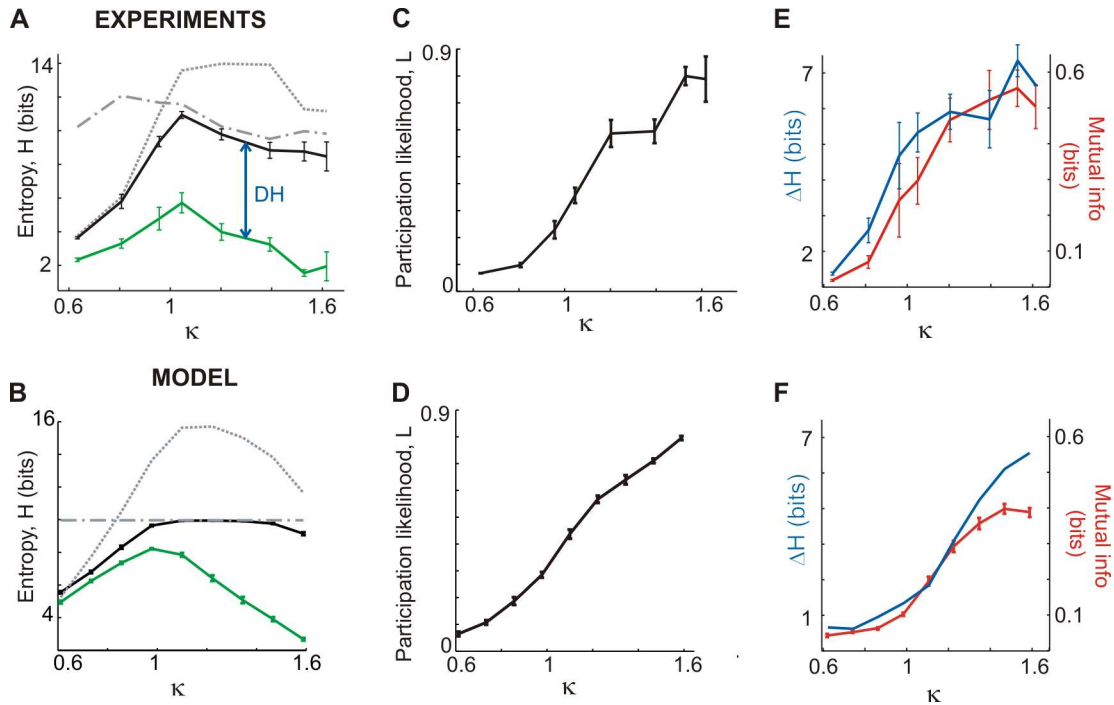


Figure 3.6: Peak information capacity explained. A detailed analysis of *in vitro* experimental results (top, Fig. 3.3D, green) and model results. **A, B** Upper bounds on entropy are set by 1) the average likelihood that sites participate in patterns (dashed) and 2) the number of patterns observed (dash-dot). When the effects of interactions are removed by shuffling (Methods), the entropy reaches these bounds (black), but the measured entropy (green) is always lower due to interactions. **C, D** Rise in participation likelihood L as E/I ratio is increased. This rise accounts for the bounds (dashed) shown in A,B. **E, F** Rise in interactions between sites (mutual information, red) is proportional to the loss in information capacity ΔH (blue). All error bars indicate s.e.m.

In summary, at low E/I, effects *ii* and *iii* compete and effect *ii* wins, *i.e.* activity rates drop sufficiently low to cause low entropy even though interactions are also low. At high E/I, effects *ii* and *iii* cooperate, *i.e.* both high activity rates and strong interactions cause low entropy. Entropy peaked at an intermediate E/I ratio at which

interactions between sites were not too low or too high (specified by $MI \approx 0.2$) and activity was not too depressed ($L \approx 0.25$).

We remark that, if N were large enough (e.g. for longer recording duration), the upper bound due to effect i would become irrelevant, in which case, we still expect H to peak near $\kappa = 1$ due to the combined effects of interactions (ΔH) and L . Nonetheless, the persistence of the peak in H for shorter duration recordings may be more relevant for cortex operations which occur on shorter time scales. We also tested the extent to which our measurements are impacted by sample size following the methods developed by Magri *et al.* 2009. The difference between our measured H and ‘corrected’ H was 0.06 ± 0.06 (mean \pm SD) bits for 4x4 *in vitro* ongoing activity patterns and 0.22 ± 0.18 bits for the 8x8 patterns. Thus, sample size effects are small compared to the variability from one experiment to another (see error bars in Fig. 3.3) We also point out that N , L , and MI are not the only factors that could potentially influence H . For example, not every site was equally likely to be active. Such spatial structure is expected to decrease entropy compared to a spatially homogeneous system with all other properties held fixed. This was not a major influence in our results.

3.3.4 Experimental results confirmed in a computational network-level model

To gain further insight on our experiments, we compared our results to a network-level simulation, which has been used previously to model neuronal avalanches

(Haldeman and Beggs, 2005; Kinouchi and Copelli, 2006; Shew *et al.*, 2009). The model consisted of 16 binary sites. The state (1 = active, 0 = inactive) of each site was intended to represent a population of neurons in the vicinity of a recording electrode (Methods). The propagation of activity from one site to another was treated probabilistically; a connection matrix p with entries p_{ij} specified the probability that site i would become activated due to site j having been activated in the previous time step. Increases (decreases) in E/I were modeled by increasing (decreasing) the average p_{ij} value through the range 0.006 to 0.1. For each ‘E/I condition’, 1000 population events were simulated, beginning with a single initially active site and the resulting patterns of activity were recorded. To facilitate comparison with our experimental results we also parameterized each E/I condition of the model using κ , based on population event size distributions.

In good agreement with our experiments, we found that entropy reached a peak for $\kappa \approx 1$ (Fig. 3.6B; green). Moreover, the explanation of peak entropy in terms of the competition between activity rates and site-to-site interactions also held for the model. Just as in the experiments, when the model data was shuffled to remove effects due to interactions, H (Fig. 3.6B; black) approached the upper bounds set by the number of events (Fig. 3.6B; dash-dot) and the likelihoods of participation (Fig. 3.6B; dashed). The model H results matched the experimental values, because the underlying changes in L versus κ (Fig. 3.6D) and the changes in site-to-site MI versus κ (Fig. 3.6F, red) were very similar to those measured experimentally. This agreement is not trivial; the same values of entropy could in principle be reached with

different combinations of the underlying L and MI versus κ . For example, a peak in H could result if L remained fixed at 0.5 and interactions were minimized at $\kappa = 1$. Site-to-site mutual information in the model reached slightly lower levels for high κ when compared to experiments (Fig. 3.6F, red), which could be due to the lack of significant structure in the model connectivity matrix p .

3.3.5 *In vivo* entropy matches *in vitro* prediction

Finally, we analyzed recordings of ongoing activity from superficial cortical layers in two awake monkeys (premotor cortex) not engaged in any particular task and in urethane-anesthetized rats ($n = 6$, barrel cortex) with no whisker stimulation. In agreement with previous studies (Gireesh and Plenz, 2008; Petermann *et al.*, 2009), we found that the ongoing activity was organized as neuronal avalanches (Fig. 3.7A). More precisely, we found that $\kappa = 1.02 \pm 0.02$ for the monkeys and $\kappa = 1.08 \pm 0.02$ for the rats. Based on our *in vitro* findings, these κ values suggest that the *in vivo* networks are operating under E/I conditions that maximize entropy and information transmission. Although we cannot fully test this idea without a full range of κ *in vivo*, we can test whether the *in vivo* values of H , L , and MI match with those predicted from the *in vitro* results. As shown in Fig. 3.7B and summarized in Table 3.1, we found good agreement with these predictions. We found no statistically significant difference between the *in vivo* results and the prediction from *in vitro* experiments with the same range of κ ($1.0 < \kappa < 1.1$, $p < 0.05$). Nonetheless, the fact that entropy values *in vivo* were slightly higher than the *in vitro* results, may be due to the corresponding slightly lower MI values.

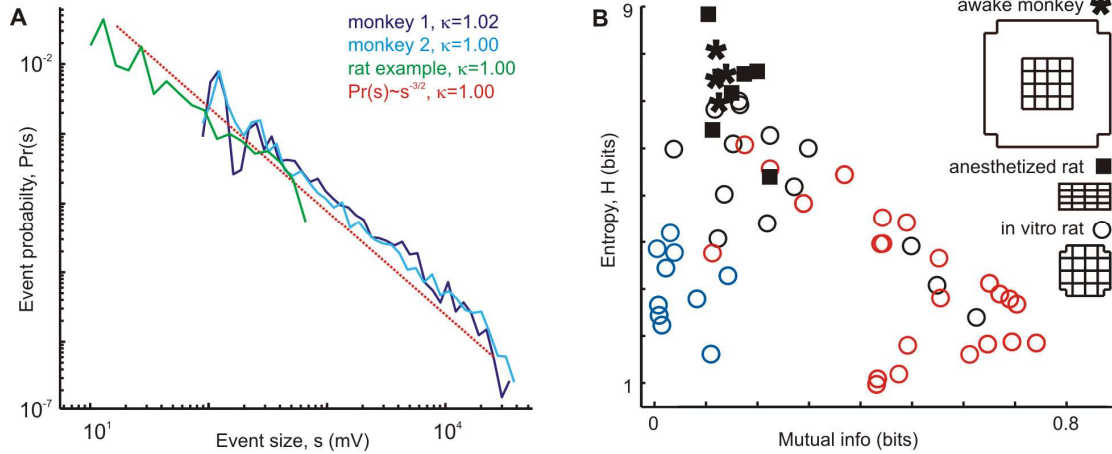


Figure 3.7: *In vivo* properties predicted from *in vitro* results. *A*, Population event size distributions from ongoing activity in two awake monkeys (blue) and an example rat (green) are near a power-law with exponent -1.5 (dashed line), *i.e.* they exhibit neuronal avalanches and $\kappa \approx 1$. *B*, In line with *in vitro* and model predictions for $\kappa \approx 1$, *in vivo* entropy was high and mutual information between recording sites was moderate. (stars - two recordings on different days from each monkey; squares - anesthetized rats, $n = 6$). The spatial extent of recorded area was approximately matched.

	<i>Entropy, H</i> (bits)	<i>Participation</i> <i>likelihood, L</i>	<i>Site-to-site mutual</i> <i>information, MI</i>
<i>In vitro</i>	5.7 ± 1.6	0.3 ± 0.1	0.2 ± 0.2
predictions for Awake monkeys	7.5 ± 0.5	0.3 ± 0.03	0.1 ± 0.01
$\kappa = 1.02 \pm 0.02$ Anesthetized rats	7.1 ± 1.2	0.4 ± 0.1	0.2 ± 0.1
$\kappa = 1.08 \pm 0.02$			

Table 3.1: *In vivo* results match *in vitro* predictions. Given the range of κ found in the *in vivo* recordings ($1 < \kappa < 1.1$), our *in vitro* results provide the predictions of H, L, and MI shown in the first row. The corresponding measurements from the awake monkeys (second

row) and anesthetized rats (third row) match the *in vitro* predictions, *i.e.* they are not significantly different ($p < 0.05$). Corresponding data are shown in Fig. 3.7B. All numbers are mean \pm SD.

We also measured the spike count cross correlation values between unit activities recorded simultaneously with the monkey LFP recordings. The average correlation between unit signals is significantly lower than that between the population signals provided by the LFP. As shown in Fig 3.8, the mean, s.e.m., and distributions of correlation coefficients were in good agreement with recent reports from awake monkeys (Ecker *et al.*, 2010) and anesthetized rats (Renart *et al.*, 2010). We note that the *in vivo* values of *MI*, which are based on LFP measurements, coexist with low values of pair-wise correlation r between spiking activity of units (mean \pm s.e.m. $r = 0.03 \pm 0.01$, Fig. 3.8), in line with recent reports for awake monkeys and anesthetized rats. The success of our prediction requires matching the number of recording sites (16 here), but is robust to large changes in spatial extent and resolution of recordings (data not shown). The prediction is also robust to changes in the threshold used for generating binary activity patterns from continuous LFP data. For thresholds -2.5, -3 and -3.5 SD we found no significant changes as shown in Table 3.2 below (mean \pm s.e.m.).

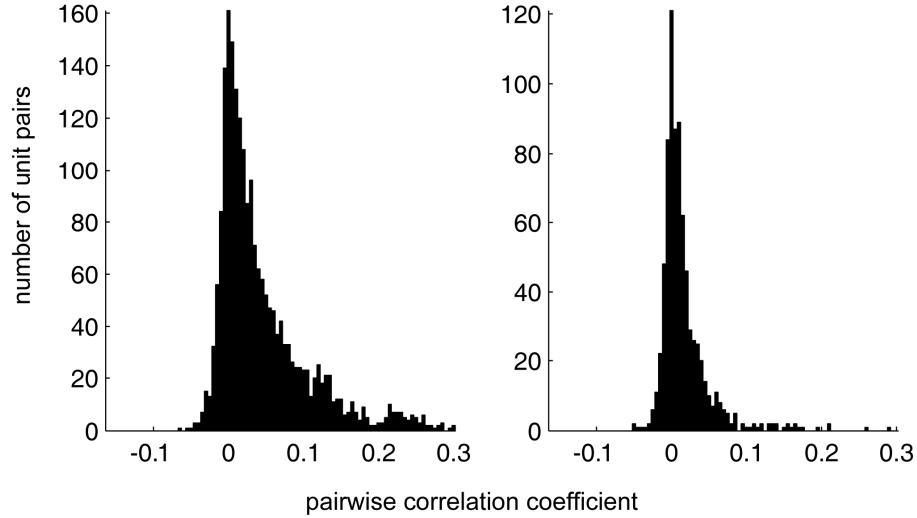


Figure 3.8: Histograms of pairwise correlation coefficients of unit activity in the awake monkeys. As reported previously (Ecker *et al.*, 2010; Renart *et al.*, 2010) the average across all pairs is near zero and positive. The histogram of all pairwise CC values for monkey 1 (left) and monkey 2 (right) are shown. The mean \pm sem CC values were 0.050 ± 0.002 and 0.015 ± 0.001 for monkey 1 and monkey 2 respectively.

	κ	H	MI
Monkey 1			
Day 1	1.02 ± 0.02	7.96 ± 0.35	0.11 ± 0.01
Day 2	1.07 ± 0.03	7.58 ± 0.32	0.14 ± 0.02
Monkey 2			
Day1	0.99 ± 0.02	6.99 ± 0.10	0.13 ± 0.01
Day 2	1.00 ± 0.02	7.51 ± 0.08	0.11 ± 0.02

Table 3.2: In line with previous studies, our *in vivo* monkey results were robust to changes in the detection threshold for nLFPs. For thresholds -2.5, -3 and -3.5 SD we found no significant changes as shown here (mean \pm s.e.m.).

3.4 Discussion

We employed *in vitro* and *in vivo* experiments as well as a computational model to study the effects of the E/I ratio on entropy and information transmission in cortical networks. We analyzed multisite measurements of LFP recorded during ongoing as well as stimulus-evoked activity. We found that entropy and information transmission are maximized for the particular E/I ratio specified by $\kappa = 1$, which is the same E/I condition under which neuronal avalanches emerge.

We emphasize that the relative changes in H as we altered E/I are the meaningful results of our *in vitro* study; the absolute entropy values in bits depend upon arbitrary aspects of the analysis and measurements, e.g. the number of electrodes in the MEA. Thus, we are not suggesting that there is an absolute cap on the information that a cortical circuit can represent at ~ 10 bits and it is not appropriate to compare our H values to those found in other studies of population entropy measures (e.g. Quiñero and Panzeri, 2009). The important feature of our result is the *peak* in H near $\kappa \approx 1$. We expect that any measure of population entropy would also peak for the same intermediate E/I, specified by $\kappa \approx 1$.

Previous studies have separately addressed the topics of entropy maximization (Laughlin, 1981; Dong and Atick, 1995; Dan *et al.*, 1996; Li, 1996; Rieke *et al.*, 1997; Dayan and Abbott, 2001; Garrigan *et al.*, 2010), neuronal avalanches (Beggs and Plenz, 2003; Haldeman and Beggs, 2005; Stewart and Plenz, 2006; Ramo *et al.*, 2007; Gireesh and Plenz, 2008; Tanaka *et al.*, 2009; Petermann *et al.*, 2009; Shew *et*

al., 2009), and the balance of E/I (van Vreeswijk and Sompolinsky, 1996; Shadlen and Newsome, 1998; Shu *et al.*, 2003; Okun and Lampl, 2008; Susillo and Abbott, 2009; Roudi and Latham, 2007), but our work is the first to show how these ideas converge in cortical dynamics.

Significant evidence suggests that maximization of entropy is an organizing principle of neural information processing systems. For example, single neurons in the blowfly visual system have been shown to exhibit spike trains with maximized entropy, considering the stimuli the fly encounters naturally (Laughlin, 1981). Applied at the level of neural populations, the principle of maximized entropy has provided successful predictions of receptive field properties in mammalian retina (Garrigan *et al.*, 2010), lateral geniculate nucleus (Dong and Atick, 1995; Dan *et al.*, 1996), and visual cortex (Li, 1996). Our work shows that the potential ability of a neural population in the cortex to achieve maximum entropy and maximum information transmission depends on the E/I ratio. Thus, if such properties are optimal for the organism, then the particular E/I ratio specified by $\kappa = 1$ may best facilitate this goal.

We note that our investigation is not directly related to ‘maximum entropy’ models (e.g. Schneidman *et al.*, 2006). In those studies, the aim was to use the maximum entropy principle (Jaynes, 1957) to find the simplest model to describe an experimental data set; entropy served as a modeling constraint. In contrast, here we compare the entropy across different experiments, searching for conditions which result in maximum entropy; entropy measurements are the results.

Several theory and modeling studies (including our own model) offer a deeper explanation of why $\kappa = 1$ and neuronal avalanches occurs under E/I conditions which maximize entropy and information transmission (Beggs and Plenz, 2003; Haldeman and Beggs, 2005; Ramo *et al.*, 2007; Tanaka *et al.*, 2009). Recall that neuronal avalanches and $\kappa = 1$, by definition, indicate a power-law event size distribution with exponent $-3/2$. This same property is found in many dynamical systems that operate near ‘criticality’. Criticality refers to a particular mode of operation balanced at the boundary between order and disorder (e.g. Stanley, 1971; Jensen, 1998), akin to the balance of excitation and inhibition that we explore in our experiments. In our model, criticality occurs when the average p_{ij} equals $1/M$ (M is the number of sites). When $p_c > 1/M$, activity propagation is widespread and highly synchronous, like a seizure, while $p_c < 1/M$ results in weakly interacting, mostly independent neurons (Beggs and Plenz, 2003; Haldeman and Beggs, 2005; Kinouchi and Copelli, 2006). The balanced propagation that occurs at criticality might be attributed to interactions between excitatory and inhibitory neurons in the cortex. Using theory of Boolean networks, Ramo *et al.* (2007) showed theoretically that entropy of the event size distribution is maximized at criticality. Similarly, simulations of a model similar to our own showed that the number of activation patterns that repeat is maximized at criticality (Haldeman and Beggs, 2005). Tanaka *et al.* (2009) found that recurrent network models in which information transmission is optimized also exhibit neuronal avalanches and repeating activation patterns. Likewise, it has been shown that mutual information of input and output in feed-forward network models is maximized near criticality (Beggs and Plenz, 2003). In line with these theory and model predictions,

our results are the first experimental demonstration of peak entropy and information transmission in relation to criticality in the cortex.

Finally, a separate line of research has focused on the E/I ratio in cortical networks. Models emphasize the importance of balanced E/I for explaining the variability observed in spike trains (van Vreeswijk and Sompolinsky, 1996; Shadlen and Newsome, 1998), low correlations between spiking units (Renart *et al.*, 2010), and generating diverse population activity patterns (Susillo and Abbott, 2009), which may play a role in memory (Roudi and Latham, 2007). Moreover, *in vivo* experiments have shown that synaptic input received by cortical neurons exhibits a fixed ratio of excitatory to inhibitory current amplitudes (Shu *et al.*, 2003; Okun and Lampl, 2008). Since we measure $\kappa \approx 1$ *in vivo*, it follows that the ‘balanced E/I’ discussed in these previous studies may also correspond to the optimal E/I that we identify here.

In summary, our results suggest that by operating at the E/I ratio specified by $\kappa \approx 1$, the cortex maintains a moderate level of network-level activity and interactions which maximizes information capacity and transmission. This finding supports the hypotheses that balanced E/I and criticality optimize information processing in the cortex.

Bibliography

Beggs JM, Plenz D (2003) Neuronal avalanches in neocortical circuits. *The Journal of Neuroscience* 23:11167-11177.

Churchland MM *et al.* (2010) Stimulus onset quenches neural variability: a widespread cortical phenomenon. *Nature Neuroscience* **13**, 369-378.

Dan Y, Atick JJ, Reid RC (1996) Efficient coding of natural scenes in the lateral geniculate nucleus: experimental test of a computational theory. *The Journal of Neuroscience* 10:3351-3362.

Dayan P, Abbott LF (2001) *Theoretical neuroscience* (MIT Press, Cambridge, Massachusetts, USA).

Dichter M, Ayala G (1987) Cellular mechanisms of epilepsy: a status report. *Science* 237:157-164.

Dong DW, Atick JJ (1995) Temporal decorrelation: a theory of lagged and nonlagged responses in the lateral geniculate nucleus. *Network: Computation in Neural Systems* 6:159-178.

Ecker AS *et al.* (2010) Decorrelated neuronal firing in cortical microcircuits. *Science* 327:584-587.

Fiser J, Chiu C, Weliky M (2004) Small modulation of ongoing cortical dynamics by sensory input during natural vision. *Nature* **431**, 573-578.

Garrigan P *et al.* (2010) Design of a trichromatic cone array. *PLoS Computational Biology* 6:e1000677.

Gireesh ED, Plenz D (2008) Neuronal avalanches organize as nested theta- and beta/gamma-oscillations during development of cortical layer 2/3. *Proceedings of the National Academy of Sciences of the United States of America* 105:7576-7581.

Haldeman C, Beggs JM (2005) Critical branching captures activity in living neural networks and maximizes the number of metastable states. *Physical Review Letter* 94:058101.

Han F, Caporale N, Dan Y (2008) Reverberation of recent visual experience in spontaneous cortical waves. *Neuron* 60:321-327.

Ji D, Wilson MA (2007) Coordinated memory replay in the visual cortex and hippocampus during sleep. *Nature Neuroscience* 10:100-107.

- Jacobs *et al.* (2009) Ruling out and ruling in neural codes. *Proceedings of the National Academy of Sciences of the United States of America* 106:5936-5941.
- Jaynes ET (1957) Information theory and statistical mechanics. *Physical Review* 106:62-79.
- Jensen HJ (1998) *Self-organized criticality: emergent complex behavior in physical and biological systems.* (Cambridge University Press, Cambridge, UK).
- Kenet T, Bibitchkov D, Tsodyks M, Grinvald A, Arieli A (2003) Spontaneously emerging cortical representations of visual attributes. *Nature* 425:954-956.
- Laughlin S (1981) A simple coding procedure enhances a neuron's information capacity. *Zeitschrift fur Naturforschung* 36:910-912.
- Li Z (1996) A theory of the visual motion coding in the primary visual cortex. *Neural Comput* 8:705-730.
- Luczak A, Barthó P, Harris KD (2009) Spontaneous events outline the realm of possible sensory responses in neocortical populations. *Neuron* 62:413-425.
- Magri C, Whittingstall K, Singh V, Logothetis NK, Panzeri S (2009) A toolbox for the fast information analysis of multiple-site LFP, EEG and spike train recordings. *BMC Neurosci.* 10:81.
- Nauhaus I, Busse L, Carandini M, Ringach DL (2009) Stimulus contrast modulates functional connectivity in visual cortex. *Nature Neuroscience* 12:70-76.
- Okun M, Lampl I (2008) Instantaneous correlation of excitation and inhibition during ongoing and sensory-evoked activities. *Nature Neuroscience* 11:535-537.
- Petermann T *et al.* (2009) Spontaneous cortical activity in awake monkeys composed of neuronal avalanches. *Proceedings of the National Academy of Sciences of the United States of America* 106:15921-15926.
- Pola G, Thiele A, Hoffmann K-P, Panzeri S (2003) An exact method to quantify the information transmitted by different mechanisms of correlational coding. *Network: Comput. Neur. Syst.* 14:35-60.
- Quiñones Quiroga R, Panzeri S (2009) Extracting information from neuronal populations: information theory and decoding approaches. *Nat Rev Neurosci* 10:173-185.
- Ramo P, Kauffman S, Kesselia J, Yli-Harja O (2007) Measures for information propagation in Boolean networks. *Physica D* 227:100-104.

- Renart A *et al.* (2010) The asynchronous state in cortical circuits. *Science* 327:587-590.
- Rieke F, Warland D, de Ruyter van Stevenick R, & Bialek W (1997) *Spikes* (MIT Press, Cambridge, Massachusetts, USA).
- Roudi Y, Latham PE (2007) A balanced memory network. *PLoS Comp Biol* 3:1679-1700.
- Schneidman E, Berry II MJ, Segev R, Bialek W (2006) Weak pairwise correlations imply strongly correlated network states in a neural population. *Nature* 440:1007-1012.
- Schneidman E, Bialek W, Berry II MJ (2003) Synergy, redundancy, and independence in population codes. *The Journal of Neuroscience* 23:11539–11553.
- Shadlen MN, Newsome WT (1998) The variable discharge of cortical neurons: implications for connectivity, computation, and information coding. *The Journal of Neuroscience* 18:3870-96.
- Shannon CE (1948) A mathematical theory of communication. *Bell System Technical J* 27:379-423, 623–656.
- Shew WL, Yang H, Petermann T, Roy R, Plenz D (2009) Neuronal avalanches imply maximum dynamic range in cortical networks at criticality. *The Journal of Neuroscience* 29:15595-15600.
- Shu Y, Hasenstaub A, McCormick DA (2003) Turning on and off recurrent balanced cortical activity. *Nature* 423:288-293.
- Stanley HE (1971) *Introduction to Phase Transitions and Critical Phenomena* (Oxford University Press, New York, USA).
- Stewart C, Plenz D (2006) Inverted-U profile of dopamine-NMDA-mediated spontaneous avalanche recurrence in superficial layers of rat prefrontal cortex. *The Journal of Neuroscience* 26:8148-8159.
- Sussillo D, Abbott LF (2009) Generating coherent patterns of activity from chaotic neural networks. *Neuron* 27:544-557.
- Tanaka T, Kaneko T, Aoyagi T (2009) Recurrent infomax generates cell assemblies, neuronal avalanches, and simple cell-like selectivity. *Neural Comput* 21:1038-1067.
- van Vreeswijk C, Sompolinsky H (1996) Chaos in neuronal networks with balanced excitatory and inhibitory activity. *Science* 274:1724-1726.

Chapter 4: Maximal variability of phase synchrony in cortical networks with neuronal avalanches

4.1 Introduction

Neurons whose dynamics are synchronized are thought to play an important role in brain function, because their combined influence on other neurons is greater than that of asynchronous neurons (Bressler and Kelso, 2001; Varela *et al.*, 2001; von der Malsburg *et al.*, 2010; Kopell *et al.*, 2010). Synchrony is modulated during many tasks including perception (Bressler *et al.*, 1993; Rodriguez *et al.*, 1999; Palva *et al.*, 2005; Melloni *et al.*, 2007; Senkowski *et al.*, 2008; Hipp *et al.*, 2011), motor control (Roelfsema *et al.*, 1997; Kelso *et al.*, 1998), attention (Fries *et al.*, 2001), and working memory (Tallon-Baudry *et al.*, 2004; Sakurai and Takahashi, 2006). Conversely, weak synchrony is associated with brain disorders such as schizophrenia (Spencer *et al.*, 2003; Uhlhaas and Singer, 2010) and autism (Wilson *et al.*, 2007), whereas excessive synchrony is a hallmark of sleep and anesthesia (Destexhe and Contreras, 2006), Parkinson's disease (Boraud *et al.*, 2005) and epilepsy (Steriade, 2003; Garcia Dominguez *et al.*, 2005). In short, too much or too little synchrony is detrimental to information processing, while moderate synchrony is typical for the awake state in normal cortex.

Synchrony is thought to be important because it facilitates binding of neuronal groups. However, synchrony must be transient to allow the cortex to dynamically switch between different bound groups (Friston, 1997; Varela *et al.*, 2001; Bressler

and Kelso, 2001; von der Malsburg *et al.*, 2010). Thus, an important property of synchrony is its dynamic variability. Indeed, variability of neuronal population activity positively correlates with task performance (McIntosh *et al.*, 2008; Garrett *et al.*, 2011). At the behavioral level, state changes in human motor coordination are marked by high variability in movement synchrony (Kelso *et al.*, 1986; Schoner and Kelso, 1988). Neuronal network simulations (Destexhe, 1994) and *in vitro* experiments (Shew *et al.*, 2011) demonstrate neural variability to increase cortical information transfer.

To identify experimental conditions under which cortical synchrony emerges with moderate mean and maximum variability, we were guided by two lines of research. First, theoretical studies of interacting oscillators (Haken *et al.*, 1985; Daido, 1990; Kopell and Somers, 1995; Ermentrout and Kleinfeld, 2001; Strogatz, 2001; Arenas *et al.*, 2008; Kitzbichler *et al.*, 2009) reveal that, as the coupling between oscillators gradually strengthens, there is a sudden increase of synchrony, when the coupling surpasses a threshold level, called ‘criticality’. At criticality, synchrony is moderate on average and maximally variable (Daido, 1990). A second line of research suggests that criticality in the cortex manifests as neuronal avalanches (Beggs and Plenz, 2003; Plenz and Thiagarajan, 2007), defined by $Pr(s) \sim s^{-1.5}$, where $Pr(s)$ is the probability that a spatio-temporal cluster of neural activity of size s occurs. Theory (Otter, 1949; Hinrichsen, 2006) and biologically detailed models of cortical networks (Levina *et al.*, 2007; Meisel and Gross, 2009; Millman *et al.*, 2010) predict this form of power-law to occur at criticality. *In vivo* and *in vitro* experiments have shown that neuronal avalanches co-exist with coherent oscillations among intricately nested frequencies

θ and β/γ (Gireesh and Plenz, 2008). Here we show experimentally that neuronal avalanches identify a state of synchrony with moderate average and maximal variability, in line with predictions from theory of criticality and coupled oscillators.

4.2 Methods

4.2.1 Phase synchrony

We first obtained a phase trace from each LFP trace. This approach treats the LFP signal $f(t)$ as the real part of a complex signal, called the analytic signal $z(t)$. The imaginary part of $z(t)$ is the Hilbert transform of $f(t)$, and $z(t) = f(t) + iH[f(t)]$. We implemented this approach using the Matlab function ‘*hilbert*’. The phase trace is calculated as:

$$\theta(t) = \arctan \frac{\text{Im}(z(t))}{\text{Re}(z(t))} = \arctan \frac{H[f(t)]}{f(t)}. \quad (4.1)$$

In this way, we extracted the instantaneous phase of every electrode over the entire duration of the recording. For pure periodic signals, e.g. $f(t) = \cos(\omega t + \theta_0)$, this approach yields the phase $\theta(t) = \omega t + \theta_0$, where θ_0 is a constant defined such that $\theta = 0, \pi/2, \pi, \dots$ when $\cos(\omega t + \theta_0) = 1, 0, -1, \dots$. The phase is insensitive to amplitude, e.g. the phase traces are identical for $A\cos(\omega t)$ and $B\cos(\omega t)$, where $A \neq B$. Note that in our analysis we ‘wrapped’ the phase so that it was always between $-\pi$ and π . Similarly, for aperiodic signals like our LFP measurements, the instantaneous phase $\theta(t)$ is

related to zero crossings and peaks/troughs of the LFP signal, while the time derivative $d\theta(t)/dt$ gives an estimate of the instantaneous frequency of the LFP.

4.2.2 Phase and phase difference histogram

To display the dynamics of phase and phase synchrony in a way that is amenable to visual examination, we used two analysis techniques. First, the dynamic phase histogram displays phase dynamics for all 59 electrodes simultaneously. At each time point, a histogram of the 59 phases from $-\pi$ to π (resolution 0.05π) is computed and displayed as one vertical strip. A color code indicates the number of electrodes with a given phase bin. For example, red pixels indicate the times when many electrodes have similar phase, *i.e.* are phase synchronized. A second method to visualize phase synchrony is the dynamic phase difference histogram. We first compute the difference in phase for every pair of electrodes ($n = 59 \times (59-1)/2 = 1711$ pairs). A histogram of the phase differences is computed and displayed as one vertical strip at every time point (resolution 0.05π) and color coded. Phase synchrony is apparent as times when many pairs have near-zero phase difference. This visualization approach is particularly suited to identify anti-phase locking, *i.e.* near- π phase differences.

4.2.3 Anti-phase locking

To quantify the degree of anti-phase locking, we selected 8 experiments for each of the three conditions $\kappa < 1$, $\kappa \sim 1$, and $\kappa > 1$. From each experiment, we computed the

time-average of the dynamic phase difference histogram for 100 randomly chosen bursts. In this calculation, we included a 5 ms window preceding and following each burst, which is necessary to capture residual synchrony around burst occurrence. We averaged histograms across bursts and computed the difference between the count of electrode pairs with phase difference near π , *i.e.* within $\pi \pm 0.05\pi$, and the minimum of the histogram. This value which quantifies the degree in anti-phase locking is reported in the variable *APL* in Results. In addition, we studied whether anti-phase locking tended to occur between electrode pairs that spanned superficial and deep cortical layers. The midline of the MEA approximately divides superficial layers from deeper layers in the cortex cultures (Gireesh and Plenz, 2008) and we computed the fraction of anti-phase locked pairs which spanned the midline. For randomly evolving phases, this number would be 0.508, which is the fraction of all possible electrode pairs that span the MEA midline.

4.2.4 Network synchrony and burst synchrony.

A simple way to quantify the network-level phase synchrony as a function of time is provided by the Kuramoto order parameter, $r(t)$, defined as

$$r(t) = \frac{1}{n} \left| \sum_{j=1}^n e^{i\theta_j(t)} \right|, \quad (4.2)$$

where $n = 59$ is the number of recording electrodes over which synchrony is estimated (Strogatz, 2001; Arenas *et al.*, 2008). We were particularly interested in the synchrony during burst activity, which we quantified using the following three measures. First, the network synchrony of the k -th burst, S_N^k , was defined as

$$S_N^k = \sum_{t_i=t_k}^{t_k+d_k} r(t_i), \quad (4.3)$$

where t_k is the burst start time and d_k is the burst duration. Second, we calculated the *instantaneous network synchrony* for the k -th burst, S_{IN}^k , by normalizing S_N^k by burst duration d_k ,

$$S_{IN}^k = S_N^k / d_k. \quad (4.4)$$

We note that S_{IN}^k is now bounded between 0 and 1. Third, we computed the *instantaneous burst synchrony*, S_{IB}^k , by applying equations (4.2) – (4.4) only to those electrodes that were active during the k -th burst. More precisely, $r(t)$ was replaced by $r_m(t)$ computed only among the set of m sites, E_k , which were active, *i.e.* displayed an nLFP, during the k -th burst

$$r_m(t) = \frac{1}{m} \left| \sum_{j \in E_k} e^{i\theta_j(t)} \right| - RC(m). \quad (4.5)$$

Note that $r_m(t)$ represents a measure of within burst synchrony normalized by the area of the burst, *i.e.* number of electrodes that participate. $RC(m)$ is a correction to account for the expected level of noise for m sites with randomly evolving phases. $RC(m)$ was estimated by direct numerical simulation (10^4 time steps) of $r_m(t)$ for m random phases. By subtracting $RC(m)$, the actual values of $r_m(t)$ are comparable even if m is different for different bursts. Accordingly, S_{IB}^k is bounded between -1 and 1.

The averages \bar{S}_N , \bar{S}_{IN} , and \bar{S}_{IB} , were obtained by averaging over bursts. For example

$$\bar{S}_N = \frac{1}{M} \sum_{k=1}^M S_N^k, \quad (4.6)$$

where M is the total number of bursts recorded in an experiment.

4.2.5 Entropy measurements

In our results, we present entropy measurements of burst spatial extent, burst duration, and the three types of synchrony defined above. First, we computed the quantity in question, say x (which can be burst area, burst duration, S_N^k , S_{IN}^k or S_{IB}^k), for all M measured bursts. Then, a probability distribution of x was estimated; the probability p_i that x fell within the range $b_i < x < b_{i+1}$ was estimated as the number of x values in that range divided by M . The entropy of the x distribution was computed as

$$H(x) = - \sum_{i=1}^N p_i \log_2 p_i, \quad (4.7)$$

where N is the number of bins used to make the distribution. Since entropy is sensitive to the choice of bins, the bin divisions were fixed for comparisons across experiments, *i.e.* for different κ . Importantly, we found that the peak in entropy persisted for a very wide range of numbers of bins, from $N = 4$ to 4000 bins. However, the numerical values of entropy in terms of bits are not meaningful, except perhaps in reference to $\log_2(N)$, which is the maximum possible entropy computed from any distribution with N bins.

Burst area is a discrete variable ranging from 1 to 59, thus, we used one bin for each possible burst area. In contrast, at a temporal resolution of 0.25 ms, burst duration was treated as a continuous variable and we constructed distributions using 100 logarithmically spaced bins ranging from the shortest to the longest duration observed from all experiments (~ 10 ms to several s). Likewise, the distribution used to compute the entropy of S_N was created with 100 logarithmically spaced bins spanning the range of observed S_N values. For the bounded quantities, S_{IN} and S_{IB} , 100 linearly spaced bins between 0 and 1, -1 and 1 were used respectively. We note that negative values can result for S_{IB} due to the $RC(m)$ correction.

Finally, entropy can be biased toward low values if a small number of samples are used to estimate the probability distribution. To account for this bias, we estimated sub-sampling corrections to entropy following an established strategy (Magri *et al.*, 2009) and found that in all cases, the entropy corrections were small compared to the variation from experiment to experiment. Thus, sub-sampling bias does not significantly impact our conclusions.

4.2.6 Power spectra

Power spectra were computed via Welch's method using the Matlab function *pwelch*. First a power spectrum was computed for each burst. To allow a spectral range from 4 – 50 Hz, 250 ms preceding and following each burst were included in the calculation and only bursts of duration greater than 10 ms were included. Each

spectrum was averaged from FFT computations over 375 ms windows with 187.5 ms overlap and then normalized by its maximal power to facilitate comparison across experimental conditions.

4.2.7 Statistical analysis

For determining the statistical significance of differences in anti-phase locking for different drug conditions, we first used a one-way ANOVA to establish that at least one κ category was different from at least one other. Next we performed a post hoc test of significant pair-wise differences between the κ categories using a *t*-test with the Bonferroni correction for multiple comparisons.

4.3 Results

4.3.1 Neuronal burst area and duration have moderate mean and maximum entropy at $\kappa \sim 1$

We studied ongoing network activity recorded in organotypic tissue cultures grown on planar integrated multi-electrode arrays (MEAs). Following established techniques (Gireesh and Plenz, 2008; Shew *et al.*, 2009; Shew *et al.*, 2011), each culture ($n = 15$) was comprised of a coronal slice of somatosensory rat cortex combined with a slice from the ventral tegmental area, which provides dopaminergic inputs to the cortex for proper network development (Gireesh and Plenz, 2008). The tissue was cultivated directly on the surface of an 8x8 grid of electrodes (Fig. 4.1A,

200 μm inter-electrode distance, 30 μm electrode diameter, no corner electrodes, 4 kHz sampling). Recordings were taken between 10 – 20 days in culture allowing several 1 hr recordings from each network (47 recordings in total; Plenz and Stewart, 2008). The recorded voltages were low-pass filtered at 50 Hz to obtain the local field potential (LFP), which was shown to correlate with the spiking activity of the local neuronal population near each electrode (Shew *et al.*, 2009).

Observed dynamics consisted of bursts of activity like the example shown in Fig. 4.1B, which often spanned many recording sites. We determined the start and end of each burst as well as which sites participated using a threshold to identify times and electrodes with large amplitude negative LFP deflections (Methods).

We applied pharmacological agents to change the network excitability, which we consider analogous to tuning the coupling strength in models. Neural synchrony is expected to be sensitive to such changes in excitatory and inhibitory interactions (Bartos *et al.*, 2007; Kopell *et al.*, 2010). Excitatory synaptic transmission was reduced with combined application of the NMDA and AMPA glutamate receptor antagonists AP5 and DNQX. Inhibitory synaptic transmission was reduced with GABA_A receptor antagonist picrotoxin (PTX). Empirically, we found that the employed concentrations of DNQX/AP5 resulted in disfacilitation, *i.e.* decreased network activity, while the partial disinhibition with PTX increased network activity. As shown in Fig. 4.1C (blue, black), we found that the frequency content of the LFP

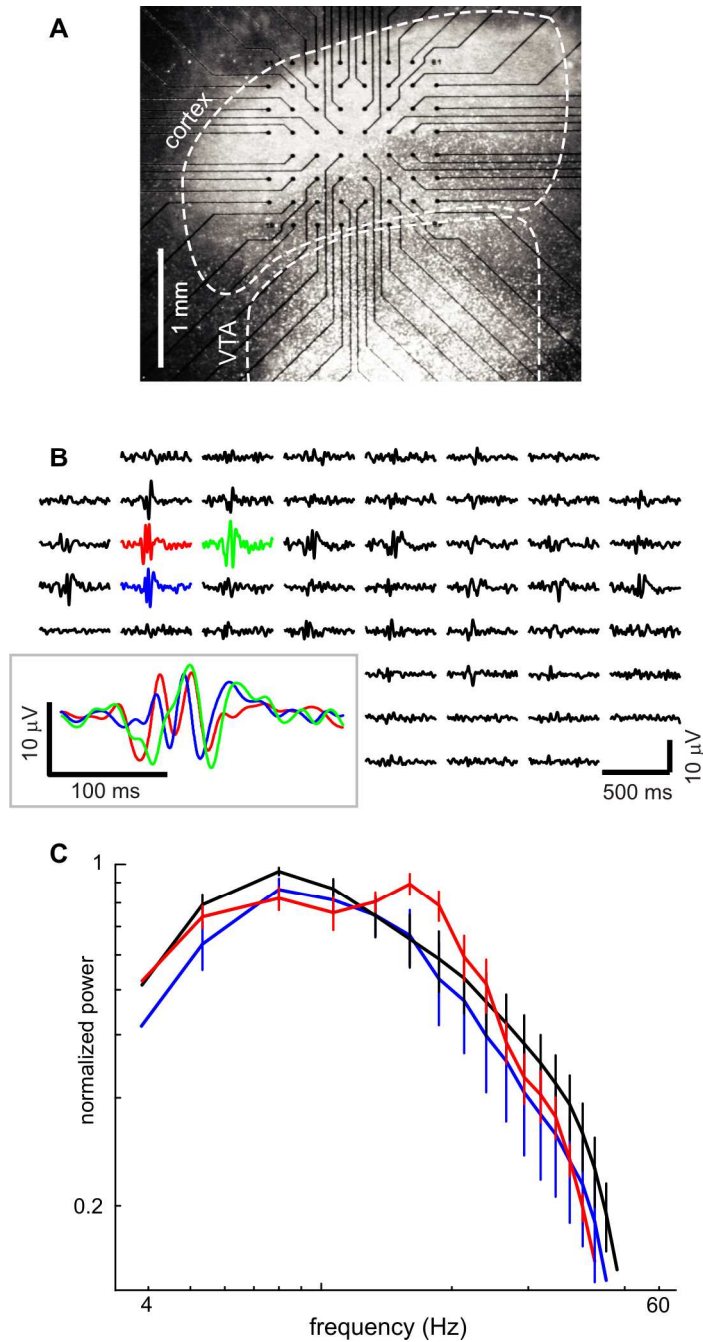


Figure 4.1: Spontaneous neuronal burst activity in cortex organotypic cultures grown on integrated planar microelectrode arrays (MEA). *A*, Light-microscopic image of a neural culture including somatosensory cortex and ventral tegmental area (VTA) grown on a 60 channel MEA. Black dots indicate the location of the $n = 59$ recording electrodes. The ground electrode is outside the imaged region. *B*, Examples of local field potential (LFP)

traces simultaneously recorded during a burst of neural activity (no drugs applied). The spatial arrangement of LFP traces matches that of the electrodes from which they were recorded. *Inset*: magnified view of three LFP traces. *C*, Average normalized power spectra for normal (black, no drug, $n = 8$), disfacilitated (blue, DNQX/AP5, $n = 8$), and disinhibited conditions (red, PTX, $n = 8$). The spectra were typically broadband without strong peaks under normal and disfacilitated conditions, while prominent β -oscillations (10 – 20 Hz) emerged under disinhibited conditions. Error bars indicate \pm SEM.

signals did not show any strong peaks at particular frequencies for the no-drug and DNQX/AP5 conditions. In contrast, β -oscillations became more prominent in disinhibited cultures as reported previously (Fig. 4.1C, *red*; Gireesh and Plenz, 2008).

To parameterize these drug effects on spontaneous network dynamics, we employed the statistical measure κ , which is based on measured distributions of burst sizes, as developed previously (Shew *et al.*, 2009; Shew *et al.*, 2011). This method takes advantage of the fact that the unperturbed condition typically results in a burst size distribution of the form $\text{Pr}(s) \sim s^{-1.5}$, *i.e.* neuronal avalanches, while the disfacilitated and disinhibited conditions result in exponential and bimodal distributions respectively. Practically, $\kappa \approx 1$ for unperturbed networks ($\kappa = 1.14 \pm 0.01$; no drug; $n = 28$), $\kappa < 1$ for disfacilitated networks ($\kappa = 0.81 \pm 0.01$; DNQX/AP5; $n = 10$) and $\kappa > 1$ for disinhibited networks ($\kappa = 1.51 \pm 0.01$; PTX; $n = 9$). This relationship is apparent in Fig. 4.2A, where each point represents the average burst area and κ value from a single recording and color represents drug condition. The average of the burst area, a , increased gradually for small κ and rose more quickly near $\kappa = 1$ and beyond

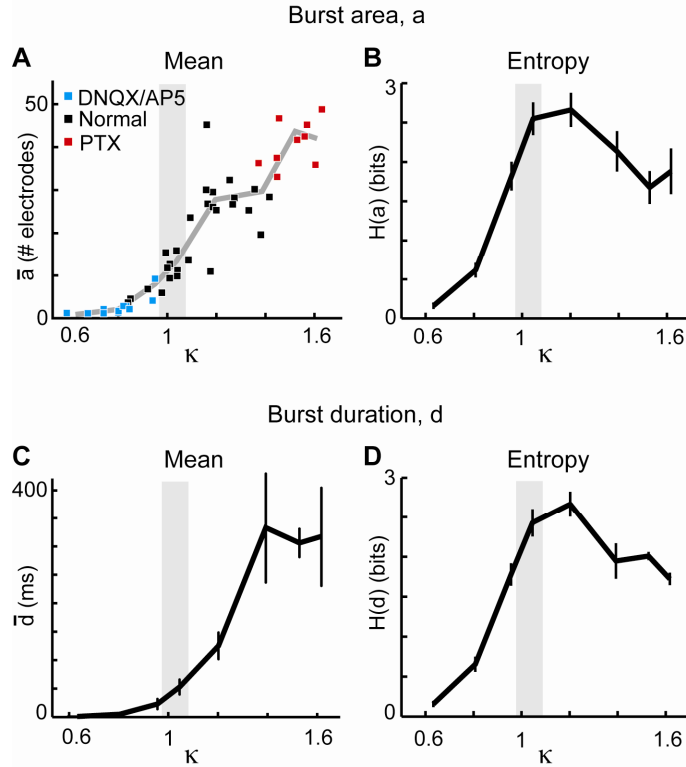


Figure 4.2: Burst area and duration have moderate mean and maximum entropy near $\kappa = 1$. *A*, Network dynamics were parameterized using κ . Low κ , $\kappa \approx 1$, and high κ indicate disfacilitated, neuronal avalanche, and disinhibited dynamics respectively. As network activity increased with an increase in κ , the average spatial extent of spontaneous bursts rose slowly for small κ , and more steeply near $\kappa = 1$. Each point is the averaged burst area from a 1 hr recording. *B*, The diversity, *i.e.* Shannon entropy, of burst area was highest near $\kappa = 1$. *C*, The average duration of bursts also rose strongly near $\kappa = 1$ and saturated for high κ . *D*, Entropy of burst duration peaked near $\kappa = 1$. Error bars indicate \pm SEM.

(Fig. 4.2A; gray line). We next quantified the diversity of burst area a by computing the Shannon entropy of the burst area distribution, $H(a)$. In line with similar previous work (Shew *et al.*, 2011), the entropy peaked near $\kappa = 1$, demonstrating that the diversity of burst area was highest under conditions which favor neuronal avalanches

(Fig. 4.2B). Similar to spatial area, the mean burst duration d increased most sharply near $\kappa = 1$ and the entropy of burst duration, $H(d)$ peaked near $\kappa = 1$ (Fig. 4.2C, D).

4.3.2 Neuronal synchrony has moderate mean and maximum entropy at $\kappa \sim 1$

During a burst, the LFP recorded from different electrodes were often, but not always synchronized (Fig. 4.1B, *inset*). We hypothesize that experimental conditions which result in neuronal avalanches also result in moderate average synchrony and maximally variable synchrony. To assess synchrony, we first obtained a phase trace for each LFP trace using the Hilbert transform (Fig. 4.3; Methods). To visualize the phases of all 59 electrodes versus time, we used dynamic phase histograms in which periods of elevated phase synchrony appear as yellow/red ‘bundles’ of phase trajectories (Fig. 4.4A, *top panel*). This is further clarified in the dynamic phase *difference* histogram, in which yellow/red pixels near a zero phase difference indicate that many pairs of electrodes have the same phase, *i.e.* are phase synchronized (Fig. 4.4A, *middle panel*). The temporal changes in phase synchrony in the network were quantified using Kuramoto’s order parameter, r , (Fig. 4.3C; Strogatz, 2001; Arenas *et al.*, 2008), which is based on all 59 phases. Periods of high phase synchrony, *i.e.* low phase difference, corresponded to high values of r (Fig. 4.4A, *bottom panel*). As shown in the examples in Fig. 4.4, the duration of phase-synchrony changed with κ from relatively short periods for $\kappa < 1$ (Fig. 4.4B), to moderate and prolonged phase-synchrony periods for $\kappa \approx 1$ and $\kappa > 1$ (Fig. 4.4A,C).

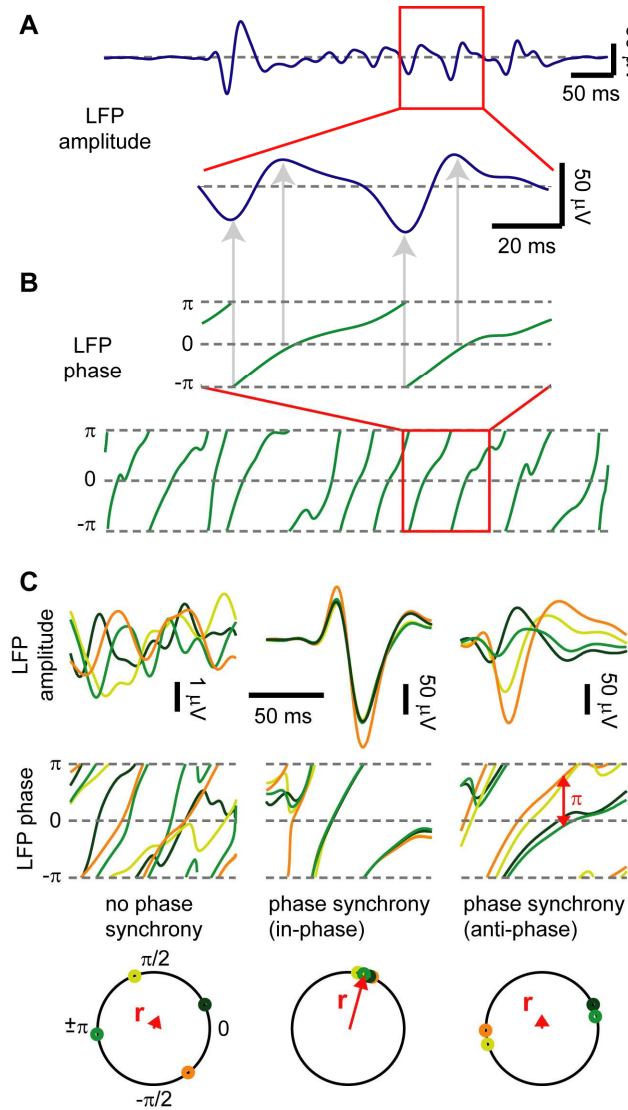


Figure 4.3: Assessing phase synchrony from multi-site LFP recordings. *A*, Example LFP amplitude trace recorded from a single electrode under disinhibited condition. A 100 ms period (red box) is expanded (lower trace). *B*, Using the Hilbert transform, the LFP amplitude trace is converted to a corresponding phase trace. Top: Expanded phase period. Note that phase near $\pm\pi$ corresponds to negative LFP peaks, while phase near zero coincides with positive LFP peaks (arrows). Lower trace shows corresponding phase for the full time period in *A*. *C*, Examples for lack of phase-locking (left), in-phase locking (middle) and combined in-phase and anti-phase locking (right) taken from four sites (colors). Top row: LFP traces. Middle row: phase traces. High phase synchrony appears as times when many

sites display a similar phase trace simultaneously (middle), while dispersed phases indicate lack of synchrony (left). Anti-phase locking appears as ‘bundles’ of in-phase traces separated by π (right; double headed arrow). Note low LFP amplitudes during lack of synchrony. Bottom row: The phases at the time indicated by the black arrow are visualized on a unit circle. The phase synchrony measure, r , is the distance (length of red arrow) between the origin and the center of mass of the phases. Note that anti-phase locking tends to reduce r .

In order to quantify these changes in synchrony with κ , we first calculated the average network synchrony per burst, \bar{S}_N . This was done by integrating r for the duration of each burst and averaging over all bursts for each experiment. We found that, as neuronal activity changed from disfacilitated to disinhibited, \bar{S}_N increased slowly at first, more sharply near $\kappa = 1$, and reached a plateau for large κ (Fig. 4.5A). Confirming the first part of our hypothesis, average network synchrony was moderate, *i.e.* 13.5% of its maximum value, near $\kappa = 1$. Next we quantified the diversity of network synchrony, $H(S_N)$. Our main finding is that $H(S_N)$ is maximized when $\kappa \approx 1$ (Fig. 4.5B) indicating that networks with neuronal avalanches achieve the most diverse repertoire of network synchronization during bursts, thus completing the confirmation of our hypothesis.

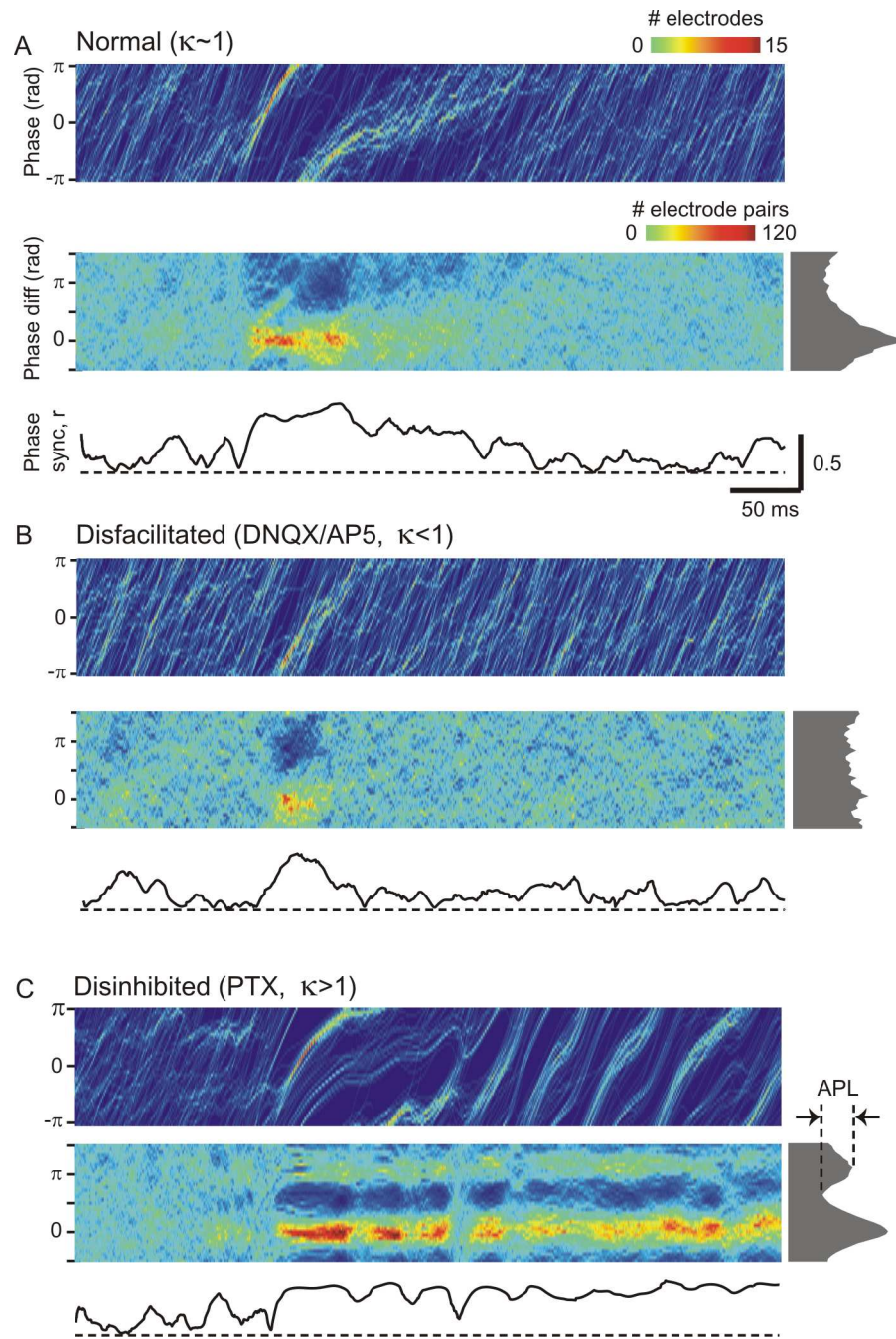


Figure 4.4: Phase synchrony dynamics for example bursts under different conditions of network excitability. *A*, Moderate levels of phase synchrony under normal condition. Time of the burst indicated by the black bar. Top: Dynamic phase histogram. Color indicates the number of electrodes with a given phase (vertical axis) at a given time (horizontal axis).

Phase ‘bundles’ marked by yellow/red pixels over time indicate many sites with the same phase, *i.e.* in-phase locking. Middle: Dynamic phase difference histogram. Color indicates the number of electrode pairs with a given phase difference (vertical axis) at a given time (horizontal axis). Phase differences near 0 indicate in-phase locking. The gray histogram to the right is the time average of the dynamic phase difference histogram. Note dominance of in-phase locking. Bottom: Phase synchrony r . Dashed line indicates $r = 0$. Phase synchrony r is high during periods of in-phase locking. **B**, Disfacilitated activity is characterized by brief and weakly synchronized bursts. Same as *A*, but during an example burst in the presence of DNQX/AP5. **C**, Disinhibited activity is characterized by strongly synchronized long-lasting bursts, anti-phase locking (phase differences near π), and an underlying prominent ~ 20 Hz β -oscillation. Same as *A*, but in the presence of PTX. Burst duration extends beyond period shown. Quantification of anti-phase locking, *APL*, is illustrated in time-averaged dynamic phase difference histogram (right).

These results on network synchrony, a priori, could depend on both the burst duration and spatial burst area. We therefore explored the degree to which these changes in network synchrony could be explained by κ -dependent changes in the spatiotemporal boundaries of the bursts. First, for each burst, we normalized network synchrony by burst duration in order to obtain the average instantaneous network synchrony, \bar{S}_{IN} (Fig. 4.5C, D) and the corresponding entropy, $H(S_{IN})$. We found that both the rising trend in synchrony and the peak in entropy at $\kappa \approx 1$ persisted, indicating that burst duration alone is insufficient to explain the trends shown in Fig. 4.5A, B. Next, to determine the influence of burst area, we recomputed the instantaneous network synchrony for each burst, but included only those electrodes that participated in the

burst, which we call instantaneous burst synchrony, \bar{S}_{IB} (Fig. 4.5E, F). We note that \bar{S}_{IB} was also corrected to account for the different expected noise levels for different numbers of electrodes, so that bursts covering different areas were fairly compared. For comparison, the instantaneous local synchrony among those electrodes outside the burst was significantly lower (Fig. 4.5E, *gray line*). Because \bar{S}_{IB} did not change significantly with κ , we conclude that the trend in Fig. 4.5A is primarily determined by a combination of κ -dependent changes in burst area and duration. This result indicates that mean synchrony within the spatiotemporal boundaries of bursts does not significantly change with network excitability. However, the entropy in instantaneous burst synchrony, $H(S_{IB})$ continued to show a peak. This indicates that entropy of synchrony arises not only from variability of the spatiotemporal boundaries of the bursts, but also from intrinsic, within-burst variability that is maximum near $\kappa = 1$.

Importantly, the findings in Fig. 4.5 were insensitive to changes in the spatial extent of the recorded region and inter-electrode distance of the MEA. This was demonstrated by repeating the analysis using subsets of electrodes from the original recordings. To test for robustness to changes in spatial extent, we used a 4x4 set of electrodes near the center of the MEA (Fig. 4.6; *red*). The spatial area of this subset is reduced by a factor of 4. To test for robustness to changes in spatial resolution, *i.e.* inter-electrode distance, we used a 4x4 set of electrodes with 400 μm inter-site spacing (Fig. 4.6, *blue*). Thus, the spatial resolution is halved, compared to the original recording. In both cases, the trends presented in Fig. 4.5 were largely

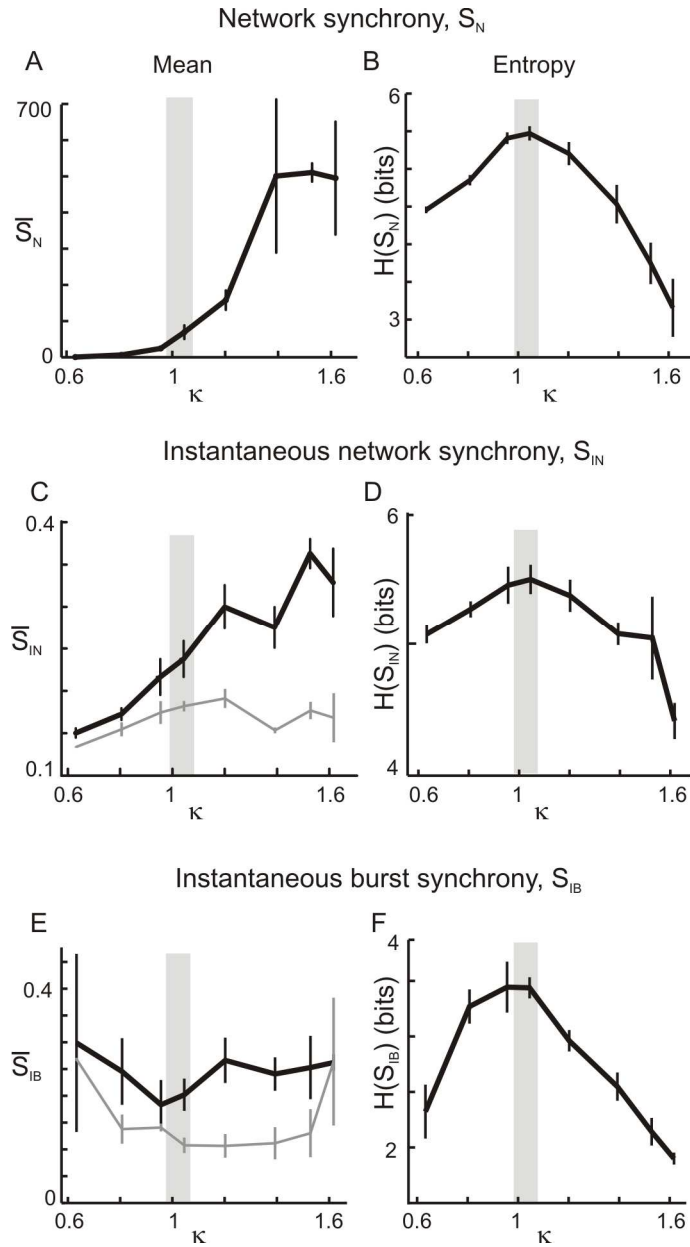


Figure 4.5: Neural synchrony attains moderate mean and maximum entropy near $\kappa = 1$.

A, Mean network synchrony showing a slow rise low κ , a sharp increase near $\kappa = 1$ (gray area), and saturation for high κ . **B**, The entropy of network synchrony showing a peak close to $\kappa = 1$. **C**, Mean instantaneous network synchrony showing a gradual rise with κ indicating that the increase in burst duration does not fully explain the rising trend in **A**. Gray line: control, computed during duration-matched non-burst periods. **D**, Entropy of instantaneous network synchrony is maximal near $\kappa = 1$. **E**, Mean instantaneous burst synchrony does not

change with κ . Thus, burst area and duration are sufficient to explain rising trend in mean synchrony. Gray line: control, computed for electrodes which do not participate in bursts. **F**, The peak in entropy persists for instantaneous burst synchrony.

unchanged. This suggests that our study should be repeatable with other MEA systems and our findings reflect cortical dynamics which span a range of spatial scales.

4.3.3 Anti-phase locking in disinhibited cortical networks with $\kappa > 1$

At high κ , anti-phase locking (Fig. 4.3C) was found for some bursts, which was visible as a tendency for π phase differences (e.g. Fig. 4.4C). We found that anti-phase locking was approximately 10 times more likely in high κ experiments compared to those with low or near $\kappa = 1$ (ANOVA, $p < 0.01$). For the 8 experiments with highest κ , we found $APL = 6.3 \pm 1.8$ (mean \pm SEM), where APL quantifies the degree of anti-phase locking, whereas $APL = 0.9 \pm 0.3$ and $APL = 0.4 \pm 0.1$ for the 8 experiments near $\kappa = 1$ and low κ respectively (Fig. 4.4C; Methods). The fraction f_{APL} of anti-phase locked sites, which extended from deep to superficial layers, was $f_{APL} = 0.64 \pm 0.02$ for the high κ experiments, which is 25% higher than expected by chance and significantly higher for experiments with low κ ($f_{APL} = 0.51 \pm 0.001$) and κ near 1 respectively ($f_{APL} = 0.52 \pm 0.01$; ANOVA, $p < 0.01$). Although such anti-phase locking in general will reduce the magnitude of r , the high κ conditions still resulted in the highest average r due to the fact that anti-phase locked groups were always small compared to the phase-locked groups.

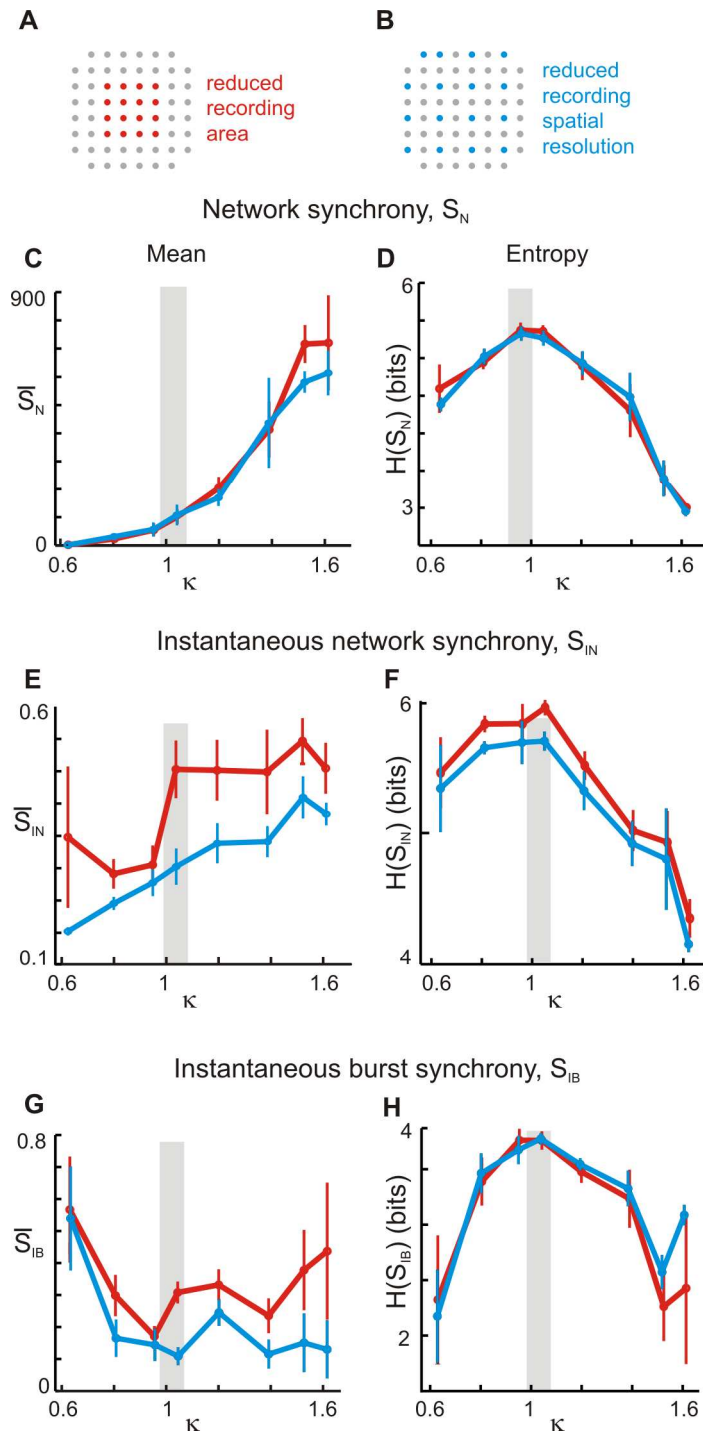


Figure 4.6: The relation of average synchrony and entropy of synchrony with respect to κ is independent of spatial extent and spatial resolution of MEA recordings. The data shown and described in Fig. 4.5 were recomputed using two different arrangements of MEA

electrodes. **A**, 4x4 compact group of electrodes covering a 800 μm x 800 μm recording area near the center of the array (red). **B**, 4x4 sparse group of electrodes covering the full 1600 μm x 1600 μm area, but with half the spatial resolution (blue). **C – H**, Same figure legend as in Fig. 4.5A – F.

4.4 Discussion

While it is well known that either too much or too little synchrony is detrimental to cortex function, it has been challenging to quantitatively identify the specific intermediate level of synchrony which is optimal. Based on our finding of peak variability of phase synchrony, we propose that $\kappa = 1$ is such a specific optimal point. This allows us to quantitatively identify the corresponding optimal level of synchrony occurring near $\kappa = 1$, which is about 13.5 % of the maximal synchrony networks can exhibit even under moderate disinhibition. Below we first relate our findings to epilepsy models which are similar to our high κ experiments. Next we highlight agreement between our work and theoretical predictions from coupled oscillators and critical phenomena, which suggests that the optimal point marked by $\kappa \approx 1$ corresponds to the critical point of a phase transition. Finally, we discuss our findings of anti-phase locking and the relevance of our work for *in vivo* studies.

4.4.1 $\kappa > 1$ identifies a pathological state of synchrony typical for epilepsy.

Cortical disinhibition is a well established model for epilepsy (Luhmann *et al.*, 1995; Prince *et al.*, 2009) and GABA_A antagonists readily induce epileptic seizures in

isolated cortex preparations (Gutnick *et al.*, 1982) that initiate in and involve deep layer pyramidal neurons (Connors, 1984; Pinto *et al.*, 2005). Provided layers 5/6 are intact (Telfeian and Connors, 1998), about 10 – 20 % reduction in GABA_A receptor function suffices to induce seizure activity (Chagnac-Amitai and Connors, 1989), in line with the relatively low dose of 5 μ M PTX concentration used in the current study, which is far from > 50 μ M required to block the GABA_A receptor. Our observation that bursts are spatially extended and include deep layers for large κ is in accordance with these studies. Moreover, for high κ , we observed increased β -oscillations (Fig. 4.1; Gireesh and Plenz, 2008), which are known to involve layer 5/6 pyramidal neurons (Yamawaki *et al.*, 2008). Importantly, the involvement and emergence of β -oscillations in epilepsy has been well documented. 10 – 15 Hz oscillations emerge spontaneously in isolated cortex preparations using the epilepsy model of low extracellular magnesium (Flint and Connors, 1996) and epileptic seizures recorded in animals during slow-wave sleep have elevated β -power (Timofeev and Steriade, 2004). In epileptic patients, long-range temporal correlations are enhanced in the β -band of intracranial EEG recorded during seizure free epochs (Monto *et al.*, 2007), and entrainment of photosensitive seizures is particularly effective with flashes between 15–20 Hz (Parra *et al.*, 2005). We conclude that the regime of $\kappa > 1$ identifies a pathological state of relatively large-scale and robust phase-synchrony across cortical layers with dominant oscillation frequencies similar to those found in epilepsy.

4.4.2 $\kappa \sim 1$ identifies a critical phase transition

Next, we turn to the theory of critical phenomena, which originates from the statistical physics of phase transitions (Hinrichsen, 2005) and has also been applied to understand network-level neural dynamics (Levina *et al.*, 2007; Buice and Cowan, 2009; Meisel and Gross, 2009; Millman *et al.*, 2010). A prominent similarity of our findings and predicted critical phenomena is the power-law probability distribution of burst sizes, which we observed when no drugs were applied. We found a power-law exponent near -1.5, which suggests that cortical networks belong to the class of non-equilibrium systems called ‘directed percolation’ (Hinrichsen, 2005; Buice and Cowan, 2009). Originally devised for the study of a fluid percolating through a porous material, this model may also be interpreted as neural activation propagating through a network. Models of this type have successfully been used to explain measurements of cortical dynamic range (Kinouchi and Copelli, 2006; Shew *et al.*, 2009; Larremore *et al.*, 2011) and information transfer (Beggs and Plenz, 2003; Shew *et al.*, 2011). In this context, the drug-induced changes in dynamics we observed may be interpreted as changes in the probability of activity propagation through the network. Reduction of excitatory synaptic transmission decreases this probability, typically resulting in brief bursts that die out quickly. Conversely, reduction of fast inhibition increases the probability, resulting in relatively large bursts of runaway excitation. The -1.5 power-law observed in drug-free networks corresponds to a balanced propagation in line with a critical branching process (Beggs and Plenz, 2003), where, in theory, propagation neither decays nor grows, on average. Importantly, this theory also predicts that variability in the spatiotemporal extent of bursts is highest at criticality, which matches our findings of peak entropy of burst

spatial area and duration for $\kappa \approx 1$. Although directed percolation models are known to produce highly fluctuating neural activity at criticality, there are no predictions from this theory regarding phase synchrony.

Thus, for perspective on our synchrony measurements, we turn to the theory of coupled oscillators, where much has been predicted about how the onset and dynamics of synchrony depends on the strength of coupling between oscillators (Haken *et al.*, 1985; Daido, 1990; Ermentrout and Kleinfeld, 2001; Strogatz, 2001; Arenas *et al.*, 2008; Kitzbichler *et al.*, 2009). Since we typically observe aperiodic LFP fluctuations, we note that the theory applies to aperiodic dynamics as well, such as synchronized chaos (Arenas *et al.*, 2008). Interpreting our experiments in this context, we consider the local population of excitatory pyramidal neurons and inhibitory interneurons that generate the LFP at each electrode as one ‘oscillatory unit’. The control parameter in the models is the coupling strength between oscillators; when coupling exceeds a critical threshold strength, synchrony emerges. The drugs used in our experiments certainly change coupling between distant neuronal groups, as well as in the local recurrent networks of excitatory and inhibitory neurons, which makes it difficult to predict the net effect of a global reduction in excitatory or inhibitory transmission (Kopell *et al.*, 2000). Nevertheless, comparing our empirical observations of synchrony to predictions from coupled oscillators suggests that PTX results in stronger coupling, while DNQX/AP5 results in weaker coupling. We note that although we used κ to parameterize these drug-induced changes, κ is not equivalent to a control parameter – it is based on measuring

network dynamics. The rapid rise, *i.e.* onset, of synchrony occurs near the coupling strength found in cortical networks which are unperturbed by drugs, *i.e.* $\kappa \approx 1$. Importantly, the theory of coupled oscillators predicts that variability of synchrony is highest near the onset of synchrony, *i.e.* our observation of peak entropy of synchrony near $\kappa \approx 1$ was predicted by this theory (Daido, 1990).

Interestingly, the observed peak entropy of synchrony persisted after the variability in burst duration and area were accounted for (Figs. 4.5*F*, 4.6*H*). Thus, the optimization of entropy results in part from intrinsic single-site variability. More precisely, each electrode samples a sub-network consisting of tens to hundreds of neurons. It is likely that the variability of synchronized activity within such sub-network neuronal groups contributes significantly to the peak in entropy of synchrony.

4.4.3 Anti-phase synchrony for $\kappa > 1$

One aspect of our experiments which is not explained by coupled oscillator models in their most basic form is the anti-phase locking found at high κ . Anti-phase LFP oscillations could arise from several possible mechanisms. First, in-phase synchronized spiking in a population of cortical pyramidal neurons with aligned long apical dendrites can produce such LFP signals (Chrobak and Buzsáki, 1998). Accordingly, the incidence of anti-phase locking is expected to increase with the involvement of deep layer neuron in generating β -oscillations at high κ . Second, 2-oscillator models reveal anti-phase locking to arise from excitatory coupling (Kopell and Somers, 1995; Neltner and Hansel, 2001) such as mutual layer-V pyramidal

neuron interactions. Third, in line with our findings at high κ , network simulations demonstrate a suppressing effect of inhibition on anti-phase synchrony (Kanamaru, 2006). The concurrence of slow β -oscillations and anti-phase locking in our experiments is in line with anti-phase locking in human motor coordination at lower frequencies as predicted by the HKB-model (Haken *et al.*, 1985; Schönér *et al.*, 1986).

4.4.4 Comparison to the cortex dynamics *in vivo*

Since our measurements were of *in vitro* spontaneous activity, two natural questions arise. First, is a large variability of spontaneous synchrony relevant when it comes to stimulus-evoked synchrony? Second, to what extent are our findings expected to hold *in vivo*? Growing evidence that spontaneous activity is intimately related to stimulus-evoked activity suggests the answer to the former question is, yes (Tsodyks *et al.*, 1999; Ohl *et al.*, 2001; Ji and Wilson, 2007; Han *et al.*, 2008; Luczak *et al.*, 2009; Berkes *et al.*, 2011; Shew *et al.*, 2011). Most importantly, we previously showed this in exactly the same experimental system studied here. Considering the same drug conditions, it was found that 1) mutual information between stimulus and response, *i.e.* information transmission, was highest at $\kappa \approx 1$ (Shew *et al.*, 2011) and that 2) the range of stimulus amplitudes that are distinguishable based on response, *i.e.* dynamic range, was highest at $\kappa \approx 1$ (Shew *et al.*, 2009). Regarding the second question, there are several lines of evidence suggesting our findings might hold *in vivo*. One is that the organotypic cortex slice cultures that we study preserve many aspects of *in vivo* cortical development, including laminar structure and the

emergence of neuronal avalanche dynamics during the second week postnatal (Gireesh and Plenz, 2008). In addition, neuronal avalanches were observed in two previous studies of ongoing cortical activity in awake monkeys, and in one case, analysis confirmed that $\kappa \approx 1$ (Petermann *et al.*, 2009; Shew *et al.*, 2011).

In summary, our experiments are in agreement with predictions from theory, suggesting that when the cortex operates at a critical intermediate excitability, near the onset of synchrony, it can benefit from moderate average synchrony and a maximal repertoire of different synchronized groups. Importantly, this critical excitability typically was found under experimental conditions in which no drug was applied, suggesting that the cortex may tune itself to this optimal condition.

Bibliography

Arenas A, Diazguilera A, Kurths J, Moreno Y, Zhou C (2008) Synchronization in complex networks. *Phys Rep* 469:93-153

Bartos M, Vida I, Jonas P (2007) Synaptic mechanisms of synchronized gamma oscillations in inhibitory interneuron networks. *Nat Rev Neurosci* 8:45-56.

Beggs JM, Plenz D (2003) Neuronal avalanches in neocortical circuits. *The Journal of Neuroscience* 23:11167-77.

Berkes P, Orban G, Lengyel M, Fiser J (2011) Spontaneous Cortical Activity Reveals Hallmarks of an Optimal Internal Model of the Environment. *Science* 331:83-87.

Boraud T, Brown P, Goldberg JA, Graybiel AM, Magill PJ (2005) OSCILLATIONS IN THE BASAL GANGLIA : The good , the bad , and the unexpected In J. P. Bolam, C. A. Ingham, & P. J. Magill, eds. *The Basal Ganglia VIII* (Editors: New York: Springer Science and Business Media, p. 3-24.

Bressler SL, Coppola R, Nakamura R (1993) Episodic multiregional cortical coherence at multiple frequencies during visual task performance. *Nature* 366:153-6.

- Bressler SL, Kelso JAS (2001) Cortical coordination dynamics and cognition. *Trends Cogn Sci* 5:26-36.
- Buice M A, Cowan JD (2009) Statistical mechanics of the neocortex. *Prog Biophys Mol Bio* 99:53-86.
- Chagnac-Amitai Y, Connors BW (1989) Horizontal spread of synchronized activity in neocortex and its control by GABA-mediated inhibition. *J Neurophys* 61:747-58.
- Chrobak JJ, Buzsáki G (1998) Gamma oscillations in the entorhinal cortex of the freely behaving rat. *The Journal of Neuroscience* 18:388-98.
- Connors BW (1984) Initiation of synchronized neuronal bursting in neocortex. *Nature* 310:685-7.
- Daido H (1990) Intrinsic fluctuations and a phase transition in a class of large populations of interacting oscillators. *J Stat Phys* 60:753-800.
- Destexhe A (1994) Oscillations, complex spatiotemporal behavior, and information transport in networks of excitatory and inhibitory neurons. *Physical Review E* 50:1594-1606.
- Destexhe A, Contreras D (2006) Neuronal computations with stochastic network states. *Science* 314:85-90.
- Ermentrout GB, Kleinfeld D (2001) Traveling electrical waves in cortex: insights from phase dynamics and speculation on a computational role. *Neuron* 29:33-44.
- Flint AC, Connors BW (1996) Two types of network oscillations in neocortex mediated by distinct glutamate receptor subtypes and neuronal populations. *J Neurophys* 75:951-7.
- Fries P, Reynolds JH, Rorie AE, Desimone R (2001) Modulation of oscillatory neuronal synchronization by selective visual attention. *Science* 291:1560-3
- Friston KJ (1997) Transients, metastability, and neuronal dynamics. *Neuroimage* 5:164-71.
- Garcia Dominguez L, Wennberg RA, Snead OC, Gaetz W, Perez Velazquez JL, Cheyne D (2005) Enhanced synchrony in epileptiform activity? Local versus distant phase synchronization in generalized seizures. *The Journal of Neuroscience* 25:8077-84.
- Garrett DD, Kovacevic N, McIntosh AR, Grady CL (2011) The Importance of Being Variable. *The Journal of Neuroscience* 31:4496-4503.

- Garrett DD, Kovacevic N, McIntosh AR, Grady CL (2010) Blood oxygen level-dependent signal variability is more than just noise. *The Journal of Neuroscience* 30:4914-21.
- Gireesh ED, Plenz D (2008) Neuronal avalanches organize as nested theta- and beta/gamma-oscillations during development of cortical layer 2/3. *Proceedings of the National Academy of Sciences of the United States of America* 105:7576-81.
- Gutnick MJ, Connors BW, Prince DA (1982) Mechanisms of neocortical epileptogenesis *in vitro*. *J Neurophys* 48:1321-35.
- Haken H, Kelso JAS, Bunz H (1985) A theoretical model of phase transitions in human hand movements. *Biol Cybern* 51:347-356.
- Han F, Caporale N, Dan Y (2008) Reverberation of recent visual experience in spontaneous cortical waves. *Neuron* 60:321-7.
- Hinrichsen H (2006) Non-equilibrium phase transitions. *Physica A* 369:1-28.
- Hipp JF, Engel AK, Siegel M (2011) Oscillatory Synchronization in Large-Scale Cortical Networks Predicts Perception. *Neuron* 69:387-396
- Ji D, Wilson MA (2007) Coordinated memory replay in the visual cortex and hippocampus during sleep. *Nature Neuroscience* 10:100-107.
- Kanamaru T (2006) Analysis of synchronization between two modules of pulse neural networks with excitatory and inhibitory connections. *Neural Comput* 18:1111-31.
- Kelso JAS, Fuchs A, Lancaster R, Holroyd T, Cheyne D, Weinberg H (1998) Dynamic cortical activity in the human brain reveals motor equivalence. *Nature* 392:814-8
- Kelso JAS, Scholz JP, Schöner G (1986) Nonequilibrium phase transitions in coordinated biological motion: critical fluctuations. *Phys Lett A* 118:279-284.
- Kinouchi O, Copelli M (2006) Optimal dynamical range of excitable networks at criticality. *Nat Phys* 2:348-351.
- Kitzbichler MG, Smith ML, Christensen SR, Bullmore E (2009) Broadband criticality of human brain network synchronization. *PLoS Computational Biology* 5:e1000314.
- Klaus A, Yu S, Plenz D. (2011) Statistical analyses support power law distributions found in neuronal avalanches. *PLoS One* 6, e19779.

- Kopell N, Ermentrout GB, Whittington M A, Traub RD (2000) Gamma rhythms and beta rhythms have different synchronization properties. *Proceedings of the National Academy of Sciences of the United States of America* 97:1867-72.
- Kopell N, Kramer M A, Malerba P, Whittington MA (2010) Are different rhythms good for different functions? *Fr Hum Neurosci* 4:187.
- Kopell N, Somers D (1995) Anti-phase solutions in relaxation oscillators coupled through excitatory interactions. *J Math Biol* 33:261-280.
- Korshoej AR, Holm MM, Jensen K, Lambert JDC (2010) Kinetic analysis of evoked IPSCs discloses mechanism of antagonism of synaptic GABAA receptors by picrotoxin. *Brit J Pharmacol* 159:636-49.
- Larremore D, Shew W, Restrepo J (2011) Predicting criticality and dynamic range in complex networks: effects of topology. *Physical Review Letters* 106:1-4
- Levina A, Herrmann JM, Geisel T (2007) Dynamical synapses causing self-organized criticality in neural networks. *Nat Phys* 3:857-860.
- Luczak A, Barthó P, Harris KD (2009) Spontaneous events outline the realm of possible sensory responses in neocortical populations. *Neuron* 62:413-25.
- Luhmann HJ, Mittmann T, Luijtelaa G van, Heinemann U (1995) Impairment of intracortical GABAergic inhibition in a rat model of absence epilepsy. *Epilepsy Res* 22:43-51.
- Magri C, Whittingstall K, Singh V, Logothetis NK, Panzeri S (2009) A toolbox for the fast information analysis of multiple-site LFP, EEG and spike train recordings. *BMC Neurosci* 10:81.
- Mallet N, Pogosyan A, Márton LF, Bolam JP, Brown P, Magill PJ (2008) Parkinsonian beta oscillations in the external globus pallidus and their relationship with subthalamic nucleus activity. *The Journal of Neuroscience* 28:14245-58.
- Malsburg C von der, Phillips WA, Singer W eds. (2010) *Dynamic Coordination in the Brain*. Cambridge, MA: MIT Press.
- McIntosh AR, Kovacevic N, Itier RJ (2008) Increased brain signal variability accompanies lower behavioral variability in development. *PLoS Computational Biology* 4:e1000106.
- Meisel, C., and Gross, T. (2009). Adaptive self-organization in a realistic neural network model. *Physical Review E* 80:1-6.

Melloni L, Molina C, Pena M, Torres D, Singer W, Rodriguez E (2007) Synchronization of neural activity across cortical areas correlates with conscious perception. *The Journal of Neuroscience* 27:2858-65.

Millman D, Mihalas S, Kirkwood A, Niebur E (2010) Self-organized criticality occurs in non-conservative neuronal networks during “up” states. *Nat Phys* 6:801-805.

Monto S, Vanhatalo S, Holmes MD, Palva JM (2007) Epileptogenic neocortical networks are revealed by abnormal temporal dynamics in seizure-free subdural EEG. *Cereb Cortex* 17:1386-93.

Neltner L, Hansel D (2001) On synchrony of weakly coupled neurons at low firing rate. *Neural Comput* 13:765-74.

Ohl FW, Scheich H, Freeman WJ (2001) Change in pattern of ongoing cortical activity with auditory category learning. *Nature* 412:733-6.

Otter R (1949) The Multiplicative Process. *The Annals of Mathematical Statistics* 20:206-224.

Palva S, Linkenkaer-Hansen K, Näätänen R, Palva JM (2005) Early neural correlates of conscious somatosensory perception. *The Journal of Neuroscience* 25:5248-58.

Parra J, Kalitzin SN, Lopes da Silva FH (2005) Photosensitivity and visually induced seizures. *Curr Opin Neurol* 18:155-9.

Petermann T, Thiagarajan TC, Lebedev MA, Nicolelis MAL, Chialvo DR, Plenz D (2009) Spontaneous cortical activity in awake monkeys composed of neuronal avalanches. *Proceedings of the National Academy of Sciences of the United States of America* 106:15921-6.

Pinto DJ, Patrick SL, Huang WC, Connors BW (2005) Initiation, propagation, and termination of epileptiform activity in rodent neocortex *in vitro* involve distinct mechanisms. *The Journal of Neuroscience* 25:8131-40.

Plenz D, Thiagarajan TC (2007) The organizing principles of neuronal avalanches: cell assemblies in the cortex? *Trends Neurosci* 30:101-10.

Prince D A, Parada I, Scalise K, Graber K, Jin X, Shen F (2009) Epilepsy following cortical injury: cellular and molecular mechanisms as targets for potential prophylaxis. *Epilepsia* 2:30-40.

Rodriguez E, George N, Lachaux JP, Martinerie J, Renault B, Varela FJ (1999) Perception's shadow: long-distance synchronization of human brain activity. *Nature* 397:430-3.

- Roelfsema PR, Engel AK, König P, Singer W (1997) Visuomotor integration is associated with zero time-lag synchronization among cortical areas. *Nature* 385:157-61.
- Sakurai Y, Takahashi S (2006) Dynamic synchrony of firing in the monkey prefrontal cortex during working-memory tasks. *The Journal of Neuroscience* 26:10141-53.
- Schoner G, Haken H, Kelso JAS (1986) A stochastic theory of phase transitions in human hand movement. *Biological Cybernetics* 53:247-257.
- Schoner G, Kelso J (1988) Dynamic pattern generation in behavioral and neural systems. *Science* 239:1513-1520.
- Sedelnikova A, Erkkila BE, Harris H, Zakharkin SO, Weiss DS (2006) Stoichiometry of a pore mutation that abolishes picrotoxin-mediated antagonism of the GABAA receptor. *J Physiol* 577:569-77.
- Senkowski D, Schneider TR, Foxe JJ, Engel AK (2008) Crossmodal binding through neural coherence: implications for multisensory processing. *Trends Neurosci* 31:401-9.
- Shew WL, Yang H, Petermann T, Roy R, Plenz D (2009) Neuronal Avalanches Imply Maximum Dynamic Range in Cortical Networks at Criticality. *The Journal of Neuroscience* 29:15595-15600.
- Shew WL, Yang H, Yu S, Roy R, Plenz D (2011) Information Capacity and Transmission Are Maximized in Balanced Cortical Networks with Neuronal Avalanches. *The Journal of Neuroscience* 31:55-63.
- Spencer KM, Nestor PG, Niznikiewicz M A, Salisbury DF, Shenton ME, McCarley RW (2003) Abnormal neural synchrony in schizophrenia. *The Journal of Neuroscience* 23:7407-11.
- Steriade M (2003) *Neuronal Substrates of Sleep and Epilepsy*. Cambridge: Cambridge University Press.
- Strogatz SH (2001) Exploring complex networks. *Nature* 410:268-76.
- Tallon-Baudry C, Mandon S, Freiwald W A, Kreiter AK (2004) Oscillatory synchrony in the monkey temporal lobe correlates with performance in a visual short-term memory task. *Cereb Cortex* 14:713-20.
- Telfeian E, Connors BW (1998) Layer-specific pathways for the horizontal propagation of epileptiform discharges in neocortex. *Epilepsia* 39:700-8.

Timofeev I, Steriade M (2004) Neocortical seizures: initiation, development and cessation. *Neuroscience* 123:299-336.

Tsodyks M, Kenet T, Grinvald A, Arieli A (1999) Linking spontaneous activity of single cortical neurons and the underlying functional architecture. *Science* 286:1943-6.

Uhlhaas PJ, Singer W (2010) Abnormal neural oscillations and synchrony in schizophrenia. *Nat Rev Neurosci* 11:100-13.

Varela F, Lachaux JP, Rodriguez E, Martinerie J (2001) The brainweb: phase synchronization and large-scale integration. *Nat Rev Neurosci* 2:229-39.

Wilson TW, Rojas DC, Reite ML, Teale PD, Rogers SJ (2007) Children and adolescents with autism exhibit reduced MEG steady-state gamma responses. *Biol Psychiat* 62:192-7.

Yamawaki N, Stanford IM, Hall SD, Woodhall GL (2008) Pharmacologically induced and stimulus evoked rhythmic neuronal oscillatory activity in the primary motor cortex *in vitro*. *Neurosci* 151:386-95.

Chapter 5: Neuronal avalanches imply maximal dynamic range in cortical networks at criticality²

5.1 Introduction

As shown in Chapters 3 and 4, the cortex is spontaneously active even in the absence of any obvious stimulus or motor output. Increasing evidence shows that such ongoing activity is intricately linked to stimulus-evoked activity. For example, orientation maps constructed from ongoing neuronal activity in the anesthetized cat match those based on visual responses (Tsodyks *et al.*, 1999; Kenet *et al.*, 2003). Spatiotemporal correlations of spikes in the visual cortex are similar when the awake animal is simply sitting in darkness or observing natural scenes (Fiser *et al.*, 2004). Likewise, population responses to auditory and somatosensory stimuli fall within the repertoire of observed spontaneous events (Luczak *et al.*, 2009). Moment to moment, ongoing activity contributes to the large variability observed in stimulus responses (Arieli *et al.*, 1996; Kisley and Gerstein, 1999; Azouz and Gray, 1999), while being only weakly modulated by stimulus presentation (Fiser *et al.*, 2004). On longer timescales, the organization of spontaneous activity is thought to reflect past inputs and influence future network responses (Ohl *et al.*, 2001; Yao *et al.*, 2007). Given such interplay between spontaneous and stimulus-evoked activity, and the maximization principles that we have found mainly during ongoing activity, we raise

² This chapter is published in *Journal of Neuroscience* 29:15595-600, 2009. I contributed to *in vitro* recordings, all data analysis, interpretation of the data and manuscript preparation.

the question whether the cortical state that optimizes its internal representational ability could maintain optimized stimulus processing in the network.

The cortical state we refer to is neuronal avalanches state, a type of spontaneous activity observed in superficial layers of cortex *in vivo* and *in vitro* (Beggs and Plenz, 2003; Plenz and Thiagarajan, 2007; Gireesh and Plenz, 2008; Petermann *et al.*, 2009). Neuronal avalanches consist of bursts of elevated population activity, correlated in space and time, that are distinguished by a particular statistical character: activity clusters of size s occur with probability $P(s) \sim s^{-\alpha}$, *i.e.* a power law with exponent $\alpha = -1.5$. Neuronal avalanches are similar to the dynamics of other systems poised at the boundary of order and disorder; more precisely, we refer to systems operating at *criticality* (Bak and Paczuski, 1995; Jensen, 1998; Stanley, 1971). Importantly, simulations predict that at criticality, neuronal networks optimize several aspects of information processing including (1) the range of stimulus intensities that can be processed, *i.e. dynamic range* (Kinouchi and Copelli, 2006) and (2) the amount of information that can be transferred (Beggs and Plenz, 2003; Tanaka *et al.*, 2009). Until now, no experiments supported these predictions. Here, we demonstrate that *in vitro* cortical networks have maximum dynamic range when spontaneous activity takes the form of neuronal avalanches. By systematically changing excitation and inhibition, we obtain a tuning curve for stimulus processing in cortical networks, with peak performance found under balanced conditions which generate neuronal avalanche activity.

5.2 *Methods*

5.2.1 Dynamic range

After measuring responses to a range of stimulus amplitudes, we used the response curve, $R(S)$, to compute dynamic range,

$$\Delta = 10 \log_{10}(S_{\max} / S_{\min}), \quad (5.1)$$

where S_{\max} , S_{\min} are the stimulation values leading to 90%, 10% of the range of R respectively.

5.2.2 Model

The model is the same as described in Chapter 3, except consisted of $N = 250, 500, 1000$ all-to-all coupled, binary-state neurons. To obtain response as a function of stimulus in the model, we simulated increasing stimulus amplitude S by increasing the number of initially activated neurons ($S = 1, 2, 4, 16, 32, 64, 128$ initially active neurons). Finally, we note that our model is very similar to $N-1$ dimensional directed percolation (Buice and Cowan, 2007). Therefore, at high dimension ($N > 5$) and weak coupling it is expected that the model behaves as a branching process, where σ is the branching parameter and the $-3/2$ power-law is predicted at criticality. To test for statistical differences between groups, a one-way ANOVA followed by a Tukey post hoc test was used.

5.3 *Results*

Cortex-VTA co-cultures from rat ($n = 16$), which closely parallel *in vivo* differentiation and maturation of cortical superficial layers (Gireesh and Plenz, 2008), were grown on 8x8 integrated planar micro-electrode arrays (Fig. 5.1A). Local field potentials (LFP) were recorded after superficial layer differentiation (> 10 DIV) and analyzed to extract spatiotemporal clusters of negative LFP deflections (nLFPs; $n = 47$ experiments). Extracellular unit activity recorded simultaneously with the LFP revealed that sizes of nLFP clusters correlated with the level of suprathreshold neuronal activity in the network (Fig. 5.1B; $R = 0.84 \pm 0.13$, mean \pm SD; $n = 5$ cultures). For each experimental condition, we first measured spontaneous activity (Fig. 5.1C) and quantified the deviation of the observed spontaneous network dynamics from neuronal avalanche dynamics by calculating κ (Fig. 5.2A). In a second step, we measured the input/output dynamic range Δ of the cultured network based on its response to a range of stimulus amplitudes (Figs. 5.1D, 5.4A). These measurements were carried out under normal conditions and repeated after changing the ratio of excitation and inhibition through bath application of the antagonists PTX or AP5/DNQX.

5.3.1 Quantifying the cortical network state based on κ

Fig. 5.2A (*top*) shows experimental cluster size PDFs obtained from three cultures under normal, unperturbed conditions and in the presence of PTX or AP5/DNQX respectively. Under normal conditions, cultures revealed a PDF close to $-3/2$ power-law, as predicted for neuronal avalanches (Fig. 5.2A, *black*). In the presence of PTX,

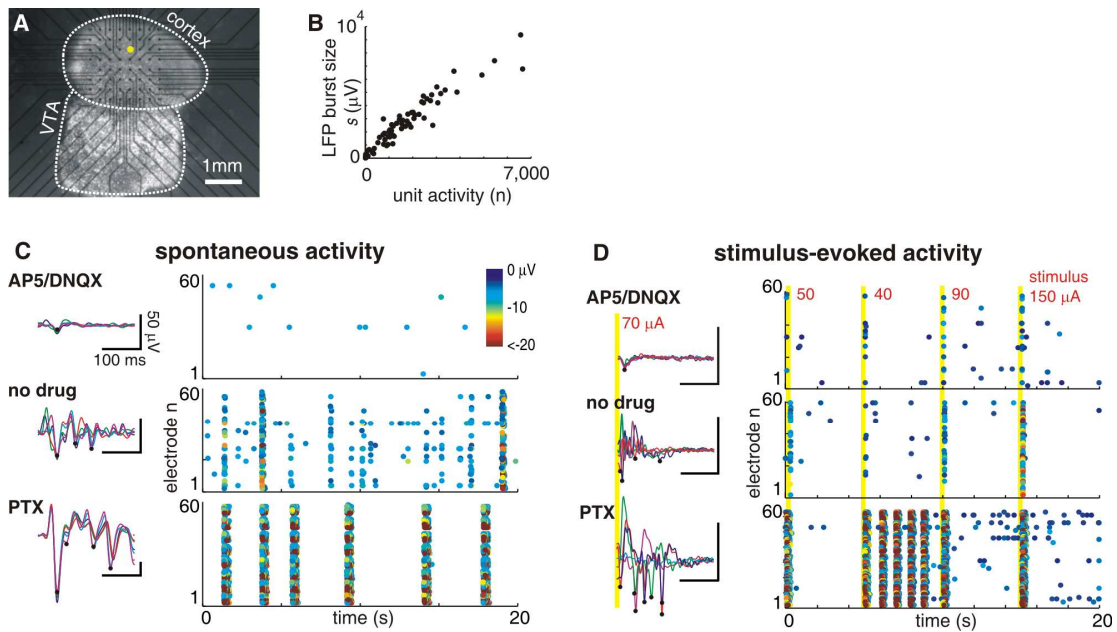


Figure 5.1: Measuring spontaneous and stimulus-evoked activity from cortical networks. *A*, Light-microscopic image of a somatosensory cortex and dopaminergic midbrain region (VTA) coronal slice cultured on a 60 channel microelectrode array. *Yellow dot*: stimulation site. *Black dots*: recording sites. *B*, Number of extracellular spikes correlates with the size of simultaneously recorded nLFP burst ($R = 0.84 \pm 0.13$; $n = 5$). Each point represents total number of spikes versus the corresponding spontaneous nLFP burst size. *C*, Example recordings of spontaneous LFP fluctuations (*left*) and nLFP rasters (*right*) for three drug conditions (*top*–AP5/DNQX, *middle*–no drug, *bottom*–PTX.) *D*, Examples of LFP evoked by 70 μA stimulus (*left*) and rasters recorded during the application of four stimuli of amplitudes 50, 40, 90, 150 μA (*yellow line*: stimulus time) (*right*) for three drug conditions. For both spontaneous (*C*) and stimulus-evoked (*D*) activity AP5/DNQX (PTX) typically results in reduced (increased) amplitude LFP events with lesser (greater) spatial extent. In (*C*), (*D*), black dots on the LFP traces indicate nLFP events, raster point color indicates nLFP amplitude, and all scale bars (*left*) represent 50 μV , 100 ms.

however, the PDF is bi-modal, revealing a high likelihood for small and large activity clusters, but a decreased probability of medium-sized clusters (Fig. 5.2A; *red*). In contrast, bath-application of AP5/DNQX reduces large clusters, resulting in mostly small clusters (Fig. 5.2A; *blue*). These differences in PDFs are robustly assessed using the corresponding CDFs (Fig. 5.2A, *bottom*). Reducing excitation results in a steep early rise of the CDF, while reducing inhibition results in a delayed rise of the CDF. κ robustly quantifies these observations using the difference between a measured CDF of cluster sizes and the theoretically expected reference CDF for neuronal avalanches (Fig. 5.2A, *bottom, gray lines*). As summarized in Fig. 5.2C, $\kappa \sim 1$ under normal conditions ($\kappa = 1.14 \pm 0.01$, \pm SE; $n = 28$), $\kappa < 1$ when excitation is reduced ($\kappa = 0.81 \pm 0.01$; $n = 10$) and $\kappa > 1$ when inhibition is reduced ($\kappa = 1.51 \pm 0.01$; $n = 9$; $F_{(2,44)} = 82.7$; $p < 0.05$ for PTX and AP5/DNQX from normal).

This experimental strategy was paralleled using a network-level computational model of binary, integrate-and-fire neurons, in which changes in the excitation/inhibition ratio (E/I) were mimicked by tuning the parameter σ (Methods). For $\sigma < 1$, on average a neuron triggers activity in less than one neuron, resulting in a hypo-excitable state. Conversely, for $\sigma > 1$, one neuron excites on average more than one neuron in the near future, resulting in a hyper-excitable condition. Accordingly, for $\sigma = 1$, propagation of activity is balanced as was found experimentally for neuronal avalanches (Beggs and Plenz, 2003; Stewart and Plenz, 2007). We simulated “spontaneous” activity clusters by activating a single randomly chosen neuron and monitoring the propagation until activity ceased or 500 time steps were executed.

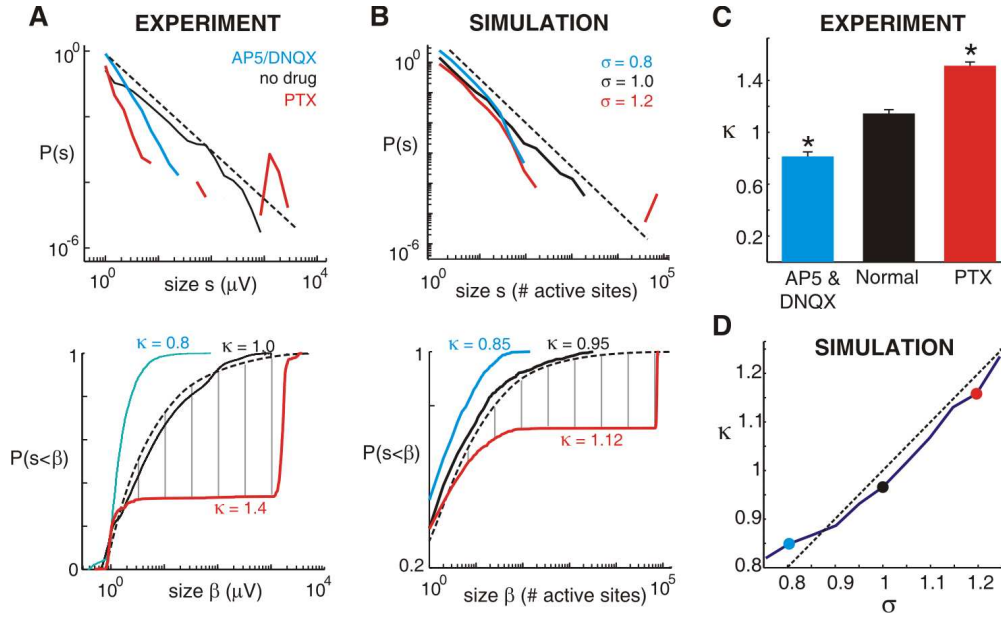


Figure 5.2: Change in the ratio of excitation/inhibition moves cortical networks away from criticality. *A*, *Top*: Probability distribution functions (PDFs) of spontaneous cluster sizes for a normal (no-drug, *black*), disinhibited (PTX, *red*), and hypo-excitable (AP5/DNQX, *blue*) cultures. *Broken line*: $-3/2$ power-law. Cluster size s is the sum of nLFP peak amplitudes within the cluster; $P(s)$ is the probability of observing a cluster of size s . *Bottom*: Corresponding cumulative distribution functions (CDFs) and quantification of the network state using κ , which measures deviation from a $-1/2$ power-law CDF (*broken line*). *Vertical gray lines*: The 10 distances summed to compute κ , shown for one example PTX condition (*red*). *B*, Simulated cluster size PDFs (*top*) and corresponding CDFs (*bottom*) for different values of the model control parameter σ . *C*, Summary statistics of average κ values for normal, hypo-excitable, and disinhibited conditions (* $p < 0.05$ from normal). *D*, In simulations, κ accurately estimates σ . *Broken line*: $\kappa = \sigma$. *Colored dots*: examples shown in *B*.

The total number of spikes in a cluster was taken as the cluster size. 1000 clusters were simulated at each of 11 levels of σ . In agreement with established theory, model

cluster size PDFs near criticality ($\sigma = 1$) fit a $-3/2$ power-law very closely (Fig. 5.2B, *top; black*; (Harris, 1989; Zapperi *et al.*, 1995). Just as in the experiment, we computed κ based on CDFs of simulated spontaneous activity for different values of σ (Fig. 5.2B *bottom*). We found that κ and σ were almost linearly related (Fig. 5.2D), which supports the following interpretation: In the experiments, $\kappa \sim 1$ is close to criticality, $\kappa < 1$ identifies the subcritical regime, and $\kappa > 1$ is analog to the supercritical regime of the model.

5.3.2 Stimulus-evoked activity and dynamic range

After obtaining κ for a given experimental condition, we recorded the response R as a function of stimulus amplitude S . Evoked responses often exhibited complex temporal evolution. Shown in Fig. 5.3 are typical peri-stimulus time histograms (PSTHs) of evoked activity for stimulus levels and three different drug conditions. The vertical axis represents average nLFP amplitude, normalized by the maximum observed nLFP. In the results, a response to a given stimulus level was quantified as the integral of the PSTH associated with that stimulus level. The three examples shown here were computed from the same data as the $R(S)$ curves shown in Fig. 5.4A.

In the AP5/DNQX example, the PSTHs were mainly flat until a stimulus level of about $60 \mu\text{A}$, demonstrating the insensitivity of the network when excitation is suppressed. At the other extreme, in the PTX example, the largest stimulus levels have similar PSTHs, demonstrating the saturation of the $R(S)$ for large S when inhibition is suppressed.

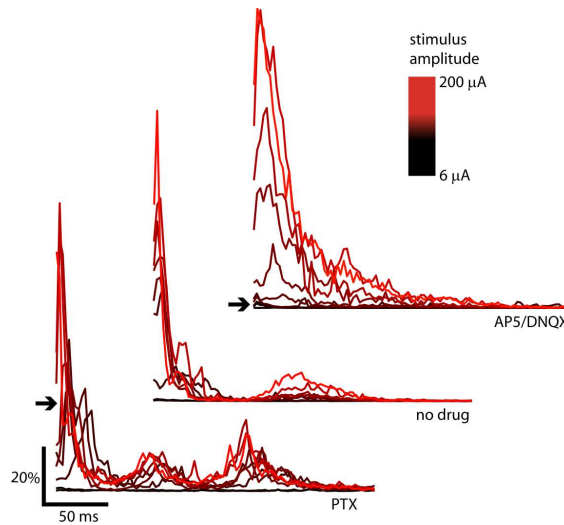


Figure 5.3: Peri-stimulus time histograms (PSTHs) of evoked activity. nLFP versus time averaged over 40 stimuli at each stimulus level (color coded) are compared for three drug conditions (left – PTX, middle – no drug, right – AP5/DNQX). In the AP5/DNQX condition the system is relatively insensitive due to suppressed excitation, *i.e.* the PSTH is flat until a stimulus level of about 60 μA is reached. In the PTX condition, the largest stimulus levels result in very similar PSTHs, demonstrating the tendency for response to saturate when inhibition is suppressed. Note that the response to a given stimulus level, R , in the main text was defined as the integral of the PSTH.

Typical response curves from experiments and simulations are shown in Fig. 5.4A and 5.4B respectively. We found that the shape of the response curves in the model closely matched the experimental findings. When excitatory synaptic transmission was reduced ($\kappa < 1$), the system was relatively insensitive (required a larger stimulus to evoke a given response). When inhibitory synaptic transmission was reduced ($\kappa > 1$) the system was hyper-excitable, with responses that saturate for relatively small stimuli. In the balanced E/I condition with $\kappa \approx 1$, the range of stimuli resulting in non-zero and non-saturated response was largest.

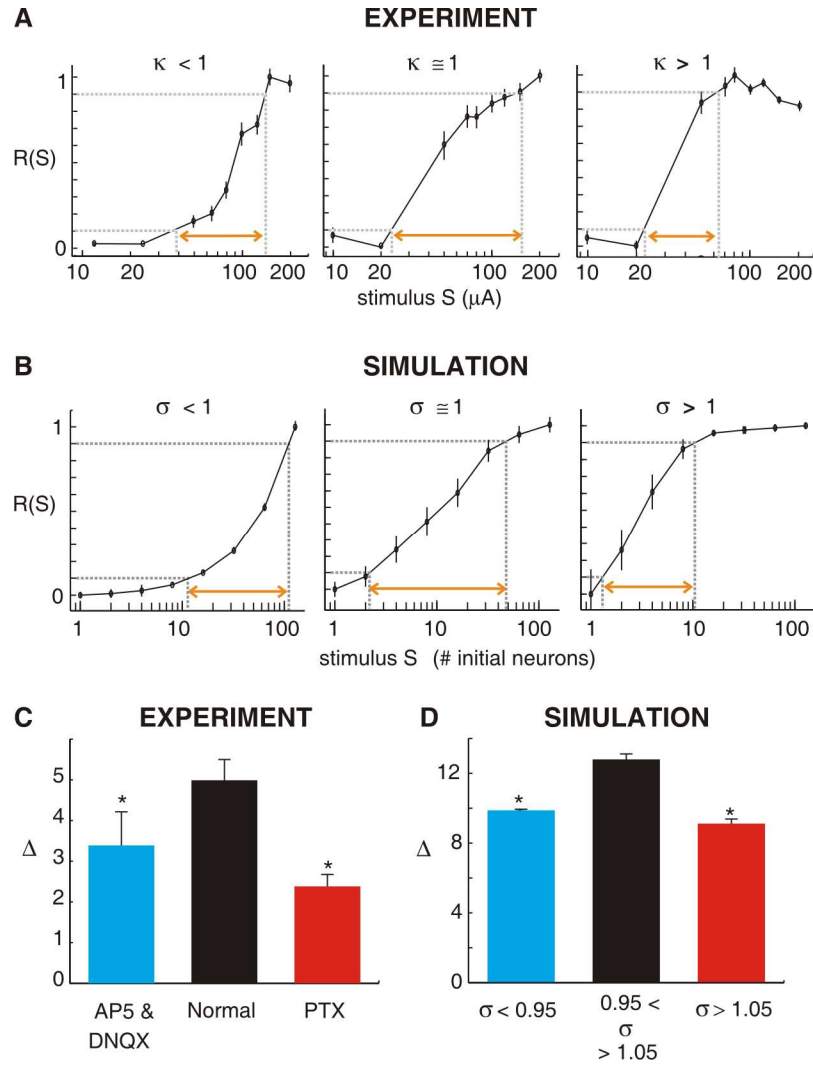


Figure 5.4: Stimulus-response curves and dynamic range Δ . **A**, Experimental response R evoked by current stimulation of amplitude S for three example cultures with different κ values. *Orange arrows*: range from S_{min} to S_{max} ; length is proportional to Δ . Note that Δ is largest for $\kappa \cong 1$. **B**, Model response evoked by different numbers of initially activated sites; Δ is largest for $\sigma \cong 1$. Like the experiment, each point is calculated from 40 stimuli. *Error bars*: 1 S.E. **C**, Experimental summary statistics for Δ under different pharmacological conditions (* $p < 0.05$ from normal). **D**, Simulation summary statistics for Δ , comparing different ranges of κ (* $p < 0.05$ from $\sigma \cong 1$).

5.3.3 Maximal Dynamic range at criticality, $\kappa \cong 1$

For each response curve, we quantified the range of stimuli the network can process, *i.e.* the dynamic range Δ (Methods). We found experimentally that $\Delta = 5.0 \pm 0.1$ (mean \pm S.E) under normal conditions, $\Delta = 2.4 \pm 0.1$ in the presence of PTX, and $\Delta = 3.4 \pm 0.3$ for AP5/DNQX (Fig. 5.4C, $F_{(2,44)} = 11.3$; $p < 0.05$ PTX and AP5/DNQX from normal). Similar overall changes in Δ were also found in our simulations (Fig. 5.4D; $F_{(2,195)} = 820$; $p < 0.05$). Importantly, the dynamic range was largest in unperturbed networks, in which neuronal avalanches are most likely to occur.

We then derived a tuning curve of Δ versus κ by combining all experimental conditions into one scatter plot (Fig. 5.5A). These data demonstrate that Δ is maximized and its variability is largest near $\kappa \cong 1$. These findings agree well with our model including changes in Δ as the system is pushed away from $\kappa \cong 1$, ~ 10 dB drop (10 fold reduction in S_{\max} / S_{\min}) for a 30% change in κ (Fig. 5.5B). The tuning curve demonstrates that the change in the dynamic range of a network due to a shift in E/I depends on both the original, unperturbed state and the resulting change in κ .

Finally we tested the robustness of this peak function. These results were robust for different maximal stimulus amplitudes. The maximum stimulus amplitude, 200 μ A, in the experiments was chosen to maximize the stimulus range without damaging the tissue. With this range of stimuli, the response curves did not always saturate. To test

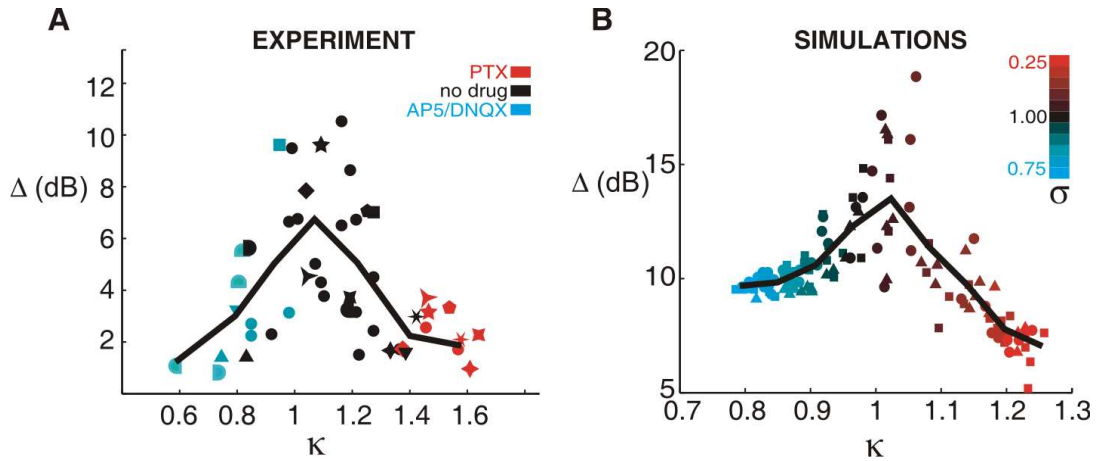


Figure 5.5: Network tuning curve for dynamic range Δ near criticality. *A*, In experiments, Δ peaks close to $\kappa \cong 1$ and drops rapidly with distance from criticality. Paired measurements share the same symbol shape; normal (no-drug) condition was measured just before the drug condition. *Circles*: unpaired measurement. *B*, In simulations, Δ is also maximum for $\kappa \cong 1$. Symbol indicates network size (*circles*: $N = 250$; *squares*: $N = 500$; *triangles*: $N = 1000$). Lines represent binned averages.

whether this limitation impacts our hypothesis, that is Δ is maximized for $\kappa = 1$, we recalculated the Δ vs. κ curve with deliberately truncated stimulus ranges in both the model and the experiment. In Fig. 5.6A we demonstrate that our data support our hypothesis even for the limited stimulus size range available to us experimentally. Only for an extremely shortened stimulus range does the hypothesis become non-testable, as shown in the corresponding model simulations (Fig. 5.6B).

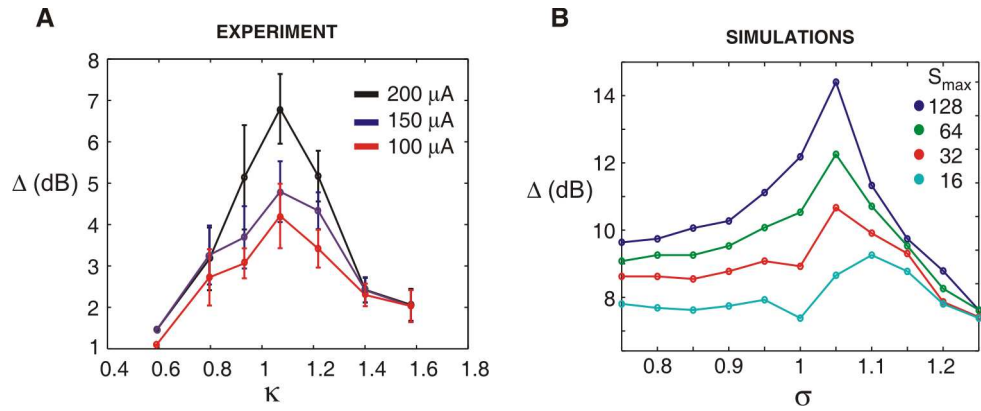


Figure 5.6: Effect of limited stimulus range on Δ . *A*, The *black* line is a re-plot of binned and averaged data from Fig. 5.5A of the main text. The *blue* and *red* lines represent the same experiments, but reprocessed using only < 150 and $< 100 \mu\text{A}$ respectively. The peak of Δ near $\kappa = 1$ is attenuated, but still exists. *B*, In the model, we verify that we should expect attenuation of the $\Delta(\kappa)$ curve, when the stimulation range is decreased. The strong peak vanishes only for a severely truncated range ($S_{\text{max}} = 16$).

Then we tested the effects of changing the number of neurons in the model. We found that for a fixed range of stimulus intensities, *i.e.* number of initially active sites, the $\Delta(\sigma)$ curve was largely unchanged. For $\sigma < 1$, there was a tendency for larger systems to have decreased Δ . Each point on the curves in Fig. 5.7 is an average over 6 different simulations (same data as shown in Fig. 5.5B)

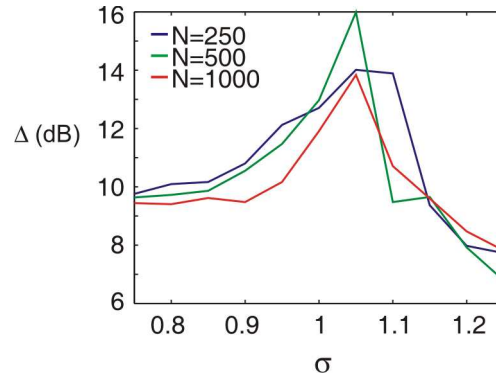


Figure 5.7: Effect of network size on Δ . Increasing the system size from $N = 250$ to $N = 1000$ model neurons causes only slight shifts in Δ . For $\sigma < 1$ there is a tendency for slightly lower Δ at higher N .

5.4 Discussion

We experimentally derived a tuning curve that linked the state of a cortical network with its ability to process inputs. When the network was closest to criticality, as indicated by neuronal avalanches, κ was close to one and dynamic range was maximized. This is among the first experimental work to confirm theoretical predictions on the computational advantage of operating at criticality. Dynamic range has been predicted in simulations to peak at criticality (Kinouchi and Copelli, 2006). Our simulations advance previous studies by linking the dynamic range of a network with the spontaneous activity it generates. Because the dynamic range increases with the ability of a network to map input differences into distinguishable network outputs, our result is also closely related to network-mediated separation, which has been predicted to peak at criticality, at the transition from ordered to chaotic dynamics (Bertschinger and Natschlager, 2004; Legenstein and Maass, 2007). In contrast, our

results show that variability of response to a given stimulus is highest at criticality. Further investigation of reliability versus variability in cortical networks is warranted.

Considering the simplicity of our model with all-to-all connectivity, absence of refractory period, and approximating inhibition by reducing σ , the overall agreement in the Δ - κ relationship between experiment and simulation is remarkable. The increase of variability in Δ as well as the drop in Δ due to deviation from $\kappa = 1$ was well matched between experiment and simulations. Such similarity supports the notion that universal principles, independent of system details, are found at criticality (Bak and Paczuski, 1995; Jensen, 1998; Stanley, 1971). The main quantitative difference was the lower Δ values for experiments compared to the model. Experimental noise, which is absent in the model, effectively adds a constant value to S_{min} and S_{max} , which systematically reduces Δ .

Further neurophysiological insight into our results can be gained from Fig. 5.4. There it is shown that networks poorly discriminate small inputs in the hypo-excitable state, whereas they tend to saturate, failing to discriminate larger inputs in the hyper-excitable state. Both these reductions in performance result in reduced dynamic range compared to balanced networks. In line with these findings, dissociated cultures respond to inputs with a ‘network spike’ if $\sigma > 1$ (Eytan and Marom, 2006) and display a ‘giant component’ in a hyperexcitable regime, which reduces the ability to discriminate inputs (Breskin *et al.*, 2006). The balance of excitation and inhibition has been shown to be crucial for proper development of sensory cortical (Hensch,

2005). Our results suggest that, functionally, the balance of excitation and inhibition is achieved when the dynamic range is maximized and cortical networks operate at criticality.

Bibliography

Arieli A, Sterkin A, Grinvald A, Aertsen A (1996) Dynamics of ongoing activity: explanation of the large variability in evoked cortical responses. *Science* 273:1868-1871.

Azouz R, Gray CM (1999) Cellular mechanisms contributing to response variability of cortical neurons *in vivo*. *The Journal of Neuroscience* 19:2209-2223.

Bak P, Paczuski M (1995) Complexity, contingency, and criticality. *Proceedings of the National Academy of Sciences of the United States of America* 92:6689-6696.

Beggs JM, Plenz D (2003) Neuronal avalanches in neocortical circuits. *The Journal of Neuroscience* 23:11167-11177.

Bertschinger N, Natschlager T (2004) Real-time computation at the edge of chaos in recurrent neural networks. *Neural Comput* 16:1413-1436.

Breskin I, Soriano J, Moses E, Tlusty T (2006) Percolation in living neural networks. *Physical Review Letters* 97:188102.

Buice MA, Cowan JD (2007) Field-theoretic approach to fluctuation effects in neural networks. *Physical Review E Stat Nonlin Soft Matter Phys* 75:051919.

Eytan D, Marom S (2006) Dynamics and effective topology underlying synchronization in networks of cortical neurons. *The Journal of Neuroscience* 26:8465-8476.

Fiser J, Chiu C, Weliky M (2004) Small modulation of ongoing cortical dynamics by sensory input during natural vision. *Nature* 431:573-578.

Gireesh ED, Plenz D (2008) Neuronal avalanches organize as nested theta- and beta/gamma-oscillations during development of cortical layer 2/3. *Proceedings of the National Academy of Sciences of the United States of America* 105:7576-7581.

Götz M, Bolz J (1992) Formation and Preservation of cortical layers in slice cultures. *J Neurobiol* 23:783-802.

Harris TE (1989) *The theory of branching processes*. New York: Dover.

Hensch TK (2005) Critical period plasticity in local cortical circuits. *Nat Rev Neurosci* 6:877-888.

Jensen HJ (1998) *Self-organized criticality*. Cambridge University Press.

Kenet T, Bibitchkov D, Tsodyks M, Grinvald A, Arieli A (2003) Spontaneously emerging cortical representations of visual attributes. *Nature* 425:954-956.

Kinouchi O, Copelli M (2006) Optimal dynamical range of excitable networks at criticality. *Nature Physics* 2:348-351.

Kisley MA, Gerstein GL (1999) Trial-to-trial variability and state-dependent modulation of auditory-evoked responses in cortex. *The Journal of Neuroscience* 19:10451-10460.

Legenstein R, Maass W (2007) Edge of chaos and prediction of computational performance for neural circuit models. *Neural Netw* 20:323-334.

Luczak A, Bartho P, Harris KD (2009) Spontaneous events outline the realm of possible sensory responses in neocortical populations. *Neuron* 62:413-425.

Ohl FW, Scheich H, Freeman WJ (2001) Change in pattern of ongoing cortical activity with auditory category learning. *Nature* 412:733-736.

Petermann T, Thiagarajan T, Lebedev MA, Nicolelis MA, Chialvo DR, Plenz D (2009) Spontaneous cortical activity in awake monkeys composed of neuronal avalanches. *Proceedings of the National Academy of Sciences of the United States of America* 10.1073/pnas.0904089106.

Plenz D, Kitai ST (1996) Generation of high-frequency oscillations in local circuits of rat somatosensory cortex cultures. *J Neurophysiol* 76:4180-4184.

Plenz D, Thiagarajan TC (2007) The organizing principles of neuronal avalanches: cell assemblies in the cortex? *Trends Neurosci* 30:101-110.

Stanley HE (1971) *Introduction to phase transitions and critical phenomena*. New York: Oxford University Press.

Stewart CV, Plenz D (2006) Inverted-U profile of dopamine-NMDA-mediated spontaneous avalanche recurrence in superficial layers of rat prefrontal cortex. *The Journal of Neuroscience* 26:8148-8159.

Stewart CV, Plenz D (2007) Homeostasis of neuronal avalanches during postnatal cortex development *in vitro*. *The Journal of Neuroscience* Meth 169:405-416.

Tanaka T, Kaneko T, Aoyagi T (2009) Recurrent infomax generates cell assemblies, neuronal avalanches, and simple cell-like selectivity. *Neural Comput* 21:1038-1067.

Tsodyks M, Kenet T, Grinvald A, Arieli A (1999) Linking spontaneous activity of single cortical neurons and the underlying functional architecture. *Science* 286:1943-1946.

Yao H, Shi L, Han F, Gao H, Dan Y (2007) Rapid learning in cortical coding of visual scenes. *Nature Neuroscience* 10:772-778.

Zapperi S, Bakgaard LK, Stanley HE (1995) Self-organized branching processes: Mean-field theory for avalanches. *Physical Review Letters* 75:4071-4074.

Chapter 6: Higher-order Interactions characterized in cortical activity

6.1 Introduction

The mammalian cortex forms a complex network with more than 10^{10} neurons, which interact at many different scales ranging from microcircuits in cortical columns to cortical areas across the whole brain. Consequently, during perceptive, cognitive, and motor functions, cortical dynamics is characterized by spatially distributed coherent activity patterns that reflect these neuronal interactions (Gray *et al.*, 1989; Abeles *et al.*, 1993; Bressler *et al.*, 1993; Vaadia *et al.*, 1995; Riehle *et al.*, 1997; Rodriguez *et al.*, 1999). During the past two decades, the simplest form of interaction—pair-wise correlations—have been studied intensively (for review see Singer, 1999). However, the understanding of higher-order interactions, *i.e.*, the ones that are manifested only in triplets, quadruplets, *etc.*, has been lacking. The fundamental problem is that the number of potential higher-order interactions grows exponentially with the system size, *i.e.*, the number of neurons considered, which makes the interaction structure quickly intractable. So far it is not clear how to generally overcome this curse of dimensionality and, consequently, the structure of higher-order interactions in cortical activity and the mechanisms underlying its generation remained largely unexplored.

Previous work suggests that pair-wise interactions alone provide a rather complete picture of neuronal activity, potentially circumventing the necessity of identifying higher-order interactions. By decomposing population activities into different order

of interactions, Schneidman *et al* (2006) and Shlens *et al* (2006) showed that pair-wise interactions explain most of the activity in randomly subsampled (≤ 10 neurons) retina networks, a finding that was soon extended to include larger system (Shlens *et al.*, 2009; Cocco *et al.*, 2009; Ganmor *et al.*, 2011b), *in vivo* cortical networks (Yu *et al.*, 2008; Ohiorhenuan *et al.*, 2010) and correlation among population activities measured with the local field potential (LFP) (Tang *et al.*, 2008; Santos *et al.*, 2010). In contrast, a number of more recent studies (Montani *et al.*, 2009; Ohiorhenuan *et al.*, 2010; Santos *et al.*, 2010; Ohiorhenuan and Victor, 2011; Ganmor *et al.*, 2011a) have identified significant higher-order interactions in neuronal dynamics, for example, the 3rd -order interactions between closely neighbored ($< 300 \mu\text{m}$) cortical neurons (Ohiorhenuan *et al.*, 2010; Ohiorhenuan and Victor, 2011) and interactions up to 8th order in retina (Ganmor *et al.*, 2011a). Clearly, the structure of higher-order interactions and their contribution to cortical dynamics are still open to debate. Here we show that pair-wise interactions alone are insufficient to identify neuronal avalanche dynamics (Beggs and Plenz, 2003) for even small system (10 elements), measured as ongoing cortical activity in the awake monkey based on the LFP. We then demonstrate that the incorporation of a specific structure of higher-order interactions that results from thresholding (Amari *et al.*, 2003; Macke *et al.*, 2011) improves the accuracy of reconstructing neuronal avalanche dynamics by up to two orders of magnitude. By using the same method, significant improvements were also obtained for the approximation of ongoing spiking activities in awake monkeys as well as visually evoked spiking responses from anesthetized cats. These results demonstrate an efficient way to characterize the higher-order interactions in different

scales of cortical dynamics and, at the same time, suggest the mechanisms underlying its generation.

6.2 Methods

6.2.1 Electrophysiological recordings

All experiments were carried out in accordance with NIH guidelines for animal use and care. Ongoing activities were recorded from two adult monkeys (*Macaca mulatta*). Multi-electrode arrays (MEA; 96 channels; 10×10 without four corners; inter-electrode distance: 400 μm; electrode length: 1 mm; BlackRock Microsystems) were chronically implanted in the arm representative region of the left pre-motor cortex (cf. Fig. 6.1A). About thirty minutes of ongoing LFP (1 – 100 Hz) and extracellularly recorded spike activities (300 – 3000 Hz) were obtained while the animals were alertly sitting in a primate chair with their heads fixed, but not engaged in a behavioural task. Spike sorting was carried out offline (Offline Sorter, Plexon). Single units were identified with clear separations in PCA or waveform feature spaces. Results for monkey A are shown. Qualitative similar results for monkey B are summarized in Tables 6.1 and 6.2.

Visually evoked activities were recorded from cortical area 17 in two adult, anesthetized cats. The animals were artificially ventilated and the anesthesia was maintained with a mixture of 70% N₂O and 30% O₂, supplemented with 0.5 – 0.6% halothane. Extracellular spike activities were recorded by one or two silicon-based

MEAs (4×4 electrode array; 200 μm inter-electrode distance; Neural Nexus). The probes were inserted roughly perpendicular to the surface of cortex at depths of approximately 1 mm. The visual stimuli (presented by ActiveStim, <http://activestim.com/>) consisted of full-contrast, drifting sinusoidal gratings that spatially covered the receptive fields of all recorded neurons. Each trial was completed with 3 – 4 s long presentations of a drifting grating with orientations randomly chosen from a set of 12 directions (0° to 360° range; steps of 30°). About 30 minutes of visually evoked responses were recorded for each cat. Single units were identified offline using a customized, PCA-based program. For more details, see previous publication with the same data sets (Yu *et al.*, 2008). Three data sets were analyzed (two probes for cat A and one probe for cat B). As the results are similar, in the figures we only show the detailed results for cat A, probe one. Results for the other two data sets are summarized in Table 6.2.

6.2.2 LFP analysis

Negative deflections in the LFP (nLFPs) were detected by applying a threshold at -2.5 standard deviations of the LFP fluctuations estimated for each electrode separately (cf. Fig. 6.1B). The time stamps of nLFPs were then binned with a small time window, Δt , to generate corresponding binary time series (1 for nLFP and 0 for the lack of it). Results were based on $\Delta t = 2$ ms. Similar results were obtained with other Δt s, ranging from 4 ms to 64ms (data not shown). Spatiotemporal cluster of nLFPs, *i.e.*, avalanches, were defined by consecutive bins that contained at least one nLFP at

any of the recording sites (Beggs and Plenz, 2003). The size of a cluster was defined as the number of nLFPs in a cluster. For simplification of the analysis, the spatiotemporal clusters were degenerated to spatial patterns only, $\mathbf{x} = (x_1, x_2, x_3, \dots, x_n)$, where n is the number of recording sites included in the analysis ($n = 91$ and 78 for monkey A and B, respectively). $x_i = 1$ if at least one nLFP occurred at channel i and $x_i = 0$ otherwise. (cf. Fig. 6.1C). Qualitative similar results for single bin, non-degenerated nLFP patterns can be found in Table 6.1 and Fig. 6.8, demonstrating that our findings on higher-order interactions in the original LFP dynamics did not rely on this specific method of extracting spatial-temporal patterns. See result section for more details on this issue. For sub-groups with 10 electrodes, the results for spatially compact ones are shown in the figures. Qualitatively similar results for randomly chosen sub-groups can be found in Table 6.1.

6.2.3 Spike analysis

In order to obtain activity patterns for spikes, spike trains were binned at $\Delta t = 20$ ms (ongoing activity) and 4 ms (evoked activity). The smaller Δt for evoked activities was chosen because of the relative high firing rate during evoked activity (Yu *et al.*, 2008). The range of Δt used here is consistent with previous studies (Schneidman *et al.*, 2006; Yu *et al.*, 2008; Ohiorhenuan *et al.*, 2010) and similar results were obtained by varying the Δt by at least two folds (e.g., 10 ms for ongoing activity and 8 ms for evoked activity). Spatial patterns were taken as the spatial distribution of spikes within one time bin without further temporal concatenation. This allows our results

to be more generally comparable with common approaches in spike train analysis. Additional analysis was performed on neuronal groups with strong pair-wise correlations (cf. Fig. 6.6). For 3-neuron groups, we calculated the average pair-wise correlation for all possible 3-neuron combinations and chose those 100 – 250 groups with the highest average correlation. For 10-neuron groups, we calculated the average pair-wise correlation for all possible 10-neuron combinations (or randomly chosen 10^6 of them if the total number of combinations was more than 10^6) out of the existing data sets. Among those we analyzed 15 – 30 groups with the highest average correlation value. We note that most neurons ($> 60\%$, see Table 6.2 for detail) participated in the analysis of strongly coupled groups. In order to test whether units with high firing rates (up to > 30 spikes/s), which tend to be highly correlated with each other, bias our results, the analysis for monkey A in Fig. 6.6 was based on subgroups chosen out of 45 neurons with the top 20% neurons with highest firing rates excluded. However, results were similar even when including those units with high firing rates, except for the inclusion of fewer total units in the strongly couples groups (data not shown). High firing units were not excluded for all other data sets and analysis.

6.2.4 Ising Model

The Ising Model (Schneidman *et al.*, 2006) is expressed as $P(\sigma) = Z^{-1} \exp(\sum_i h_i \sigma_i + \sum_{ij} J_{ij} \sigma_i \sigma_j)$, where $P(\sigma)$ is the probability of the pattern $\sigma = (\sigma_1, \sigma_2, \dots, \sigma_n)$. σ_i equals 1 or -1 , representing the state of the i^{th} element (1 for active and -1 for inactive). The

normalization factor Z , intrinsic property h_i , and interaction J_{ij} were determined according to the experimentally observed averages $\langle \sigma_i \rangle$ and $\langle \sigma_i \sigma_j \rangle$. For 3 and 10-element systems, the Ising model was numerically resolved by using the customized Matlab code, utilizing the optimization toolbox (function *fsolve*). For systems with up to 10 elements, the Ising model can be resolved exactly with an error in fitting the rates and pair-wise correlations $< 10^{-9}$. This resulted in almost identical lower-order statistics (e.g., event rates and pair-wise correlation) for the Ising model and the data. For example, for the 10-electrode group shown in Fig. 6.1E, the approximation error for the Ising model, defined as $|v_{\text{model}} - v_{\text{data}}| / v_{\text{data}}$, was $< 10^{-10}$, where v_{data} is the value of the rates or pair-wise correlations calculated from the data, and v_{model} is the corresponding value calculated from the pattern probabilities of the model.

6.2.5 DG model

The DG model (Amari *et al.*, 2003; Macke *et al.*, 2009; Macke *et al.*, 2011) has a threshold operation based on multi-dimensional Gaussian variables: $y_i = 1$ when $u_i > 0$ and $y_i = 0$ otherwise, where $u = (u_1, u_2, \dots, u_n) \sim N(\gamma, \Lambda)$. In order to match the observed rate (r) and covariance (Σ) for binary variables, the mean (γ) and covariance (Λ) of the Gaussian variables need to be adjusted according to $\gamma_i = \Phi^{-1}(r_i)$ and Λ_{ij} as the solution for $\Sigma_{ij} = \Phi_2(\gamma_i, \gamma_j, \Lambda_{ij}) - \Phi(\gamma_i)\Phi(\gamma_j)$, where Φ and Φ^{-1} are cumulative probability function of standard Gaussian distribution (Φ for 1D and Φ_2 for 2D) and its inverse function. Implementation of the model with Matlab can be found in (Macke *et al.*, 2009). The pattern probabilities for the DG model were calculated

using the cumulative distribution of multivariate Gaussians (Matlab function *mvncdf*) or running simulations (for large systems). In terms of event rates and pair-wise correlation, the fitting precision of DG model was usually 10^{-3} , which reaches or exceeds the criteria used in related studies (e.g., Ganmor *et al.*, 2011a; Ganmor *et al.*, 2011b) but was inferior compared with the of the Ising model. This limit is mainly due to the noise introduced in calculating the cumulative probability distributions of the multi-dimensional Gaussian, for which the tolerant error was set to be $< 10^{-4}$. Therefore, the performance differences between the two models in approximating higher-order statistics, *i.e.*, pattern probability and cluster size/neuronal synchrony (see result), are not reflecting the precision with which the event rates and pair-wise correlations are fitted but represent the degree to which the model captures the internal structural of the data.

6.2.6 Model performance measures

To quantify the total interdependence in the data that can be explained by the pair-wise correlations only, the entropy-based approach (Schneidman *et al.*, 2006) was used. The entropy H was calculated as $H = -\sum P(x) \log P(x)$, where $x = (x_1, x_2, \dots, x_n)$. $x_i = 0$ (-1) or 1 indicates the status of element i to be active or inactive, respectively. Then the proportion of correlation that can be explained by pair-wise interactions is represented by the ratio $(H_1 - H_2)/(H_1 - H)$, where H , H_1 , and H_2 are the entropy of the data, independent model and Ising model, respectively.

The Jensen-Shannon (JS) divergence was used to quantify the performance of different models in approximating the data. The JS divergence is a symmetric, bounded measure of the distance between two distributions and has been used in related studies (Schneidman *et al.*, 2006; Ganmor *et al.*, 2011b). The JS divergence between probability distribution p and q is noted as $D_{JS}(p||q)$ and calculated as $D_{JS}(p||q) = 0.5 D_{KL}(p||m) + 0.5 D_{KL}(q||m)$, where $m = (p+q)/2$ and D_{KL} is the Kullback–Leibler divergence, calculated as $D_{KL}(p||q) = \sum p_i \log(p_i/q_i)$. The 2-fold cross-validation (Santos *et al.*, 2010) was used for model comparison. That is, time bins of the original data set were randomly assigned to one of two sets. Model parameters were determined from one set only and predictions were made for the second set. Besides the DG and Ising model, the independent model, which matches the event rates of the data but assumes no correlation among elements and the “half-data” model, which uses the results (e.g., pattern probabilities and cluster sizes) measured in one half of the data set to predict the corresponding behavior of the other half were also included in model comparison.

To eliminate the systematic bias in assessing models’ performances in predicting the probability for non-observed patterns (Nemenman *et al.*, 2002), only the patterns with non-zero probability (*i.e.*, patterns that are actually observed during the recordings) in both the data and all models (including the “half-data” model) were taken into account in calculating D_{JS} . Three controls were conducted to ensure that the conclusions of model performance are not affected by the exclusion of non-observed patterns. Firstly, we analyzed the DG model’s predictions about non-observed

patterns. One can expect from a good model to estimate probabilities of non-observed patterns to be considerably smaller than $1/N$. Accordingly, we found that this was the case for the DG model. For example, for the thirty 10-electrode groups analyzed in Fig. 6.4C, the average prediction of the DG model for the probability for non-observed patterns is $(0.46 \pm 0.04) / N$ (mean \pm SD, across 30 groups). In the second control, we empirically tested how the number of non-observed patterns affects our model comparison. We systematically changed the sample size from 10% to 100% of the recording length of the original data set and computed the ratio $D_{JS}(p_{data}||p_{Ising})/D_{JS}(p_{data}||p_{DG})$. The ratio was consistently above 1 already for small sample sizes (e.g., with 10% recording length, the ratio is ~ 4 for nLFP patterns and ~ 1.4 for spike patterns) and increased further or remained relatively stable with the increase of sample size (e.g., with 100% recording length, the ratio is >10 for nLFP patterns and ~ 1.6 for spike patterns). This demonstrates the superiority of the DG model over the Ising model across varying proportions of non-observed patterns. It further suggests that our findings are likely to hold even if sample size would be sufficiently increased to estimate reliably the probabilities of all potential patterns in a system. In our final control, we assigned the zero probability to non-observed patterns, which allowed us to include all patterns in the computation of D_{JS} for the DG and Ising model. Unlike in the case for KL divergence, the additional zero-probability patterns increase the magnitude of the JS divergence, given that the corresponding probabilities are non-zero in the model. However, we found that this approach did not change the conclusions (data not shown).

To assess the statistical significance of performance differences, we used the Kolmogorov–Smirnov (KS) test, Mann–Whitney U test and paired-sample Wilcoxon signed rank test. The level for statistical significance was set to be $p < 0.05$.

6.2.7 Calculating interactions of different orders

Calculation of interactions in the 3-element groups were based on full log-linear expansion (Nakahara and Amari, 2002; Amari *et al.*, 2003): $\log P(x) = \sum \theta_i x_i + \sum \theta_{ij} x_i x_j + \sum \theta_{ijk} x_i x_j x_k - \psi$, where $P(x)$ is the probability of the pattern $x = (x_1, x_2, x_3)$. x_i equals 0 or 1, representing the state of the i^{th} element. ψ is a normalization factor. θ_i , θ_{ij} , θ_{ijk} and ψ were determined according to the $P(x)$, which is either experimentally observed (for the data) or directly calculated (for both the DG and Ising models). In principle, the calculations can be done for arbitrarily high orders, *i.e.*, up to the system size. However, the amount of data needed for accurate calculation increases exponentially with higher order. Therefore, although interactions of higher orders larger than 3 exist in the DG model (Amari *et al.*, 2003), and maybe also in the data, we restricted our analysis to maximal 3rd order interactions given the limited length of our data sets.

6.3 Results

6.3.1 Higher-order interactions are essential for ongoing cortical dynamics

We first examined if the pair-wise interactions alone can sufficiently explain a well-characterized mode of cortical dynamics — the neuronal avalanches. Neuronal

avalanches describe the spatiotemporal organization of synchronized activity in superficial layers of cortex. They have been demonstrated in the spontaneous activity *in vitro* (Beggs and Plenz, 2003; Stewart and Plenz, 2006; Stewart and Plenz, 2008) and ongoing activity *in vivo* (Gireesh and Plenz, 2008; Petermann *et al.*, 2009; Hahn *et al.*, 2010; Ribeiro *et al.*, 2010). Avalanche sizes, s , distribute according to a power law, *i.e.*, $P(s) \sim s^\alpha$, with exponent α close to -1.5 — a hallmark of critical state dynamics (Plenz and Thiagarajan, 2007; Klaus *et al.*, 2011). Both theoretical (Kinouchi and Copelli, 2006) and empirical studies (Shew *et al.*, 2009; Shew *et al.*, 2011) suggest that avalanches optimize various aspects of information processing in cortical networks. To investigate if pair-wise interactions are sufficient to explain avalanche dynamics, we first constructed a maximum entropy model (Schneidman *et al.*, 2006) based on the neural activity, a widely used approach (also known in physics as the Ising model) that only utilizes the observed 1st order (event rate) and 2nd order (pair-wise correlation). It ensures that no higher-order interactions are taken into consideration for reconstruction of the observed activities.

Using implanted 10×10 microelectrode arrays, we measured ~ 30 min of the ongoing LFP in pre-motor cortex of two alert macaque monkeys (Fig. 6.1A). We identified negative LFP deflections (nLFPs, Fig. 6.1B), which correlated in our recordings with neuronal firing (data not shown; see also Petermann *et al.*, 2009). Importantly, the sizes (s) of nLFP clusters distributed according to a power law with exponent of -1.5 and the distribution showed finite-size scaling, *i.e.*, the cut-off changed systematically with array size (Fig. 6.1C, D; see also Klaus *et al.*, 2011). The power law in cluster sizes indicates the presence of correlations between cortical sites and is destroyed

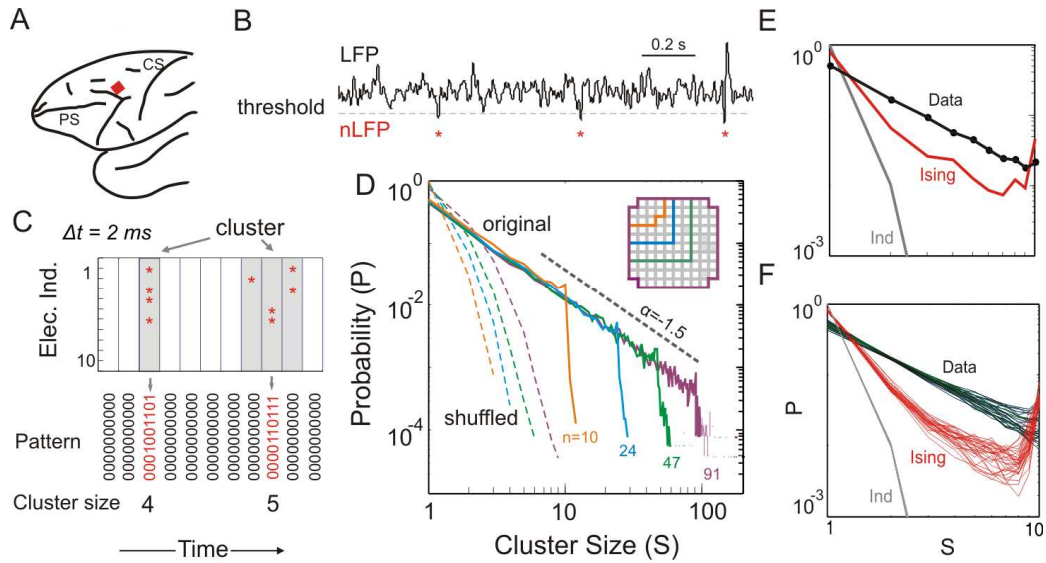


Figure 6.1: Power law organization of neuronal avalanches identifies interactions between locally synchronized neuronal groups and the insufficiency of pair-wise model in explaining it. *A*, Lateral view of the macaque brain showing the position of the multi-electrode array in pre-motor cortex (*red square; not to scale*). *PS*, Principal Sulcus. *CS*, Central Sulcus. *B*, Example period of continuous LFP at a single electrode. Asterisks indicate the peak negative deflections in the LFP (nLFPs) detected by thresholding (*broken line; -2.5SD*). *C*, Identification of nLFP clusters and patterns. *Top*: nLFPs that occur in the same time bin or consecutive bins ($\Delta t = 2$ ms) define a spatiotemporal cluster, whose size was measured by its number of nLFPs (two clusters of size 4 and 5 shown; gray areas). *Bottom*: Patterns represent the spatial information of clusters only. *D*, Neuronal avalanche dynamics are identified when the sizes of all clusters distribute according to a power law with slope close of -1.5. The cut-off of the power law reflects the finite size of the microelectrode array and changes with the area of the array used for analysis. Four distributions from the same original data set (*solid lines*, Monkey A) using different areas (*inset*), *i.e.*, number of electrodes (n), are superimposed. The power law reflects interactions between neuronal groups from different sites and vanishes for shuffled data (*broken lines*). A theoretical power

law with slope of -1.5 is provided for reference (*dotted line*). **E** and **F**, the Ising model (*red*) fails to reconstruct the power law distribution of the 10-electrode group as showing in **D** (*orange*) (**E**) and other thirty randomly chosen, spatially compact 10-electrode groups (**F**). For comparison, the prediction when no interactions are assumed is also given (Independent model; *Ind.*, *grey*)

when nLFPs are shuffled randomly (Fig. 6.1D, broken lines). To solve the Ising model exactly is computationally feasible for neuronal groups with $n \leq 10$, limiting our reconstruction of avalanche dynamics to array sizes of 10. In line with previous studies (Tang *et al.*, 2008; Santos *et al.*, 2010), the Ising model captured $> 80\%$ of interdependence for 10-electrode groups (85% for the example shown in Fig. 6.1E, and $83 \pm 2\%$ for 30 randomly chosen, spatially compact 10-electrode groups shown in Fig. 6.1F; see method for calculation of this quantity). However, the model failed to reconstruct the power law distribution of nLFP cluster sizes thereby significantly underestimating the probability of medium-sized clusters and overestimating the probability of both the small and large clusters (Fig. 6.1E, F). We conclude that pairwise interactions are insufficient to reconstruct essential cortical dynamics.

6.3.2 Avalanche dynamics contain internal thresholding for spatial coupling

To identify the higher-order interactions required to reconstruct neuronal avalanches, we analysed in detail how the nLFP patterns were generated by interplays among spatially distributed channels in light of the coherence potentials. Coherence potentials have been previously identified in ongoing neuronal avalanche activity as

dynamics with an intrinsic threshold at the neuronal population level (Thiagarajan *et al.*, 2010). We repeated the coherence potential analysis for simultaneously occurring nLFPs in the current recordings. A coherence potential was identified if the nLFP waveforms (baseline to baseline excursion) at different electrodes show a similarity larger than $R_{min} = 0.8$ (Fig. 6.2A and B). It was shown previously (Thiagarajan *et al.*, 2010) that the probability of coherence potentials, which are spatially distributed but broadband coherent nLFP waveforms, follows a highly non-linear, threshold function and depends on the amplitude of the participating nLFPs. Fig. 6.2C demonstrates this threshold in our recordings for ongoing activity in monkey A. The non-linear relation between the nLFP amplitude and spatial coherence is robust against different degrees of minimal similarity requirements, *i.e.*, choices of R_{min} (Fig. 6.2D). Collapse of the function by calculating the expected occurrence of coherence potentials minus the a priori random occurrence as a function of threshold also identifies a non-linear regime that begins at about -2.5 SD (Fig. 6.2E). These results justified the identification of nLFP clusters by applying a threshold of -2.5 SD for nLFP amplitude, which is sufficiently high to capture nLFPs in the coherence potential regime, yet, it is low enough to yield sufficiently high numbers of nLFPs for robust statistical analysis. Importantly, these results suggest a non-linear operation (*i.e.*, the thresholding) that is intrinsic to the generation of nLFP patterns, while previous theoretical studies have identified such operation as potential origin for higher-order interactions (Amari *et al.*, 2003; Macke *et al.*, 2011).

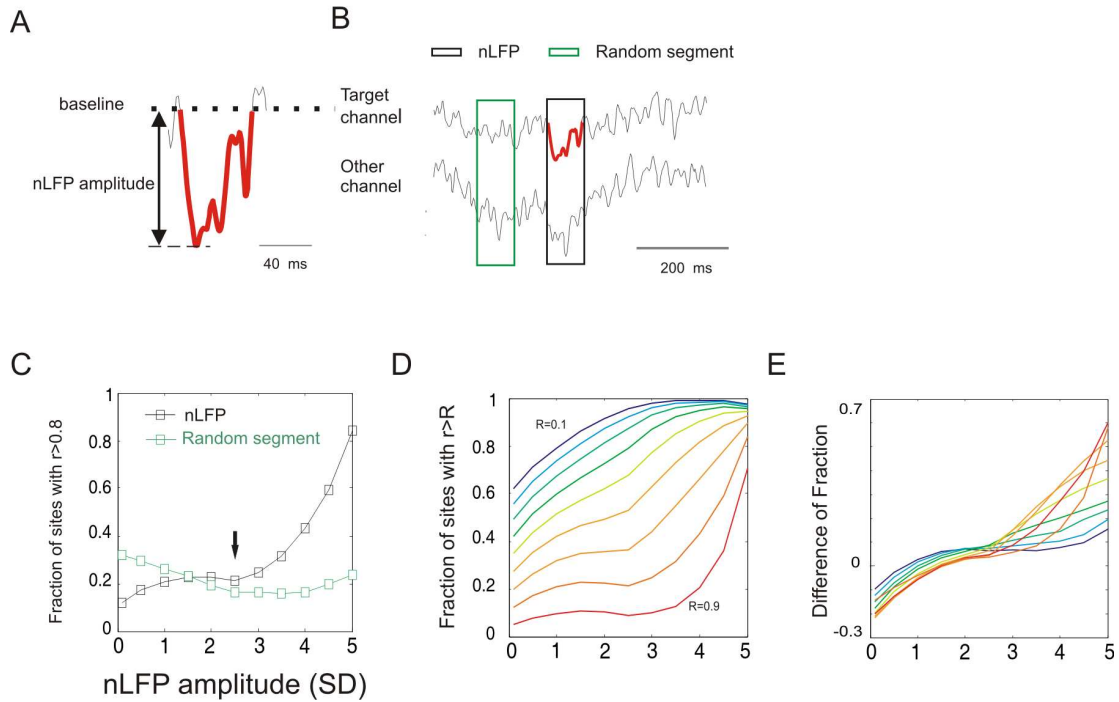


Figure 6.2: Coherence potentials indicate the presence of intrinsic threshold in the nLFP cluster formation. *A*, Coherence potential analysis utilizes the full baseline excursion of the nLFP waveform (*red*). *B*, The nLFP waveform at a target electrode is compared with the simultaneously recorded LFP at other electrodes (*black rectangle*). Similarities for each pairwise comparison are quantified by the Pearson correlation coefficient r . Comparisons for randomly chosen, length-matched LFP segments from the source electrode serve as control (random; *green rectangle*). *C*, Similarity in nLFP waveforms at distant sites increases non-linearly with the increase in nLFP amplitude. Plotted are the fraction of electrodes on the array with high similarity ($r > 0.8$) with the source electrode nLFP as a function of nLFP amplitude (Note that it is different from the minimal nLFP amplitude used in Thiagarajan *et al.*, 2010). *Black*: average increase in nLFP waveform similarity over all target channels ($n = 91$). *Green*: Expectation in similarity for random comparisons. Arrows mark threshold (-2.5 SD) used for nLFP detection in the current neuronal avalanche analysis. *D*, The non-linear coherence potential function is revealed for high-similarity requirements. Coherence potential

probability plotted as a function of minimal similarity $r > R_{min}$. Note the increase in non-linearity with higher similarity requirement. E , Difference between functions in (D) and expectation from random controls.

6.3.3 Accurate approximation of nLFP activity by a simple parametric model

To investigate if the higher-order interactions in neuronal avalanches can be explained by a mechanism of thresholding, we used the dichotomized Gaussian (DG) model (Amari *et al.*, 2003;Macke *et al.*, 2009;Macke *et al.*, 2011) to fit the data. The DG model, like the Ising model, is a stochastic model without “free” parameters—all parameters are determined by the observed nLFP rates at each electrode and pair-wise correlations between nLFP sites. The model is based on multi-dimensional Gaussian variables followed by a thresholding operation, which converts the continuous, Gaussian variables to binary ones. The DG model is fit to the data by adjusting i) the threshold level for each dimension in order to match the observed event (nLFP or spike) rate and ii) the covariance for individual pairs of dimension to ensure that the resulting binary time series will have the same pair-wise correlation as observed in nLFP or spike trains [see Fig. 6.3, methods and Macke *et al.* (2009) for details]. In contrast to the Ising model, which contains only pair-wise interactions, the DG model contains only pair-wise interactions among the continuous, Gaussian variables, and in addition introduces higher-order interactions through thresholding. We found that the power law of avalanche sizes was correctly reconstructed when utilizing the DG model [Fig. 6.4A; Jensen–Shannon (JS) divergence between the predicted distribution

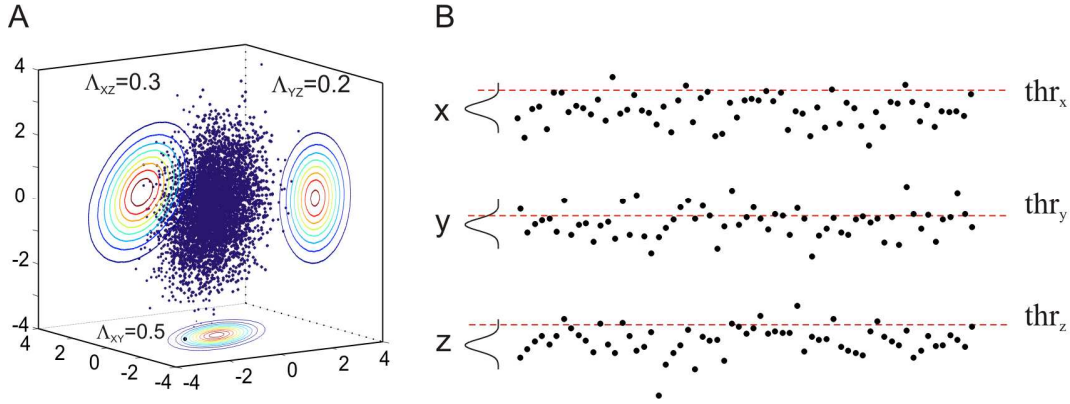


Figure 6.3: Dichotomized Gaussian (DG) model. *A*, The distribution of a 3-dimensional Gaussian and its projections at individual 2-dimensional subspaces. Marginal distributions at a 2-dimensional space are represented by probability density contours. Λ : pair-wise covariance. *B*, Converting continuous variables to binary variables (events) by thresholding. Three continuous Gaussian variables with pair-wise covariance as specified in (*A*) and without high-order interactions. *Red line*: threshold applied to each variable. To fit the DG model to the data, the pair-wise covariance (Λ) of the multi-dimensional Gaussian and the level of each threshold need to be adjusted in such a way that the resulting binary variables have the identical event rates and pair-wise correlations as the data.

and the true distribution was reduced by $\sim 98\%$; 0.002 for the DG model vs. 0.085 for the Ising model].

Moreover, the DG model predicted avalanche (cluster) patterns much more accurately than the Ising model (10 sites; Fig. 6.4B, JS divergence is 1.3×10^{-4} for DG model; 1.8×10^{-3} for Ising model). When applying the two models to 30 randomly chosen, spatially compact 10-electrode groups, we found that the DG model consistently

outperformed the Ising model (on average $68\times$ better for size distribution and $11\times$ better for pattern probability; Fig. 6.4C. See Table 6.1 for more details). With respect to pattern probability, the accuracy of the DG model was even significantly better than the prediction based on the data directly (Fig. 6.4C *right*, see method for details). This is possible because the DG model requires relatively few parameters to be determined thereby reducing estimate errors originating from finite sampling (see below section for more analysis regarding this property). In Fig. 6.4D, we directly calculated the 3rd order interactions in the original data set and corresponding predictions from the DG and the Ising models demonstrating that, indeed, the DG model accurately predicted higher-order interactions in neuronal avalanches. This analysis not only confirmed that the Ising model failed to predict any 3rd order interactions as expected, but, in addition, it demonstrated that the Ising model was also much less accurate in characterising the true pair-wise interactions when compared to the DG model (Fig. 6.4D, upper right, arrow). Correspondingly, avalanche pattern probabilities predicted by the Ising model exhibited significant deviations from the observed values even in such small systems with only three electrodes (Fig. 6.4E). Importantly, the DG model can be easily applied to larger systems ($\gg 10$ elements), for which the Ising model is computationally difficult (Cocco *et al.*, 2009; Ganmor *et al.*, 2011a; Ganmor *et al.*, 2011b). In Fig. 6.4F, we show accurate predictions of the DG model for neuronal avalanche dynamics (size distribution) that engage up to ~ 100 sites and cover $\sim 16 \text{ mm}^2$ of cortex. We note that some of the results for large systems are well above the “perturbation regime” (Roudi *et al.*, 2009), which is characterized as $Nr \ll 1$, where N is the number of elements

and r is the average probability of event. The DG model accurately captures the cluster size distributions for 91-electrode group with larger Δt (data not shown) and in those cases Nr can increase to larger than 1 (e.g., $Nr = 1.8$ and 3.5 for $\Delta t = 32$ and 64 ms, respectively). This suggests that our findings may generalize to even larger systems in which correlations become the dominant force in shaping the neuronal dynamics (Schneidman *et al.*, 2006). Qualitatively similar results for monkey B are summarized in Table 6.1.

Table 6.1: Comparison of the performance of the DG and the Ising model in approximating the nLFP patterns.

	Degenerated patterns 10-elec. group		3-elec. group	Non-degenerated patterns 10-elec. Group		3-elec. group
	Compact Gr.	Random Gr.		Compact Gr.	Random Gr.	
Monkey A						
<i>Pattern probability</i>						
<i>N</i>	30	30	98	30	30	98
<i>D_{DG} ($\times 10^{-4}$)</i>	1.52 \pm 0.16	1.48 \pm 0.14	0.026 \pm 0.016	1.28 \pm 0.19	1.01 \pm 0.10	0.036 \pm 0.023
<i>D_{Ising} ($\times 10^{-4}$)</i>	16.9 \pm 1.1	14.7 \pm 1.0	0.98 \pm 0.20	15.2 \pm 2.6	9.95 \pm 0.86	0.20 \pm 0.12
<i>DG < Ising</i>	100%	100%	100%	100%	100%	92%
<i>Size distribution</i>						
<i>N</i>	30	30	98	30	30	98
<i>D_{DG} ($\times 10^{-4}$)</i>	14.3 \pm 6.6	19.7 \pm 6.9	3.3 \pm 3.0	11.1 \pm 3.3	13.1 \pm 2.2	4.0 \pm 3.5
<i>D_{Ising} ($\times 10^{-4}$)</i>	945 \pm 123	624 \pm 72	175 \pm 55	668 \pm 139	379 \pm 49	29 \pm 17
<i>DG < Ising</i>	100%	100%	100%	100%	100%	93%
Monkey B						
<i>Pattern probability</i>						
<i>N</i>	30	30	97	30	30	98
<i>D_{DG} ($\times 10^{-4}$)</i>	1.97 \pm 0.25	1.85 \pm 0.23	0.032 \pm 0.019	1.65 \pm 0.34	1.51 \pm 0.26	0.020 \pm 0.013
<i>D_{Ising} ($\times 10^{-4}$)</i>	16.9 \pm 2.5	17.1 \pm 1.9	0.59 \pm 0.36	12.8 \pm 3.2	11.4 \pm 2.0	0.17 \pm 0.14
<i>DG < Ising</i>	100%	100%	99%	100%	100%	86%
<i>Size distribution</i>						
<i>N</i>	30	30	97	30	30	98
<i>D_{DG} ($\times 10^{-4}$)</i>	10.2 \pm 4.6	8.6 \pm 4.5	3.6 \pm 3.0	9.6 \pm 8.6	8.4 \pm 5.3	1.39 \pm 1.59
<i>D_{Ising} ($\times 10^{-4}$)</i>	681 \pm 175	627 \pm 116	84 \pm 65	460 \pm 147	389 \pm 93	20.5 \pm 18.9
<i>DG < Ising</i>	100%	100%	97%	100%	100%	93%

Compact Gr. and Random Gr. represent the results for spatially compact (cf. inset of Fig. 6.1D, main text) groups and randomly chosen groups, respectively. Note that all 3-electrode groups were randomly chosen. N is the number of groups analyzed. D is the JS divergence, *i.e.*, $D_{JS}(P_{data}||P_{model})$. “DG < Ising” is the percentage of groups for which the JS divergence of the DG model is smaller than that of the Ising model. Results are presented as mean \pm SD. P-values for KS test and Mann-Whitney U test were $< 10^{-9}$ in all cases, demonstrating that the JS divergence for the two models came from different distributions.

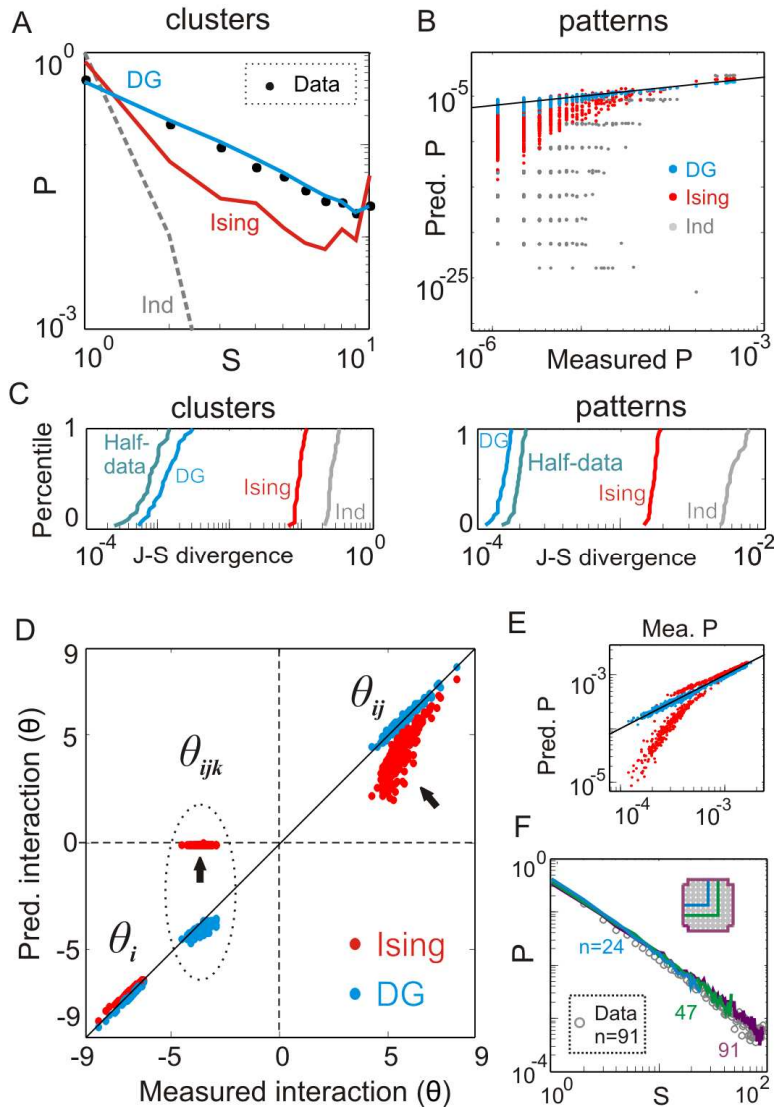


Figure 6.4: The DG model predicts 2nd as well as higher-order interactions in neuronal avalanches significantly better than the Ising model. *A*, The DG model (blue) reconstructs the power law in avalanche size probability (dots) more accurately than the Ising model (red). The results for data, the Ising and Ind model are replotted from Fig. 6.1E (top panel). *B*, The DG model is also superior in predicting the probabilities of individual patterns (corresponding data from a). Observed pattern probability P is plotted against model predictions. Solid line indicates equality. Most common pattern (all zeros; inactive) not shown for visual clarity. *C*, Quantification of model prediction demonstrates 1–2 orders of

magnitude of improvement when using the DG model as compared to the Ising model. *Left*: Cumulative distribution of JS divergence between the observed and predicted cluster size distribution for $n = 30$ randomly chosen, spatially compact 10-electrode groups out of $n = 91$ electrodes (monkey A; cf. Fig. 6.1F). *Right*: Corresponding analysis for pattern probability distributions. Time bins of the original data set were randomly assigned to one of two sets. Model parameters were determined from one set only and predictions were made for the second set. *Half-data*: to use the results measured in one half to predict the corresponding behavior of the other half. **D**, The DG model accurately predicts 2nd (θ_{ij}) and 3rd order (θ_{ijk}) interactions. In comparison, the Ising model is less accurate for 2nd order interactions (*arrow*) and fails completely to predict 3rd order interactions (ellipsoid, *arrow*). Measured interactions of 1st to 3rd order (θ_i , θ_{ij} , and θ_{ijk} , respectively) are plotted against model predictions for $n = 98$ randomly chosen 3-electrode groups from 91-electrode activity (monkey A). **E**, Corresponding measured pattern probability plotted against model predictions (over all 3-electrode groups). Solid line indicates equality. **F**, The DG model accurately predicts the power law in avalanche sizes also for systems much larger than 10 sites. Prediction for $n = 24, 47, 91$ electrode sites are shown (cf. Fig. 6.1D).

6.3.4 The nature of higher-order interactions generated by thresholding

To better understand the nature of the higher-order interactions in the DG model that are introduced by thresholding, we systematically varied the mean and covariance of a 3-dimensional Gaussian, which served as the layer of continuous variables in the DG model, before applying a fixed threshold (> 0) and investigated how these changes affected the 3rd order interactions in the resulting binary variables. As shown in Fig. 6.5A, thresholding of continuous variables indeed introduced 3rd order

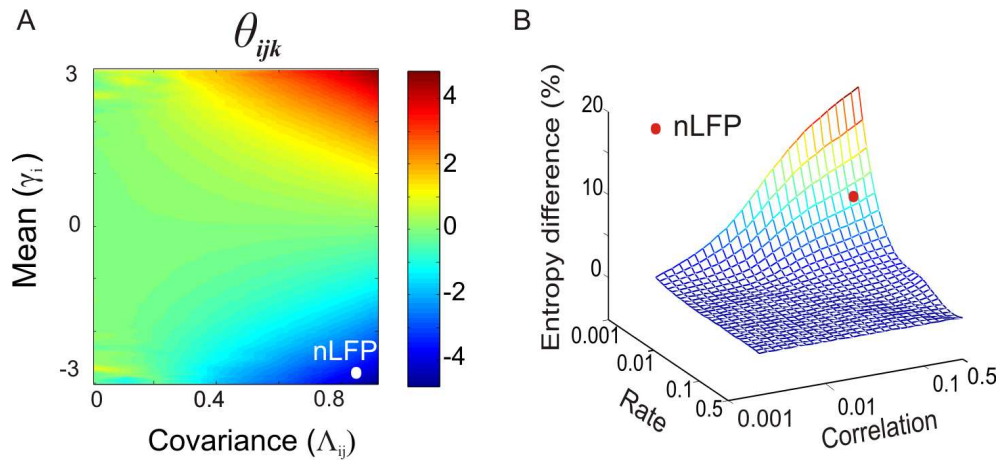


Figure 6.5: The magnitude of higher-order interactions introduced by thresholding depends on event rate and strength of pair-wise correlations. *A*, 3rd order interactions in the binary variables cannot be neglected if, for the Gaussian variable, the covariance is strong and the mean is far below or above 0. Change in the magnitude of 3rd order interaction (θ_{ijk}) is shown as a function of the mean (γ) and the covariance (A) of an underlying 3-dimensional Gaussian, $\mathbf{u} \sim N(\gamma, A)$. θ_{ijk} was calculated for binary variables obtained by applying the threshold $u_i > 0$. The white dot marks the average mean and covariance of the hidden Gaussians estimated in the DG model for nLFPs (cf. Fig. 6.4D). *B*, Differences in pattern probabilities between the Ising and the DG model, here quantified as entropy difference, are most pronounced when, for the binary variables, the rate deviates far away from 0.5 and pair-wise correlations are strong, as is the case for avalanche nLFPs (high-rate regime produces a symmetric plot; not shown). Entropy difference is plotted as a function of average rate and pair-wise correlation. Dot (*red*) marks the average rate and pair-wise correlation for nLFP (average of 91 channels and all pairs). For both (*A*) and (*B*), simulations assume homogenous rate and pair-wise correlations for simplicity.

interactions that were absent in the pre-thresholded Gaussian, especially when event probabilities were far above or below 0.5 and pair-wise correlations are strong. We point out that an event probability (r) equal to 0.5 corresponds to a Gaussian mean (γ) equal to 0. We then varied the event probability and pair-wise correlations for 10-element systems (binary variables) and constructed both the DG and the Ising model using identical constraints. The difference between the two models indicates the total amount of higher-order interactions introduced by thresholding and was expressed as entropy difference (Fig. 6.5B). Consistent with our results shown in Fig. 6.5A and previous findings (Macke *et al.*, 2009; Macke *et al.*, 2011), this difference is more pronounced when rates are low and pair-wise correlations are strong, which is typically the case for nLFPs in ongoing activity (Petermann *et al.*, 2009).

6.3.5 Accurate approximation of the ongoing and evoked spiking activity

We then extended our analysis to spiking activity of both ongoing and evoked cortical dynamics. We firstly analyzed extracellularly recorded spiking activity of up to 56 neurons during ongoing avalanche activity in the two awake monkeys. Similar with our nLFP analysis, the DG model significantly outperformed the Ising model in predicting both firing patterns and concurrent spikes, *i.e.*, neuronal synchrony (see Table 6.2 for details). In line with the analysis shown in Fig. 6.5, the improvement by the DG model over the Ising model was less pronounced compared to the LFP analysis, given the higher rates (0.075 vs. 0.002, monkey A) and weaker pair-wise correlations (0.04 vs. 0.35) of that spiking activity compared to nLFPs. Accordingly,

Table 6.2: Comparison of the performance of the DG and the Ising model in approximating the spike patterns.

	Strongly coupled groups				Randomly chosen groups			
	10-neuron		3-neuron		10-neuron		3-neuron	
	pp	sync	pp	sync	pp	sync	pp	sync
Monkey A								
N_group	30		240		30		197	
N_neuron	35/56		40/56		55/56		56/56	
D_DG ($\times 10^{-4}$)	19.4 \pm 2.1	2.5 \pm 1.5	0.13 \pm 0.17	0.82 \pm 1.39	11.8 \pm 3.7	1.3 \pm 0.7	0.06 \pm 0.16	0.22 \pm 0.40
D_Ising ($\times 10^{-4}$)	27.8 \pm 3.0	16.5 \pm 5.9	0.40 \pm 0.50	2.9 \pm 4.6	12.5 \pm 4.0	2.1 \pm 1.2	0.07 \pm 0.19	0.29 \pm 0.59
DG < Ising	100%	97%	77%	78%	83%	93%	58%	58%
P _{KS}	<10 ⁻¹¹	<10 ⁻¹²	<10 ⁻¹²	<10 ⁻¹⁰	0.936	0.011	0.771	0.601
P _U	<10 ⁻¹⁰	<10 ⁻¹⁰	<10 ⁻¹⁴	<10 ⁻¹²	0.549	0.002	0.489	0.464
P _S	<10 ⁻⁵	<10 ⁻⁵	<10 ⁻²⁰	<10 ⁻²⁰	0.001	<10 ⁻⁵	<10 ⁻³	<10 ⁻³
Monkey B								
N_group	16		198		15		163	
N_neuron	35/42		41/42		38/42		42/42	
D_DG ($\times 10^{-4}$)	9.3 \pm 1.7	1.1 \pm 0.8	0.046 \pm 0.094	0.22 \pm 0.52	5.9 \pm 1.6	0.64 \pm 0.59	0.0078 \pm 0.017	0.10 \pm 0.25
D_Ising ($\times 10^{-4}$)	11.8 \pm 1.8	7.2 \pm 2.7	0.07 \pm 0.14	0.32 \pm 0.56	6.1 \pm 1.9	1.3 \pm 1.2	0.0081 \pm 0.017	0.10 \pm 0.23
DG < Ising	100%	100%	64%	64%	73%	100%	54%	53%
P _{KS}	0.002	<10 ⁻⁶	0.046	0.060	0.998	0.308	1.000	1.000
P _U	0.003	<10 ⁻⁵	0.027	0.041	0.836	0.106	0.935	0.951
P _S	<10 ⁻³	<10 ⁻³	<10 ⁻⁶	<10 ⁻⁶	0.083	<10 ⁻⁴	0.024	0.017
Cat A, Probe 1								
N_group	30		98		30		99	
N_neuron	19/24		22/24		24/24		24/24	
D_DG ($\times 10^{-4}$)	4.1 \pm 0.4	0.34 \pm 0.27	0.026 \pm 0.035	0.35 \pm 0.61	2.4 \pm 0.5	0.22 \pm 0.23	0.010 \pm 0.017	0.11 \pm 0.27
D_Ising ($\times 10^{-4}$)	7.0 \pm 0.5	7.8 \pm 2.4	0.10 \pm 0.14	1.4 \pm 2.6	2.9 \pm 0.8	1.1 \pm 1.3	0.026 \pm 0.066	0.35 \pm 0.94
DG < Ising	100%	100%	80%	80%	100%	97%	66%	66%
P _{KS}	<10 ⁻¹³	<10 ⁻¹³	<10 ⁻⁶	<10 ⁻⁵	0.055	<10 ⁻⁶	0.549	0.437
P _U	<10 ⁻¹⁰	<10 ⁻¹⁰	<10 ⁻⁸	<10 ⁻⁷	0.004	<10 ⁻⁶	0.372	0.525
P _S	<10 ⁻⁵	<10 ⁻⁵	<10 ⁻⁹	<10 ⁻⁹	<10 ⁻⁵	<10 ⁻⁵	<10 ⁻⁴	<10 ⁻⁴
Cat A, Probe 2								
N_group	15		100		30		100	
N_neuron	15/18		18/18		15/18		18/18	
D_DG ($\times 10^{-4}$)	3.6 \pm 0.3	0.088 \pm 0.04	0.012 \pm 0.026	0.07 \pm 0.14	2.4 \pm 0.5	0.12 \pm 0.07	0.0056 \pm 0.010	0.040 \pm 0.071
D_Ising ($\times 10^{-4}$)	4.0 \pm 0.3	0.72 \pm 0.24	0.023 \pm 0.051	0.13 \pm 0.27	2.5 \pm 0.5	0.23 \pm 0.18	0.0065 \pm 0.013	0.046 \pm 0.091
DG < Ising	100%	100%	65%	65%	90%	83%	59%	59%
P _{KS}	0.017	<10 ⁻⁶	0.140	0.069	0.936	0.011	0.961	0.961
P _U	0.002	<10 ⁻⁵	0.174	0.182	0.464	0.002	0.791	0.744
P _S	<10 ⁻⁴	<10 ⁻⁴	<10 ⁻⁴	<10 ⁻⁵	<10 ⁻⁴	<10 ⁻⁴	0.115	0.074
Cat B								
N_group	30		98		30		99	
N_neuron	15/22		16/22		22/22		22/22	
D_DG ($\times 10^{-4}$)	2.7 \pm 0.2	0.28 \pm 0.19	0.0072 \pm 0.009	0.09 \pm 0.11	1.8 \pm 0.3	0.41 \pm 0.31	0.0042 \pm 0.007	0.05 \pm 0.10
D_Ising ($\times 10^{-4}$)	4.1 \pm 0.2	6.3 \pm 2.7	0.032 \pm 0.027	0.40 \pm 0.36	2.0 \pm 0.4	1.3 \pm 1.6	0.0061 \pm 0.010	0.08 \pm 0.16
DG < Ising	100%	100%	85%	85%	87%	77%	58%	58%
P _{KS}	<10 ⁻¹³	<10 ⁻¹³	<10 ⁻¹²	<10 ⁻¹²	0.200	0.011	0.338	0.338
P _U	<10 ⁻¹⁰	<10 ⁻¹⁰	<10 ⁻¹³	<10 ⁻¹²	0.070	0.003	0.151	0.155
P _S	<10 ⁻⁵	<10 ⁻⁵	<10 ⁻¹⁴	<10 ⁻¹⁴	<10 ⁻⁴	<10 ⁻⁴	0.038	0.026

pp and sync stand for pattern probability and number of concurrent spikes (neuronal synchrony), respectively. N_group is the number of groups analyzed. N_neuron is the number of neurons that included. D is the JS divergence, *i.e.*, $D_{JS}(P_{data}||P_{model})$. “DG < Ising” is the percentage of groups for which the JS divergence of the DG model is smaller than that of the

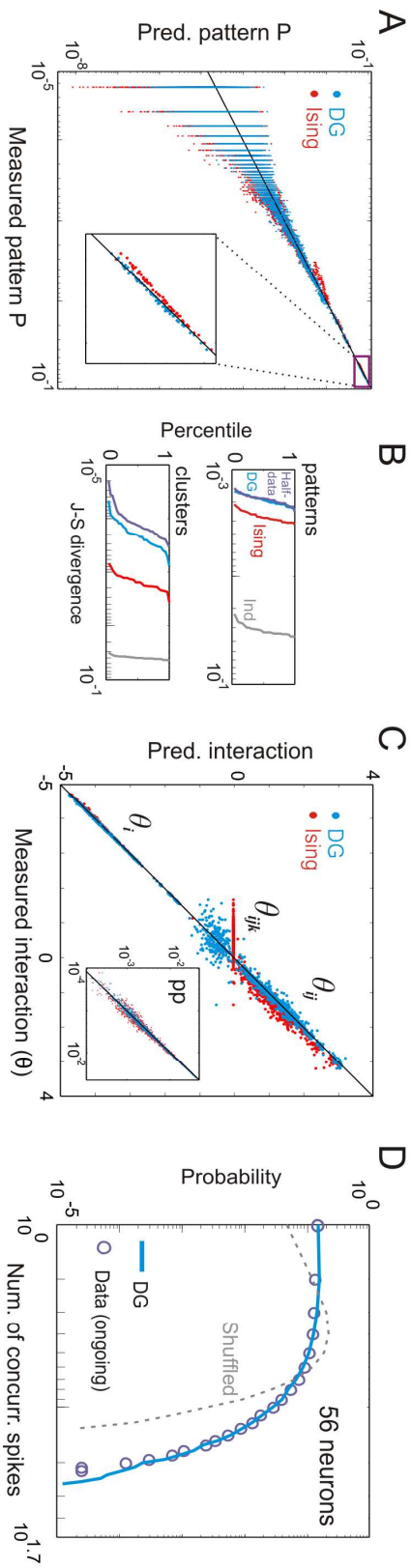
Ising model. Results are presented as mean \pm SD. P_{KS} , P_U and P_S are p-values for KS test, Mann-Whitney U test and paired-sample Wilcoxon signed rank test, respectively. The paired test is appropriate here as the two models are fitted to the same individual neuronal groups.

when analyzing separately neuronal groups with relatively strong pair-wise correlations (see method for more details), predictions of the DG model for spike patterns, synchrony, and 3rd order interactions further improved over the Ising model (Fig. 6.6A-C, Table 6.2). We note that these groups included the majority of recorded neurons ($> 60\%$). Again, the DG model was readily extended to accurately predict the probability in spike synchrony for large number of neurons (56 neurons, Fig. 6.6D). These results were not limited to ongoing activity only. We obtained similar results when analyzing spiking activity recorded from area 17 in anesthetized cats in response to grating stimuli (Fig. 6.6E-H).

6.3.6 Efficient characterization of population activity

The approximation of higher-order interactions by a simple threshold operation allows for an efficient characterization of neuronal activity with relatively little data sampling, which is desirable in studies of e.g. neural coding or brain-machine interfaces that require higher-order statistics of the population activity (e.g., the pattern probabilities). Such statistics could be directly measured from the data (e.g., see Fig. 6.4B). However, as outlined in the introduction this approach becomes readily unfeasible for larger system sizes. In contrast, the DG model only requires event rates and pair-wise correlations to approximate those pattern probabilities,

Ongoing spiking activities (awake monkey)



Evoked spiking activities (anesthetized cat)

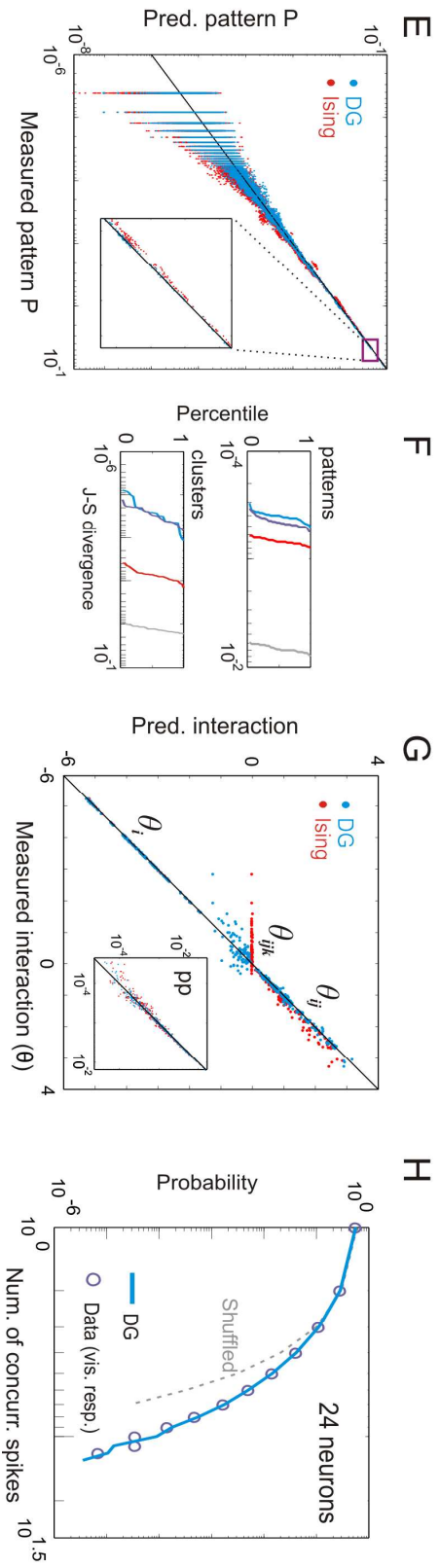


Figure 6.6: For strongly coupled sub-groups, the DG model predicts spike patterns in ongoing and stimulus-evoked activities significantly better than the Ising model. A-C, Ongoing spiking activity during avalanche dynamics in monkey A. *A*, DG and Ising model prediction in pattern probability (thirty 10-neuron groups with strongest pair-wise correlation). *Inset*: zoomed-in view, showing that the DG model more accurately predicted high probability patterns. *B*, Cumulative distributions of JS divergence for the groups shown in (*A*). *C*, Measured and predicted interactions for more than 200 3-neuron groups with strongest pair-wise correlation. *Inset*, measured (*x-axis*) and predicted (*y-axis*) pattern probabilities (pp) for the same 3-neuron groups. For more details, see legend of Fig. 6.4B–D. *D-F*, Corresponding results for spiking activity evoked by drifting gratings recorded in area 17 of an anesthetized cat (Cat A, probe 1).

which can be obtained within relatively short durations (< 30 min in our analysis), and importantly, those durations are independent of system size. The DG model is also simple enough to be treated analytically (Amari *et al.*, 2003; Burak *et al.*, 2009; Tchumatchenko *et al.*, 2010; Macke *et al.*, 2011), which allows for direct calculation of pattern probabilities. This advantage holds even for small systems ($N = 10$ elements) as shown in Fig. 6.7A. As typically done in brain machine interface studies, here a training data set is used to make inference about future data (testing set). We randomly separated our 30-min recordings of nLFPs into two 15-min sets, which represented the testing and the training set respectively. We then systematically shortened the length of the training set and compared the performance in predicting the pattern probability for testing set between the DG model and the direct sampling. We found that the DG model increasingly outperformed direct sampling for shorter

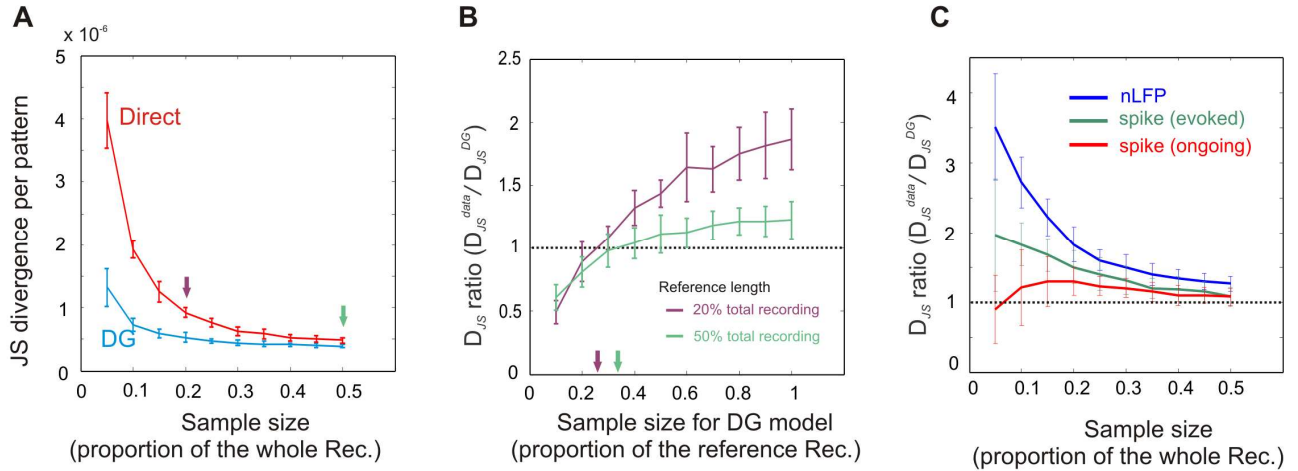


Figure 6.7: The DG model requires less data to characterize pattern probabilities

compared to direct estimates. *A*, The DG model outperformed the direct sampling method

in predicting pattern probabilities for nLFPs. Variably sized samples were drawn from 15-min of recording (training set) to predict pattern probability in another 15 min data set (testing set). Performance quantified by average JS divergence per pattern in the testing set and plotted against the sample size taken from the training set.

B, The DG model needs much less amount of data to reach the same accuracy compared with direct sampling. Two reference recordings were chosen for the direct sampling method, with 6-min and 15-min in lengths respectively (arrows in *A*). Then various proportions of the reference recording were used for the DG model.

The difference in performance of these two methods, measure by the ratio of JS divergence, was plotted against the amount of samples used by the DG model. The ratio of one, which indicates the equal performance, was marked by the dotted line and the sample sizes to reach equal performance were marked by arrows.

C, The ratio of JS divergence was plotted against the sample size taken from the training set for both the nLFP and spiking activities. Almost all data points were significantly larger than 1 (sign rank test, $p < 0.05$), except for the leftmost two points for ongoing spikes, which correspond to smallest sample sizes and, therefore, largest measurement errors. The total sample sizes were 9×10^5 ,

9×10^4 and 4.5×10^5 for nLFP, ongoing and evoked spikes, respectively. In all panels, data is represented as mean \pm SD. Twenty randomly chosen 10-element groups for nLFP (monkey A), ongoing spikes (monkey A) and evoked spikes (cat 1, probe 1) were analyzed.

and shorter training set (Fig. 6.7A and C). To achieve the same prediction accuracy, the DG model required much shorter recording length ($< 1/3$) compared to direct sampling (Fig. 6.7B). Similar advantages of using the DG model in characterizing the pattern probabilities were also found for both ongoing and evoked spiking activities (Fig. 6.7C).

6.3.7 Control analysis

In this section, we demonstrate that the conclusion we obtained regarding the structure of higher-order interactions is not reply on any specific method that we used in extracting the activities patterns. For spiking activities, this fact is readily visible as 1) we only applied a simply binning to the raw data and 2) the conclusions do not rely on specific choice of bin-width (see method for details). Therefore, here we focus on the extraction of neuronal avalanche, *i.e.*, the nLFP, patterns.

Neuronal avalanches represent spatiotemporal clusters of nLFPs, and thus reflect spatiotemporal correlations among neuronal activities at different sites. The contribution of these correlations in establishing avalanche dynamics is readily illustrated by the fact that the power law distribution in avalanche sizes is destroyed in shuffled datasets where all correlations are removed (cf. Fig. 6.1D). To

demonstrate the specific contribution of temporal correlations longer than Δt , we applied “bin-shuffling” to the data. More specifically, after binning the original time stamps of nLFPs with Δt , the spatial pattern of individual bins were kept unchanged while the order of bins was randomized. This maintains the original spatial correlation structure at resolution Δt . As demonstrated in Fig. 6.8A and B, bin-shuffling destroys the power law in avalanche sizes, demonstrating the presence of temporal correlations beyond Δt in neuronal avalanche dynamics. On the other hand, both the DG and the Ising model intrinsically lack temporal structure. In fact, interactions for both models are assumed to be instantaneous and activities at different times are completely independent. In order to use these models to study neuronal interactions, we took the strategy of mapping the spatiotemporal organization of clusters into a spatial structure only, thus degenerating adjacent bins of nLFPs to a single bin (cf. Fig. 6.1C). This approach is supported by the well established finding that repetitive participations of a single site, *i.e.*, activation of the same electrode, are rare for individual spatial-temporal clusters when Δt is not too large. This is readily suggested by finite-size scaling of avalanche dynamics where the cut-off of the power law size distribution is simply determined by the maximal number of sites analyzed (cf. Fig. 6.1D and Beggs and Plenz, 2003; Petermann *et al.*, 2009). Accordingly, our temporal-spatial mapping resulted in size distributions of degenerated spatial clusters that matched well the power law distributions found in the original spatial-temporal clusters (e.g., compare Fig. 6.1D with 1E and 4F).

We then devised two controls to demonstrate that our findings on higher-order interactions in the original LFP dynamics did not rely on this specific method of

extracting spatial-temporal patterns. First, we repeated the same analysis for non-degenerated spatial patterns obtained after binning nLFPs into windows of Δt , but without concatenating successive bins with active sites. As shown in Fig. 6.8C-G, the performance of the two models and the demonstration of higher-order interactions were highly similar to our results obtained with degenerated patterns. Because temporal correlations beyond Δt were neglected in this analysis, the power law distribution of cluster sizes was missed. Furthermore, the magnitude of higher-order interactions is less for single bin patterns (cf. Fig. 6.4D and Fig. 6.8F), demonstrating that the higher-order interactions calculated for degenerated patterns have spatial as well as temporal origin.

In the second control, we quantified the amount of 3rd order interactions related to temporal correlations. Specifically, we demonstrate that 3rd order interactions are not introduced spuriously by the degenerating method itself. Conceptually, this statement implies that the following relation holds:

$$|\theta_{ijk}^d| > |\theta_{ijk}^{s-d}| \approx |\theta_{ijk}^{nd}|, \quad (6.1)$$

where the three θ terms are 3rd order interactions obtained from degenerated patterns based on original data, degenerate patterns based on bin-shuffled data, and non-degenerate patterns, respectively. $|\theta_{ijk}^d| > |\theta_{ijk}^{nd}|$ implies that the degeneration procedure introduces a sizeable amount of 3rd order interactions, which reflects i) the mapping of true temporal correlations into a spatial pattern, and ii) an unknown contribution from the concatenation of active bins that just happened to be successive. $|\theta_{ijk}^{s-d}| \approx |\theta_{ijk}^{nd}|$ implies that the second component, *i.e.*, the amount of spurious 3rd

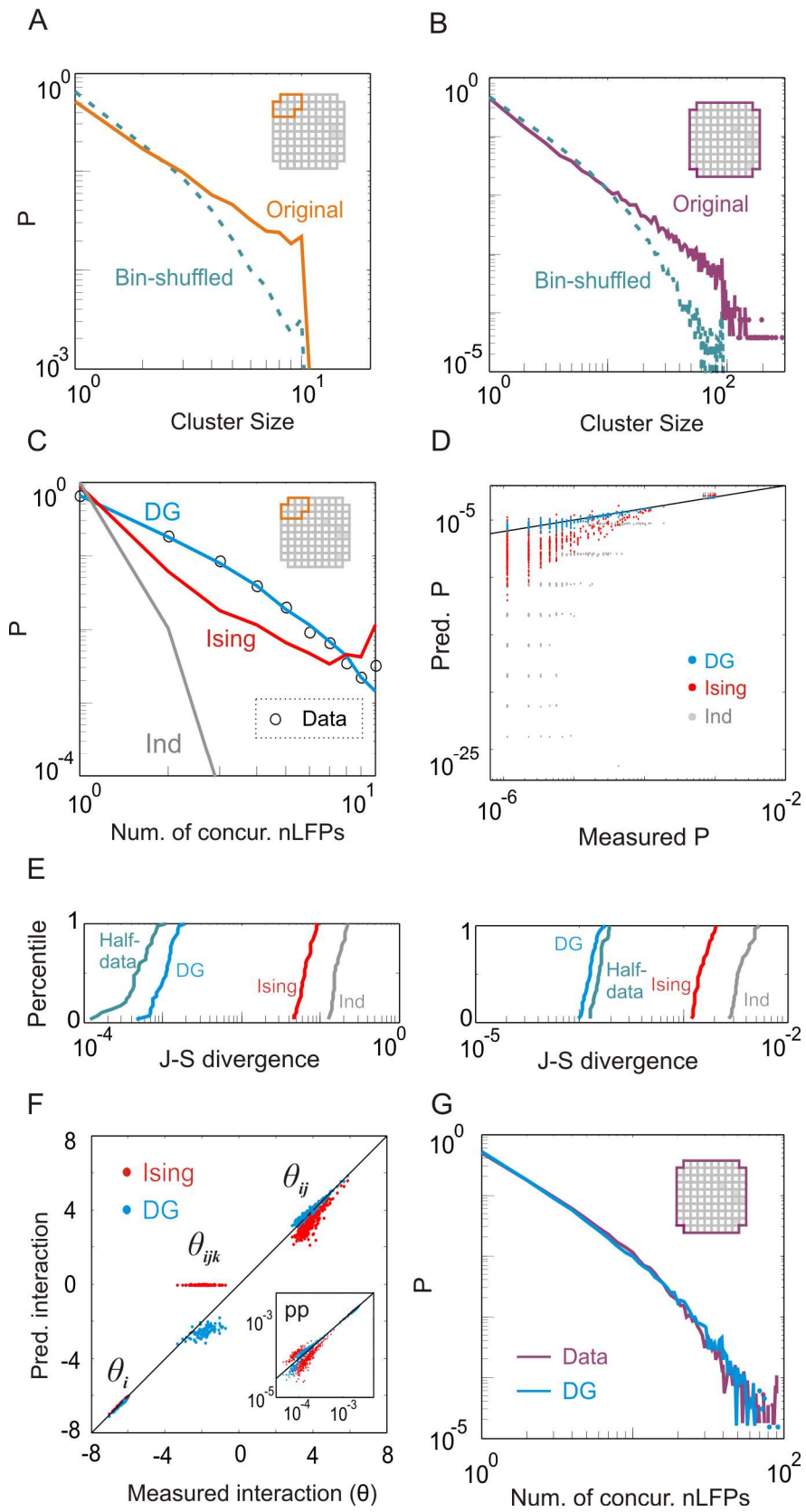


Figure 6.8: Temporal correlation in avalanche dynamics and the performances of different models in predicting the single-bin (un-degenerated) nLFP activities. *A-B*, The power law distribution of nLFP cluster sizes indicates a unique spatiotemporal correlation structure and is not found for bin-shuffled data, in which the spatial correlation within individual time bins were reserved but the temporal correlation among different time bins were removed. *A*, 10-electrode sub-group. *B*, 91-electrode group. *Insets*: the areas used for analysis. *C-G*, The DG model accurately predicts the single-bin (un-degenerated) nLFP activities. The data set used in *C-G* is the same as in Fig. 6.4A-F and all the analyses were performed in a corresponding way, except that the activity patterns were un-degenerated. For more details, see legend of Fig. 6.4A-F.

order interactions due to the concatenation, is relatively small. In order to measure the degree to which relation (1) holds, we computed the quantity

$$\beta = (\theta_{ijk}^d - \theta_{ijk}^{s-d}) / (\theta_{ijk}^d - \theta_{ijk}^{nd}). \quad (6.2)$$

Intuitively, β measures the distance between θ_{ijk}^d and θ_{ijk}^{s-d} relative to the distance between θ_{ijk}^d and θ_{ijk}^{nd} . Assuming all the θ terms have the same sign, the better the relation (1) holds, the closer to 1 will β be. We found that $\beta = 0.9$ and 0.8 for monkey A and B, respectively, which demonstrates that our results on 3rd order interactions reflect mainly spatiotemporal correlations in the original dynamics.

6.4 Discussion

In the present study, we demonstrated that higher-order interactions are essential to understand neuronal interdependence in the cortex, both at the population level of

neuronal avalanches, and at the level of individual neurons, especially when pairs of neurons are coupled strongly. This is consistent with recent findings that the inclusion of higher-order interactions yields better approximation of LFP patterns (Santos *et al.*, 2010) as well as neuronal synchrony (Montani *et al.*, 2009) and the shortcomings of the Ising model to predict correlated activity of nearby neurons (Ohiorhenuan *et al.*, 2010; Ohiorhenuan and Victor, 2011) or large network activity (~ 100 retina ganglion cells) in response to natural stimuli (Ganmor *et al.*, 2011a). The current results shed new light to understand these recent findings. For example, the insufficiency of the Ising model to account for population activities of nearby neurons (Ohiorhenuan *et al.*, 2010; Ohiorhenuan and Victor, 2011) has been interpreted as an indication that higher-order interactions are scale dependent. Our results provided direct evidence that the more pronounced 3rd order interactions are simply due to stronger pair-wise correlations (see also Macke *et al.*, 2011). Moreover, the same mechanism may provide a coherent explanation for the failure of Ising model specific to responses for natural stimuli (Ganmor *et al.*, 2011a), as such responses are often characterized by sparse firing and strong pair-wise correlations (Stuttgen and Schwarz, 2008; Jadhav *et al.*, 2009). In a more general scope, our results also provide a satisfactory account for the lacking of higher-order interactions in many previous reports (e.g., Schneidman *et al.*, 2006; Shlens *et al.*, 2006; Tang *et al.*, 2008; Yu *et al.*, 2008), as those interactions are most pronounced in the regime of low-rates and high pair-wise correlation, which previous studies often did not discriminate.

The significance of the current study also lies in the demonstration that higher-order interactions in cortical dynamics can be well approximated by a simple non-linear

operation, which has been parallelly proposed in a recent theoretical study (Macke *et al.*, 2011). In the DG model, higher-order interactions are solely determined by the rates and pair-wise correlations, so they do not serve as free parameters of the system and, therefore, do not add extra complexity to the model. Importantly, the DG and Ising models have the same number of parameters. Thus, our results suggest an easy way to tame the daunting complexity of higher-order interactions in the cortex. The current results imply that higher-order interactions in the cortex are, at least partly, due to non-linear operations, e.g., thresholding, in neuronal processing. The intrinsic nature of such thresholding is readily visible for the case of action potential generation. With respect to the LFP, our analysis confirms the recent finding that the correlation among spatially distributed sites increase non-linearly as a function of nLFP amplitude (Thiagarajan *et al.*, 2010), identifying a threshold operation at the population dynamic level that is analogous to action potential formation. Unlike the threshold for generating action potential, the neural mechanisms underlying this threshold at the population level has not been revealed yet. However, it was demonstrated that this threshold can not be simply explained by i) enhanced signal to noise ratio with high LFP amplitudes; ii) stronger volume conduction or iii) stronger common inputs. Instead, it reflects the intrinsic non-linear dynamics in both recruiting local synchronized neuronal groups and exciting other, spatially separated groups (Thiagarajan *et al.*, 2010).

Regarding the origin of higher-order interactions in neuronal system, it is interesting to compare the current results with the recent finding that an accurate approximation of population activity can be achieved by incorporating the observed higher-order

interactions (Ganmor *et al.*, 2011a). Ganmor *et al.* developed an effective method to directly measure higher-order interactions by exploiting the sparseness of neuronal responses. However, as those parameters are measured from the data, although this method provides a good fit for population activity, it can not give mechanical understanding about the nature of this interaction structure and does not provide clue for the origin of those higher-order interactions. In contrast, the current results demonstrated that the higher-order interactions are introduced by thresholding and therefore, they can be predicted without direct measurement. This yields important insight into the structure of neuronal interaction. For example, a number of key findings reported by Ganmor *et al.* can be naturally explained in light of the current results, including the stimulus specific failure of the Ising model (see above), the tendency of higher-order interactions to be negative (cf. our Figs. 6.3, 6.4) and the absence of interactions with very high order (the strength of interactions that are introduced by thresholding are expected to decrease rapidly with the increase of order. See Amari *et al.*, 2003). More fundamentally, the sparseness of the neuronal population responses, which makes the method of Ganmor *et al.* applicable in the first place, is likely to be a result of this threshold-based structure of neuronal interactions (Macke *et al.*, 2011)

In the DG model, the multi-dimensional Gaussian structure ensures no higher-order interaction existing before the thresholding. It may also capture some essential features of the neuronal system. As a neuron usually receive large number of synaptic inputs, if the correlation among those inputs is not too strong, central limit theorem indicates that the distribution of the membrane potential (V_m) will be approximately

Gaussian. Actually, this is a commonly used assumption in theoretical studies (Burak *et al.*, 2009; Tchumatchenko *et al.*, 2010) and also consistent with empirical findings (Rudolph *et al.*, 2004; Okun *et al.*, 2010; Constantinople and Bruno, 2011) [but see DeWeese and Zador, (2006) for non-Gaussian distribution of V_m found under anesthesia]. We suggest that to understand the joint distribution of V_m may be crucial to reveal fundamental constraints for neuronal operation. Specifically, if the distribution deviates from multi-dimensional Gaussian, it is likely that higher-order interactions will be present even before the thresholding. The Gaussian assumption is simple enough to allow for a thorough analysis, which we demonstrate in the current study is reasonably accurate. The insight obtained from it can serve as useful reference to study how and when the neuronal system may deviate from this structure and what its functional implication will be. However, we note that some assumptions in the DG model, e.g., lacking of temporal structure, stationarity and equal variance for every dimension are, almost certainly, oversimplified and await future studies to improve.

The existence of higher-order interactions in neural systems has direct implications for studies of functional networks in the brain (Bullmore and Sporns, 2009). Those studies, by far, were based exclusively on pair-wise relations. Our findings show that taking into account of potential higher-order interactions is necessary to reveal the true pair-wise relations (e.g., J_{ij} estimated by the Ising model, see Yu *et al.*, 2008; Ganmor *et al.*, 2011b). More generally, the existence of higher-order interactions highlights the limitation of using conventional graph theoretical network analysis to study interactions among complex systems, as graph theory is usually confined to the

study of pair-wise relations among elements. The current results suggest that to fully understand the functional network of neural systems, conceptual and methodological advances will be required for the representation and analysis of higher-order interactions.

Bibliography

Abeles M, Bergman H, Margalit E, Vaadia E (1993) Spatiotemporal firing patterns in the frontal cortex of behaving monkeys. *J Neurophysiol* 70: 1629-1638.

Amari S, Nakahara H, Wu S, Sakai Y (2003) Synchronous firing and higher-order interactions in neuron pool. *Neural Computation* 15: 127-142.

Beggs JM, Plenz D (2003) Neuronal avalanches in neocortical circuits. *Journal of Neuroscience* 23: 11167-11177.

Bressler SL, Coppola R, Nakamura R (1993) Episodic Multiregional Cortical Coherence at Multiple Frequencies During Visual Task-Performance. *Nature* 366: 153-156.

Bullmore E, Sporns O (2009) Complex brain networks: graph theoretical analysis of structural and functional systems. *Nature Reviews Neuroscience* 10: 186-198.

Burak Y, Lewallen S, Sompolinsky H (2009) Stimulus-Dependent Correlations in Threshold-Crossing Spiking Neurons. *Neural Computation* 21: 2269-2308.

Cocco S, Leibler S, Monasson R (2009) Neuronal couplings between retinal ganglion cells inferred by efficient inverse statistical physics methods. *Proceedings of the National Academy of Sciences of the United States of America* 106: 14058-14062.

Constantinople CM, Bruno RM (2011) Effects and mechanisms of wakefulness on local cortical networks. *Neuron* 69: 1061-1068.

DeWeese MR, Zador AM (2006) Non-Gaussian membrane potential dynamics imply sparse, synchronous activity in auditory cortex. *Journal of Neuroscience* 26: 12206-12218.

Ganmor E, Segev R, Schneidman E (2011a) Sparse low-order interaction network underlies a highly correlated and learnable neural population code. *Proceedings of the National Academy of Sciences of the United States of America*

- Ganmor E, Segev R, Schneidman E (2011b) The Architecture of Functional Interaction Networks in the Retina. *Journal of Neuroscience* 31: 3044-3054.
- Gireesh ED, Plenz D (2008) Neuronal avalanches organize as nested theta- and beta/gamma-oscillations during development of cortical layer 2/3. *Proceedings of the National Academy of Sciences of the United States of America* 105: 7576-7581.
- Gray CM, Konig P, Engel AK, Singer W (1989) Oscillatory Responses in Cat Visual-Cortex Exhibit Inter-Columnar Synchronization Which Reflects Global Stimulus Properties. *Nature* 338: 334-337.
- Hahn G, Petermann T, Havenith MN, Yu S, Singer W, Plenz D, Nikolic D (2010) Neuronal Avalanches in Spontaneous Activity *In vivo*. *Journal of Neurophysiology* 104: 3312-3322.
- Jadhav SP, Wolfe J, Feldman DE (2009) Sparse temporal coding of elementary tactile features during active whisker sensation. *Nature Neuroscience* 12: 792-2328.
- Kinouchi O, Copelli M (2006) Optimal dynamical range of excitable networks at criticality. *Nature Physics* 2: 348-352.
- Klaus A, Yu S, Plenz D (2011) Statistical analyses support power law distributions found in neuronal avalanches. *Plos One* 6: e19779.
- Macke JH, Opper M, Bethge M (2011) Common Input Explains Higher-Order Correlations and Entropy in a Simple Model of Neural Population Activity. *Physical Review Letters* 106: 208102.
- Macke JH, Berens P, Ecker AS, Tolias AS, Bethge M (2009) Generating Spike Trains with Specified Correlation Coefficients. *Neural Computation* 21: 397-423.
- Montani F, Ince RAA, Senatore R, Arabzadeh E, Diamond ME, Panzeri S (2009) The impact of high-order interactions on the rate of synchronous discharge and information transmission in somatosensory cortex. *Philosophical Transactions of the Royal Society A-Mathematical Physical and Engineering Sciences* 367: 3297-3310.
- Nakahara H, Amari S (2002) Information-geometric measure for neural spikes. *Neural Computation* 14: 2269-2316.
- Nemenman I, Shafee F, Bialek W (2002) Entropy and inference, revisited. In: *Adv. Neural Inf. Proc. Syst.* 14 (Dietterich TG, Becker S, Ghahramani Z, eds), Cambridge, MA: MIT Press.
- Ohiorhenuan IE, Mechler F, Purpura KP, Schmid AM, Hu Q, Victor JD (2010) Sparse coding and high-order correlations in fine-scale cortical networks. *Nature* 466: 617-621.

- Ohiorhenuan IE, Victor JD (2011) Information-geometric measure of 3-neuron firing patterns characterizes scale-dependence in cortical networks. *Journal of Computational Neuroscience* 30: 125-141.
- Okun M, Naim A, Lampl I (2010) The Subthreshold Relation between Cortical Local Field Potential and Neuronal Firing Unveiled by Intracellular Recordings in Awake Rats. *Journal of Neuroscience* 30: 4440-4448.
- Petermann T, Thiagarajan TC, Lebedev MA, Nicolelis MAL, Chialvo DR, Plenz D (2009) Spontaneous cortical activity in awake monkeys composed of neuronal avalanches. *Proceedings of the National Academy of Sciences of the United States of America* 106: 15921-15926.
- Plenz D, Thiagarajan TC (2007) The organizing principles of neuronal avalanches: cell assemblies in the cortex? *Trends in Neurosciences* 30: 101-110.
- Ribeiro TL, Copelli M, Caixeta F, Belchior H, Chialvo DR, Nicolelis MAL, Ribeiro S (2010) Spike Avalanches Exhibit Universal Dynamics across the Sleep-Wake Cycle. *Plos One* 5: e14129.
- Riehle A, Grun S, Diesmann M, Aertsen A (1997) Spike synchronization and rate modulation differentially involved in motor cortical function. *Science* 278: 1950-1953.
- Rodriguez E, George N, Lachaux JP, Martinerie J, Renault B, Varela FJ (1999) Perception's shadow: long-distance synchronization of human brain activity. *Nature* 397: 430-433.
- Roudi Y, Nirenberg S, Latham PE (2009) Pairwise Maximum Entropy Models for Studying Large Biological Systems: When They Can Work and When They Can't. *Plos Computational Biology* 5.
- Rudolph M, Piwkowska Z, Badoual M, Bal T, Destexhe A (2004) A method to estimate synaptic conductances from membrane potential fluctuations. *Journal of Neurophysiology* 91: 2884-2896.
- Santos GS, Gireesh ED, Plenz D, Nakahara H (2010) Hierarchical Interaction Structure of Neural Activities in Cortical Slice Cultures. *Journal of Neuroscience* 30: 8720-8733.
- Schneidman E, Berry MJ, Segev R, Bialek W (2006) Weak pairwise correlations imply strongly correlated network states in a neural population. *Nature* 440: 1007-1012.
- Shew WL, Yang H, Petermann T, Roy R, Plenz D (2009) Neuronal Avalanches Imply Maximum Dynamic Range in Cortical Networks at Criticality. *Journal of Neuroscience* 29: 15595-15600.

- Shew WL, Yang H, Yu S, Roy R, Plenz D (2011) Information Capacity and Transmission Are Maximized in Balanced Cortical Networks with Neuronal Avalanches. *Journal of Neuroscience* 31: 55-63.
- Shlens J, Field GD, Gauthier JL, Greschner M, Sher A, Litke AM, Chichilnisky EJ (2009) The Structure of Large-Scale Synchronized Firing in Primate Retina. *Journal of Neuroscience* 29: 5022-5031.
- Shlens J, Field GD, Gauthier JL, Grivich MI, Petrusca D, Sher A, Litke AM, Chichilnisky EJ (2006) The structure of multi-neuron firing patterns in primate retina. *Journal of Neuroscience* 26: 8254-8266.
- Singer W (1999) Neuronal synchrony: A versatile code for the definition of relations? *Neuron* 24: 49-65.
- Stewart CV, Plenz D (2006) Inverted-U profile of dopamine-NMDA-mediated spontaneous avalanche recurrence in superficial layers of rat prefrontal cortex. *Journal of Neuroscience* 26: 8148-8159.
- Stewart CV, Plenz D (2008) Homeostasis of neuronal avalanches during postnatal cortex development *in vitro*. *Journal of Neuroscience Methods* 169: 405-416.
- Stuttgen MC, Schwarz C (2008) Psychophysical and neurometric detection performance under stimulus uncertainty. *Nature Neuroscience* 11: 1091-1099.
- Tang A, Jackson D, Hobbs J, Chen W, Smith JL, Patel H, Prieto A, Petrusca D, Grivich MI, Sher A, Hottowy P, Dabrowski W, Litke AM, Beggs JM (2008) A maximum entropy model applied to spatial and temporal correlations from cortical networks *in vitro*. *Journal of Neuroscience* 28: 505-518.
- Tchumatchenko T, Geisel T, Volgushev M, Wolf F (2010) Signatures of synchrony in pairwise count correlations. *Frontiers in Computational Neuroscience* 4.
- Thiagarajan TC, Lebedev MA, Nicolelis MA, Plenz D (2010) Coherence Potentials: Loss-Less, All-or-None Network Events in the Cortex. *PLoS Biol* 8: e1000278.
- Vaadia E, Haalman I, Abeles M, Bergman H, Prut Y, Slovin H, Aertsen A (1995) Dynamics of Neuronal Interactions in Monkey Cortex in Relation to Behavioral Events. *Nature* 373: 515-518.
- Yu S, Huang D, Singer W, Nikolic D (2008) A Small World of Neuronal Synchrony. *Cerebral Cortex* 18: 2891-2901.

Chapter 7: Conclusion and discussion

Understanding how the brain works has always been the central topic in neuroscience. Great advances have been made in the past century, for example, we know a lot about the wiring diagram in the brain, the functions of different brain regions, the biophysical properties of ion channels, the dynamics of single neurons, the roles of different cell types, the effects of neural modulators, and even the genes that are responsible for certain mental diseases. However, as physicists are diligently searching for a unified theory that can explain almost every phenomenon, neuroscientists also need such a ‘grand unified theory’ to form an coherent image of how the brain works, *i.e.* the computational algorithms the brain uses, and the rules that determine the dynamical processes in the brain, if there are any. We are still far from that achievement.

7.1 Conclusion

In this dissertation, we experimentally examined a hypothesis that a healthy cortical network operates near the critical point (Beggs and Plenz, 2003; 2004; Gireesh and Plenz, 2008; Pasquale *et al.*, 2008; Petermann *et al.*, 2009; Hahn *et al.*, 2010). By using various *in vitro* and *in vivo* preparations, we not only provided further evidence that the cortex may work close to the critical state, but also experimentally demonstrated the advantages of information processing when the cortical network is

in such a state. Therefore, we suggest criticality as a potential principle of information processing in the cortex.

In Chapter 3, we study the diversity of the patterns repertoire of neuronal activity and the efficiency of communication between different neuronal groups (Shew *et al.*, 2011). These factors would inherently constrain the network to store, transfer and process information. We measured activity patterns obtained from multisite local field potential recordings in cortex cultures, urethane anesthetized rats, and awake macaque monkeys and quantified the information capacity of the pattern repertoire of ongoing and stimulus-evoked activity using Shannon entropy. We also quantified the efficacy of information transmission between stimulus and response using mutual information. By systematically changing the ratio of excitation/inhibition (E/I) *in vitro* and in a network model, we discovered that both information capacity and information transmission are maximized at a particular intermediate E/I, at which ongoing activity emerges as neuronal avalanches.

In Chapter 4, another aspect of the optimization principles in ongoing neuronal activity is studied by examining how different groups of neurons can be synchronized and the repertoire of synchronized neuronal assemblies. This study also links our hypothesis to the existing theory of neuronal synchronization. If synchrony is important, so is the variability of synchrony, because a diverse and variable repertoire of brain functions is thought to require a diverse and variable repertoire of synchronized neural groups. We found that when E/I is balanced, where ongoing

activity organizes as neuronal avalanches, maximized variability of synchronous neural groups coincides with the onset of synchrony.

In Chapter 5, the study is focused on the sensitivity of neuronal response to external stimuli, *i.e.* the dynamic range (Shew *et al.*, 2009). We demonstrated that cortical networks that generate neuronal avalanches benefit from a maximized dynamic range, *i.e.*, the ability to respond to the greatest range of stimuli.

In Chapter 6, we study the underlying interaction structures that give rise to population neuronal activity, in terms of neuronal avalanches and population spikes. We showed that only including up to 2nd order interactions (the Ising model) fails to capture essential features in ongoing neuronal avalanche dynamics of awake monkeys as well as evoked activities in the cat visual cortex. Instead, these dynamics are accurately predicted by a pair-wise Gaussian interaction model, in which high-order interactions are introduced through a simple non-linear, *i.e.* thresholding, operation. These findings suggest that cortical dynamics naturally contain high-order interactions that arise from intrinsic non-linear processes, such as local field potential and spike generation. This would apply inherent constraints on information processing in neural network.

7.2 Discussion

7.2.1 Converging the views of criticality, balanced E/I and optimal brain functions

Our results strongly suggest that the cortex operates close to the critical point, and our findings put the following phenomena and models into the same general framework: 1) neuronal avalanches, 2) the balance of excitation and inhibition, 3) criticality, 4) the optimization of information processing functions, *i.e.* ongoing pattern repertoire, the efficacy of information transmission between neuronal groups, ongoing synchronized neuronal assemblies, and discrimination to external stimuli.

The excitation and inhibition in a neural network is usually balanced (Shu *et al.*, 2003; Wehr and Zador, 2003; Haider *et al.*, 2006; Okun and Lampl, 2008), where neuronal avalanches are observed (Shew *et al.*, 2009; 2011). Unbalanced E/I will lead to abnormal, pathological states (Uhlhaas and Singer, 2006; 2010), and the signature of neuronal avalanches, *i.e.* the power law size distribution, will turn into either exponential decay or bimodality. In theories of criticality, the balance of successful propagation and failure is required to reach the critical state as well. Departure from such balance will also lead to abnormal dynamical properties observed in unbalanced neural networks (Beggs and Plenz, 2003; Haldeman and Beggs, 2005).

These findings suggest that cortical dynamics can be studied and understood within a general and coherent framework and principle, that is criticality or E/I balance. By adjusting the excitatory and inhibitory signaling during development, the matured cortical network is poised around the E/I balance state, where the network dynamics

are organized as neuronal avalanches, and cortical functions of information processing are optimized.

7.2.2 Criticality might be a preferred state for the brain

The brain is able to execute a variety of diverse functions, which is thought to be effected by transient assemblies of neuronal activity (Haken *et al.*, 1985; Rodriguez *et al.*, 1999). The variety of brain functions requires a variety of transient neuronal assemblies (Friston, 1997; McIntosh *et al.*, 2008; Garrett *et al.*, 2011), manifested either by binary patterns or transient synchronization. As predicted by criticality models in physics and more biologically relevant neural network models, and subsequently confirmed by experiments, the variety of transiently co-activated neuronal assemblies is maximized in the E/I balanced state, *i.e.* the critical state (Bertschinger and Natschläger, 2004; Haldeman and Beggs, 2005; Tanaka *et al.*, 2009; de Arcangelis and Herrmann, 2010; Shew *et al.*, 2011). The optimization of internal representational capability will lead to the optimal representation of external stimuli, which is also predicted by theory and verified in experiments (Kinouchi and Copelli, 2006; Shew *et al.*, 2009). Achieving such functional advantages in order to survive in the natural selection process (e.g. be able to spot the enemy in a dark environment or sense the slightest vibration when predator is approaching) might be a reason that the neural network chooses to evolve toward the critical state.

7.2.3 Pharmacological manipulation of E/I is a complicated process

Regardless of the great similarities found between experiments and models, the exact mapping from drug effects to changing connection strength is difficult (Bartos *et al.*, 2007). For example, by applying GABA_A antagonists, mutual inhibition in interneurons is reduced, and interneuron activation is known to support certain types of neuronal synchronization. At the same time, reduced inhibition could enhance mutual excitation in pyramidal neurons, which could lead to increased synchrony. As can be seen, the reduction of inhibition has two competing effects, and just increasing overall connection strength in models can be an oversimplified approach. The net effect of the change of global synchronized activity is difficult to predict and require more sophisticated models to incorporate such detailed aspects. The availability of light-gated ion channels provides experimentalists with new tools to suppress or enhance the activity of specific cell types (Boyden *et al.*, 2005), such that different effects of changing E/I can be studied separately.

The model is also oversimplified in some other aspects. For example, it is a purely probabilistic model, and it lacks the structures in the degree of connectivity and the strength of connection.

7.2.4 Questions that remain

Diverging correlation length is a fundamental property of criticality. Linking distant brain regions is obviously favored because the execution of many functions requires

coordinating different brain areas, and neuronal firing patterns are sparse (Jadhav *et al.*, 2009; Poo and Isaacson, 2009; Ohiorhenuan *et al.*, 2010), where long distance correlation is also a necessity. However, experimental evidence of diverging correlation length is still lacking, mainly due to the constraints of experimental apparatus. In addition, the idea that cortical network at criticality is endowed with maximal capacity to represent and transmit information also brings a problem: how could the brain readout/decode information if the responses to the same stimulus are maximally variable? In the critical state, system is also very sensitive to external perturbation, *i.e.* the divergence of susceptibility. By enhancing the ability to represent a larger range of stimuli, would it pay the price of responding to the same stimulus with less accuracy? Is there a solution to such a dilemma?

7.3 Future directions

7.3.1 Implications from the DG model

The study in Chapter 6 may have profound influence on understanding how the brain processes information. The DG model can precisely predict the occurrence of population activity patterns, indicating that the mechanism in the model, *i.e.* thresholding multivariate Gaussian distribution, provides insights into the neuronal network. Indeed, a neuron receives thousands of weakly correlated inputs, which can be approximated as Gaussian (Okun *et al.*, 2010), and that spike generation is a thresholding process. Importantly, this mechanism indicates that the higher order interactions are not free parameters, and they are determined by the underlying

covariance of membrane potentials, firing rates and 2nd order interactions. It also suggests that higher order interactions convey no additional information. This might greatly impact our understanding of how information is processed.

Another interesting feature inferred from this study is that when the underlying covariance of Gaussian distribution is fixed, firing rates and pair-wise correlation have a destined relation (Macke *et al.*, 2011), which means under such condition, pair-wise correlation is not a free parameter either. To examine such relations, we can perform dual patch experiments.

7.3.2 Imaging

So far, most of the studies of neuronal avalanches are focused on local field potentials measurements. If critical branching is the dynamical rule, size distribution with the same statistical properties should be observed at the scale of spike propagation. However, other studies on population spiking activity did not find a robust -1.5 power law (Pasquale *et al.*, 2008; Takahashi *et al.*, 2010). It is very likely that due to severe sub-sampling problem, the complete correlation structure of neuronal network can not be easily captured by sparsely constructed electrode arrays. New techniques need to be employed, such as calcium imaging of neuronal tissue *in vitro* and *in vivo* (Bonifazi *et al.*, 2009), possibly combined with genetically encoded calcium indicators (Tian *et al.*, 2009), which provides the ability to image more neurons in a local circuit. Under such conditions, it may be possible to study the propagation of spiking activity with improved results. In addition, two photon calcium imaging can

be combined with parallel multi-electrode array recording in the same cortical area, and the statistical properties of calcium signals can be correlated to the emergence or disappearance of avalanche dynamics.

7.3.3 Optimal functions *in vivo*

Most of the optimization functions we have identified are from *in vitro* studies, and big differences exist between *in vitro* and *in vivo* experiments. Questions like how the animal responds to varying levels of natural stimuli and what is the relation between the behavior performance and the underlying neuronal activity are currently unknown, and only can be investigated with *in vivo* setups. Animal can be head-fixed under two photon microscope, and calcium imaging is performed in a specific cortical area while the animal is trained to perform a behavior task. Optogenetic tools can be used in the same cortical region to finely tune E/I balance. The relations among E/I balance, circuit level dynamics and behavior performance can be studied.

Bibliography

Arcangelis L de, Herrmann HJ (2010) Learning as a phenomenon occurring in a critical state. Proceedings of the National Academy of Sciences of the United States of America 107:3977-81

Bartos M, Vida I, Jonas P (2007) Synaptic mechanisms of synchronized gamma oscillations in inhibitory interneuron networks. Nature reviews. Neuroscience 8:45-56

Beggs JM, Plenz D (2003) Neuronal avalanches in neocortical circuits. The Journal of neuroscience 23:11167-77

- Beggs JM, Plenz D (2004) Neuronal avalanches are diverse and precise activity patterns that are stable for many hours in cortical slice cultures. *The Journal of neuroscience* 24:5216-29
- Bertschinger N, Natschläger T (2004) Real-time computation at the edge of chaos in recurrent neural networks. *Neural computation* 16:1413-36
- Bonifazi P, Goldin M, Picardo M a, Jorquera I, Cattani a, Bianconi G, Represa a, Ben-Ari Y, Cossart R (2009) GABAergic hub neurons orchestrate synchrony in developing hippocampal networks. *Science (New York, N.Y.)* 326:1419-24
- Boyden ES, Zhang F, Bamberg E, Nagel G, Deisseroth K (2005) Millisecond-timescale, genetically targeted optical control of neural activity. *Nature neuroscience* 8:1263-8
- Fries P, Nikolić D, Singer W (2007) The gamma cycle. *Trends in neurosciences* 30:309-16
- Friston KJ (1997) Transients, metastability, and neuronal dynamics. *NeuroImage* 5:164-71
- Garrett DD, Kovacevic N, McIntosh a R, Grady CL (2011) The Importance of Being Variable. *Journal of Neuroscience* 31:4496-4503
- Gireesh ED, Plenz D (2008) Neuronal avalanches organize as nested theta- and beta/gamma-oscillations during development of cortical layer 2/3. *Proceedings of the National Academy of Sciences of the United States of America* 105:7576-81
- Hahn G, Petermann T, Havenith MN, Yu S, Singer W, Plenz D, Nikolic D (2010) Neuronal avalanches in spontaneous activity *in vivo*. *Journal of neurophysiology*:3312-3322
- Haider B, Duque A, Hasenstaub AR, McCormick D a (2006) Neocortical network activity *in vivo* is generated through a dynamic balance of excitation and inhibition. *The Journal of neuroscience* 26:4535-45
- Haken H, Kelso JAS, Bunz H (1985) A theoretical model of phase transitions in human hand movements. *Biological Cybernetics* 51:347-356
- Haldeman C, Beggs J (2005) Critical Branching Captures Activity in Living Neural Networks and Maximizes the Number of Metastable States. *Physical Review Letters* 94:1-4
- Jadhav SP, Wolfe J, Feldman DE (2009) Sparse temporal coding of elementary tactile features during active whisker sensation. *Nature neuroscience* 12:792-800

Kinouchi O, Copelli M (2006) Optimal dynamical range of excitable networks at criticality. *Nature Physics* 2:348-351

Macke J, Opper M, Bethge M (2011) Common Input Explains Higher-Order Correlations and Entropy in a Simple Model of Neural Population Activity. *Physical Review Letters* 106:1-4

McIntosh AR, Kovacevic N, Itier RJ (2008) Increased brain signal variability accompanies lower behavioral variability in development. *PLoS computational biology* 4:e1000106

Ohiorhenuan IE, Mechler F, Purpura KP, Schmid AM, Hu Q, Victor JD (2010) Sparse coding and high-order correlations in fine-scale cortical networks. *Nature* 466:617-621

Okun M, Lampl I (2008) Instantaneous correlation of excitation and inhibition during ongoing and sensory-evoked activities. *Nature neuroscience* 11:535-7

Okun M, Naim A, Lampl I (2010) The subthreshold relation between cortical local field potential and neuronal firing unveiled by intracellular recordings in awake rats. *The Journal of neuroscience* 30:4440-8

Pasquale V, Massobrio P, Bologna LL, Chiappalone M, Martinoia S (2008) Self-organization and neuronal avalanches in networks of dissociated cortical neurons. *Neuroscience* 153:1354-69

Petermann T, Thiagarajan TC, Lebedev M a, Nicolelis M a L, Chialvo DR, Plenz D (2009) Spontaneous cortical activity in awake monkeys composed of neuronal avalanches. *Proceedings of the National Academy of Sciences of the United States of America* 106:15921-6

Poo C, Isaacson JS (2009) Odor representations in olfactory cortex: "sparse" coding, global inhibition, and oscillations. *Neuron* 62:850-61

Rodriguez E, George N, Lachaux JP, Martinerie J, Renault B, Varela FJ (1999) Perception's shadow: long-distance synchronization of human brain activity. *Nature* 397:430-3

Shew WL, Yang H, Petermann T, Roy R, Plenz D (2009) Neuronal avalanches imply maximum dynamic range in cortical networks at criticality. *The Journal of neuroscience* 29:15595-600

Shew WL, Yang H, Yu S, Roy R, Plenz D (2011) Information Capacity and Transmission Are Maximized in Balanced Cortical Networks with Neuronal Avalanches. *JOURNAL OF NEUROSCIENCE* 31:55-63

Shu Y, Hasenstaub A, McCormick DA (2003) Turning on and off recurrent balanced cortical activity. *Nature* 423

Singer W (1999) Neuronal Synchrony : A Versatile Code for the Definition of Relations ? Most of our knowledge about the functional organization. *Neuron* 24:49-65

Takahashi N, Sasaki T, Matsumoto W, Matsuki N, Ikegaya Y (2010) Circuit topology for synchronizing neurons in spontaneously active networks. *Proceedings of the National Academy of Sciences of the United States of America* 107:10244-10249

Tanaka T, Kaneko T, Aoyagi T (2009) Recurrent infomax generates cell assemblies, neuronal avalanches, and simple cell-like selectivity. *Neural computation* 21:1038-67

Tian L, Hires SA, Mao T, Huber D, Chiappe ME, Chalasani SH, Petreanu L, Akerboom J, McKinney S a, Schreiter ER, Bargmann CI, Jayaraman V, Svoboda K, Looger LL (2009) Imaging neural activity in worms, flies and mice with improved GCaMP calcium indicators. *Nature methods* 6:875-81

Uhlhaas PJ, Singer W (2006) Neural synchrony in brain disorders: relevance for cognitive dysfunctions and pathophysiology. *Neuron* 52:155-68

Uhlhaas PJ, Singer W (2010) Abnormal neural oscillations and synchrony in schizophrenia. *Nature reviews. Neuroscience* 11:100-13

Wehr M, Zador AM (2003) Balanced inhibition underlies tuning and sharpens spike timing in auditory cortex. *Nature* 426:442-6

Bibliography

Abeles M, Bergman H, Margalit E, Vaadia E (1993) Spatiotemporal firing patterns in the frontal cortex of behaving monkeys. *J Neurophysiol* 70: 1629-1638.

Amari S, Nakahara H, Wu S, Sakai Y (2003) Synchronous firing and higher-order interactions in neuron pool. *Neural Computation* 15: 127-142.

Aon MA, Cortassa S, O'Rourke B (2004) Percolation and criticality in a mitochondrial network. *Proceedings of the National Academy of Sciences of the United States of America* 101:4447-52

Arcangelis L de, Perrone-Capano C, Herrmann H (2006) Self-Organized Criticality Model for Brain Plasticity. *Physical Review Letters* 96:1-4

Arcangelis L de, Herrmann HJ (2010) Learning as a phenomenon occurring in a critical state. *Proceedings of the National Academy of Sciences of the United States of America* 107:3977-81

Arenas A, Diazguilera A, Kurths J, Moreno Y, Zhou C (2008) Synchronization in complex networks. *Phys Rep* 469:93-153

Arieli A, Sterkin A, Grinvald A, Aertsen A (1996) Dynamics of ongoing activity: explanation of the large variability in evoked cortical responses. *Science* 273:1868-1871.

Azouz R, Gray CM (1999) Cellular mechanisms contributing to response variability of cortical neurons *in vivo*. *The Journal of Neuroscience* 19:2209-2223.

Bak P, Paczuski M (1995) Complexity, contingency, and criticality. *Proceedings of the National Academy of Sciences of the United States of America* 92:6689-6696.

Bartos M, Vida I, Jonas P (2007) Synaptic mechanisms of synchronized gamma oscillations in inhibitory interneuron networks. *Nat Rev Neurosci* 8:45-56.

Beggs JM, Plenz D (2003) Neuronal avalanches in neocortical circuits. *Journal of Neuroscience* 23: 11167-11177.

Beggs JM, Plenz D (2004) Neuronal avalanches are diverse and precise activity patterns that are stable for many hours in cortical slice cultures. *The Journal of neuroscience* 24:5216-29

- Beggs JM (2008) The criticality hypothesis: how local cortical networks might optimize information processing. *Philosophical transactions. Series A, Mathematical, physical, and engineering sciences* 366:329-43
- Berkes P, Orban G, Lengyel M, Fiser J (2011) Spontaneous Cortical Activity Reveals Hallmarks of an Optimal Internal Model of the Environment. *Science* 331:83-87.
- Bertschinger N, Natschlag T (2004) Real-time computation at the edge of chaos in recurrent neural networks. *Neural Comput* 16:1413-1436.
- Bienenstock E, Lehmann D (1999) Regulated Criticality in the Brain? *Advances in Complex Systems* 1:361-384
- Bonifazi P, Goldin M, Picardo M a, Jorquera I, Cattani a, Bianconi G, Represa a, Ben-Ari Y, Cossart R (2009) GABAergic hub neurons orchestrate synchrony in developing hippocampal networks. *Science (New York, N.Y.)* 326:1419-24
- Boraud T, Brown P, Goldberg JA, Graybiel AM, Magill PJ (2005) OSCILLATIONS IN THE BASAL GANGLIA : The good , the bad , and the unexpected In J. P. Bolam, C. A. Ingham, & P. J. Magill, eds. *The Basal Ganglia VIII* (Editors: New York: Springer Science and Business Media, p. 3-24.
- Bornholdt S, Röhl T (2003) Self-organized critical neural networks. *Physical Review E* 67:1-5
- Boyden ES, Zhang F, Bamberg E, Nagel G, Deisseroth K (2005) Millisecond-timescale, genetically targeted optical control of neural activity. *Nature neuroscience* 8:1263-8
- Breskin I, Soriano J, Moses E, Tlustý T (2006) Percolation in living neural networks. *Physical Review Letters* 97:188102.
- Bressler SL, Coppola R, Nakamura R (1993) Episodic Multiregional Cortical Coherence at Multiple Frequencies During Visual Task-Performance. *Nature* 366:153-156.
- Bressler SL, Kelso JAS (2001) Cortical coordination dynamics and cognition. *Trends Cogn Sci* 5:26-36.
- Buice MA, Cowan JD (2007) Field-theoretic approach to fluctuation effects in neural networks. *Physical Review E Stat Nonlin Soft Matter Phys* 75:051919.
- Buice M A, Cowan JD (2009) Statistical mechanics of the neocortex. *Prog Biophys Mol Bio* 99:53-86.
- Bullmore E, Sporns O (2009) Complex brain networks: graph theoretical analysis of structural and functional systems. *Nature Reviews Neuroscience* 10: 186-198.

Burak Y, Lewallen S, Sompolinsky H (2009) Stimulus-Dependent Correlations in Threshold-Crossing Spiking Neurons. *Neural Computation* 21: 2269-2308.

Cang J, Rentería RC, Kaneko M, Liu X, Copenhagen DR, Stryker MP (2005) Development of precise maps in visual cortex requires patterned spontaneous activity in the retina. *Neuron* 48:797-809

Chagnac-Amitai Y, Connors BW (1989) Horizontal spread of synchronized activity in neocortex and its control by GABA-mediated inhibition. *J Neurophys* 61:747-58.

Chen D-mei, Wu S, Guot A, Yang ZR (1995) Self-organized criticality in a cellular automaton model of pulse-coupled integrate-and-fire neurons. *Journal of Physics A: Mathematical and General* 28:5177

Chialvo DR (2010) Emergent complex neural dynamics. *Nature Physics* 6:744-750

Chiu C, Weliky M (2004) Small modulation of ongoing cortical dynamics by sensory input during natural vision. *Nature*

Chrobak JJ, Buzsáki G (1998) Gamma oscillations in the entorhinal cortex of the freely behaving rat. *The Journal of Neuroscience* 18:388-98.

Churchland MM *et al.* (2010) Stimulus onset quenches neural variability: a widespread cortical phenomenon. *Nature Neuroscience* 13, 369-378.

Cocco S, Leibler S, Monasson R (2009) Neuronal couplings between retinal ganglion cells inferred by efficient inverse statistical physics methods. *Proceedings of the National Academy of Sciences of the United States of America* 106: 14058-14062.

Connors BW (1984) Initiation of synchronized neuronal bursting in neocortex. *Nature* 310:685-7.

Constantinople CM, Bruno RM (2011) Effects and mechanisms of wakefulness on local cortical networks. *Neuron* 69: 1061-1068.

Cragg BG, Temperley HN (1955) Memory: the analogy with ferromagnetic hysteresis. *Brain : a journal of neurology* 78:304-16

Crutchfield J, Young K (1989) Inferring statistical complexity. *Physical Review Letters* 63:105-108

Daido H (1990) Intrinsic fluctuations and a phase transition in a class of large populations of interacting oscillators. *J Stat Phys* 60:753-800.

- Dan Y, Atick JJ, Reid RC (1996) Efficient coding of natural scenes in the lateral geniculate nucleus: experimental test of a computational theory. *The Journal of Neuroscience* 10:3351-3362.
- Dayan P, Abbott LF (2001) *Theoretical neuroscience* (MIT Press, Cambridge, Massachusetts, USA).
- Destexhe A (1994) Oscillations, complex spatiotemporal behavior, and information transport in networks of excitatory and inhibitory neurons. *Physical Review E* 50:1594-1606.
- Destexhe A, Contreras D (2006) Neuronal computations with stochastic network states. *Science* 314:85-90.
- DeWeese MR, Zador AM (2006) Non-Gaussian membrane potential dynamics imply sparse, synchronous activity in auditory cortex. *Journal of Neuroscience* 26: 12206-12218.
- Dichter M, Ayala G (1987) Cellular mechanisms of epilepsy: a status report. *Science* 237:157-164.
- Dong DW, Atick JJ (1995) Temporal decorrelation: a theory of lagged and nonlagged responses in the lateral geniculate nucleus. *Network: Computation in Neural Systems* 6:159-178.
- Ecker AS *et al.* (2010) Decorrelated neuronal firing in cortical microcircuits. *Science* 327:584-587.
- Ermentrout GB, Kleinfeld D (2001) Traveling electrical waves in cortex: insights from phase dynamics and speculation on a computational role. *Neuron* 29:33-44.
- Eytan D, Marom S (2006) Dynamics and effective topology underlying synchronization in networks of cortical neurons. *The Journal of Neuroscience* 26:8465-8476.
- Fiser J, Chiu C, Weliky M (2004) Small modulation of ongoing cortical dynamics by sensory input during natural vision. *Nature* 431:573-578.
- Flint AC, Connors BW (1996) Two types of network oscillations in neocortex mediated by distinct glutamate receptor subtypes and neuronal populations. *J Neurophys* 75:951-7.
- Fries P, Nikolić D, Singer W (2007) The gamma cycle. *Trends in neurosciences* 30:309-16

- Fries P (2009) Neuronal gamma-band synchronization as a fundamental process in cortical computation. *Annual review of neuroscience* 32:209-24
- Fries P, Reynolds JH, Rorie AE, Desimone R (2001) Modulation of oscillatory neuronal synchronization by selective visual attention. *Science* 291:1560-3
- Friston KJ (1997) Transients, metastability, and neuronal dynamics. *Neuroimage* 5:164-71.
- Ganmor E, Segev R, Schneidman E (2011a) Sparse low-order interaction network underlies a highly correlated and learnable neural population code. *Proceedings of the National Academy of Sciences of the United States of America*
- Ganmor E, Segev R, Schneidman E (2011b) The Architecture of Functional Interaction Networks in the Retina. *Journal of Neuroscience* 31: 3044-3054.
- Garcia Dominguez L, Wennberg R a, Gaetz W, Cheyne D, Snead OC, Perez Velazquez JL (2005) Enhanced synchrony in epileptiform activity? Local versus distant phase synchronization in generalized seizures. *The Journal of neuroscience* 25:8077-84
- Garrett DD, Kovacevic N, McIntosh AR, Grady CL (2010) Blood oxygen level-dependent signal variability is more than just noise. *The Journal of Neuroscience* 30:4914-21.
- Garrett DD, Kovacevic N, McIntosh a R, Grady CL (2011) The Importance of Being Variable. *Journal of Neuroscience* 31:4496-4503
- Garrigan P *et al.* (2010) Design of a trichromatic cone array. *PLoS Computational Biology* 6:e1000677.
- Gireesh ED, Plenz D (2008) Neuronal avalanches organize as nested theta- and beta/gamma-oscillations during development of cortical layer 2/3. *Proceedings of the National Academy of Sciences of the United States of America* 105:7576-81
- Götz M, Bolz J (1992) Formation and Preservation of cortical layers in slice cultures. *J Neurobiol* 23:783-802.
- Gray CM, König P, Engel AK, Singer W (1989) Oscillatory Responses in Cat Visual-Cortex Exhibit Inter-Columnar Synchronization Which Reflects Global Stimulus Properties. *Nature* 338: 334-337.
- Gutnick MJ, Connors BW, Prince DA (1982) Mechanisms of neocortical epileptogenesis *in vitro*. *J Neurophys* 48:1321-35.

- Hahn G, Petermann T, Havenith MN, Yu S, Singer W, Plenz D, Nikolic D (2010) Neuronal avalanches in spontaneous activity *in vivo*. *Journal of neurophysiology*:3312-3322
- Haider B, Duque A, Hasenstaub AR, McCormick D a (2006) Neocortical network activity *in vivo* is generated through a dynamic balance of excitation and inhibition. *The Journal of neuroscience* 26:4535-45
- Haider B, McCormick D a (2009) Rapid neocortical dynamics: cellular and network mechanisms. *Neuron* 62:171-89
- Haken H, Kelso JAS, Bunz H (1985) A theoretical model of phase transitions in human hand movements. *Biological Cybernetics* 51:347-356
- Haldeman C, Beggs J (2005) Critical Branching Captures Activity in Living Neural Networks and Maximizes the Number of Metastable States. *Physical Review Letters* 94:1-4
- Han F, Caporale N, Dan Y (2008) Reverberation of recent visual experience in spontaneous cortical waves. *Neuron* 60:321-327.
- Harris TE (1989) *The theory of branching processes*. New York: Dover
- Hebb DO (1949) *The Organization of Behavior* (New York: Wiley)
- Hensch TK (2005) Critical period plasticity in local cortical circuits. *Nat Rev Neurosci* 6:877-888.
- Herz A, Hopfield J (1995) Earthquake cycles and neural reverberations: Collective oscillations in systems with pulse-coupled threshold elements. *Physical review letters* 75:1222-1225
- Hinrichsen H (2006) Non-equilibrium phase transitions. *Physica A* 369:1-28.
- Hipp JF, Engel AK, Siegel M (2011) Oscillatory Synchronization in Large-Scale Cortical Networks Predicts Perception. *Neuron* 69:387-396
- Ikegaya Y, Aaron G, Cossart R, Aronov D, Lampl I, Ferster D, Yuste R (2004) Synfire chains and cortical songs: temporal modules of cortical activity. *Science* (New York, N.Y.) 304:559-64
- Jacobs *et al.* (2009) Ruling out and ruling in neural codes. *Proceedings of the National Academy of Sciences of the United States of America* 106:5936-5941.
- Jadhav SP, Wolfe J, Feldman DE (2009) Sparse temporal coding of elementary tactile features during active whisker sensation. *Nature neuroscience* 12:792-800

Jagers, P. (1975) *Branching Processes with Biological Applications*. Wiley, Chichester.

Jaynes ET (1957) Information theory and statistical mechanics. *Physical Review* 106:62–79.

Jensen HJ (1998) *Self-organized criticality: emergent complex behavior in physical and biological systems*. (Cambridge University Press, Cambridge, UK).

Ji D, Wilson MA (2007) Coordinated memory replay in the visual cortex and hippocampus during sleep. *Nature Neuroscience* 10:100-107.

Kanamaru T (2006) Analysis of synchronization between two modules of pulse neural networks with excitatory and inhibitory connections. *Neural Comput* 18:1111-31.

Kanold PO (2009) Subplate neurons: crucial regulators of cortical development and plasticity. *Frontiers in neuroanatomy* 3:16

Katz LC, Shatz CJ (1996) *Synaptic Activity and the Construction of Cortical Circuits*. *Science* 274:1133-1138

Katzner S, Nauhaus I, Benucci A, Bonin V, Ringach DL, Carandini M (2009) Local origin of field potentials in visual cortex. *Neuron* 61:35-41

Kelso JAS, Scholz JP, Schöner G (1986) Nonequilibrium phase transitions in coordinated biological motion: critical fluctuations. *Phys Lett A* 118:279-284.

Kelso JAS (1992) A phase transition in human brain and behavior. *Physics Letters A* 169:134-144

Kelso JAS, Fuchs A, Lancaster R, Holroyd T, Cheyne D, Weinberg H (1998) Dynamic cortical activity in the human brain reveals motor equivalence. *Nature* 392:814-8

Kelso JAS (2008) *An Essay on Understanding the Mind*. *Ecological psychology : a publication of the International Society for Ecological Psychology* 20:180-208

Kenet T, Bibitchkov D, Tsodyks M, Grinvald A, Arieli A (2003) Spontaneously emerging cortical representations of visual attributes. *Nature* 425:954-956.

Kinouchi O, Copelli M (2006) Optimal dynamical range of excitable networks at criticality. *Nature Physics* 2:348-351.

- Kisley MA, Gerstein GL (1999) Trial-to-trial variability and state-dependent modulation of auditory-evoked responses in cortex. *The Journal of Neuroscience* 19:10451-10460.
- Kitzbichler MG, Smith ML, Christensen SR, Bullmore E (2009) Broadband criticality of human brain network synchronization. *PLoS Computational Biology* 5:e1000314.
- Klaus A, Yu S, Plenz D (2011) Statistical analyses support power law distributions found in neuronal avalanches. *Plos One* 6: e19779.
- Kopell N, Somers D (1995) Anti-phase solutions in relaxation oscillators coupled through excitatory interactions. *J Math Biol* 33:261-280.
- Kopell N, Ermentrout GB, Whittington M A, Traub RD (2000) Gamma rhythms and beta rhythms have different synchronization properties. *Proceedings of the National Academy of Sciences of the United States of America* 97:1867-72.
- Kopell N, Kramer M A, Malerba P, Whittington MA (2010) Are different rhythms good for different functions? *Fr Hum Neurosci* 4:187.
- Korshoej AR, Holm MM, Jensen K, Lambert JDC (2010) Kinetic analysis of evoked IPSCs discloses mechanism of antagonism of synaptic GABAA receptors by picrotoxin. *Brit J Pharmacol* 159:636-49.
- Kürten KE (1988) Critical phenomena in model neural networks. *Physics Letters A* 129:157-160
- Langton CG (1990) Computation at the edge of chaos : phase transition and emergent computation. *Physica D: Nonlinear Phenomena* 42:12
- Larremore D, Shew W, Restrepo J (2011) Predicting criticality and dynamic range in complex networks: effects of topology. *Physical Review Letters* 106:1-4
- Laughlin S (1981) A simple coding procedure enhances a neuron's information capacity. *Zeitschrift fur Naturforschung* 36:910-912.
- Legenstein R, Maass W (2007) Edge of chaos and prediction of computational performance for neural circuit models. *Neural Netw* 20:323-334.
- Levina a, Herrmann JM, Geisel T (2007) Dynamical synapses causing self-organized criticality in neural networks. *Nature Physics* 3:857-860
- Li Z (1996) A theory of the visual motion coding in the primary visual cortex. *Neural Comput* 8:705-730.

- Linkenkaer-Hansen K, Nikouline VV, Palva JM, Ilmoniemi RJ (2001) Long-range temporal correlations and scaling behavior in human brain oscillations. *The Journal of neuroscience* 21:1370-7
- Luczak A, Barthó P, Harris KD (2009) Spontaneous events outline the realm of possible sensory responses in neocortical populations. *Neuron* 62:413-425.
- Luhmann HJ, Mittmann T, Luijtelaa G van, Heinemann U (1995) Impairment of intracortical GABAergic inhibition in a rat model of absence epilepsy. *Epilepsy Res* 22:43-51.
- Macke JH, Berens P, Ecker AS, Tolias AS, Bethge M (2009) Generating Spike Trains with Specified Correlation Coefficients. *Neural Computation* 21: 397-423.
- Macke JH, Opper M, Bethge M (2011) Common Input Explains Higher-Order Correlations and Entropy in a Simple Model of Neural Population Activity. *Physical Review Letters* 106: 208102.
- Magri C, Whittingstall K, Singh V, Logothetis NK, Panzeri S (2009) A toolbox for the fast information analysis of multiple-site LFP, EEG and spike train recordings. *BMC Neurosci* 10:81.
- Mallet N, Pogosyan A, Márton LF, Bolam JP, Brown P, Magill PJ (2008) Parkinsonian beta oscillations in the external globus pallidus and their relationship with subthalamic nucleus activity. *The Journal of Neuroscience* 28:14245-58.
- Malsburg C von der (1999) The What and Why of Binding : The Modeler ' s Perspective. *Neuron* 24:95-104
- Malsburg C von der, Phillips WA, Singer W eds. (2010) *Dynamic Coordination in the Brain*. Cambridge, MA: MIT Press.
- Mazzoni A, Broccard FD, Garcia-Perez E, Bonifazi P, Ruaro ME, Torre V (2007) On the dynamics of the spontaneous activity in neuronal networks. *PloS one* 2:e439
- McIntosh AR, Kovacevic N, Itier RJ (2008) Increased brain signal variability accompanies lower behavioral variability in development. *PLoS Computational Biology* 4:e1000106.
- Meisel C, Gross T (2009) Adaptive self-organization in a realistic neural network model. *Physical Review E* 80:1-6
- Melloni L, Molina C, Pena M, Torres D, Singer W, Rodriguez E (2007) Synchronization of neural activity across cortical areas correlates with conscious perception. *The Journal of Neuroscience* 27:2858-65.

- Miller KJ, Sorensen LB, Ojemann JG, Nijs M den (2009) Power-law scaling in the brain surface electric potential. *PLoS computational biology* 5:e1000609
- Millman D, Mihalas S, Kirkwood A, Niebur E (2010) Self-organized criticality occurs in non-conservative neuronal networks during “up” states. *Nature Physics* 6:801-805
- Montani F, Ince RAA, Senatore R, Arabzadeh E, Diamond ME, Panzeri S (2009) The impact of high-order interactions on the rate of synchronous discharge and information transmission in somatosensory cortex. *Philosophical Transactions of the Royal Society A-Mathematical Physical and Engineering Sciences* 367: 3297-3310.
- Monto S, Vanhatalo S, Holmes MD, Palva JM (2007) Epileptogenic neocortical networks are revealed by abnormal temporal dynamics in seizure-free subdural EEG. *Cereb Cortex* 17:1386-93.
- Nakahara H, Amari S (2002) Information-geometric measure for neural spikes. *Neural Computation* 14: 2269-2316.
- Nauhaus I, Busse L, Carandini M, Ringach DL (2009) Stimulus contrast modulates functional connectivity in visual cortex. *Nature Neuroscience* 12:70-76.
- Neltner L, Hansel D (2001) On synchrony of weakly coupled neurons at low firing rate. *Neural Comput* 13:765-74.
- Nemenman I, Shafee F, Bialek W (2002) Entropy and inference, revisited. In: *Adv. Neural Inf. Proc. Syst.* 14 (Dietterich TG, Becker S, Ghahramani Z, eds), Cambridge, MA: MIT Press.
- Netoff TI, Schiff SJ (2002) Decreased neuronal synchronization during experimental seizures. *The Journal of neuroscience* 22:7297-307
- Ohiorhenuan IE, Mechler F, Purpura KP, Schmid AM, Hu Q, Victor JD (2010) Sparse coding and high-order correlations in fine-scale cortical networks. *Nature* 466:617-621
- Ohiorhenuan IE, Victor JD (2011) Information-geometric measure of 3-neuron firing patterns characterizes scale-dependence in cortical networks. *Journal of Computational Neuroscience* 30: 125-141.
- Ohl FW, Scheich H, Freeman WJ (2001) Change in pattern of ongoing cortical activity with auditory category learning. *Nature* 412:733-736.
- Okun M, Lampl I (2008) Instantaneous correlation of excitation and inhibition during ongoing and sensory-evoked activities. *Nature Neuroscience* 11:535-537.

- Okun M, Naim A, Lampl I (2010) The Subthreshold Relation between Cortical Local Field Potential and Neuronal Firing Unveiled by Intracellular Recordings in Awake Rats. *Journal of Neuroscience* 30: 4440-4448.
- Otter R (1949) The Multiplicative Process. *The Annals of Mathematical Statistics* 20:206-224.
- Palva S, Linkenkaer-Hansen K, Näätänen R, Palva JM (2005) Early neural correlates of conscious somatosensory perception. *The Journal of Neuroscience* 25:5248-58.
- Parra J, Kalitzin SN, Lopes da Silva FH (2005) Photosensitivity and visually induced seizures. *Curr Opin Neurol* 18:155-9.
- Pasquale V, Massobrio P, Bologna LL, Chiappalone M, Martinoia S (2008) Self-organization and neuronal avalanches in networks of dissociated cortical neurons. *Neuroscience* 153:1354-69
- Petermann T, Thiagarajan TC, Lebedev MA, Nicolelis MAL, Chialvo DR, Plenz D (2009) Spontaneous cortical activity in awake monkeys composed of neuronal avalanches. *Proceedings of the National Academy of Sciences of the United States of America* 106:15921-6.
- Pinto DJ, Patrick SL, Huang WC, Connors BW (2005) Initiation, propagation, and termination of epileptiform activity in rodent neocortex *in vitro* involve distinct mechanisms. *The Journal of Neuroscience* 25:8131-40.
- Plenz D, Kitai ST (1996) Generation of high-frequency oscillations in local circuits of rat somatosensory cortex cultures. *J Neurophysiol* 76:4180-4184.
- Plenz D (2005) Comment on “Critical Branching Captures Activity in Living Neural Networks and Maximizes the Number of Metastable States.” *Physical Review Letters* 95:219801-219801
- Plenz D, Thiagarajan TC (2007) The organizing principles of neuronal avalanches: cell assemblies in the cortex? *Trends Neurosci* 30:101-110.
- Poil S-S, Ooyen A van, Linkenkaer-Hansen K (2008) Avalanche dynamics of human brain oscillations: relation to critical branching processes and temporal correlations. *Human brain mapping* 29:770-7
- Pola G, Thiele A, Hoffmann K-P, Panzeri S (2003) An exact method to quantify the information transmitted by different mechanisms of correlational coding. *Network: Comput. Neur. Syst.* 14:35-60.
- Poo C, Isaacson JS (2009) Odor representations in olfactory cortex: “sparse” coding, global inhibition, and oscillations. *Neuron* 62:850-61

- Prince D A, Parada I, Scalise K, Graber K, Jin X, Shen F (2009) Epilepsy following cortical injury: cellular and molecular mechanisms as targets for potential prophylaxis. *Epilepsia* 2:30-40.
- Quiari Quiroga R, Panzeri S (2009) Extracting information from neuronal populations: information theory and decoding approaches. *Nat Rev Neurosci* 10:173-185.
- Ramo P, Kauffman S, Kesselia J, Yli-Harja O (2007) Measures for information propagation in Boolean networks. *Physica D* 227:100-104.
- Renart A *et al.* (2010) The asynchronous state in cortical circuits. *Science* 327:587-590.
- Ribeiro TL, Copelli M, Caixeta F, Belchior H, Chialvo DR, Nicolelis MAL, Ribeiro S (2010) Spike Avalanches Exhibit Universal Dynamics across the Sleep-Wake Cycle. *Plos One* 5: e14129.
- Riehle A, Grun S, Diesmann M, Aertsen A (1997) Spike synchronization and rate modulation differentially involved in motor cortical function. *Science* 278: 1950-1953.
- Rieke F, Warland D, de Ruyter van Stevenick R, & Bialek W (1997) *Spikes* (MIT Press, Cambridge, Massachusetts, USA).
- Ringach DL (2009) Spontaneous and driven cortical activity: implications for computation. *Current opinion in neurobiology* 19:439-44
- Rodriguez E, George N, Lachaux JP, Martinerie J, Renault B, Varela FJ (1999) Perception's shadow: long-distance synchronization of human brain activity. *Nature* 397:430-3.
- Roelfsema PR, Engel AK, König P, Singer W (1997) Visuomotor integration is associated with zero time-lag synchronization among cortical areas. *Nature* 385:157-61.
- Roskies AL (1999) The Binding Problem. *Neuron* 24:7-9
- Roudi Y, Latham PE (2007) A balanced memory network. *PLoS Comp Biol* 3:1679-1700.
- Roudi Y, Nirenberg S, Latham PE (2009) Pairwise Maximum Entropy Models for Studying Large Biological Systems: When They Can Work and When They Can't. *Plos Computational Biology* 5.
- Rudolph M, Piwkowska Z, Badoual M, Bal T, Destexhe A (2004) A method to estimate synaptic conductances from membrane potential fluctuations. *Journal of Neurophysiology* 91: 2884-2896.

- Sakurai Y, Takahashi S (2006) Dynamic synchrony of firing in the monkey prefrontal cortex during working-memory tasks. *The Journal of Neuroscience* 26:10141-53.
- Santos GS, Gireesh ED, Plenz D, Nakahara H (2010) Hierarchical Interaction Structure of Neural Activities in Cortical Slice Cultures. *Journal of Neuroscience* 30: 8720-8733.
- Schneidman E, Bialek W, Berry II MJ (2003) Synergy, redundancy, and independence in population codes. *The Journal of Neuroscience* 23:11539 –11553.
- Schneidman E, Berry II MJ, Segev R, Bialek W (2006) Weak pairwise correlations imply strongly correlated network states in a neural population. *Nature* 440:1007-1012.
- Schoner G, Haken H, Kelso JAS (1986) A stochastic theory of phase transitions in human hand movement. *Biological Cybernetics* 53:247-257.
- Schoner G, Kelso J (1988) Dynamic pattern generation in behavioral and neural systems. *Science* 239:1513-1520.
- Sedelnikova A, Erkkila BE, Harris H, Zakharkin SO, Weiss DS (2006) Stoichiometry of a pore mutation that abolishes picrotoxin-mediated antagonism of the GABA_A receptor. *J Physiol* 577:569-77.
- Senkowski D, Schneider TR, Foxe JJ, Engel AK (2008) Crossmodal binding through neural coherence: implications for multisensory processing. *Trends Neurosci* 31:401-9.
- Shadlen MN, Newsome WT (1998) The variable discharge of cortical neurons: implications for connectivity, computation, and information coding. *The Journal of Neuroscience* 18:3870-96.
- Shadlen MN, Movshon J a (1999) Synchrony unbound: a critical evaluation of the temporal binding hypothesis. *Neuron* 24:67-77, 111-25
- Shannon CE (1948) A mathematical theory of communication. *Bell System Technical J* 27:379-423, 623–656.
- Shew WL, Yang H, Petermann T, Roy R, Plenz D (2009) Neuronal Avalanches Imply Maximum Dynamic Range in Cortical Networks at Criticality. *The Journal of Neuroscience* 29:15595-15600.
- Shew WL, Yang H, Yu S, Roy R, Plenz D (2011) Information Capacity and Transmission Are Maximized in Balanced Cortical Networks with Neuronal Avalanches. *Journal of Neuroscience* 31: 55-63.

Shlens J, Field GD, Gauthier JL, Grivich MI, Petrusca D, Sher A, Litke AM, Chichilnisky EJ (2006) The structure of multi-neuron firing patterns in primate retina. *Journal of Neuroscience* 26: 8254-8266.

Shlens J, Field GD, Gauthier JL, Greschner M, Sher A, Litke AM, Chichilnisky EJ (2009) The Structure of Large-Scale Synchronized Firing in Primate Retina. *Journal of Neuroscience* 29: 5022-5031.

Shu Y, Hasenstaub A, McCormick DA (2003) Turning on and off recurrent balanced cortical activity. *Nature* 423:288-293.

Singer W (1999) Neuronal synchrony: A versatile code for the definition of relations? *Neuron* 24: 49-65.

Spencer KM, Nestor PG, Niznikiewicz M A, Salisbury DF, Shenton ME, McCarley RW (2003) Abnormal neural synchrony in schizophrenia. *The Journal of Neuroscience* 23:7407-11.

Stam CJ, Bruin EA de (2004) Scale-free dynamics of global functional connectivity in the human brain. *Human brain mapping* 22:97-109

Stanley HE (1971) *Introduction to Phase Transitions and Critical Phenomena* (Oxford University Press, New York, USA).

Steriade M (2003) *Neuronal Substrates of Sleep and Epilepsy*. Cambridge: Cambridge University Press.

Stewart CV, Plenz D (2006) Inverted-U profile of dopamine-NMDA-mediated spontaneous avalanche recurrence in superficial layers of rat prefrontal cortex. *The Journal of Neuroscience* 26:8148-8159.

Stewart CV, Plenz D (2008) Homeostasis of neuronal avalanches during postnatal cortex development *in vitro*. *Journal of neuroscience methods* 169:405-16

Strogatz SH (2001) Exploring complex networks. *Nature* 410:268-76.

Stuttgen MC, Schwarz C (2008) Psychophysical and neurometric detection performance under stimulus uncertainty. *Nature Neuroscience* 11: 1091-1099.

Sussillo D, Abbott LF (2009) Generating coherent patterns of activity from chaotic neural networks. *Neuron* 27:544-557.

Tagliazucchi E, Chialvo DR (2011) The collective brain is critical. *arXiv:1-14*

- Takahashi N, Sasaki T, Matsumoto W, Matsuki N, Ikegaya Y (2010) Circuit topology for synchronizing neurons in spontaneously active networks. *Proceedings of the National Academy of Sciences of the United States of America* 107:10244-10249
- Tallon-Baudry C, Mandon S, Freiwald W A, Kreiter AK (2004) Oscillatory synchrony in the monkey temporal lobe correlates with performance in a visual short-term memory task. *Cereb Cortex* 14:713-20.
- Tanaka T, Kaneko T, Aoyagi T (2009) Recurrent infomax generates cell assemblies, neuronal avalanches, and simple cell-like selectivity. *Neural computation* 21:1038-67
- Tang A, Jackson D, Hobbs J, Chen W, Smith JL, Patel H, Prieto A, Petrusca D, Grivich MI, Sher A, Hottowy P, Dabrowski W, Litke AM, Beggs JM (2008) A maximum entropy model applied to spatial and temporal correlations from cortical networks *in vitro*. *Journal of Neuroscience* 28: 505-518.
- Tchumatchenko T, Geisel T, Volgushev M, Wolf F (2010) Signatures of synchrony in pairwise count correlations. *Frontiers in Computational Neuroscience* 4.
- Telfeian E, Connors BW (1998) Layer-specific pathways for the horizontal propagation of epileptiform discharges in neocortex. *Epilepsia* 39:700-8.
- Thiagarajan TC, Lebedev MA, Nicolelis MA, Plenz D (2010) Coherence Potentials: Loss-Less, All-or-None Network Events in the Cortex. *PLoS Biol* 8: e1000278.
- Tian L, Hires SA, Mao T, Huber D, Chiappe ME, Chalasani SH, Petreanu L, Akerboom J, McKinney S a, Schreiter ER, Bargmann CI, Jayaraman V, Svoboda K, Looger LL (2009) Imaging neural activity in worms, flies and mice with improved GCaMP calcium indicators. *Nature methods* 6:875-81
- Timofeev I, Steriade M (2004) Neocortical seizures: initiation, development and cessation. *Neuroscience* 123:299-336.
- Tsodyks M, Kenet T, Grinvald A, Arieli A (1999) Linking spontaneous activity of single cortical neurons and the underlying functional architecture. *Science* 286:1943-6.
- Uhlhaas PJ, Singer W (2010) Abnormal neural oscillations and synchrony in schizophrenia. *Nature reviews. Neuroscience* 11:100-13
- Vaadia E, Haalman I, Abeles M, Bergman H, Prut Y, Slovin H, Aertsen A (1995) Dynamics of Neuronal Interactions in Monkey Cortex in Relation to Behavioral Events. *Nature* 373: 515-518.
- van Vreeswijk C, Sompolinsky H (1996) Chaos in neuronal networks with balanced excitatory and inhibitory activity. *Science* 274:1724-1726.

Varela F, Lachaux JP, Rodriguez E, Martinerie J (2001) The brainweb: phase synchronization and large-scale integration. *Nat Rev Neurosci* 2:229-39.

Vreeswijk C van, Sompolinsky H (1996) Chaos in neuronal networks with balanced excitatory and inhibitory activity. *Science (New York, N.Y.)* 274:1724-6

Wehr M, Zador AM (2003) Balanced inhibition underlies tuning and sharpens spike timing in auditory cortex. *Nature* 426:442-6

Wilson TW, Rojas DC, Reite ML, Teale PD, Rogers SJ (2007) Children and adolescents with autism exhibit reduced MEG steady-state gamma responses. *Biol Psychiat* 62:192-7.

Yamawaki N, Stanford IM, Hall SD, Woodhall GL (2008) Pharmacologically induced and stimulus evoked rhythmic neuronal oscillatory activity in the primary motor cortex *in vitro*. *Neurosci* 151:386-95.

Yao H, Shi L, Han F, Gao H, Dan Y (2007) Rapid learning in cortical coding of visual scenes. *Nature Neuroscience* 10:772-778.

Yu S, Huang D, Singer W, Nikolic D (2008) A Small World of Neuronal Synchrony. *Cerebral Cortex* 18: 2891-2901.

Zapperi S, Bakgaard LK, Stanley HE (1995) Self-organized branching processes: Mean-field theory for avalanches. *Physical Review Letters* 75:4071-4074.